Search for Supersymmetric Electroweak Production and the Measurement of Higgs Production Cross-sections at the ATLAS Experiment

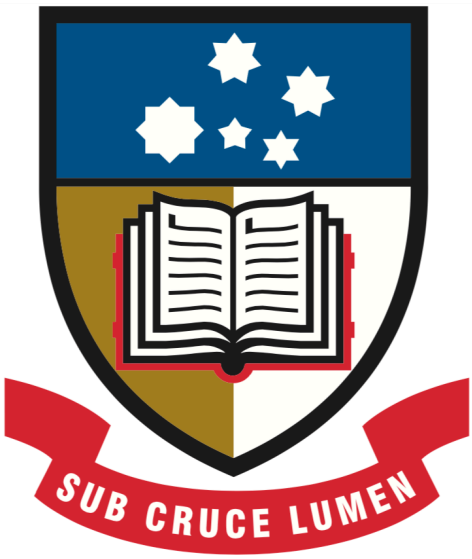

Jason Oliver

Faculty of Sciences

University of Adelaide

A thesis submitted toward the degree of
Doctor of Philosophy

December 2020

To those long passed,
and those yet to come,
and those who shared it with me.

Journey before Destination,
- Brandon Sanderson,

The Way of Kings

Abstract

This thesis presents a search for electroweak production of supersymmetric particles in two-lepton and three-lepton final states. The search uses the data collected from 2015 to 2018 by the ATLAS experiment in $\sqrt{s} = 13$ TeV proton–proton collisions at the CERN Large Hadron Collider, which corresponds to an integrated luminosity of $139.9\ \mathrm{fb}^{-1}$. We present the results of this search using model-independent upper limits. We also present a measurement of the Higgs boson gluon–gluon fusion production cross-section, via the $H \to WW \to \ell\nu\ell\nu$ final state, we use the data collected in 2015 by the ATLAS experiment, which corresponds to an integrated luminosity of $36.1\ \mathrm{fb}^{-1}$. We measure the cross-section of gluon–gluon fusion Higgs production and subsequent decay via WW to be $11.4^{+2.2}_{-2.1}\ \mathrm{pb}$ (statistical and systematic). Finally, we outline prospects in future upgrade works, in the fast simulation of the Fast Tracker ATLAS subsystem and the development of digitisation software in the ATLAS Inner Tracker Strips Detector.

Acknowledgements

The work presented in this thesis wouldn't be possible without the significant support of a great many people. Some contributions have been professional, and others have been personal. Neither is inherently more or less important than the other. Still, as physicists, we tend to downplay the personal, which leaves a large number of unnamed and unacknowledged people. To this end, I'd like to thank all those who will go unnamed, who helped me to learn, laugh, or smile, who shared a coffee with me, or made my coming into the office exciting. No doubt, many acts of kindness have gone by completely forgotten, that's the nature of things. However, I wish to acknowledge the role those acts played in getting me here.

To begin, I would like to pay my special regards to my supervisors Jack and Martin. I began my PhD in ATLAS with approximately no knowledge in the field what-so-ever. Through your supervision and mentoring, I'm now able to teach new students, and that is a great gift. Jack, in moments where I was unsure if I was a good fit for experimental particle physics, you offered words of encouragement, and they went a long way in bolstering my confidence as an physicist. Martin, you've helped me understand the relationship between theory and experiment, and the importance of good science communication.

Big thanks to Abhishek, we've travelled to CERN and back multiple times, and it's always been a pleasure. I'm very proud of the work we've produced together, and I look forward to continuing to work with you in the future. I would also like to thank Andreas Petridis, Benjamin Hooberman, and Max Swiatlowski, each of who provided critical guidance in the development of my projects, and I'd also like to recognise the invaluable assistance the two-lepton team played in our analyses.

Sharon and Silvana, thank you for organising my travel to and from CERN, and for organising many amazing events, including some truly memorable conferences! These were amazing for professional development, and they couldn't have taken place without all of your hard work.

To Zach and Andre, we started our undergrad together, and I'm very grateful we could share our PhD years together too. The Adelaide physics department is filled with people of great character, and I'm incredibly lucky to have the problem of not being able to thank you all individually. Shout out to the CoVfefe chat — if you know, you know.

To Arwa, you have shared in the stresses of my PhD more than perhaps anyone else. You've given me a great deal of support, and you never asked for anything in return. I'm really happy the universe decided to bring us together.

Finally, thank you to Mum and Dad, you've always been supportive and loving, and you've taught me more than anyone to cherish the journey over the destination.

Acknowledgement of CERN and ATLAS

We thank CERN for the very successful operation of the LHC, as well as the support staff from our institutions without whom ATLAS could not be operated efficiently.

We acknowledge the support of ANPCyT, Argentina; YerPhI, Armenia; ARC, Australia; BMWFW and FWF, Austria; ANAS, Azerbaijan; SSTC, Belarus; CNPq and FAPESP, Brazil; NSERC, NRC and CFI, Canada; CERN; ANID, Chile; CAS, MOST and NSFC, China; COLCIENCIAS, Colombia; MSMT CR, MPO CR and VSC CR, Czech Republic; DNRF and DNSRC, Denmark; IN2P3-CNRS and CEA-DRF/IRFU, France; SRNSFG, Georgia; BMBF, HGF and MPG, Germany; GSRT, Greece; RGC and Hong Kong SAR, China; ISF and Benoziyo Center, Israel; INFN, Italy; MEXT and JSPS, Japan; CNRST, Morocco; NWO, Netherlands; RCN, Norway; MNiSW and NCN, Poland; FCT, Portugal; MNE/IFA, Romania; JINR; MES of Russia and NRC KI, Russian Federation; MESTD, Serbia; MSSR, Slovakia; ARRS and MIZŠ, Slovenia; DST/NRF, South Africa; MICINN, Spain; SRC and Wallenberg Foundation, Sweden; SERI, SNSF and Cantons of Bern and Geneva, Switzerland; MOST, Taiwan; TAEK, Turkey; STFC, United Kingdom; DOE and NSF, United States of America. In addition, individual groups and members have received support from BCKDF, CANARIE, Compute Canada, CRC and IVADO, Canada; Beijing Municipal Science & Technology Commission, China; COST, ERC, ERDF, Horizon 2020 and Marie Skłodowska-Curie Actions, European Union; Investissements d'Avenir Labex, Investissements d'Avenir Idex and ANR, France; DFG and AvH Foundation, Germany; Herakleitos, Thales and Aristeia programmes co-financed by EU-ESF and the Greek NSRF, Greece; BSF-NSF and GIF, Israel; La Caixa Banking Foundation, CERCA Programme Generalitat de Catalunya and PROMETEO and GenT Programmes Generalitat Valenciana, Spain; Göran Gustafssons Stiftelse, Sweden; The Royal Society and Leverhulme Trust, United Kingdom.

The crucial computing support from all WLCG partners is acknowledged gratefully, in particular from CERN, the ATLAS Tier-1 facilities at TRIUMF (Canada), NDGF (Denmark, Norway, Sweden), CC-IN2P3 (France), KIT/GridKA (Germany), INFN-CNAF (Italy), NL-T1 (Netherlands), PIC (Spain), ASGC (Taiwan), RAL (UK) and BNL (USA), the Tier-2 facilities worldwide and large non-WLCG resource providers.

Statement of Originality

I certify that this work contains no material which has been accepted for the award of any other degree or diploma in my name, in any university or other tertiary institution and, to the best of my knowledge and belief, contains no material previously published or written by another person, except where due reference has been made in the text. In addition, I certify that no part of this work will, in the future, be used in a submission in my name, for any other degree or diploma in any university or other tertiary institution without the prior approval of the University of Adelaide and where applicable, any partner institution responsible for the joint-award of this degree. This thesis respects the ATLAS experiment policy of not having ATLAS labels on figures produced by a student. Figures which contain the ATLAS label have been produced by the ATLAS collaboration.

I give permission for the digital version of my thesis to be made available on the web, via the University's digital research repository, the Library Search and also through web search engines, unless permission has been granted by the University to restrict access for a period of time.

I acknowledge the support I have received for my research through the provision of an Australian Government Research Training Program Scholarship.

Signed

Jason Oliver

Contents

List of Figures

List of Tables

Preface

This document will outline my contributions in the ATLAS Collaboration; the work completed is naturally split between analysis work and detector development.

Chapter 1 covers the introduction of the Standard Model of particle physics, focusing specifically on particle content, fundamental forces, particle interactions and the Higgs boson. In focusing on the Higgs boson, I provide an overview of electroweak symmetry breaking.

Chapter 2 introduces supersymmetry, focusing on motivations for existence and particle content. I introduce the Minimal Supersymmetric Standard Model (MSSM), the superspace formalism, and highlight electroweak symmetry breaking in the MSSM, as well as the origin of neutralinos and charginos.

In Chapter 3, I introduce the Large Hadron Collider machine, as well as the topics of dataset limitations, proton substructure, and the physics reach of the project. I also introduce the ATLAS experiment, where particular attention is shown to hardware, object reconstruction and Monte Carlo simulation conventions.

In Chapter 4, I detail all work for the search for supersymmetric electroweak production, all techniques leveraged, and all data-driven estimation methodologies employed in the estimation of crucial region backgrounds are described in detail. I provide validation of the techniques, and finally, I present model-independent limits on visible cross-sections of signal processes present within the signal region selections.

In Chapter 5, I present measurements of the gluon–gluon fusion, and vector boson fusion Higgs production cross-sections. I pay special attention to a data-driven b-tagging efficiency estimation technique, which was the core of my contribution, and finish by summarising the combined results from run-II measurements.

In Chapter 6, I introduce the Fast Tracker ATLAS subsystem and the work in implementing a fast simulation alternative to the currently implemented, CPU-expensive full simulation. The fast simulation methodology is described and validated.

In Chapter 7, phase-II ATLAS upgrades are described, focusing specifically on the ATLAS inner detector replacement, known as the Inner Tracker (ITk). I introduce the geometry and design of the ITk, and then focus on the current ATLAS digitisation software implementations. The core question here is the suitability for existing digitisation frameworks for ITk purposes. Finally, I provide validation of implementation, and a comparison between the induced charge model and the simplified model, which is currently the nominal digitisation implementation of the ATLAS experiment.

Chapter 1

The Standard Model

In this chapter, we provide an introduction to the foundational concepts in the Standard Model. We focus on symmetries, particle content, and interactions. We detail electroweak symmetry breaking and mass generation. We summarise the mass dependence of the Higgs boson decay properties, and finally, we outline phenomenological properties of the strong force, which are vital for understanding hadron collider physics.

In the Standard Model (SM), we introduce a field for each type of particle. We can split the symmetries governing the behaviour of these particles into *internal* symmetries and *external* symmetries. Internal symmetries govern the interactions of the particles and are often called *gauge* symmetries. The external symmetries define the Lorentz structure of space-time itself. We formulate the SM on Minkowski space-time, with its symmetries corresponding to those of the Poincaré group. We apply Noether's theorem to determine the conservation laws from the underlying symmetries of the SM.

1.1 Particle Content

We introduce particles in the SM with quantum numbers corresponding to gauge symmetries. The gauge symmetries of the SM are $\mathrm{SU(3)_C} \times \mathrm{SU(2)_L} \times \mathrm{U(1)_Y}$. Where C is the colour, L is chirality, and Y is hypercharge. The unbroken group $\mathrm{SU(2)_L} \times \mathrm{U(1)_Y}$ has four spin-1 gauge bosons B, W^1, W^2 and W^3. The *Brout–Englert–Higgs* mechanism breaks $\mathrm{SU(2)_L} \times \mathrm{U(1)_Y}$ to $\mathrm{U(1)_Q}$, and the electroweak gauge bosons mix into the electromagnetic force carrier - the photon, three weak force carrier bosons (W^+, W^-, and Z^0), and a Higgs boson is introduced [1–6]. The symmetry group $SU(3)_C$ is not involved in electroweak symmetry breaking and remains a symmetry at all measurable energies.

In order to describe observations, we introduce three generations of spin-1/2 fermions which have different masses, which interact with the force carriers identically. We can split the fermions into two different groups - leptons and quarks. The leptons of the SM are the electron, muon and tau (e, μ and τ), and each has a corresponding massless, and neutral, neutrino (ν_e, ν_μ and ν_τ). The SM assumes that neutrinos are massless, given we have measured neutrinos to have non-zero masses, this is a failed prediction of the SM [8].

We can further split the quarks into the up-type and down-type quarks. The up-type quarks are the up, charm, and top quarks (u, c, t). The down-types are down, strange, and bottom (d, s, b). All quarks interact via the strong, weak and electromagnetic forces. The strength of the strong force results in many complex states called mesons ($q\bar{q}$), baryons (qqq) and pentaquarks. We summarise the full particle content of the SM in Figure 1.1,

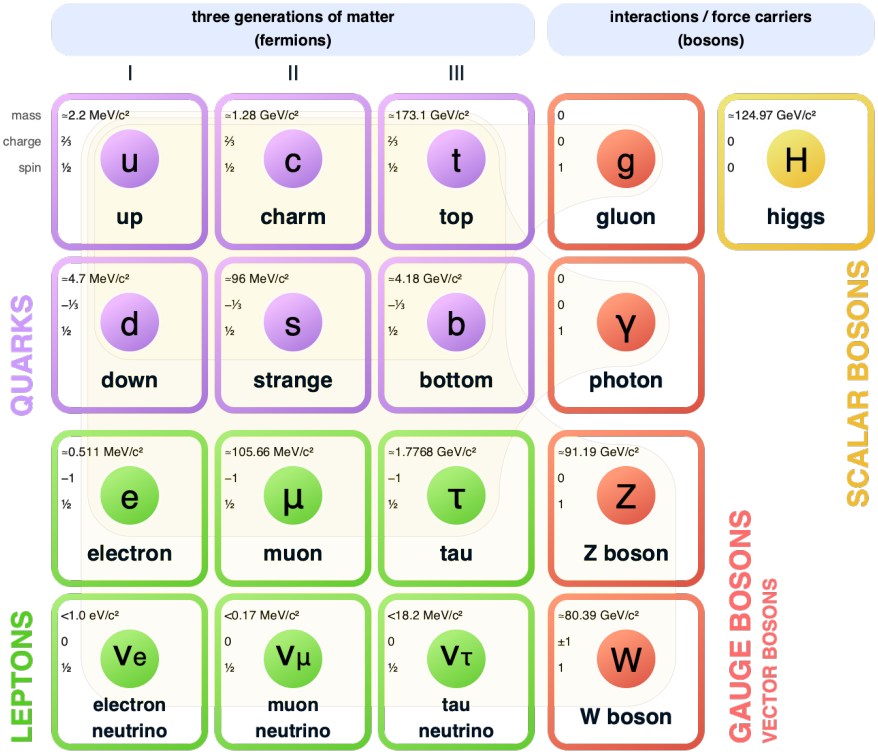

Figure 1.1: A summary of the SM particle content [7].

Table 1.1: SM gauge group representations of gauge bosons.

Gauge group	Gauge boson	$\mathrm{SU(3)_C}$	$SU(2)_L$	$\mathrm{U(1)_Y}$
$\mathrm{SU(3)_C}$	g	**8**	**1**	0
$\mathrm{SU(2)_L}$	W^i	**1**	**3**	0
$\mathrm{U(1)_Y}$	B^0	**1**	**1**	0

the SM group representations for gauge bosons in Table 1.1, with the fermion and Higgs doublet group representations in Table 1.2.

Table 1.2: SM gauge group representations of particle content.

Fields	$\mathrm{SU(3)_C}$	$SU(2)_L$	$\mathrm{U(1)_Y}$
$\begin{pmatrix} u_L & d_L \end{pmatrix}_i$	3	2	$-1/6$
$u^\dagger_{R_i}$	$\bar{3}$	1	-2/3
$d^\dagger_{R_i}$	$\bar{3}$	1	1/3
$\begin{pmatrix} \nu & e_L \end{pmatrix}_i$	1	2	$1/2$
$e^\dagger_{R_i}$	1	1	1
$\begin{pmatrix} \phi^+ & \phi^0 \end{pmatrix}_i$	1	2	1

1.2 The Standard Model Lagrangian

We can represent the symmetries, particle content, and group representations in a mathematical object called a Lagrangian. The Lagrangian describes all interactions and properties of the SM and can be written in the form:

$$\begin{aligned}\mathcal{L}_{SM} = &-\frac{1}{4}F_{\mu\nu}F^{\mu\nu} \\ &+ i\bar{\psi}\gamma^{\mu}D_{\mu}\psi + h.c \\ &+ \bar{\psi}_i y_{ij}\psi_j\phi + h.c \\ &+ |D_{\mu}\phi|^2 - V(\phi),\end{aligned} \tag{1.1}$$

where each term has a unique interpretation,

- $-\frac{1}{4}F_{\mu\nu}F^{\mu\nu}$ governs the self-interactions of the gluons, photon, $W^{\pm}$ and Z^0 bosons.
- $i\bar{\psi}\gamma^{\mu}D_{\mu}\psi + \text{h.c}$ governs the interaction of the fermions with the gauge bosons.
- $\bar{\psi}_i y_{ij}\psi_j\phi + \text{h.c}$ governs the interaction between the fermions and the Higgs boson and generates the fermion masses.
- $|D_{\mu}\phi|^2$ governs the self-interaction of the Higgs boson and generates the gauge boson masses.
- $V(\phi)$ governs the breaking of the electroweak sector into the electromagnetic and weak, and generates the mass for the Higgs boson.

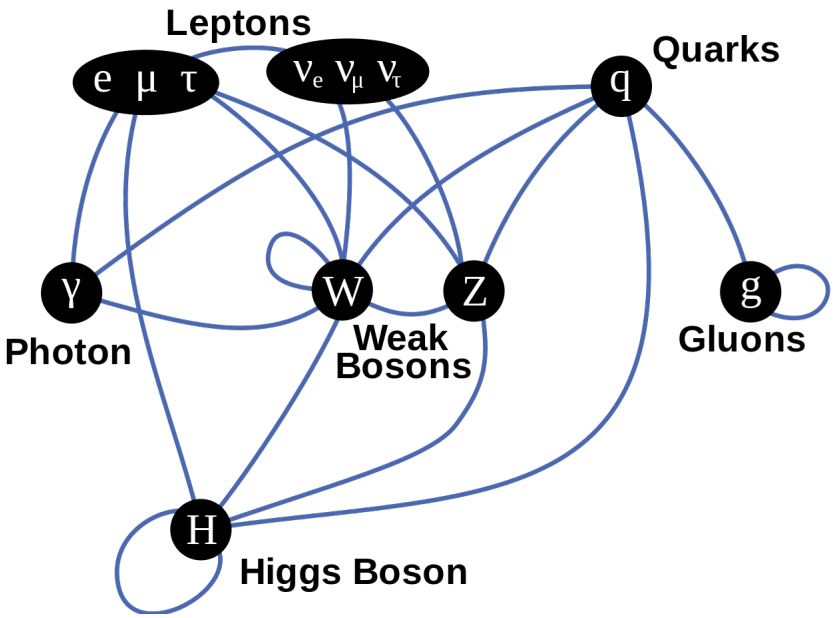

Figure 1.2: Overview of particle interactions in the SM [9].

We can show the interactions between the different particles of the SM in a network graph shown in Figure 1.2. The network graph shows the electromagnetically charged

particles interacting with the photon, and the coloured particles interacting with the gluon. We can see the neutrino is neutral as there is no connection between it and the photon. We can see the gluon and Higgs have a self-interaction as there is a loop connecting to themselves. The network graph also has connections between the Higgs boson and all particles which have mass and we will now explore the mechanism which provides mass to fundamental particles in the Standard Model.

1.3 Electroweak Symmetry Breaking

In 2014, the Nobel prize was awarded to Peter Higgs and Francois Englert for the theoretical discovery of the mechanism that contributes to our understanding of the origin of mass of subatomic particles. Another physicist who notably contributed to the theoretical development of the mechanism was Robert Brout, who passed away in 2011 and was therefore not a recipient.

The Brout-Englert-Higgs mechanism introduces a scalar potential, now known as the Higgs field, which exists at all points in space-time. At high energies, the Higgs field has a vacuum expectation value (VEV) of zero, in Figure 1.3 a VEV of zero corresponds to the central point. At low background energies, such as a universe which has undergone cooling, the Higgs field acquires a non-zero VEV, which corresponds to the trough surrounding the central peak in Figure 1.3. The non-zero VEV results in the acquisition of a non-zero mass for particles interacting with the scalar potential, as detailed from Equation 1.1. We now demonstrate how a non-zero VEV in a scalar potential is able to generate a mass [10].

The Brout-Englert-Higgs mechanisms begins with an $\mathrm{SU}(2)_\mathrm{L}$ Higgs doublet of the form:

$$\phi = \begin{pmatrix} \phi^0 \\ \phi^+ \end{pmatrix} = \frac{1}{\sqrt{2}} \begin{pmatrix} \phi_1 + i\phi_2 \\ \phi_3 + i\phi_4 \end{pmatrix}, \tag{1.2}$$

where ϕ_i are real-valued fields. We take the Higgs doublet and we construct a potential of the form:

$$V(\phi) = \frac{1}{2}\mu^2 \left(\sum_{i=1}^{4} \phi_i^2 \right) + \frac{1}{4}\lambda \left(\sum_{i=1}^{4} \phi_i^2 \right)^2, \tag{1.3}$$

where i runs over each real-valued field in the Higgs doublet. To understand physics at low energies we must expand around the minima of the potential. In order to find the minimum of the potential we minimise the potential and solve for the zeroes. There are an infinite number of degenerate solutions. To resolve the choice of the infinite possible solutions we chose an axis and expand around our choice. Without loss of generality,

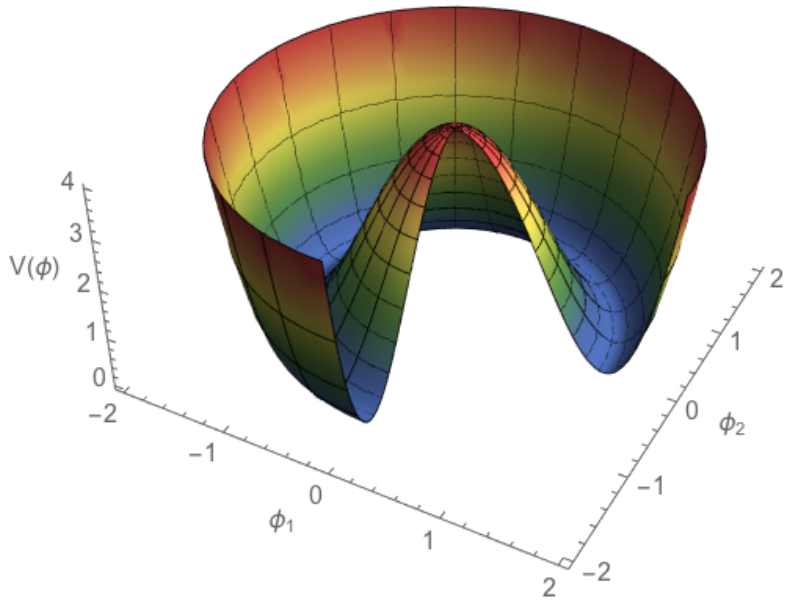

Figure 1.3: A pictorial depiction of the Higgs potential. There are two types of extrema in the Higgs potential, the first being the origin $\phi = 0$ and the second being the at $v = \sqrt{\frac{-\mu^2}{\lambda}}$, which corresponds to an infinite number of minima, one of which is randomly chosen by nature.

we choose $\langle 0|\phi_3|0\rangle = v \geq 0$ with all other components taken to be zero, this gives us:

$$\phi \to \langle 0|\phi|0\rangle \equiv v = \frac{1}{\sqrt{2}} \begin{pmatrix} 0 \\ v \end{pmatrix}. \tag{1.4}$$

Taking this choice of axis we retrieve a vacuum potential:

$$V(\phi) \to V(v) = \frac{1}{2}\mu^2 v^2 + \frac{1}{4}\lambda v^4. \tag{1.5}$$

The minimum of this potential is:

$$\frac{dV(v)}{dv} = v(\mu^2 + \lambda v^2) = 0, \tag{1.6}$$

which has two solutions regimes:

- $\mu^2 > 0$ in which case $v = 0$ and there is no electroweak symmetry breaking.
- $\mu^2 < 0$ in which case $v = \sqrt{\frac{-\mu^2}{\lambda}}$ and there is electroweak symmetry breaking.

The SM Higgs doublet kinetic term is responsible for the generation of electroweak gauge

boson masses and takes the form:

$$\mathcal{L}_{\text{Higgs,Kin}} \subset (D_\mu\phi)^\dagger(D^\mu\phi) = \frac{1}{2}\begin{pmatrix} 0 & v \end{pmatrix}\left[\frac{g}{2}\sigma^i W_\mu^i + \frac{g'}{2}B_\mu\right]^2\begin{pmatrix} 0 \\ v \end{pmatrix} + \text{Other terms}, \tag{1.7}$$

where W_μ^i are the gauge fields for $\mathrm{SU}(2)_\mathrm{L}$; B_μ^0 is the gauge field for $\mathrm{U}(1)_\mathrm{Y}$; g is the coupling for $\mathrm{SU}(2)_\mathrm{L}$, and g' is the coupling for $\mathrm{U}(1)_\mathrm{Y}$. After we take a non-zero VEV we can write the Higgs kinetic term in the form:

$$\mathcal{L}_{\text{Higgs,Kin}} = M_W^2 W^{+\mu}W_\mu^- + \frac{M_Z^2}{2}Z^\mu Z_\mu, \tag{1.8}$$

where the gauge fields of $\mathrm{SU}(3)_\mathrm{C} \times \mathrm{SU}(2)_\mathrm{L} \times \mathrm{U}(1)_\mathrm{Y}$ have mixed according to:

$$W^\pm = \frac{W^1 \mp iW^2}{\sqrt{2}}, \qquad Z \equiv \frac{-g'B_\mu + gW_\mu^3}{\sqrt{g^2+g'^2}} = -\sin(\theta_W)B + \cos(\theta_W)W^3, \tag{1.9}$$

where θ_W is the Weinberg angle and $\tan\theta_W = g'/g$. We can take the combination of B and W^3 which is orthogonal to Z, given by:

$$A = \cos\theta_W B + \sin\theta_W W^3., \tag{1.10}$$

and this corresponds exactly to the photon. We can further express the masses of the photon, W, and Z in the form:

$$M_W = \frac{gv}{2}, \qquad M_Z = \frac{M_W}{\cos\theta_W}, \qquad M_A = 0. \tag{1.11}$$

By taking Equations 1.9 and 1.10, we are able to write the electroweak gauge fields in the matrix form:

$$\begin{pmatrix} Z_\mu^0 \\ A_\mu \end{pmatrix} = \begin{pmatrix} \cos\theta_w & -\sin\theta_w \\ \sin\theta_w & \cos\theta_w \end{pmatrix}\begin{pmatrix} W^3 \\ B^0 \end{pmatrix}. \tag{1.12}$$

We can see from this matrix form that the Z boson and photon are mixings of the same underlying electroweak bosons. The concept of fundemantal gauge fields mixing to form other bosons is incredibly important for our search for supersymmetric electroweak production, and will be explored further in the next chapter.

1.3.1 Higgs Branching Fractions

The branching ratio of the Higgs boson to a given final state ($H \to XX$, or $H \to XY$) is a function of the Higgs mass. In fact, given the SM particle masses, we only require the Higgs mass in order to calculate the SM prediction of $\mathrm{BR}(H \to XX)$. We can see in Figure 1.4 the branching ratios of the Higgs boson to different final states. We can

see there are different regimes for which different processes dominate. In the low mass regime, the $H \to b\bar{b}$ decay process dominates, for intermediate masses, $H \to WW^*$ increases substantially in importance, and for high masses, the $H \to WW^*$ and $H \to ZZ$ decay channels increase significantly.

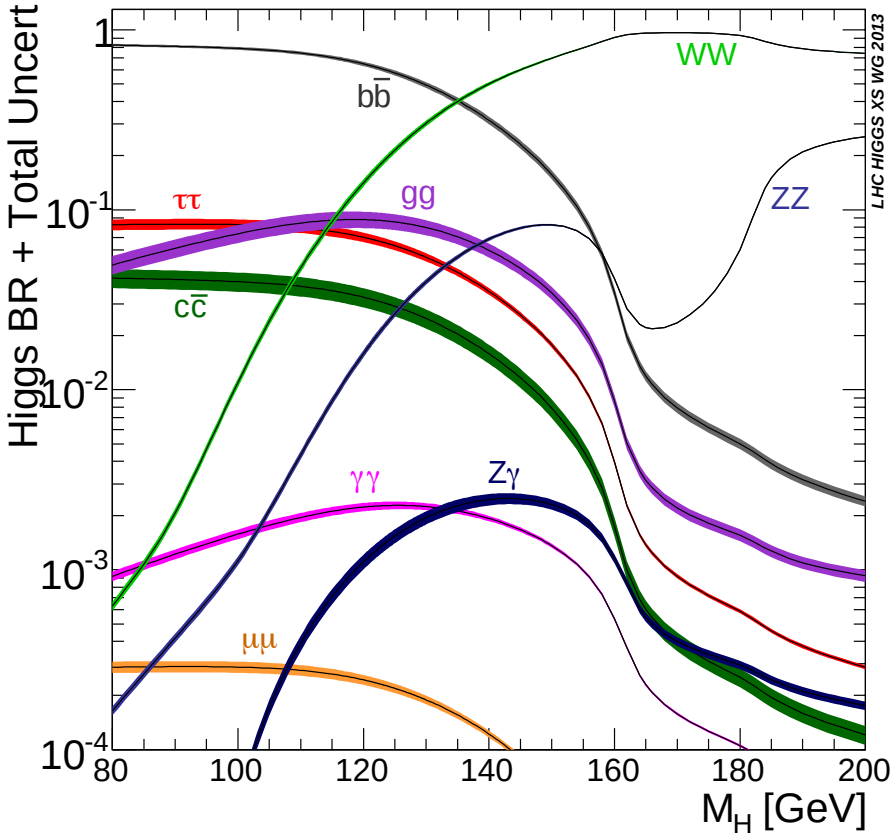

Figure 1.4: Branching ratios of SM Higgs boson vs m_H [11]

The SM predictions of $m_H = 126$ GeV are shown in Table 1.3 [11].

Table 1.3: Branching ratios of SM Higgs boson for $m_H = 126$ GeV [11].

Channel	$\mathrm{BR}_{H\to XX}[\%]$
$b\bar{b}$	56.1
WW^*	23.1
gg	8.48
$\tau\tau$	6.16
ZZ	2.89
cc	2.83
$\gamma\gamma$	0.23
$Z\gamma$	0.16
$\mu\mu$	0.02

1.4 The Strong Force

We have seen that through the Brout-Englert-Higgs mechanism the symmetry group $\mathrm{SU(2)_L} \times \mathrm{U(1)_Y}$ is broken to the symmetry group $\mathrm{U_Q}$ resulting in the generation of mass for the electroweak sector particles. Unlike $\mathrm{SU(2)_L} \times \mathrm{U(1)_Y}$, which is broken by the Brout-Englert-Higgs mechanism, the symmetry group $\mathrm{SU(3)_C}$ remains intact and remains a gauge symmetry even below the electroweak scale.

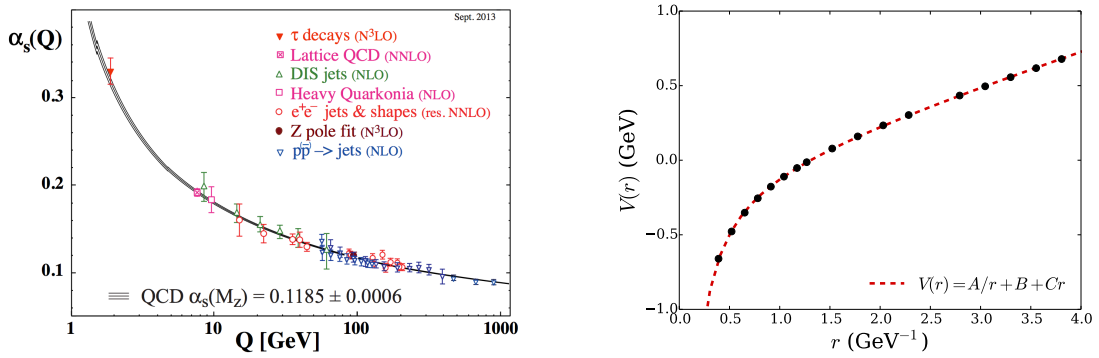

(a) The running of α_S.

(b) $N_f = 0$ heavy quark potential.

Figure 1.5: In (a) we show the running of the strong coupling α_S versus the energy scale Q [GeV]. In (b) we show the $N_f = 0$ heavy quark potential from short to intermediate distances [12]. The running of α_s, and the increasing linear potential both contribute to confinement.

The strong force has several properties which are of interest, such as the gluon's self-interaction, asymptotic freedom and confinement. In Figure 1.5a, we show the strength of the strong force coupling α_S as a function of energy scale Q. We see that for higher energy scales, the $alpha_S$ reduces significantly, resulting in asymptotically free particles at high energies. At high energies, α_s is much smaller than 1, and we can therefore perform the calculation using perturbation theory. Inversely, the lower the energy scale, the stronger α_S becomes resulting ultimately in confinement of coloured particles, which produces mesons, baryons, and other complex bound states. When a coloured particle undergoes acceleration, we see a gluon bremsstrahlung-like effect. Due to the gluon possessing colour, the coloured radiation interacts with itself, causing a complex showering. When the coupling is relatively large, we are unable to calculate quantities using perturbation theory, as non-perturbative effects dominate.

In Figure 1.5b we show a plot which demonstrates the $N_f = 0$ heavy quark potential's confining behaviour [12]. We see here there are three components to this potential, a scalar term, a Coulombic term, and a linear term. The presence of the monotonically increasing linear term results in a completely confined particle within the potential well. Once a particle has enough energy in this well it becomes energetically favourable to produce a quark-antiquark pair from the vacuum, resulting in complex showering behaviour. The subsequent objects of this process are called jets.

Chapter 2

The Minimal Supersymmetric Standard Model

Building from the Standard Model, we now introduce supersymmetry. We explore its relationship to the spin of particles and the necessity of supersymmetry being a broken symmetry in nature. We will explore the Minimal Supersymmetric Standard Model - highlighting the gauge and mass eigenstates, as well as the interactions in the theory. Finally, we summarise the solutions supersymmetry provides to Standard Model problems.

2.1 Introduction to Supersymmetry

Supersymmetry is a property that many modern theories possess and corresponds to a symmetry between bosons and fermions. The generator of the symmetry, Q, is an operator and takes a bosonic state $|\mathrm{Boson}\rangle$ to a fermionic state $|\mathrm{Fermion}\rangle$ and vice versa. Mathematically this can be expressed using bra-ket notation:

$$Q|\mathrm{Boson}\rangle = |\mathrm{Fermion}\rangle, \qquad Q|\mathrm{Fermion}\rangle = |\mathrm{Boson}\rangle. \tag{2.1}$$

By changing the spin properties of a state, we have introduced a new space-time symmetry, which implies the presence of *at least* one partner for each state, called a *superpartner*. The existence of superpartners is a key prediction of any model which has the supersymmetric property.

To appreciate the importance of a symmetry between bosons and fermions, we will first review the SM symmetries and then introduce the *Coleman–Mandula* theorem, which provides powerful constraints on possible extensions to the SM space-time symmetries [13].

In the previous chapter, we stated the SM was formulated on Minkowski space-time with Poincaré group symmetries. The corresponding generators of the Poincaré group are $M_{\mu\nu}$ and P_μ. The internal symmetry group of the SM is $\mathrm{SU}(3)_\mathrm{C} \times \mathrm{SU}(2)_\mathrm{L} \times \mathrm{U}(1)_\mathrm{Y}$, if we take $\mathrm{SU}(3)$ colour as an example, the fundamental generators are T_a and obey the commutation relations:

$$[T^a, T^b] = if^{abc}T^c. \tag{2.2}$$

It turns out all internal symmetries in the SM commute with the Poincaré group generators.

In looking for extensions to the Poincaré group we want to ask *Can internal symmetries have space-time indices and commute with the Poincaré group generators?* In the 1960s, the Coleman–Mandula theorem provided a powerful restriction on internal symmetries, with space-time indices, commuting with the Poincaré group generators [13]. The theorem finds that if we assume the theory has locality, causality, positivity of energy, and the finiteness of the number of particles, then internal symmetries with space-time indices can not commute with Poincaré group generators. Mathematically, if we take G to be any internal symmetry generator, and we take P^μ and $M^{\mu\nu}$ to be the generators for the Poincaré group, then the Coleman–Mandula theorem requires:

$$[G, P^\mu] = 0, \quad [G, M^{\mu\nu}] = 0. \tag{2.3}$$

By introducing generators (Q and $Q^\dagger$) which *anti-commute* as opposed to commute, supersymmetry extends the SM space-time symmetries and sidesteps the Coleman–Mandula theorem. The anti-commutation relations for Q and $Q^\dagger$ are:

$$\{Q, Q^\dagger\} = P^\mu, \quad \{Q, Q\} = 0, \quad \{Q^\dagger, Q^\dagger\} = 0. \tag{2.4}$$

The supersymmetric generator Q commutes with the translation generators, the internal quantum numbers associated with gauge symmetries, and global symmetries. The generators Q and $Q^\dagger$ commute with the translation generator P^μ but do not commute with the rotation generator $M^{\mu\nu}$. The commutation relations with Q are:

$$[Q, P_\mu] = 0, \quad [Q, G] = 0, \quad [Q, M^{\mu\nu}] \neq 0. \tag{2.5}$$

These commutation relations show us that states under Q have different spins, though they have the same quantum numbers. The Poincaré group generator for translations, P^μ, commutes with Q. Given that the two generators commute, the superpartners have the same P^μ and P^2 eigenstates, the relativistic relation $P^2 = m^2$ tells us that superpartners have the same masses. It turns out we have not measured boson-fermion pairs with identical quantum numbers and masses, and therefore we can be confident that supersymmetry is not an unbroken symmetry. At this point, we could give up - but by being familiar with electroweak symmetry breaking, we know that there are situations where a symmetry expressed at a higher energy can be broken at a lower one. If supersymmetry is observed in nature at all, then it must be broken at low energy scales.

Moving forward, we want to write down a gauge field theory that incorporates supersymmetry as an extension to space-time. The most elegant way to do this is through the *superspace* formalism. Superspace is an extension to the usual space-time coordinates x^μ which corresponds to one time coordinate and three spatial coordinates. Superspace takes the spacetime coordinates x^μ and includes four fermionic degrees of freedom, θ_1, θ_2, $\bar{\theta}_1$ and $\bar{\theta}_2$. These fermionic degrees of freedom are Grassman variables. The space-time coordinate using superspace formalism is given by:

$$z = (x^\mu, \theta, \bar{\theta}). \tag{2.6}$$

In superspace we get an expression for our supersymmetric fermionic generator Q:

$$\begin{aligned} Q_\alpha &= i\left(\frac{\partial}{\partial\theta^\alpha} + i\sigma^\mu_{\alpha\dot{\alpha}}\bar{\theta}^{\dot{\alpha}}\partial_\mu\right), \\ Q_{\dot{\alpha}} &= i\left(\frac{\partial}{\partial\theta^{\dot{\alpha}}} - i(\theta_\alpha\sigma^\alpha)_{\dot{\alpha}}\partial_\mu\right), \end{aligned} \tag{2.7}$$

with $\dot{\alpha}$ being the Weyl index. The covariant derivatives take the form:

$$\begin{aligned} D_\alpha &= -i\partial_\alpha - (\sigma^\mu\bar{\theta})_\alpha\partial_\mu, \\ \bar{D}_{\dot{\alpha}} &= \quad i\bar{\partial}_{\dot{\alpha}} + (\theta\sigma^\mu)_{\dot{\alpha}}\partial_\mu. \end{aligned} \tag{2.8}$$

Particle content is introduced in the superspace formalism by incorporating different spin states into one object known as a *superfield*. The general definition of a superfield is given by:

$$\begin{aligned} F(z) = &\underbrace{\phi(x)}_{\text{scalar}} + \underbrace{\theta\eta(x) + \bar{\theta}\bar{\chi}(x)}_{\text{spinor terms}} \\ &+ \underbrace{\theta^2 m(x) + \bar{\theta}^2 n(x)}_{\text{scalar}} + \underbrace{\theta\sigma^\mu\bar{\theta}V_\mu(x)}_{\text{vector term}} \\ &+ \underbrace{\theta^2\bar{\theta}\bar{\lambda}(x) + \bar{\theta}^2\theta\psi(x)}_{\text{spinor term}} \\ &+ \underbrace{\theta^2\bar{\theta}^2 D(x)}_{\text{scalar}} \end{aligned}. \tag{2.9}$$

Here we have a scalar field $\phi(x)$ followed by two spinoral terms - $\eta(x)$ and $\chi(x)$. The next line has two scalar fields - $m(x)$ and $n(x)$ followed by a vector field $V_\mu(x)$. The third line of Equation 2.9 has two spinoral terms - $\lambda(x)$ and $\psi(x)$, with the final term being a scalar $D(x)$. We now introduce the minimal implementation of supersymmetry with the SM.

2.2 Particle Content

The Minimal Supersymmetric Standard Model (MSSM) is the supersymmetric extension of the SM, which considers the minimum number of particle states and interactions which are consistent with current experimental results [14, 15]. The MSSM is written in terms of *chiral* and *vector supermultiplets*. The MSSM is a chiral theory, and thus there is a supermultiplet for the left doublet and right singlet states. The supermultiplets also contain both fermionic and bosonic states.

There are two naming conventions for superpartners. The superpartners of the SM fermions are known as scalar fermions or *sfermions*, with *squarks* (scalar quarks) and *sleptons* (scalar leptons). The superpartners of the SM bosons have the suffix *-ino*. The

Table 2.1: Summary of the gauge supermultiplets of the MSSM and gauge group representations.

Supermultiplet	spin-$\frac{1}{2}$	spin-1	$\mathrm{SU(3)_C}$	$SU(2)_L$	$\mathrm{U(1)_Y}$
$\hat{G}$	$\widetilde{g}$	g	**8**	**1**	0
$\hat{W}$	$\widetilde{W}^i$	W^i	**1**	**3**	0
$\hat{B}$	$\widetilde{B}^0$	B^0	**1**	**1**	0

superpartner of any SM particle can also be called a *sparticle*. In order to easily show that a particle is a superpartner, we use a tilde above the SM field name. For instance, the left-handed top quark, t_L, has a superpartner $\tilde{t}_L$.

The mathematical form of the chiral supermultiplet $\widetilde{\Phi}(x,\theta)$ is:

$$\widetilde{\Phi}(x,\theta) = \phi(x) + \sqrt{2}\theta^\alpha\psi_\alpha(x) + \theta\theta F(x), \tag{2.10}$$

where $\phi(x)$ is the scalar state, $\psi_\alpha(x)$ is the fermionic state and F is a scalar and a so-called auxiliary field. The mathematical form of the vector supermultiplet is:

$$\widetilde{V}_{WZ}(z) = -\theta\sigma^\mu\bar{\theta}V_\mu(x) + i\theta^2\bar{\theta}\bar{\lambda}(x) - i\bar{\theta}^2\theta\lambda(x) + \frac{1}{2}\theta^2\bar{\theta}^2 D(x), \tag{2.11}$$

where $V_\mu(x)$ corresponds to a gauge boson state, $\lambda(x)$ corresponds to a the gauge boson superpartners, called the gaugino state, and $D(x)$ corresponds to an auxiliary field.

We summarise the vector supermultiplets and chiral supermultiplets of the MSSM in Tables 2.1 and 2.2. The guage supermultiplets in Table 2.1 are $\hat{G}$ which contains the gluons and their superpartners; $\hat{W}$ which corresponds to the electroweak bosons W^i and their superpartners the *winos* $\widetilde{W}^i$; and finally $\hat{B}$ which corresponds to the gauge boson B^0 and its superpartner the *bino* $\widetilde{B}^0$. Collectively the superpartners of gauge bosons are called Gauginos. The electroweak gauge boson superpartners are sometimes called electroweakinos.

The chiral supermultiplets of the MSSM contain all the fermions of the SM, as well as their partners. Unlike the SM, the MSSM requires not one but two Higgs doublets. These doublets are labeled H_u and H_d and the Brout–Englert–Higgs mechanism generates masses for the *up* type fermions and the *down* type fermions separately. The superpartners of the Higgs doublets, Higgsinos, are denoted $\widetilde{H}_u$ and $\widetilde{H}_d$. In terms of the MSSM formalism, the $\mathrm{SU(2)_L}$ doublets are found in a single supermultiplet. Taking all this information, we summarise the MSSM SM particle content in 2.1 and the supersector particle content in Table 2.2.

Table 2.2: Summary of the chiral supermultiplets of the MSSM and their gauge group representations.

Supermultiplet	spin-0	spin-$\frac{1}{2}$	$\mathrm{SU(3)_C}$	$SU(2)_L$	$\mathrm{U(1)_Y}$
$\hat{Q}_i$	$\left(\widetilde{u}_L \quad \widetilde{d}_L\right)_i$	$\left(u_L \quad d_L\right)_i$	3	2	1/6
$\bar{u}_i$	$\widetilde{u}^*_{R_i}$	$u^\dagger_{R_i}$	$\bar{3}$	1	-2/3
$\bar{d}_i$	$\widetilde{d}^*_{R_i}$	$d^\dagger_{R_i}$	$\bar{3}$	1	1/3
$\hat{L}_i$	$\left(\widetilde{\nu} \quad \widetilde{e}_L\right)_i$	$\left(\nu \quad e_L\right)_i$	1	2	-1/2
$\bar{e}_i$	$\widetilde{e}^*_{R_i}$	$e^\dagger_{R_i}$	1	1	1
$\hat{H}_u$	$\left(H_u^+ \quad H_u^0\right)$	$\left(\widetilde{H}_u^+ \quad \widetilde{H}_u^0\right)$	1	2	+1/2
$\hat{H}_d$	$\left(H_d^+ \quad H_d^0\right)$	$\left(\widetilde{H}_d^+ \quad \widetilde{H}_d^0\right)$	1	2	-1/2

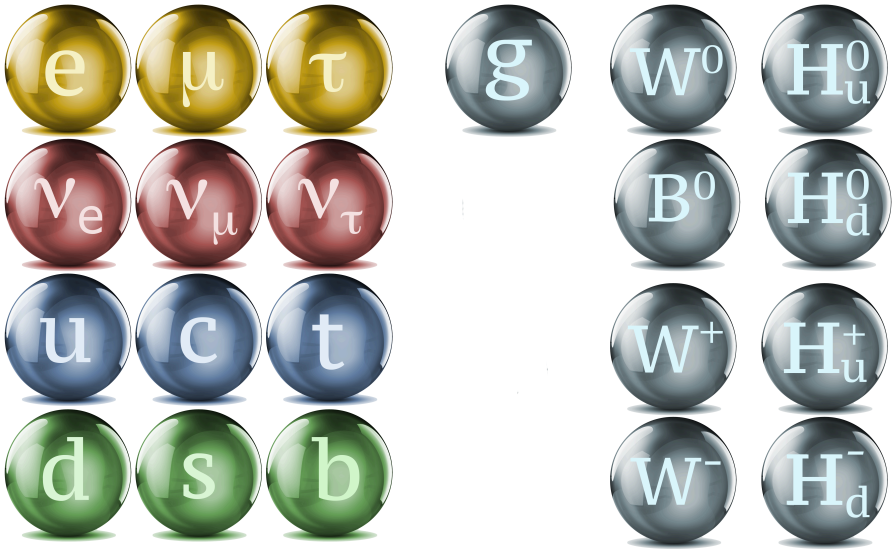

Figure 2.1: The summary of the unbroken SM sector fields for the MSSM. Left and right chirality are not shown.

2.3 The MSSM Lagrangian

In Section 2.2 we summarised the particle content of the MSSM and where that particle content resided within the chiral and vector supermultiplets. We can take those supermultiplets and write them in a Lagrangian. The Lagrangian of the MSSM can be split into four general terms. These are the gauge term, the superpotential term, the Kähler potential term, and the soft symmetry breaking term. Mathematically we write this as:

$$\mathcal{L}_{\mathrm{MSSM}} = \mathcal{L}_{\mathcal{W}} + \mathcal{L}_{\mathrm{Gauge}} + \mathcal{L}_{\mathcal{K}} + \mathcal{L}_{\mathrm{Soft}}. \tag{2.12}$$

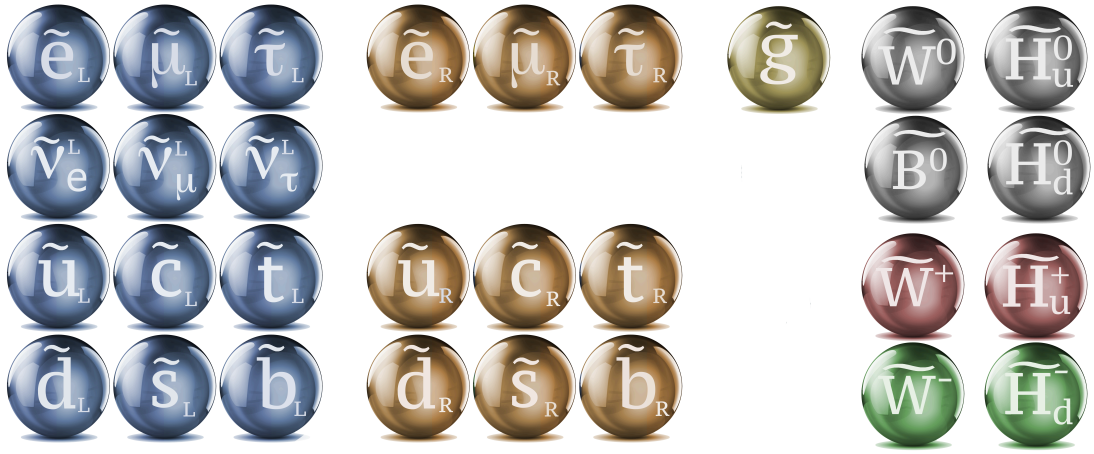

Figure 2.2: The summary of the unbroken SUSY sector flavour field content.

The gauge term written in terms of the supermultiplets is:

$$\mathcal{L}_{\text{Gauge}} = \frac{1}{4}\int d\theta^2 \left(W_g^{a\alpha}W_{g\,\alpha}^a + \mathbf{W}_W^\alpha \cdot \mathbf{W}_{W\,\alpha} + W_Y^\alpha W_{Y\,\alpha}\right) + \text{h.c}, \tag{2.13}$$

where the integral is over the fermionic degrees of freedom, and the gauge terms are split in terms of their gauge symmetries - $\mathrm{SU}(3)_\mathrm{C}$, $\mathrm{SU}(2)_\mathrm{L}$ and $\mathrm{U}(1)_\mathrm{Y}$. These terms are responsible for all gauge boson–gauge boson interactions, as well as gauge boson–gaugino interactions and they contribute to gaugino–gaugino interactions. A summary of these interactions is shown in Figure 2.5. The other terms require a little more detail, which we will now provide.

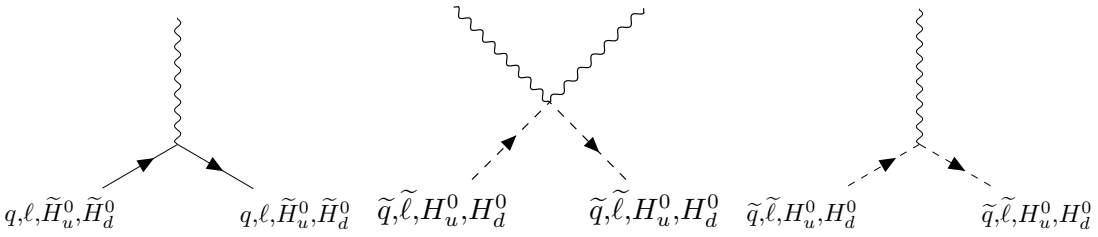

Figure 2.3: The MSSM electroweak sector interactions from the gauge term.

2.4 Superpotential and R-Parity

The next term of the MSSM Lagrangian we want to explore is the superpotential. We write the superpotential in the form:

$$\mathcal{L}_\mathcal{W} = \int d^2\theta \mathcal{W}\left(\Phi_i\right), \tag{2.14}$$

where Φ_i are all the supermultiplets in Table 2.2 and $\mathcal{W}$ is the superpotential, defined as:

$$\begin{aligned}\mathcal{W} = \varepsilon_{\alpha\beta}\left(y_u^{ij}\hat{H}_u^{\alpha}\bar{u}_i\hat{Q}_j^{\beta} - y_d^{ij}\hat{H}_d^{\alpha}\bar{d}_i\hat{Q}_j^{\beta} - y_e^{ij}\hat{H}_d^{\alpha}\bar{e}_i\hat{L}_j^{\beta} + \mu\hat{H}_u^{\alpha}\hat{H}_d^{\beta}\right) \\ + \frac{1}{2}\lambda^{ijk}L_iL_j\bar{e}_k + \lambda'^{ijk}L_iQ_j\bar{d}_k + \mu'^{i}L_iH_u + \frac{1}{2}\lambda''^{ijk}\bar{u}_i\bar{d}_j\bar{d}_k.\end{aligned} \tag{2.15}$$

This expression is of vital phenomenological importance as in the SM conservation of baryon number (B), and lepton number (L) are not explicit symmetries of the Lagrangian, and their emergence is accidental. The MSSM also does not impose a baryon number or lepton number symmetry, but unlike the SM, we run into a problem with proton decay due to the following terms in the superpotential:

$$\mathcal{W}^{\text{Decay}} = \frac{1}{2}\lambda^{ijk}L_iL_j\bar{e}_k + \lambda'^{ijk}L_iQ_j\bar{d}_k + \mu'^{i}L_iH_u + \frac{1}{2}\lambda''^{ijk}\bar{u}_i\bar{d}_j\bar{d}_k. \tag{2.16}$$

In order to suppress the presence of these terms and have a phenomenologically viable theory, we must impose a $\mathbb{Z}_2$ symmetry, called R-parity. Its effect is the elimination of B and L violating terms in the MSSM Lagrangian [16]. R-Parity is defined as:

$$P_{\text{R}} = (-1)^{3(B-L)+2s}, \tag{2.17}$$

with s being the spin of the particle in question [16]. R-Parity is closely related to Matter-Parity, which is defined as:

$$P_{\text{M}} = (-1)^{3(B-L)}. \tag{2.18}$$

All SM particles have, including the expanded Higgs sector, a $P_R = +1$, while all the superpartners have an R-Parity of $P_R = -1$. The result of imposing this symmetry is the elimination of the problematic terms, and a superpotential of the form:

$$\mathcal{W}^{\text{MSSM}} = \varepsilon_{\alpha\beta}\left(y_u^{ij}\hat{H}_u^{\alpha}\bar{u}_i\hat{Q}_j^{\beta} - y_d^{ij}\hat{H}_d^{\alpha}\bar{d}_i\hat{Q}_j^{\beta} - y_e^{ij}\hat{H}_d^{\alpha}\bar{e}_i\hat{L}_j^{\beta} + \mu\hat{H}_u^{\alpha}\hat{H}_d^{\beta}\right). \tag{2.19}$$

The dominant superpotential interaction terms which contribute to supersymmetric electroweak production are summarised in Figure 2.4

2.5 The Kähler Potential

The third term of interest in Equation 2.12 contains the kinetic terms of the Lagrangian, and is of the form

$$\mathcal{L}_{\mathcal{K}} = \int d^4\theta K(\Phi_i, \Phi_i^{\dagger}), \tag{2.20}$$

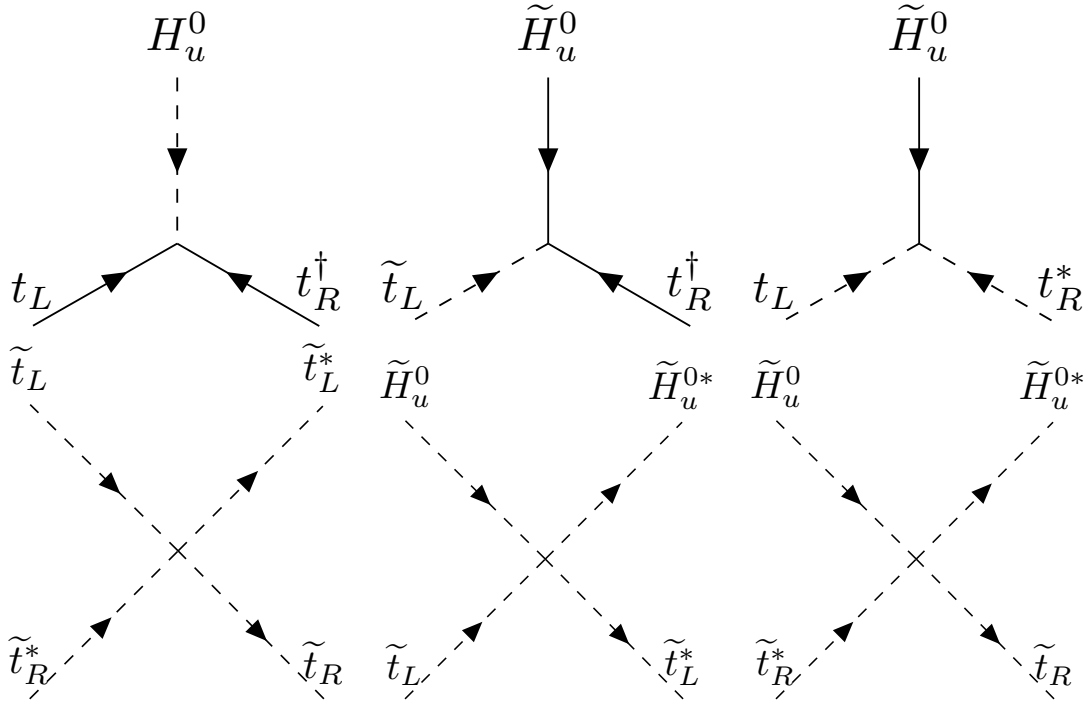

Figure 2.4: The MSSM electroweak sector interactions from the superpotential.

where K is known as the Kähler potential. The generalised form of the Kähler potential given by:

$$\mathcal{L}_{\mathcal{K}} = \int d^2\theta \sum_i \Phi_i^\dagger e^{2gV} \Phi_i. \tag{2.21}$$

Here each V_X corresponds to the scalar potential associated with each gauge symmetry. Expanding this equation out to include the supermultiplets of the MSSM gives us the following form:

$$\begin{aligned}\mathcal{L}_{\mathcal{K}} = \int d^2\theta d^2\bar{\theta} \Big(& \hat{L}_{L_i}^\dagger e^{g\mathbf{V}_W\cdot\tau + g'V^Y Y} \hat{L}_{L_i} + \bar{e}_i^\dagger e^{g'V^Y Y} \bar{e}_i + \bar{u}_i^\dagger e^{-g_S V_g^a \bar{\lambda}^a + g'V^Y Y} \bar{u}_i \\ & + \bar{d}_i^\dagger e^{-g_S V_g^a \bar{\lambda}^a + g'V^Y Y} \bar{d}_i + \bar{Q}_i^\dagger e^{g_S V_g^a \bar{\lambda}^a + g\mathbf{V}_W\cdot\tau + g'V^Y Y} \bar{Q}_i \\ & + \hat{H}_d^\dagger e^{g\mathbf{V}_W\cdot\tau + g'V^Y Y} \hat{H}_d + \hat{H}_u^\dagger e^{g\mathbf{V}_W\cdot\tau + g'V^Y Y} \hat{H}_u \Big).\end{aligned} \tag{2.22}$$

We show three interaction terms which are relevant for supersymmetric electroweak production in Figure 2.5.

2.6 MSSM Electroweak Symmetry Breaking

Before expanding on the final term in the MSSM Lagrangian $\mathcal{L}_{\text{Soft}}$ we will first explain how electroweak symmetry breaking works in the MSSM. We know that the Higgs

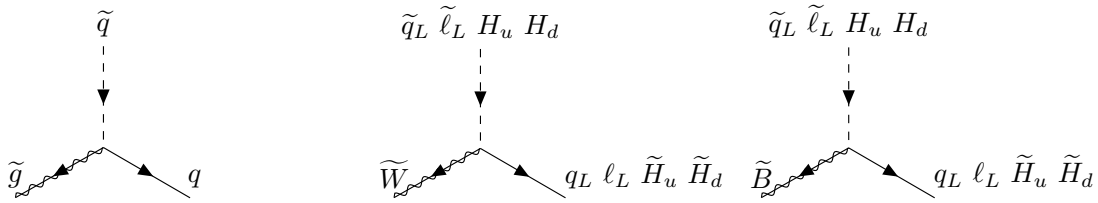

Figure 2.5: The MSSM electroweak sector interactions from the Kähler potential.

bosons are embedded within two chiral supermultiplets $\tilde{H}_u$ and $\tilde{H}_d$, as detailed in Section 2.2. These Higgs doublets contain the scalar components of $\tilde{H}_u$ and $\tilde{H}_d$ and also contain the spin-1/2 superpartners. The Higgs boson components can be written in the form:

$$H_u = \begin{pmatrix} H_u^+ \\ H_u^0 \end{pmatrix}, \qquad H_d = \begin{pmatrix} H_d^0 \\ H_d^- \end{pmatrix}, \tag{2.23}$$

where we label the two Higgs doublets with u and d. The u Higgs doublet is responsible for the mass generation of the up-type fermions, while d Higgs doublets effect the Yukawa couplings of the down-type fermions. The scalar potential in the MSSM [17] is given by:

$$\begin{aligned} V \subset\ & (\mu^2 + m_{H_u}^2)(|H_u^0|^2 + |H_u^+|^2) + (\mu^2 + m_{H_d}^2)(|H_d^0|^2 + |H_d^+|^2) \\ & + b\left[(H_u^+ H_d^- - H_u^0 H_d^0) + c.c\right] \\ & + \frac{1}{8}(g^2 + (g')^2)\left[|H_u^0|^2 + |H_u^+|^2 - |H_d^0|^2 - |H_d^-|^2\right]^2 \\ & + \frac{g^2}{2}|H_u^+ \left(H_d^0\right)^* + H_u^0 \left(H_d^-\right)^*|^2 \end{aligned} . \tag{2.24}$$

We can allow the two doublets to acquire a VEV independently such that $\langle H_u \rangle = v_u$ and $\langle H_d \rangle = v_d$. These are related to the SM VEV via:

$$v_u^2 + v_d^2 = v_{SM}^2 = \frac{2m_Z^2}{g^2 + (g')^2}, \tag{2.25}$$

and so we see that we can generate masses for $W^\pm$ and Z, just as in the single Higgs doublet EWSB. After EWSB the MSSM has five Higgs mass eigenstates ($H^\pm$, h^0, H^0 and A). We define the ratio between the up and down Higgs doublet VEVs with:

$$\tan\beta = \frac{v_u}{v_d}. \tag{2.26}$$

It turns out that in the MSSM the Yukawa couplings are functions of $\tan\beta$. For example, the Yukawa couplings to the top quarks and bottom quark in the MSSM are:

$$y_t = \frac{\sqrt{2}m_t}{v\sin\beta}, \qquad y_b = \frac{\sqrt{2}m_b}{v\cos\beta}. \tag{2.27}$$

In the MSSM the Yukawa couplings are enhanced with respect to the SM predictions. Then enhancement goes like:

$$\begin{aligned} y_b &= \frac{\sqrt{2}m_b}{v\cos\beta} = \frac{\sqrt{2}m_b}{v\sin\beta}\tan\beta \\ &\approx \frac{\sqrt{2}m_b}{v}\tan\beta \end{aligned} . \tag{2.28}$$

For large $\tan\beta$, typically much greater than 1, y_b can approach y_t as $\tan\beta \approx \frac{m_t}{m_b}$.

2.7 Soft Symmetry Breaking

We now arrive at our final term in the MSSM Lagrangian – $\mathcal{L}_{\text{Soft}}$. We knew from the beginning that supersymmetry had to be a broken symmetry of nature, and this final term is primarily responsible for breaking that symmetry. Its helpful to define what we mean by broken, the idea is that supersymmetry is broken at some scale M_s, where at energies $E > M_s$ the theory is supersymmetric. In the case where $E < M_s$ supersymmetry is broken, and we are left with a model which is non-supersymmetric - like the SM. The two primary ways of generating a broken supersymmetric theory are *spontaneous* and *explicit*. Spontaneous supersymmetry breaking is the scenario where the theory is supersymmetric, but it has a scalar potential, the scalar field(s) acquire a VEV which is of the order of M_s and the VEV breaks supersymmetry. When the lagrangian contains terms which are not supersymmetric at low energies, but which become irrelevant at high energies, then the lagrangian is said to exhibit soft breaking. In both cases the scale M_s is present in the Lagrangian. In the MSSM we use the explicit symmetry breaking [18]. The expansion of the $\mathcal{L}_{\text{Soft}}$ is:

$$\begin{aligned} -\mathcal{L}_{\text{soft}}^{\text{MSSM}} = &\frac{1}{2}\left[M_3\lambda_{\tilde{g}}\lambda_{\tilde{g}} + M_2\widetilde{W}^a\widetilde{W}^a + M_3\widetilde{B}\widetilde{B} + \text{h.c}\right] \\ &+ \varepsilon_{\alpha\beta}\left[B\mu H_d^\alpha H_u^\beta - a_{u_{ij}}H_u^\alpha\widetilde{\bar{u}}_i\widetilde{Q}_j^\beta + a_{d_{ij}}H_d^\alpha\widetilde{\bar{d}}_i\widetilde{Q}_j^\beta + a_{e_{ij}}H_d^\alpha\widetilde{\bar{e}}_i\widetilde{L}_j^\beta + \text{h.c}\right] \\ &+ m_{H_d}^2|H_d|^2 + m_{H_u}^2|H_u|^2 + \widetilde{Q}_i^\alpha m_{Q_{ij}}^2\widetilde{Q}_j^{\alpha^*} \\ &+ \widetilde{L}_i^\alpha m_{L_{ij}}^2\widetilde{L}_j^{\alpha^*} + \widetilde{\bar{u}}_{R_i}^\alpha m_{u_{ij}}^2\widetilde{\bar{u}}_j + \widetilde{\bar{d}}_i^* m_{d_{ij}}^2\widetilde{\bar{d}}_j + \widetilde{\bar{e}}_i^* m_{e_{ij}}^2\widetilde{\bar{e}}_j. \end{aligned} \tag{2.29}$$

This soft breaking term is responsible for the vast majority of the new parameters which enter into the MSSM. We introduce one new mass parameter for each new particle.

2.8 Electroweakino Mass Eigenstates

As stated in Section 2.1, the superpartners of a SM particle have the same quantum numbers as the SM particle, an unlike the SM particle are spin-1/2. In particular $\widetilde{W}^0$,

$\widetilde{H}_u^0$, $\widetilde{B}^0$ and $\widetilde{H}_d^0$ have the same quantum numbers and mix to form four neutral mass eigenstates, which we call neutralinos. The superpartners, $\widetilde{W}^+$ and $\widetilde{H}_u^+$, mix to form two positively charged mass eigenstates, which we call charginos. Finally, the $\widetilde{W}^-$ and $\widetilde{H}_u^-$ superpartners mix to form the negatively charged mass eignestates, which we also call charginos.

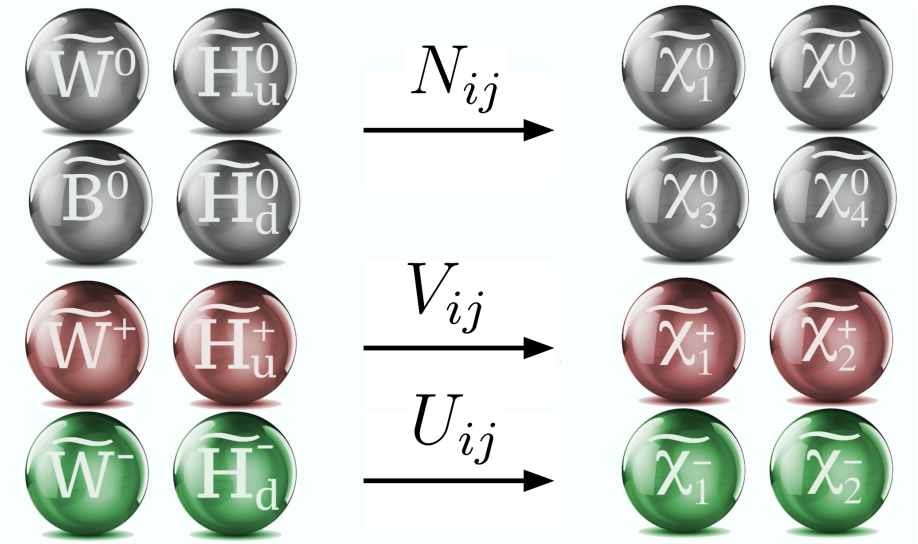

Figure 2.6: A pictorial view of gaugino mixing. We see the neutral gauginos and Higgsinos mix to form the mass eigenstate neutralinos. The positive winos and Higgsinos mix to form the positive charginos. Likewise for the negative winos and Higgsinos.

We can label the different neutralino states simply as $\tilde{\chi}_i^0$, where $i = 1, 2, 3, 4$. We take $i = 1$ to be the least massive, whereas $i = 4$ is the most massive. Mathematically the hierarchy is given as:

$$m_{\tilde{\chi}_1^0} < m_{\tilde{\chi}_2^0} < m_{\tilde{\chi}_3^0} < m_{\tilde{\chi}_4^0}. \tag{2.30}$$

We can show the mixing between the neutral gauginos to neutralinos in an analogous way to Equation 1.12:

$$\begin{pmatrix} \tilde{\chi}_1^0 \\ \tilde{\chi}_2^0 \\ \tilde{\chi}_3^0 \\ \tilde{\chi}_4^0 \end{pmatrix} = \begin{pmatrix} N_{11} & N_{12} & N_{13} & N_{14} \\ N_{21} & N_{22} & N_{23} & N_{24} \\ N_{31} & N_{32} & N_{33} & N_{34} \\ N_{41} & N_{42} & N_{43} & N_{44} \end{pmatrix} \begin{pmatrix} \tilde{W}^0 \\ \tilde{B}^0 \\ \tilde{H}_u^0 \\ \tilde{H}_d^0 \end{pmatrix}. \tag{2.31}$$

On the left-hand side we have the mass eigenstates, on the right-hand side of the equation we have the neutral gaugino eigenstates $\tilde{W}^0$, $\tilde{B}^0$, $\tilde{H}_u^0$ and $\tilde{H}_d^0$. These four separate states mix via the N_{ij} matrix elements, and $N_{i1}^2 + N_{i2}^2 + N_{i3}^2 + N_{i4}^2 = 1$, to ensure unity of the probability.

Next we look at the mixing of the positive gaugino eigenstates. We can label the different chargino states as $\tilde{\chi}_i^+$ with $i = 1, 2$, and with the mass hierarchy of the charginos is given

Table 2.3: A summary of gauge eigenstates and their corresponding mass eigenstates in the MSSM.

	Gauge Eigenstates	Mass Eigenstates
Up squarks	$\widetilde{u}_L \quad \widetilde{u}_R \quad \widetilde{c}_L \quad \widetilde{c}_R \quad \widetilde{t}_L \quad \widetilde{t}_R$	$\widetilde{u}_1 \quad \widetilde{u}_2 \quad \widetilde{c}_1 \quad \widetilde{c}_2 \quad \widetilde{t}_1 \quad \widetilde{t}_2$
Down squarks	$\widetilde{d}_L \quad \widetilde{d}_R \quad \widetilde{s}_L \quad \widetilde{s}_R \quad \widetilde{b}_L \quad \widetilde{b}_R$	$\widetilde{u}_1 \quad \widetilde{u}_2 \quad \widetilde{s}_1 \quad \widetilde{s}_2 \quad \widetilde{t}_1 \quad \widetilde{t}_2$
Sleptons	$\widetilde{e}_L \quad \widetilde{e}_R \quad \widetilde{\mu}_L \quad \widetilde{\mu}_R \quad \widetilde{\tau}_L \quad \widetilde{\tau}_R$	$\widetilde{e}_1 \quad \widetilde{e}_2 \quad \widetilde{\mu}_1 \quad \widetilde{\mu}_2 \quad \widetilde{\tau}_1 \quad \widetilde{\tau}_2$
Sneutrinos	$\widetilde{\nu}_e \quad \widetilde{\nu}_\mu \quad \widetilde{\nu}_\tau$	$\widetilde{\nu}_e \quad \widetilde{\nu}_\mu \quad \widetilde{\nu}_\tau$
Higgs bosons	$H_u^0 \quad H_d^0 \quad H_u^+ \quad H_d^-$	$h^0 \quad H^0 \quad A^0 \quad H^\pm$
Neutralinos	$\widetilde{B}^0 \quad \widetilde{W}^0 \quad \widetilde{H}_u^0 \quad \widetilde{H}_d^0$	$\widetilde{\chi}_1^0 \quad \widetilde{\chi}_2^0 \quad \widetilde{\chi}_3^0 \quad \widetilde{\chi}_4^0$
Charginos	$\widetilde{W}^\pm \quad \widetilde{H}_u^+ \quad \widetilde{H}_d^-$	$\widetilde{\chi}_1^\pm \quad \widetilde{\chi}_2^\pm$
Gluino	$\widetilde{g}$	g

by:

$$m_{\tilde{\chi}_1^+} < m_{\tilde{\chi}_2^+} \tag{2.32}$$

The mixing of the gauginos in the mass eigenstates, for the positive charginos is given by:

$$\begin{pmatrix} \tilde{\chi}_1^+ \\ \tilde{\chi}_2^+ \end{pmatrix} = \begin{pmatrix} V_{11} & V_{12} \\ V_{21} & V_{22} \end{pmatrix} \begin{pmatrix} \tilde{W}^+ \\ \tilde{H}^+ \end{pmatrix}. \tag{2.33}$$

Where the matrix parameterising this mixture is V. Next, we look at the mixing of the negative gaugino eigenstates. The negative charginos are a mixture of the negative Higgsino and the negative wino. The mass eigenstates are $\tilde{\chi}_i^-$ with $i = 1, 2$ and:

$$m_{\tilde{\chi}_1^-} < m_{\tilde{\chi}_2^-}. \tag{2.34}$$

The mixing of the gauginos in the mass eigenstate is given by:

$$\begin{pmatrix} \tilde{\chi}_1^- \\ \tilde{\chi}_2^- \end{pmatrix} = \begin{pmatrix} U_{11} & U_{12} \\ U_{21} & U_{22} \end{pmatrix} \begin{pmatrix} \tilde{W}^- \\ \tilde{H}^- \end{pmatrix}. \tag{2.35}$$

The matrix parameterising this mixture is U and is a 2×2 matrix. The mass eigenstates of the MSSM are summarised in Table 2.3.

2.9 Solutions to Standard Model Problems

There are two natural energy scales that we know about in the universe, the electroweak scale($M_{\text{EW}} \approx 100$ GeV), and the Planck scale ($M_P \approx 10^{16}$ GeV). The electroweak scale corresponds to the energy scale where the electromagnetic and weak forces unify into a single electroweak force. The Planck scale is the approximate scale at which quantum

gravitational effects become important.

We know that the SM is not the final theory, but rather a low energy effective theory with an ultraviolet cutoff scale Λ_{UV}, which is an energy scale between the electroweak and the Planck scales. This defines three cut off energies, M_{EW} , M_{P} and Λ_{UV}. This large cut off scale is the major question of the hierarchy problem, why is the disparity between these three energy scales so massive? If the high energy cut off of our effective theory is large, then the Higgs boson should receive quadratically divergent corrections to its mass through loop contributions [15]. The quadratically divergent terms are of the form:

$$\Delta m_H^2 = -\frac{|\lambda_f|^2}{8\pi^2}\Lambda_{\mathrm{UV}}^2 + \dots . \tag{2.36}$$

The presence of these quadratically divergent corrections is known as the Higgs mass problem. By introducing two superpartner bosons for each fermion of the SM, as well as a fermion for each boson, supersymmetry solves this quadratic divergence by introducing superpartners to the SM particles. Fermion loops produce an overall negative sign in their contributions and thus the fermionic and bosonic contributions precisely cancel if supersymmetry is an exact symmetry.

We show pictorially show the diagrams from bosons and fermions in Figure 2.7.

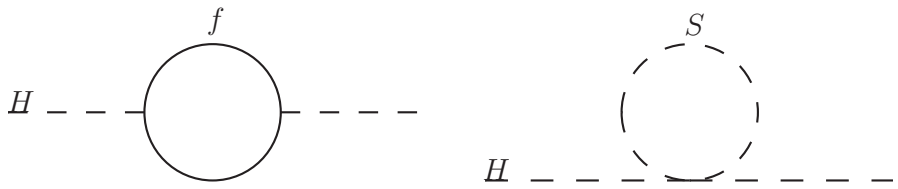

Figure 2.7: The corrections to the Higgs boson propagator, where f can be any MSSM particle with mass, and S can be any bosonic particle with mass.

The Higgs mass correction once supersymmetry is taken into account goes like:

$$\Delta m_H^2 = m_{\mathrm{soft}}^2 \left[\frac{\lambda}{16\pi^2} \ln(\Lambda_{\mathrm{UV}}/m_{\mathrm{soft}}) + \dots \right], \tag{2.37}$$

where λ is a dimensionless coupling, and "..." indicates higher-order terms. This relation gives us a natural scale for supersymmetry, which is denoted as m_{soft}. The m_{soft} term is the mass scale at which supersymmetry is broken. If m_{soft} is too large, then the corrections to m_H^2 are again unnaturally large. An estimate for this soft breaking scale is on the order of a $\approx$ TeV. When m_{soft} is of the order of a TeV we have *natural supersymmetry*. This is the reason the theorists expected to find supersymmetry in the next run of the LHC [15].

2.9.1 Coupling Unification Problem

The next significant problem of the SM is that of the non-convergence of the coupling constants at high energies. When we take the coupling constants of the SM and take them to run with energy via the use of their beta functions, we find that they do not converge at high energies. If we believe in unified theories, then this should startle us. The idea of unification has been a reliable driver in both classical and modern physics, we see the possibility of a unified force as a compelling possibility. The MSSM becomes attractive in that, without any deliberate tuning we have the couplings of the theory converging at approximately 10^{16} GeV. We show the running of the coupling constants in Figure 2.8.

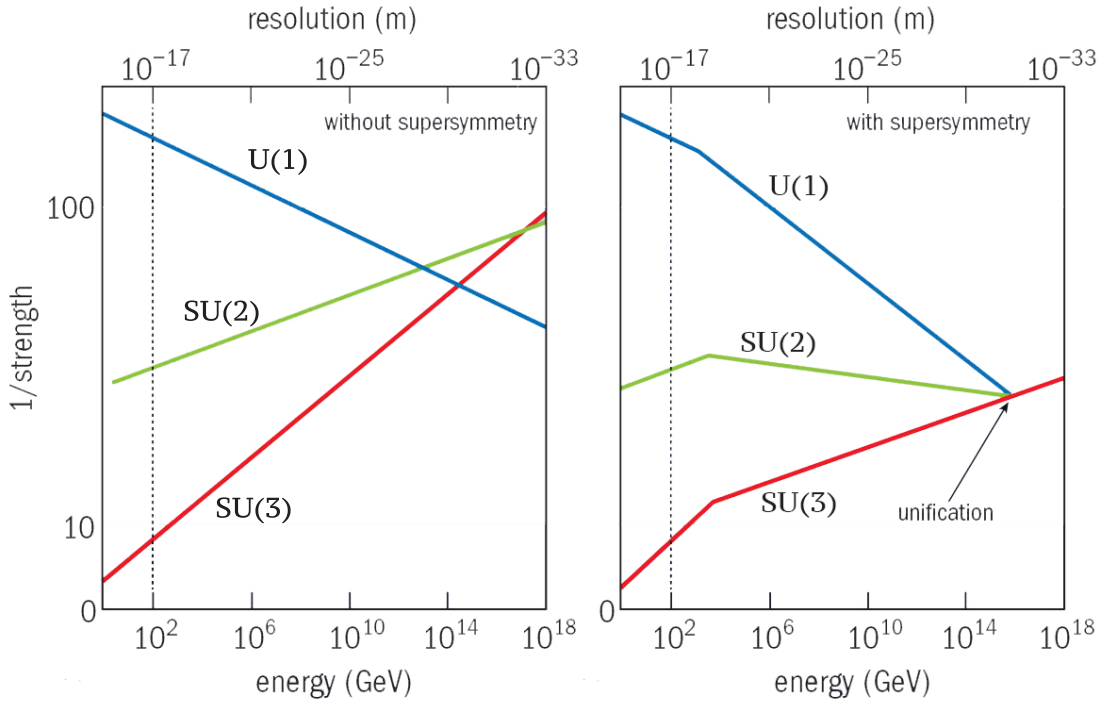

Figure 2.8: The running of the SM couplings is shown by the solid lines. Displayed by dotted lines, the MSSM provides a unification of these couplings at approximately 10^{16} GeV which is below the Planck scale.

2.9.2 The Neutralino WIMP

Current measurements place luminous baryonic matter as comprising less than 5% of all matter in the universe, with the dark matter being roughly five times more abundant. Broadly speaking dark matter hypotheses can be split into Massive Compact Halo Objects (MACHOS) and particle dark matter. There are many varieties of particle dark matter, but a common variety is known as the Weakly Interacting Massive Particle (WIMP). WIMPs are particles that are neutral and weakly interacting, much like the neutrino. If

R-Parity is a conserved quantity in the MSSM, then the neutralino is a typical WIMP - electrically neutral, weakly interactive, and typically very massive. The neutralino under certain mass hypotheses is consistent with dark matter abundance in the universe [19].

Chapter 3

The ATLAS Experiment

In this chapter, we introduce the Large Hadron Collider accelerator complex, and provide an overview of the ATLAS experiment subsystems and object reconstruction methods. We then pivot and provide details for the full run-II ATLAS dataset, we summarise the physics reach of the Large Hadron Collider, and we outline our approach to simulation of the Standard Model and Beyond the Standard Model processes. Finally, we give a timeline for ATLAS detector development into the 2020s.

3.1 The LHC Acccelerator

The Large Hadron Collider (LHC) [20] is the world's largest particle accelerator, and is located under the Franco–Swiss border in the 27 km Large Electron–Positron Collider (LEP) tunnel [21]. Planning for the LHC began in the 1980s, with operations first starting in 2008. Unlike fixed-target experiments, a synchrotron design allows for the full conversion of the energy from the co-circulating beams into collision products. The energy loss of an accelerating particle is given by:

$$\frac{dE}{dt} \propto \frac{E^4}{m^4 R}, \tag{3.1}$$

where E is the energy of the charged particle; m is the mass of the particle, and R is the radius of the curvature of the LHC. Taking this energy-loss equation into account justifies the large mass of the hadron accelerants (H^+, Pb^+, and Xe^+), as well as the large circumference of the LHC synchrotron. Given a core scientific goal of the LHC is to probe the energy frontier, a synchrotron design is the only technologically feasible solution.

We now detail the LHC accelerator complex, a schematic is provided in Figure 3.1. The LHC begins with a hydrogen gas canister which is the primary hadron source for the LHC acceleration pipeline [22]. We inject the hydrogen into an electric field which strips the electrons and leaves only bare protons. We form the protons into bunches, each of which contains approximately 10^{11} protons. The bunches are then accelerated by the LINAC 2 using radiofrequency cavities to charge consecutive cylindrical conductors, resulting in a source of protons at approximately 50 MeV. LINAC 2 is in the process of being replaced by LINAC 4 which brings double the intensity and brightness of the beam [23].

From the LINAC system, we then pass the bunches into the Proton Synchrotron Booster [22] which further accelerates the protons from 50 MeV to 1.4 GeV and then the 7 km

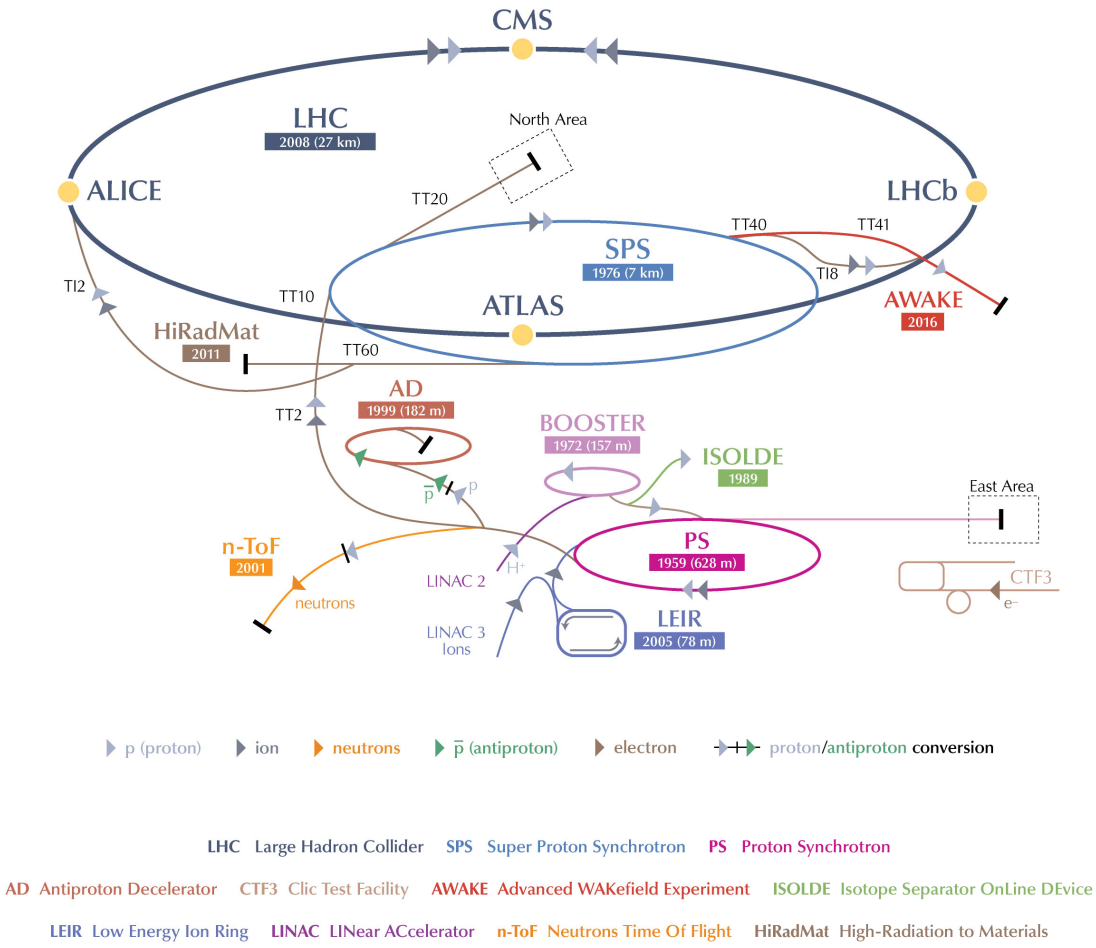

Figure 3.1: Schematic of the CERN accelerator configuration [22].

Super Proton Synchrotron accelerates the bunches from 25 GeV to 450 GeV [22]. We then pass the bunches into the main counter-rotating vacuum beamlines of the LHC machine itself. The two beamlines are encapsulated within two beampipes.

To constrain the co-circulating beams the LHC requires ultra-cool 8 T superconducting magnets [24]. The LHC utilises both dipole magnets, responsible for the acceleration of the bunches, and quadrupole magnets — responsible for the focusing and defocusing of the beams into narrow transverse orbits. The pairing of these two kinds of magnets is known as the accelerator lattice and comprises the base-unit of the LHC. Using this lattice structure, the LHC accelerates the protons in the bunches to a maximum centre-of-mass energy of 14 TeV.

Once the bunches are at the intended centre-of-mass energy, the LHC collapses the co-circulating beams every 25 ns at four primary locations around the ring ATLAS [25], CMS [26], ALICE [27] and LHCb experiments [28]. These four experiments are each responsible for measuring and recording the collisions which the LHC produces. The result of this independent approach is the generation of four completely independent

datasets, each at $\sqrt{s} = 13$ TeV. We now outline one of these four primary experiments — the ATLAS experiment.

3.2 The ATLAS Experiment

The ATLAS experiment is a general-purpose detector located at Point 1 of the LHC. To operate under the extreme conditions produced by the LHC, the electronics of the experiment require fast readout and sufficient radiation hardness. To measure the decay products of the collisions to appropriate precision, we require high detector granularity, as well as a detector coverage approaching 4π steradians. ATLAS uses a right-handed coordinate system with its origin at the nominal interaction point in the centre of the detector. The positive x-axis is defined by the direction from the interaction point to the centre of the LHC ring, with the positive y-axis pointing upward, while the beam direction defines the z-axis. Cylinderical coordinates (r,ϕ) are used in the transverse plane, ϕ being the azimuthal angle around the z axis. The pseudorapidity η is defined in terms of the polar angle θ by $\eta = -\ln \tan(\theta/2)$ The transverse momentum p_T, the transverse energy E_T and the missing transverse momentum E_T^{miss}, which will be detailed in later sections, are defined in the transverse plane.

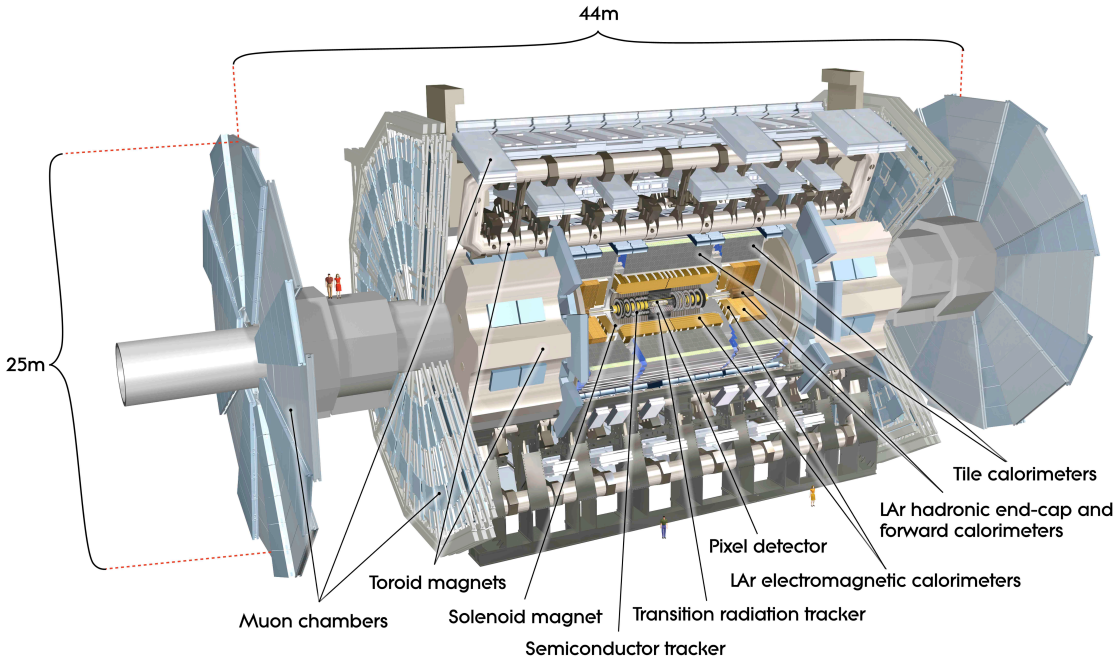

Figure 3.2: The ATLAS detector [25].

The accurate identification and precise measurement of leptons is of vital importance to a large number of benchmark physics scenarios. To identify particles with displaced vertices such as τ-leptons and b-jets, we require vertex detectors to be close to the interaction point. The measurement of electrons and muons requires accurate and pre-

cise electromagnetic calorimetry. To identify and measure hadronic activity, we need hadronic calorimetry. We must have an efficient trigger system so we can select physics scenarios of interest.

We show the schematic overview of the ATLAS detector in Figure 3.2. The ATLAS detector is $25\ \mathrm{m}$ in height and $44\ \mathrm{m}$ in length. The detector weighs approximately 7000 tonnes. The key subdetectors are the Inner B-Layer (IBL) [29], the pixel detector [30], the Semiconductor Tracker (SCT) [31], the Transition Radiation Tracker (TRT) [32–36], the Liquid Argon Electromagnetic Calorimeters (LAr), the solenoid and toroidal magnets, the Tile Hadronic Calorimeters (TileCal), and the Muon spectrometer. These detectors, in conjunction with support systems, comprise the ATLAS detector.

3.2.1 Tracking System

The ATLAS tracking system measures the tracks of charged particles and is composed of four subdetectors, they are collectively referred to as the inner detector. The different subsystems have different methods of extracting a charged particle's position, a recorded position of a particle's position is known as a *hit*. The inner tracking system reconstructs the best fit track for a given configuration of hits. The inner tracking system records a particle's position non-destructively, which allows other subdetectors, further from the collision point, to also make accurate measurements of incident particles. The inner detector provides tracking capability up to $|\eta| < 2.5$. We show an illustration of the inner detector in Figure 3.3.

The four subdetectors in the tracking system are the IBL, the pixel detector, the SCT, and the TRT. The IBL is located closest to the nominal interaction point starting at $R = 33.25\ \mathrm{mm}$ [29]. The pixel detector is located from $R = 50.5\ \mathrm{mm}$ to $R = 122.5\ \mathrm{mm}$ and comprises three layers [30]. The SCT is located from $R = 299\ \mathrm{mm}$ to $R = 514\ \mathrm{mm}$ and is comprised at four nominal radii with eight layers in total. In the barrel region the SCT uses a double-layer design, with the second layer being rotated by $40\ \mathrm{mrad}$. This design allows the extraction of not only $R - \phi$ but also z [31].

The TRT inner radius starts from $R = 554\ \mathrm{mm}$ to $R = 1082\ \mathrm{mm}$ and provides tracking up to $|\eta| < 2.0$. The TRT, unlike the other three subsystems, does not provide a z coordinate, however, it does provide a large number of hits, and measures the track over a longer length than the SCT, pixel, and IBL [32–36]. The combination of all of these tracking subsystems provides a robust measurement of $R - \phi$ and z. The output of the inner detector consists of a collection of hits for every $25\ \mathrm{ns}$ time-slice, which provides the information required to reconstruct charge particle trajectories.

3.2.2 Calorimetry System

The ATLAS calorimeters measure the energy of charged secondary particles created by electromagnetic and hadronic showers. Electrons, positrons, and photons initiate elec-

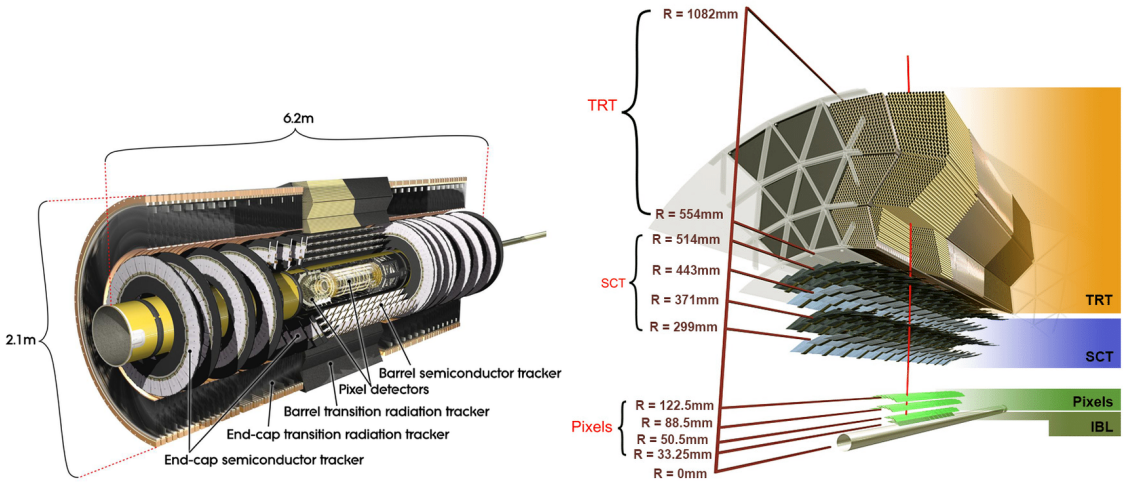

(a) Inner detector subsystem breakdown. (b) Inner detector cross-section.

Figure 3.3: The inner detector of the ATLAS experiment. In (a) we show a subsystem breakdown, and in (a) we show a cross-section slice, showing the radii that the subsystems occupy [37].

tromagnetic showers, which typically evolve in the direction of motion with a transverse spread. At very low energies electromagnetic shower evolution is driven by ionisation of electrons, Compton scattering, and the photoelectric effect. At higher energies pair creation and bremsstrahlung dominate electromagnetic shower evolution.

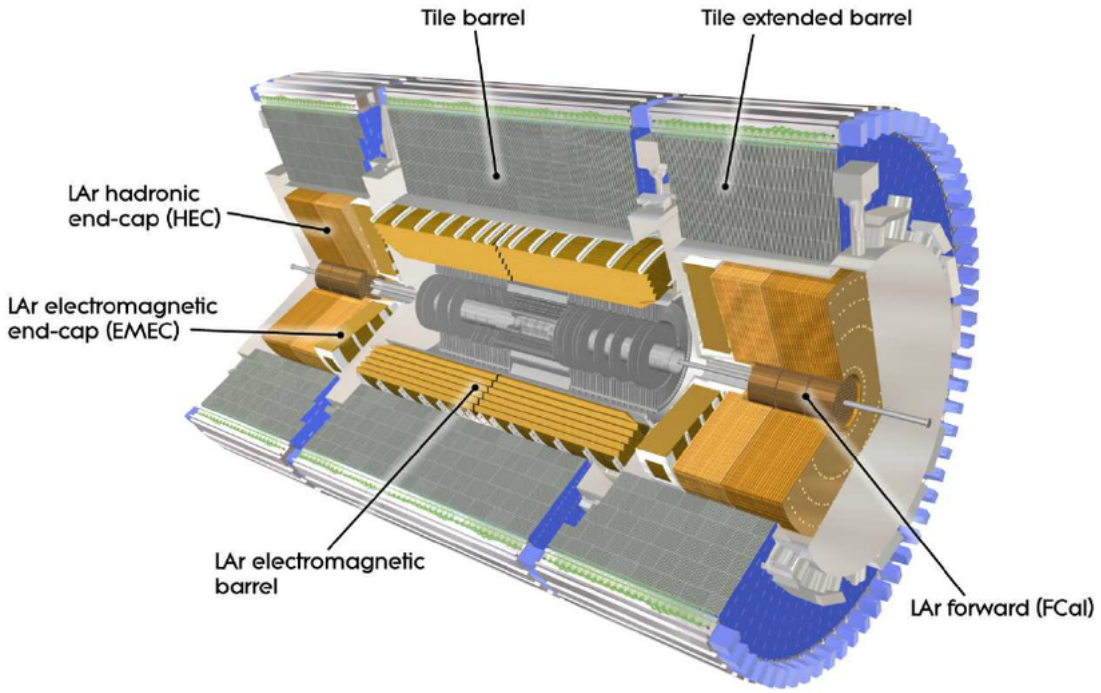

Figure 3.4: A cross-section view of the ATLAS calorimeter [37].

The fully hermetic nature of the calorimetry system provides a strong handle on missing transverse energy. We provide a schematic of the ATLAS calorimetry systems in Figure 3.4. The LAr systems serve the role of both electromagnetic and hadronic calorimeters. The LAr calorimeters use liquid argon as the active medium and use lead, tungsten, and copper as passive absorbers. The electromagnetic calorimeter has three core systems; the LAr electromagnetic barrel, the endcap (EMEC), and the forward calorimeter (FCal). The electromagnetic barrel covers a range of $|\eta| < 1.475$, and the electromagnetic end-cap covers a range of $1.375 < |\eta| < 3.2$ [37].

The LAr performs hadronic calorimetry in the endcap, whereas the TileCal, covers the barrel region. The TileCal uses alternating steel and plastic scintillator plates. The steel plates act as the absorber and the plastic scintillator as the active medium. Photons from the active medium are captured by wavelength shifting fibres to photomultiplier tubes where the data passes to the data-acquisition systems. The TileCal covers a region of $|\eta| < 1.7$ [37].

3.2.3 Muon Spectrometer and Toroidal Magnet System

The Muon Spectrometer (MS) is the outermost subdetector of the ATLAS experiment [38]. We provide a schematic for the MS system in Figure 3.5. The MS measures high-p_T muons with high precision and to provide fast readout capability, which allows triggering. The momentum of a muon can be measured by applying an external magnetic field.

The MS encompasses four different subdetector technologies as well as the barrel and endcap toroidal magnets. The four subdetectors are the Resistive Plate Chambers (RPC), the Thin Gap Chambers (TGC), the Monitored Drift Tube (MDT) chambers, and the Cathode Strip Chambers (CSC). The MDT and CSC are used for tracking in the $|\eta| < 2.5$ and $2.0 < |\eta| < 2.5$ ranges respectively. The RPC and TGC are used for triggering capabilities in the ranges $|\eta| < 1.05$ and $1.05 < |\eta| < 2.5$.

The toroidal magnet system consists of three air-core superconducting systems located around the barrel and both end caps. The systems have an eightfold symmetry of coils located azimuthally around the beam axis. The barrel region has a bending power of $1.5-5.5\ \mathrm{Tm}$ for $|\eta| < 1.4$ whereas the endcap system has a bending power of $1-7.5\ \mathrm{Tm}$ for the region between $1.6 < |\eta| < 2.7$. The region between the barrel region magnetic field and the endcap magnet field is called the transition region; the η range for the transition region is $1.4 < |\eta| < 1.6$. In the transition region, the bending power is smaller, and so the uncertainties on muon momenta are larger.

3.2.4 Trigger System

During nominal run-II operations, there is a bunch crossing every 25ns, which translates to a bunch crossing rate of 40 MHz. Every event in run-II had an approximate size of

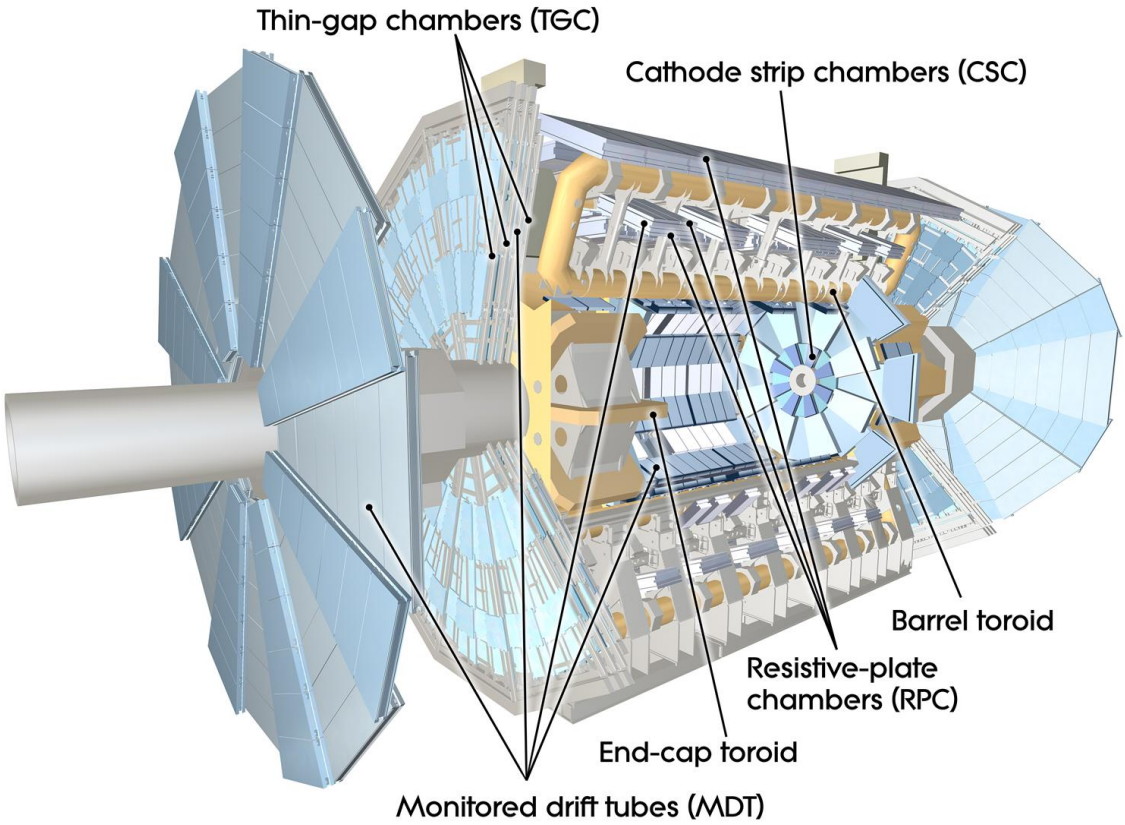

Figure 3.5: Muon Spectrometer in the ATLAS detector [38].

2.4 MB. If we were to record all bunch crossings, then we would need the capability to record 96 TB/s, which is currently a technological impossibility. The data acquisition (DAQ) system is responsible for transporting all event data from the front-end buffers to permanent storage. The DAQ system is summarised in Figure 3.6. DAQ starts at a proton–proton collision and subsequent response from ATLAS subsystems. The tracking information and other detectors pass directly into the detector readout system, and the calorimeter and muon systems pass information into both the trigger system and the detector readout system.

To handle this massive amount of data, the ATLAS trigger system has two levels the Level-1 (L1) and the High-Level Trigger (HLT) [40–42]. The L1 system has two primary subsystems; these are the L1 calorimeter and the L1 muon system. The two subsystems are responsible for selecting physics signatures from the calorimeter and muon systems, respectively. The L1-Calo and L1-Muon send their data through to the L1 Topological Processor, where we can select on more derived quantities such as the scalar sum of the object momenta, or the dilepton invariant mass. If there is a signature of interest, then the L1 trigger accepts the given event, this is known as an L1 Accept.

The detector readout passes all data to the front-end electronics, where it awaits an L1 Accept. The readout drivers (ROD) receive the events, the readout system (ROS) then

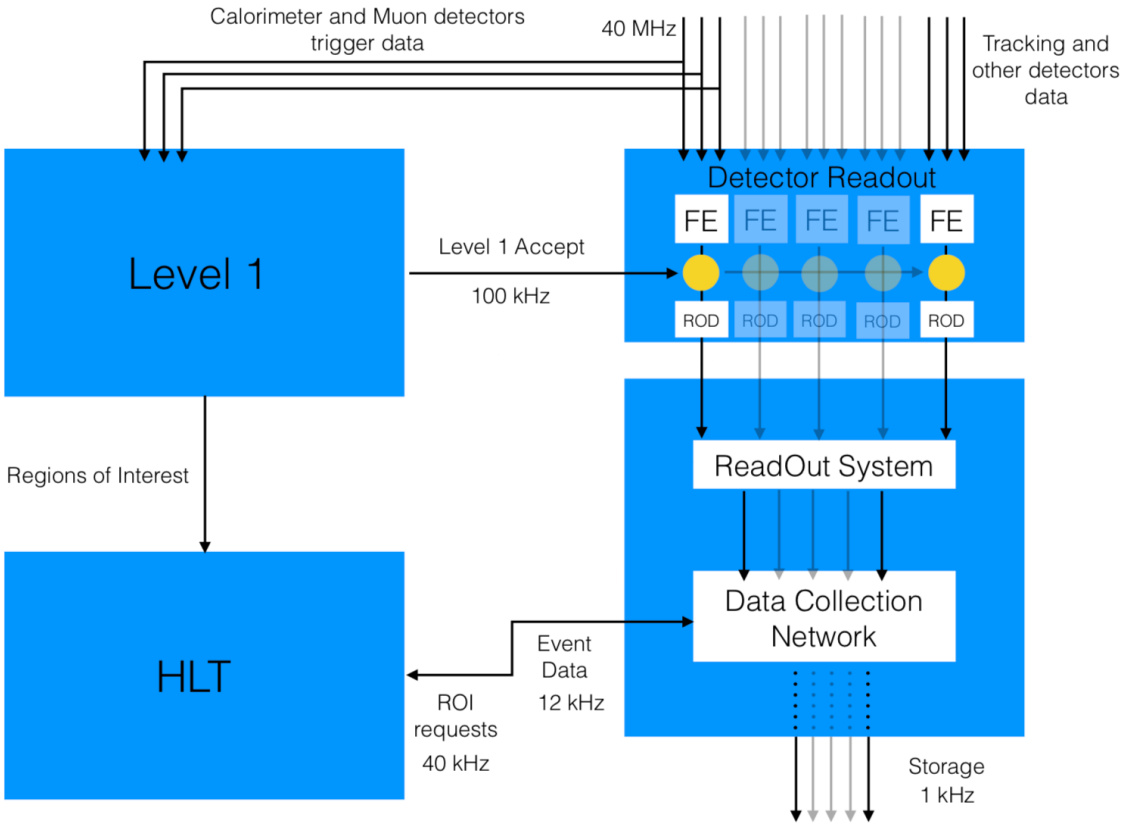

Figure 3.6: Overview of the ATLAS trigger system [39].

reconstructs the events; this happens at the same time the L1 trigger creates Regions of Interest (ROI) around triggered features. The HLT then receives the ROI and applies a software approach to triggering.

The trigger menu contains the full suite of triggers available to the ATLAS experiment. The physics use case dictates the bandwidth available to different triggers. Physics measurements typically are awarded large bandwidth and can run on every bunch crossing. These primary triggers usually incorporate topological information as well as momentum thresholds for different triggered particles such as electrons, muons, jets, and even missing transverse energy. Some triggers may record too many events; if this is the case, we may restrict (prescale) the trigger to only operate on a subset of bunch crossings. The result of this triggering system was a rate of recorded events in run-II of 1 kHz, with a required readout speed of 2.4 GB/s, which when compared to 40 MHz is a substaintial reduction.

3.3 Object Reconstruction

In this section, we outline the various methods used to reconstruct and identify objects in the detector. These objects include tracks, vertices, electrons, photons, muons, τ-

leptons, jets, and missing transverse energy. We show the correspondence between the SM objects and reconstructed objects in Figure 3.7.

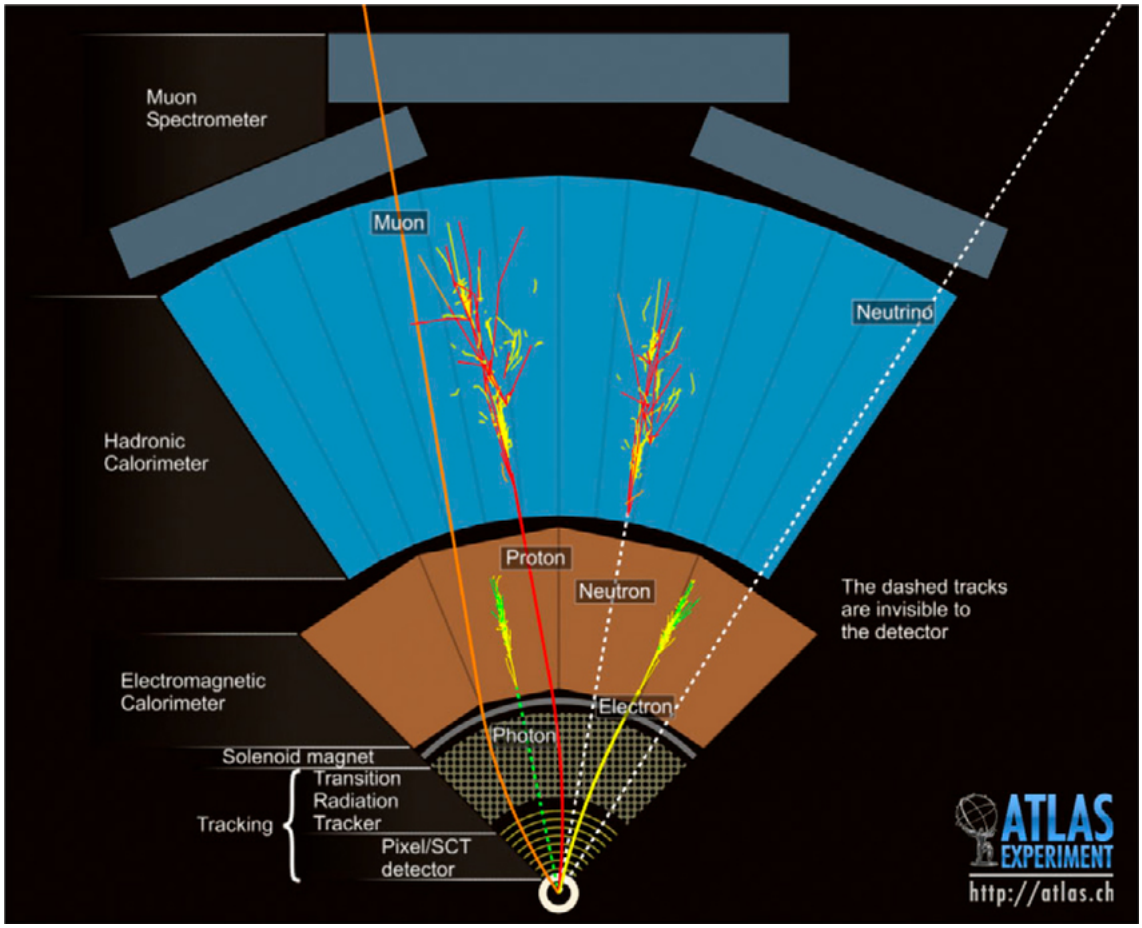

Figure 3.7: Overview of SM particle vs ATLAS object reconstruction [43].

We describe the trajectory of a charged particle in a solenoidal magnetic field $\vec{B}$ using a five-parameter helical approximation, shown in Figure 3.8. The five parameters which define a track are the transverse impact parameter (d_0), the longitudinal impact parameter (z_0), the azimuthal angle (ϕ), the pseudorapidity (η), and the curvature ($Q/2p_T$).

To reconstruct a track we used a staged pattern-recognition approach [37]. We apply a track-finding algorithm beginning from track seeds, which consist of 3 hits in the pixel detector or Layer 1 of the SCT. The output of the track finding algorithm is a candidate track. To extend the track candidates to the full SCT, we rank candidates by track quality criteria and use neural networks to solve for combinatoric ambiguities [44]. Beyond track reconstruction we also apply global χ^2 fit requirements [45] and Kalman filtering [46]. To reduce the number of fake tracks, we demand kinematic requirements such as minimum $p_T > 400$ MeV, and we require a track is located within the barrel of the inner detector ($|\eta| < 2.5$). We complete the track reconstruction process by extending the candidate track from the Pixel and SCT detectors into the TRT.

In each collision, there are many simultaneous proton–proton collisions known as pileup,

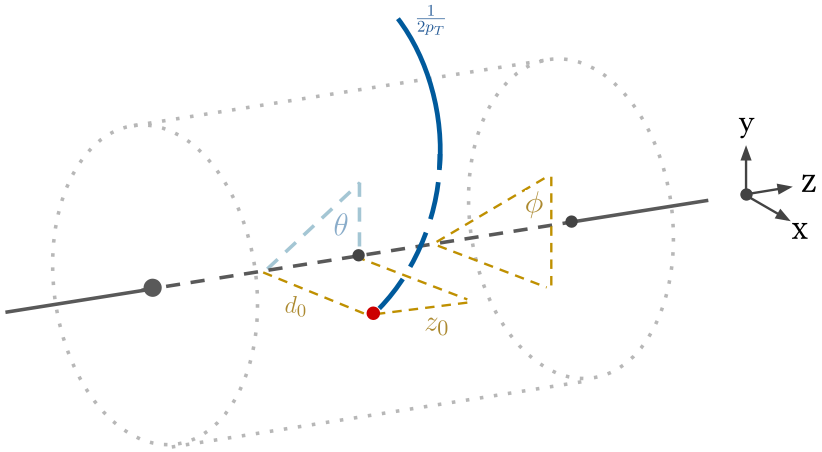

Helical Track Parameterisation

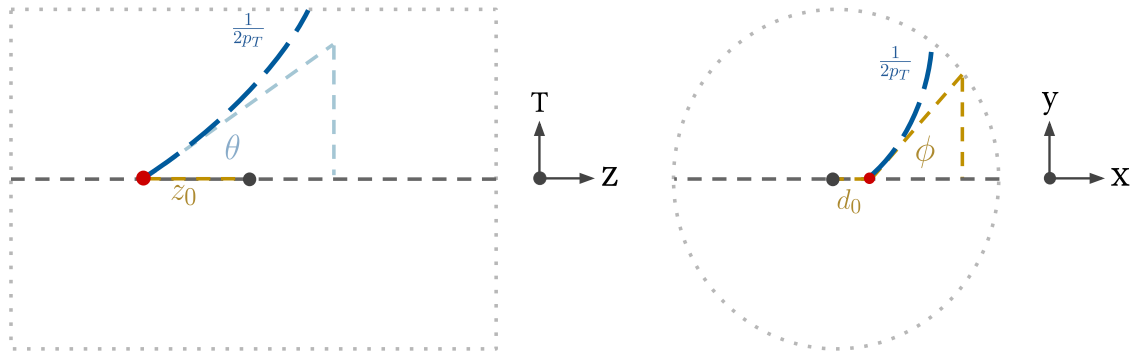

Longitudinal Projection

Transverse Projection

Figure 3.8: Helical track parameterisation projections.

and each of these collisions produces tracks. We determine the vertices by extrapolating the tracks back to the beamline. We can reconstruct multiple vertices, but of these, we define the primary vertex to be the one with the highest $\sum p_{T,i}^2$, summed over all tracks. Once we have a primary proton–proton collision, we can impose conservation of momentum constraints to its decay products. After defining the primary vertex, we define secondary vertices. Secondary vertices come from decay products of the proton–proton collision and are typically the result of heavy-flavour decays and photon conversions.

Electrons and Photons

Electrons and photons are identified by matching tracks to electromagnetic calorimeter signatures [47–49]. These signatures are required to meet both energy thresholds and shower shape criteria. At the beginning of run-II, we have updated our method of determining electromagnetic seeds for electron identification. The original method was a fixed-size sliding-window approach, where we scanned the calorimeter in $\eta - \phi$ space in 3×5 towers to find clusters which had an energy deposit of 2.5 GeV [47–49]. A new method allows dynamic variable-sized clusters known as superclusters, we call this method the *supercluster* method. We create superclusters for electrons and photons independently of one another, which allows us to better account for the energy losses associated with bremsstrahlung and photon conversions. We then apply energy calibrations as well as position corrections to the clusters. To reconstruct an electron, we match between the inner detector tracks and the superclusters; the matching uses χ^2 pattern matches in $\eta - \phi$ space [45]. By determining the superclusters for electrons and photons independently, we can have ambiguities in reconstruction. Where there are ambiguities, this is left up to the analysis to resolve. We are able to define benchmark identification points for electrons and photons by using a number of shower shape variables [47, 50]. The three benchmark electron identification points are defined `Loose+b-layer`, `Medium`, and `Tight`, each of which have impact parameter selections applied. The photon identification points are `Loose`, `Medium`, and `Tight` [51].

Muons

The muon ionises significantly less than the electron. As a result, muons are not stopped in the calorimeters. Tracks for muons are reconstructed separately to the electron and photon reconstruction method. We sort the muon candidates into three categories: combined, tagged, and standalone. The combined category corresponds to when tracks from the inner detector and MS are reconstructed and fitted together; this is the most common category of muon candidate. The tagged category corresponds to muon candidates reconstructed with hits from only one layer of the MS and either an inner detector track (muon-tagged) or energy deposit from the calorimeter (calo-tagged). The MS layer can be either in the monitored drift tube or the cathode strip chambers. The standalone category corresponds to muon candidates which only used the MS in reconstruction. We extrapolate standalone candidates from the MS to the primary vertex, even through the

region $2.5 < |\eta| < 2.7$ which has no inner detector coverage [52]. There are four working points which are defined for muon identification, these are `Loose` (tagged-muons), `Medium` (combined or standalone), `Tight` (`medium` plus additional track requirements), and *high* p_T [52].

Jets

In the ATLAS experiment, we observe hadronised particle showers, or jets, not individual quarks and gluons which were involved in the proton–proton collisions. Jets radiate secondary gluons, resulting in the formation of colourless particle showers, which can subsequently decay into leptons and photons. These showers leave tracks in the inner detector as well as energy deposits in the electromagnetic and hadronic calorimeters. All the energy of a shower is absorbed and stopped in the calorimeter, and so very little of the shower makes it to the MS. In order to reconstruct these particles we apply the anti-k_T algorithm [53] to the topological clusters [54] in the calorimeters, typically with a radius of $R = 0.4$. After reconstruction, we calibrate the individual jet energies and incorporate systematic uncertainties.

b-tagged Jets

Once we have reconstructed jets using the anti-k_T algorithm, we can then apply a hypothesis test to determine the likelihood of which type of object initiated them [55]. After we have produced a b-quark from the proton–proton collisions, it propagates for a short time before hadronising; this seeds a jet with a measurably displaced vertex with respect to the primary vertex. We can discriminate between light-quark seeded jets and b-quark seeded jets, by leveraging this displaced vertex information. We use a Boosted Descision Tree (BDT) based algorithm to determine how likely a jet is to have originated from a b-quark, this algorithm is called `MV2c10` and is typically referred to as b-tagging [55]. The `MV2c10` algorithm uses the input of three other algorithms as input. These three algorithms are `IP2D`, `IP3D` which are impact parameter based algorithms, `SV` which is an algorithm that fits for secondary vertices and `JetFitter` (JF) which performs a global fit of the full hadron decay chain and attempts to reconstruct successive vertices with a jet. The output of the `MV2c10` algorithm is a distribution [55] which, given different requirements allows us to select on b-tag efficiency, usually 60%, 70% or 85%.

Missing Transverse Energy

Missing transverse energy is an important observable for the ATLAS experiment. The experiment has no subdetectors which are capable of measuring the presence of weakly interacting particles, and yet there are many processes which produce them. Given their importance to the physics reach of the experiment, it is vital to have a variable which can at the very least act as a proxy for the weakly interacting particle's momentum. From the

design of the LHC we know that the proton–proton beam has no significant momentum transverse to the beam axis. This gives us a relationship between the initial and final state momentum:

$$\sum_f p_{x,f} = \sum_f p_{y,f} = 0, \tag{3.2}$$

where $p_{x,f}$ and $p_{y,f}$ are the x and y components of all final-state particles which were produced by the initial parton-parton collision. We can split this relation into visible and invisible components,

$$\sum_{i=\text{visibles}} p_{x,i} + \sum_{j=\text{invisibles}} p_{x,j} = 0. \tag{3.3}$$

We cannot resolve the individual invisible particles' momenta but we can infer their total vectorial sum in the x (y) direction(s):

$$E^{\text{miss}}_{x(y)} = \sum_{\text{invisibles}} p_{x(y),i} = -\sum_{\text{visibles}} p_{x(y),i}, \tag{3.4}$$

from this we can construct $\vec{E}^{\text{miss}}_T$ to be equal to:

$$E^{\text{miss}}_T = \sqrt{\left(E^{\text{miss}}_x\right)^2 + \left(E^{\text{miss}}_y\right)^2} \tag{3.5}$$

$$\phi^{\text{miss}} = \arctan\left(E^{\text{miss}}_y / E^{\text{miss}}_x\right). \tag{3.6}$$

When we treat the missing energy as a 3-vector, we canonically set the z-component to zero.

The reconstruction of E^{miss}_T requires the input of all detector subsystems and strong understanding of the initial conditions of the collision [56]. The reconstructed E^{miss}_T has two components, these are the hard-event and the soft-event components. Hard-event signals correspond to fully reconstructed and calibrated objects. The soft-event contribution to E^{miss}_T corresponds to tracks correspond to energy deposits not associated with reconstructed objects. We define different working points for missing transverse energy, these working points applying different criteria on the jet treatment in the forward endcaps of the detector; these are `Loose`, `Tight`, `Tighter`, and `Tenacious` [56]. We can write out the missing transverse energy's dependence on reconstructed objects in the following way:

$$E^{\text{miss}}_{x(y)} = E^{\text{miss},e}_{x(y)} + E^{\text{miss},\gamma}_{x(y)} + E^{\text{miss},\tau}_{x(y)} + E^{\text{miss,jets}}_{x(y)} + E^{\text{miss},\mu}_{x(y)} + E^{\text{miss,soft}}_{x(y)}. \tag{3.7}$$

3.4 The ATLAS Experiment Dataset

As stated earlier, it is the responsibility of each experiment location around the LHC to record the results of the LHC beam collisions. The goal of each of the experiment is to produce high quality large statistics datasets. An important quantity for defining the amount of data able to be recorded is given by:

$$\mathcal{L} = \frac{N_b^2 n_b f_{\text{rev}} \gamma_r}{4\pi \epsilon_n \beta^*} F, \tag{3.8}$$

where N_b is the number of particles per bunch, n_b is the number of bunches per beam, f_{rev} is the revolution frequency, γ_R is the relativistic gamma factor, ϵ_n is the normalised transverse beam emittance, β^* is the beta function at the collision point and F is a geometric reduction factor due to the non-zero crossing angle between the beams at the interaction point.

The design instantaneous luminosity of the LHC is $\mathcal{L} = 10^{34}\ \text{cm}^{-2}\text{s}^{-1}$ [20, 57]. During 2018, the LHC delivered peak luminosities of more than double the design specifications; we show this in Figure 3.9. As a direct result of the increase of luminosity, we have been able to record more events than our run-II baseline expectations.

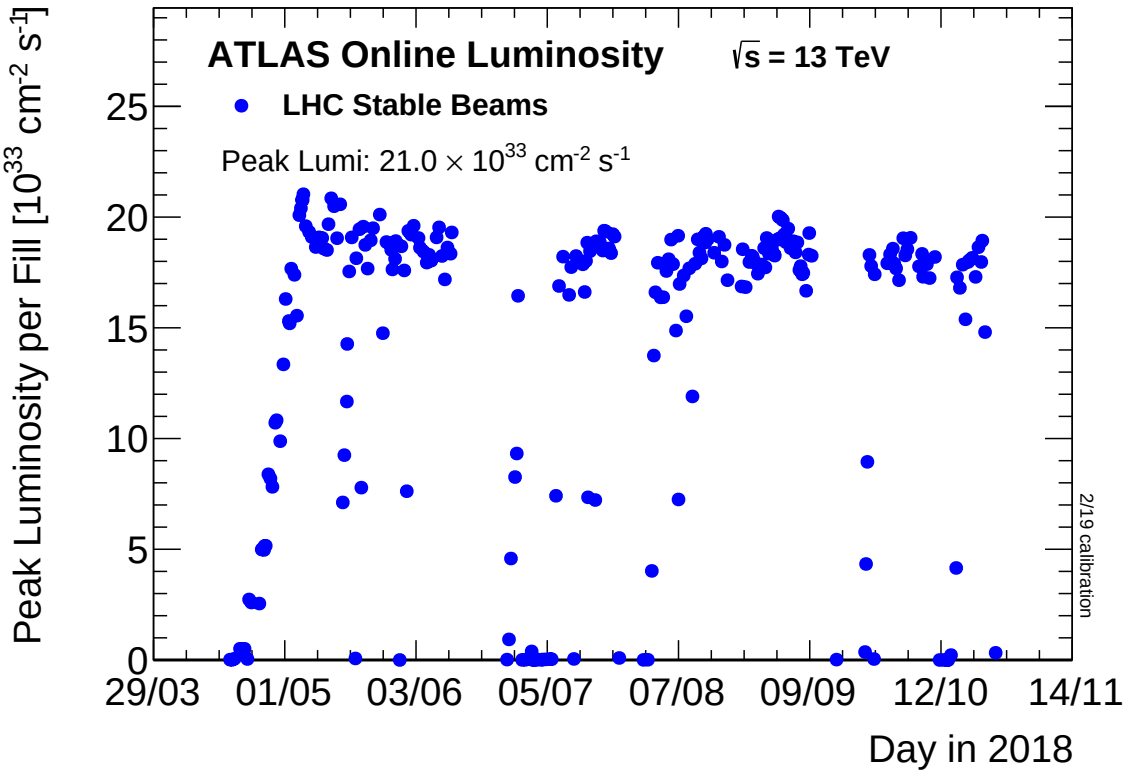

Figure 3.9: The instantaneous luminosity recorded during the 2018 data-taking period by the ATLAS experiment. The peak instantaneous luminosity is $\mathcal{L} = 2.1 \times 10^{34}\ \text{cm}^{-2}\text{s}^{-1}$ [57, 58].

Once we have recorded a dataset, we then want to compare to theory. We can quantify the number of collisions corresponding to a given decay process with the relation:

$$N_{\text{observed}} = \sigma_{\text{process}} \times \text{BR} \times \epsilon \times \int dt\mathcal{L}, \tag{3.9}$$

where N_{observed} is the number of collisions recorded at a given experiment, σ_{process} is the cross-section of the production of a specific process, BR is the branching ratio to a given final state, ϵ corresponds to all efficiencies considered for a given measurement, and $\int dt\mathcal{L}$ corresponds to the integrated luminosity of the given dataset.

3.5 The Proton Parton Distribution Function

In Equation 3.9 we introduced σ_{process} which was the cross-section of a specific process being produced in a proton–proton collision. The parton model describes the interactions between the constituent quarks and gluons of the proton and gives us a method to calculate σ_{process}. The MSTW 2008 parton density functions (PDFs) are shown in Figure 3.10.

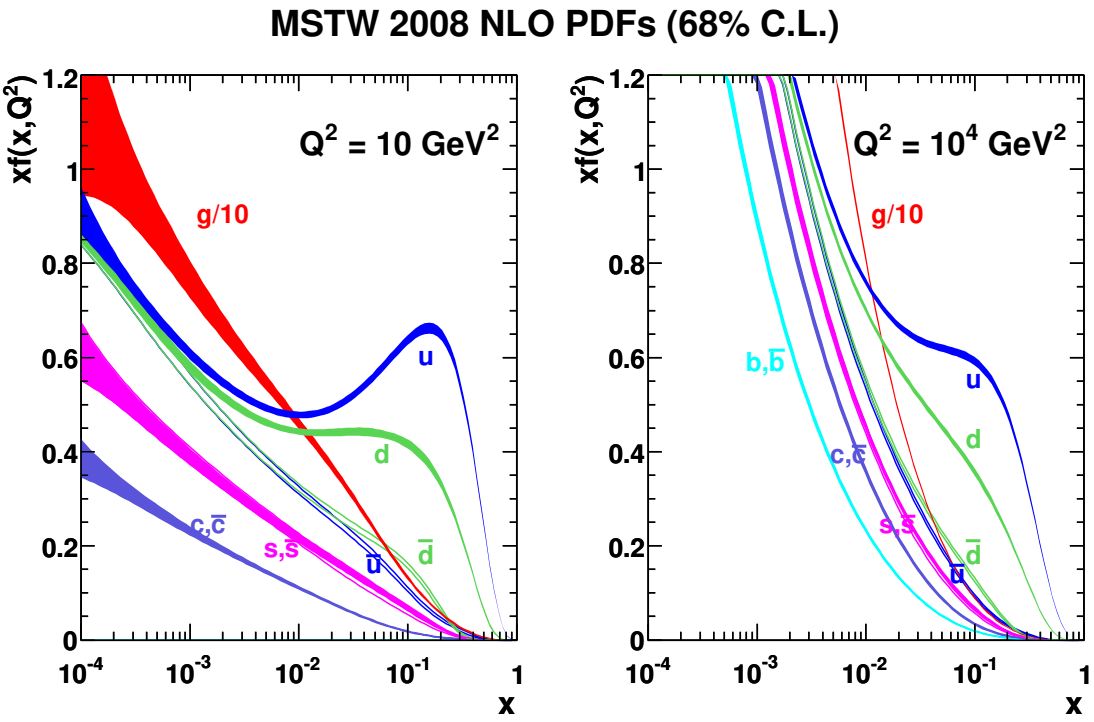

Figure 3.10: The MSTW 2008 parton density functions, with the total momentum fraction, x, of a given proton constituent as the independent variable [59].

The proton can be understood by the momentum fraction of each constituent particle. Incorporating all the internal behaviour of the proton yields us the proton itself. The

inclusive cross-section of proton–proton collisions is the most general way to describe proton–proton collisions resulting in a final state X. The inclusive proton–proton cross-section is given by:

$$\sigma_{\mathrm{p_1,p_2\to X}} = \sum_{a,b\in\{q,g\}} \int dx_a \int dx_b f_a^{p1}\left(Q^2, x_a\right) f_b^{p2}\left(Q^2, x_b\right) \sigma_{ab\to X}\left(Q\right), \tag{3.10}$$

where $\sigma_{ab}\left(Q^2\right)$ is the partonic cross-section. The PDFs $f_{a(b)}^{P}$ describes the probability for a given parton of flavour a (b) to have a particular fraction x of the transferred momentum Q between the two partonic states at a given resolution scale Q^2. This brings us naturally to describing the physics reach of the LHC.

3.6 Physics Reach of the Large Hadron Collider

We now detail which processes dominate in a LHC environment given the luminosity dependence laid out in Equation 3.9.

In Figure 3.11 we plot the cross-section of many SM processes measured at the LHC for a given centre-of-mass energy [60]. The grey shows the theory predictions. The blue, orange, and purple are the measurements at the centre-of-mass energies of 7, 8, and 13 TeV. The total pp cross-section is at least six orders of magnitude higher than the next most prevalant process. In order of most dominant cross-section we have W production followed by Z, $t\bar{t}$, t t-channel, WW, H, Wt, WZ, t s-channel, $t\bar{t}W$, $t\bar{t}Z$, and finally tZj.

In Figure 3.12 we plot the cross-section of Higgs boson production under different mass assumptions [61]. We see in particular that for the measured Higgs boson mass of $m_H \approx 125$ GeV the most dominant production mechansim for the Higgs is gluon–gluon fusion ($pp \to H$), followed by vector boson fusion ($pp \to qqH$), W and Z bremsstrahlung ($pp \to VH$), $t\bar{t}$ fusion ($pp \to ttH$), and finally $pp \to tH$. Each of these production mechanisms provides a means of measuring the Higgs boson. In Chapter 5 we target $pp \to H$ and $pp \to qqH$ and the subsequent decay via $H \to WW$ and extract the gluon–gluon fusion and vector boson fusion Higgs boson production cross-sections.

In Figure 3.13 we show the cross-sections in pb at $\sqrt{s} = 13$ TeV for supersymmetric strong production and supersymmetric electroweak production [62]. When the masses of gluinos, squarks, neutralinos and charginos are equal, the production process with the highest cross-section is di-gluino production, followed by gluino-squark production and di-squark production. After the strong production processes, we have electroweakino production, which has cross-sections at least one order of magnitude less than strong production cross-sections. The production cross-sections of the neutralino and charginos are a function of the wino and bino mixing, with wino mixing having the highest cross-sections. If the masses of the gluinos and squarks are much larger than the electroweakino masses, the cross-sections of electroweakino production become more

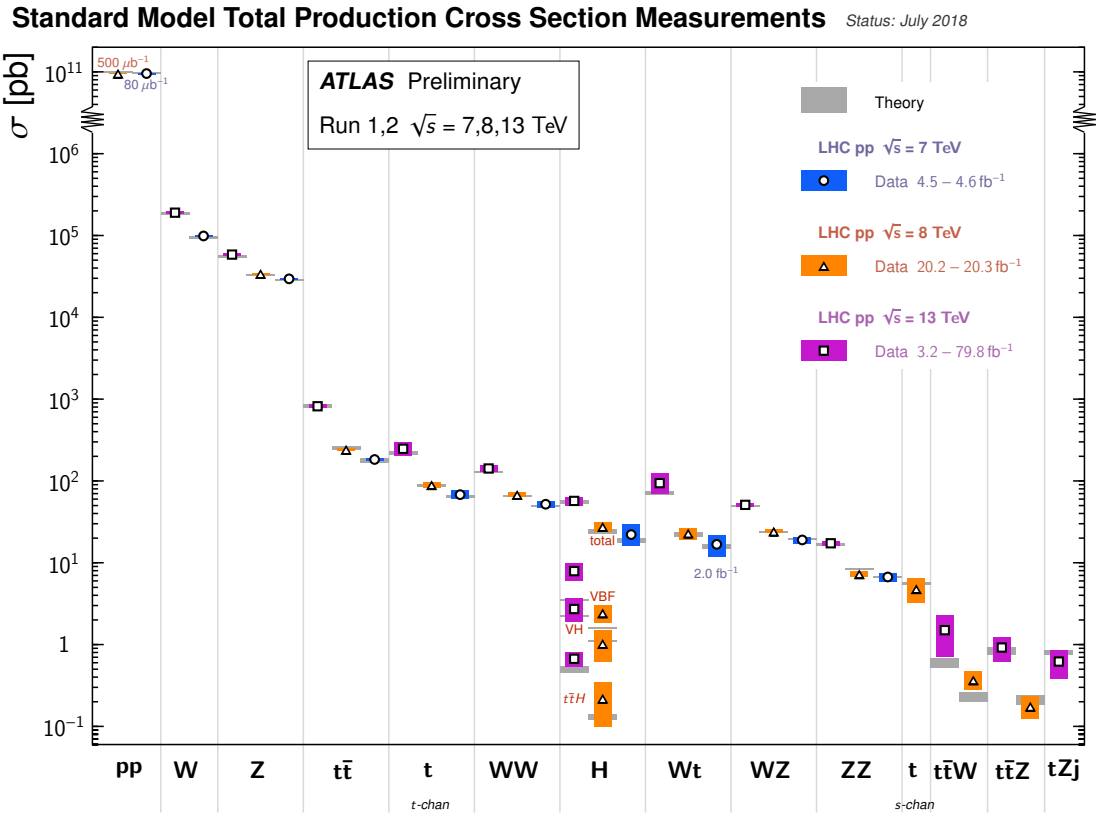

Figure 3.11: Cross-sections of SM processes vs centre-of-mass energy [60].

significant than the strongly produced sparticle cross-sections. In these situations, we might discover supersymmetry through an electroweakino production process. This regime is of particular interest to our work, and in Chapter 4, we outline our search for electroweak production of supersymmetric particles.

3.7 Monte Carlo Simulation & Simplified Models

The typical design of a search analysis in the ATLAS experiment is a counting experiment, where we compare the expected number of events with the observed. At the ATLAS experiment, we use Monte Carlo (MC) generators to simulate both the background processes and the signal processes. The background processes constitute the expected behaviour of the SM. In a search analysis, the signal processes correspond to what new physics we believe may be present under a given number of selection criteria. We often call a selection of criteria a *Region*. The search analyses in ATLAS optimise the selection criteria based on these simulated events, and we determine the sensitivity of ATLAS to new physics using these events. Where applicable, we may use the available dataset to generate a *data-driven* background estimate. These data-driven estimates typically have specialised validation procedures to ensure the applicability of the estimation in

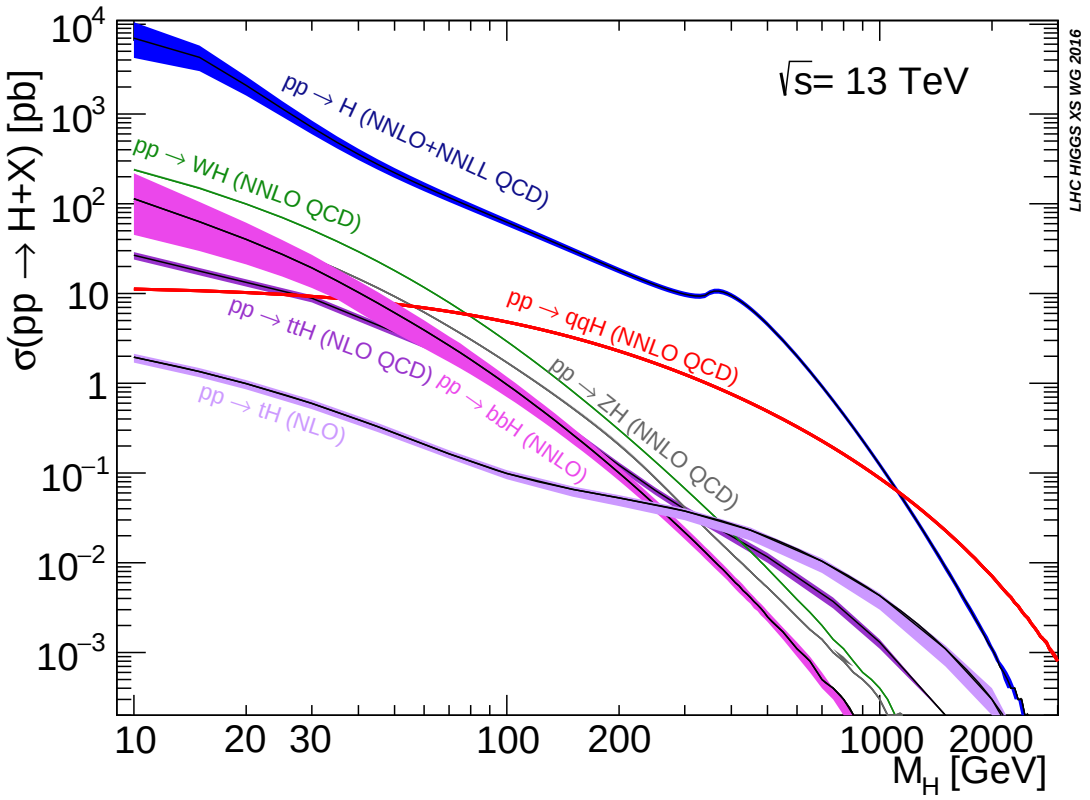

Figure 3.12: Higgs production cross-sections vs Higgs boson mass [61]

the given region.

Simulating the SM in the conditions the LHC provides is a difficult technical challenge. To simulate run-II LHC conditions, we include initial state radiation (ISR) which comes from the two incident protons. We account for the non-point-like structure of the proton by acounting for our modelling of the PDFs.

We calcualte the matrix elements to a given order to capture a given theory's behaviour. We incorporate the effect of constructive or destructive interference of leading-order and next-to-leading order diagrams so we can accurately forecast the sensitivity of our experiments. We calculate the effect of the sizable amount of pileup, of parton showering, of high-to-low energy evolution of parton showers, and we must be able to model final-state radiation (FSR), and account for detector response.

Using a MC approach, we factorise these challenges into sub-tasks and improve our understanding of each of them in turn. There is no "correct" way to solve these tasks, and there are a large number of competing MC generators that take different approaches to simulate events in the $\sqrt{s} = 13$ TeV LHC collisions.

When searching for supersymmetry we do not use fully-complete signal models; instead, we use *simplified* models [63]. Simplified models define new physics with a TeV scale Lagrangian, instead of a much higher-energy scale such as the GUT scale or the Planck

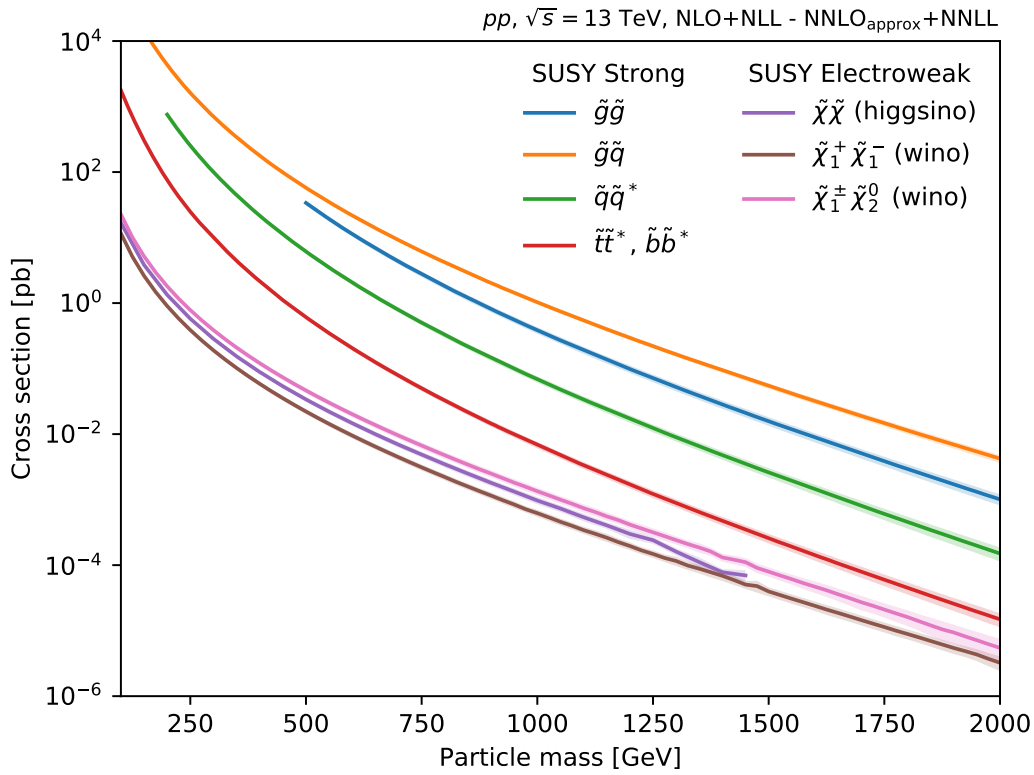

Figure 3.13: The cross-section vs mass for gluinos, squarks and electroweakinos in a subset of the MSSM. In general we can see for a given mass, electroweakino cross-sections are smaller than supersymmetric strong production [62].

scale. Simplified models assume the interactions, and also assume the branching ratios and cross-sections of such a model, typically branching ratios are taken to be 100%. These are model-dependent assumptions and ones which, when relaxed, can have massive effects on exclusion and discovery reach. The benefits of using a simplified model approach include: identifying the boundaries of search sensitivity, characterising new physics signals, and deriving limits on more general models beyond supersymmetric theories.

Often searches for beyond the SM are model-dependent and are cast as exclusions of particular alternative hypotheses, or signal models. This approach runs the risk of too narrowly defining selection criteria. A complementary approach is model-independent limits, which assume no alternative hypothesis but do provide limits on the contribution of beyond the SM physics to a given measurement. In Chapter 4, we present our results in a model-independent fashion.

3.8 LHC & ATLAS Upgrade Timeline

The LHC has a long history of development, construction, and operations. The vast majority of LHC operations corresponds to data-taking (Runs) and machine maintenance periods (Long shutdowns). The scientific programme of the LHC spans over the next 20 years and includes a series of technical upgrades and replacements of detectors. We show the full timeline for LHC operations in Figure 3.14. The result of this 20 year scientific programme will be the accumulation of a 3000 fb^{-1} proton–proton collision dataset.

As of 2020, the LHC is in Long Shutdown 2 (LS2). During LS2, the individual experiments have been performing routine maintenance and installation of upgrade subdetectors. The LHC simultaneously has been undergoing maintenance and laying the groundwork for Long Shutdown 3 (LS3), which will take place in 2024 through to 2027; LS3 will be the major machine maintenance upgrade during the lifetime of the LHC. During LS3 we will be upgrading the LHC to the high-luminosity LHC (HL-LHC), as well as replacing ATLAS subsystems.

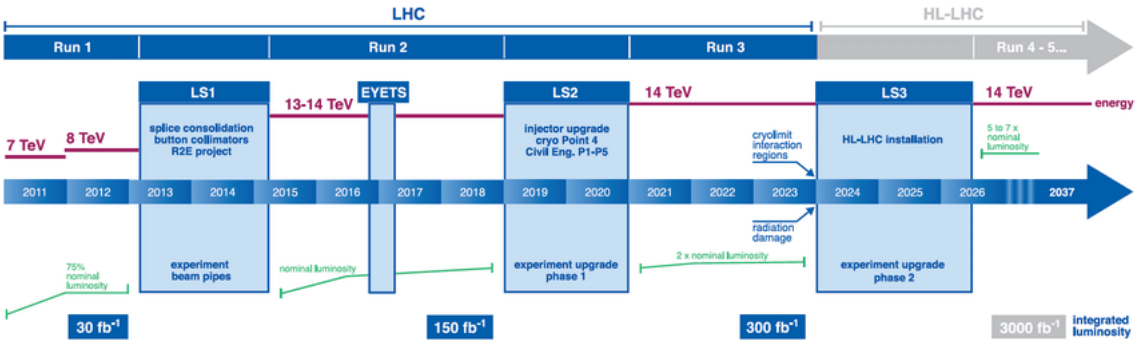

Figure 3.14: The timeline of the LHC project. There are two major eras in this timeline; the LHC era, and the High-Luminosity LHC era. The major units of these timelines are Long Shutdowns (LS) and runs labelled run-I through to run-IV. In red we have the expected centre-of-mass energy of the LHC, and in green, we have the expected luminosity as compared to the nominal LHC luminosity [64].

In ATLAS, we call the first upgrade phase-I, which started in 2018. The upgrade projects covered by phase-I include the Liquid Argon Calorimeter (LAr), Tile Calorimeter (TILE), the New Small Wheel (NSW), BIS78, and the Trigger and Data Acquisition System (TDAQ), as well as the Fast Tracker (FTK). The FTK project due to unexpected funding constraints has been ramped down with a modified scope and will not be installed in the ATLAS detector. In Section 6.1, we explore the FTK and the lessons we have learned in Fast Simulation. In Figure 3.15, we show the number of hits in each layer of the pixel and SCT detectors as a function of instantaneous luminosity. The increased number of hits will have a substantial effect on the reconstruction time. In the second plot in Figure 3.15, we see the effect of increased pileup on the reconstruction time in seconds per event. The current configuration of the LHC operates at a nominal pileup of approximately 60. We designed the FTK to operate under the challenging conditions the LHC machine provides.

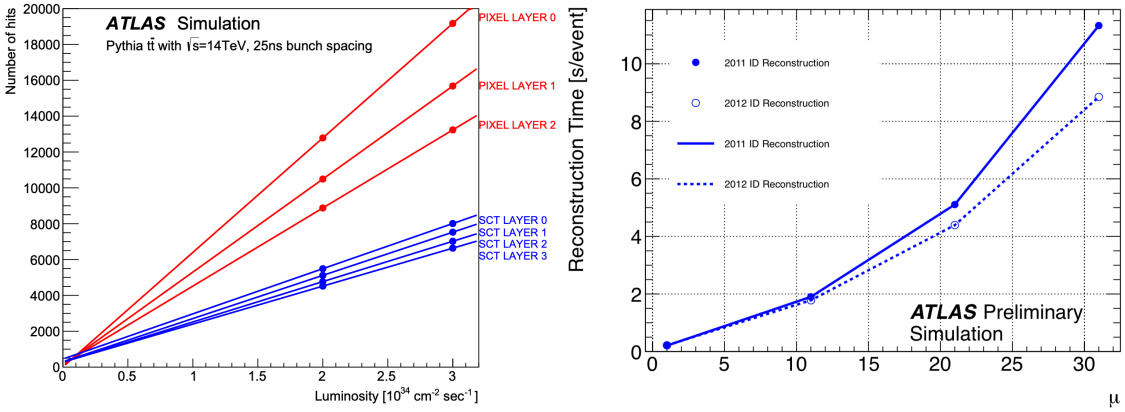

(a) Number of hits vs luminosity.

(b) Reconstruction time vs pileup (μ).

Figure 3.15: Tracking is highly dependent on detector conditions. Here in (a) we show number of hits vs luminosity for the pixel detector and SCT respectively, and in (b) we show reconstruction time vs pileup.

As has been described in Section 3.2.4, the ATLAS trigger system is split into a hardware-based Level-1 and a CPU based HLT. Tracking is computationally expensive and requires a lot of processing capability. The HL-LHC, which will operate not only at slightly greater centre-of-mass energies but also at higher instantaneous luminosities, and with a more substantial nominal pileup, will have more difficult data-taking conditions.

In 2024 the major machine maintenance period LS3 will begin, and with it, ATLAS will commence installation of its phase-II detector upgrades. These detector upgrades are comprehensive and will provide replacements for parts of the ATLAS detector. These phase-II upgrades include the Inner Tracker (ITk), the Liquid Argon Calorimeter, the Tile Calorimeter, and the high Granularity Timing Detector (HGTD), Muon spectrometer upgrade, TDAQ upgrades and a Hardware Tracking for Trigger (HTT) system. The ITk is the replacement detector for the pixel detector, SCT, and TRT detectors and will use two principal technologies; strips and pixels, with no TRT analogue. A significant difference between the SCT strips and ITk strips systems is the switch from p-n-p doped silicon to n-p-n doped silicon. The change of silicon doping has effects on the digitisation software used for the ITk. In Chapter 7, we will explore the operating conditions of the HL-LHC and we detail work performed to validate the use of existing software implementations of digitisation, and provide a report into what is required of the ITk project in order to move forward.

Chapter 4

Search for Supersymmetric Electroweak Production

In this chapter, we detail the work performed on the chargino–neutralino supersymmetry search using the full run-II $\sqrt{s} = 13$ TeV ATLAS experiment dataset.

The production cross-sections of supersymmetric particles are functions of the centre-of-mass of the LHC. In the scenario where the strong sector supersymmetric particles are much more massive than electroweakinos, the visible cross-section of the gluino and squarks is smaller than the visible cross-section of electroweakino production. In this analysis, we specifically target a search for supersymmetry via the electroweak production mode, and our analysis is also a follow-up to a previous chargino–neutralino search [65]. In 2015–2016 an analysis was published focusing on the search for $\tilde{\chi}_1^{\pm}\tilde{\chi}_2^0$ production using a 36.1 fb^{-1} dataset. The analysis saw four excesses in four orthogonal regions. These signal regions were SR2ℓ_Low, SR2ℓ_ISR, SR3ℓ_Low, and SR3ℓ_ISR. We summarise the excesses in Figure 4.1. This chapter will summarise our follow-up to this analysis.

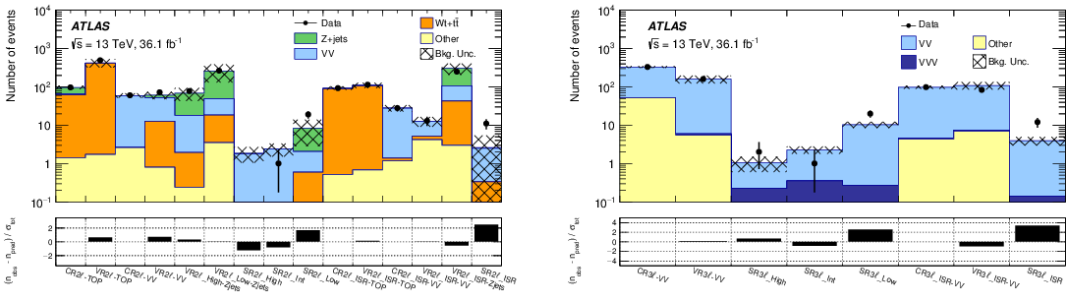

(a) 2ℓ (b) 3ℓ

Figure 4.1: A summary of control, validation, and signal regions for the 2015–2016 analyis.

4.1 Our Signal

The signal we target in this analysis is associated produced electroweakino $\tilde{\chi}_1^{\pm}\tilde{\chi}_2^0$ production with conserved R-parity. A feature of hadron colliders is initial state radiation (ISR) of quarks and gluons, which will boost any produced sparticles while contributing extra jets to the measured events. Given this ISR feature, we designed our analysis to target $\tilde{\chi}_1^{\pm}\tilde{\chi}_2^0$ associated production with and without the presence of additional jets.

We study the $\tilde{\chi}_1^\pm\tilde{\chi}_2^0$ production modes in the context of simplified models. We assume wino-like $\tilde{\chi}_1^\pm\tilde{\chi}_2^0$ production, with a bino-like $\tilde{\chi}_1^0$, which is identified as the Lightest Supersymmetric Particle (LSP). The signal process we target is $\tilde{\chi}_1^\pm\tilde{\chi}_2^0$ decaying via a SM $W^\pm$ and Z^0 which gives us a two-lepton or three-lepton final-state — depending on whether $W^\pm$decays hadronically or leptonically. Overall, we target four signal scenarios, these are two and three-lepton final states with and without additional jets from initial state radiation. We illustrate the four targetted signal scenarios in Figure 4.2.

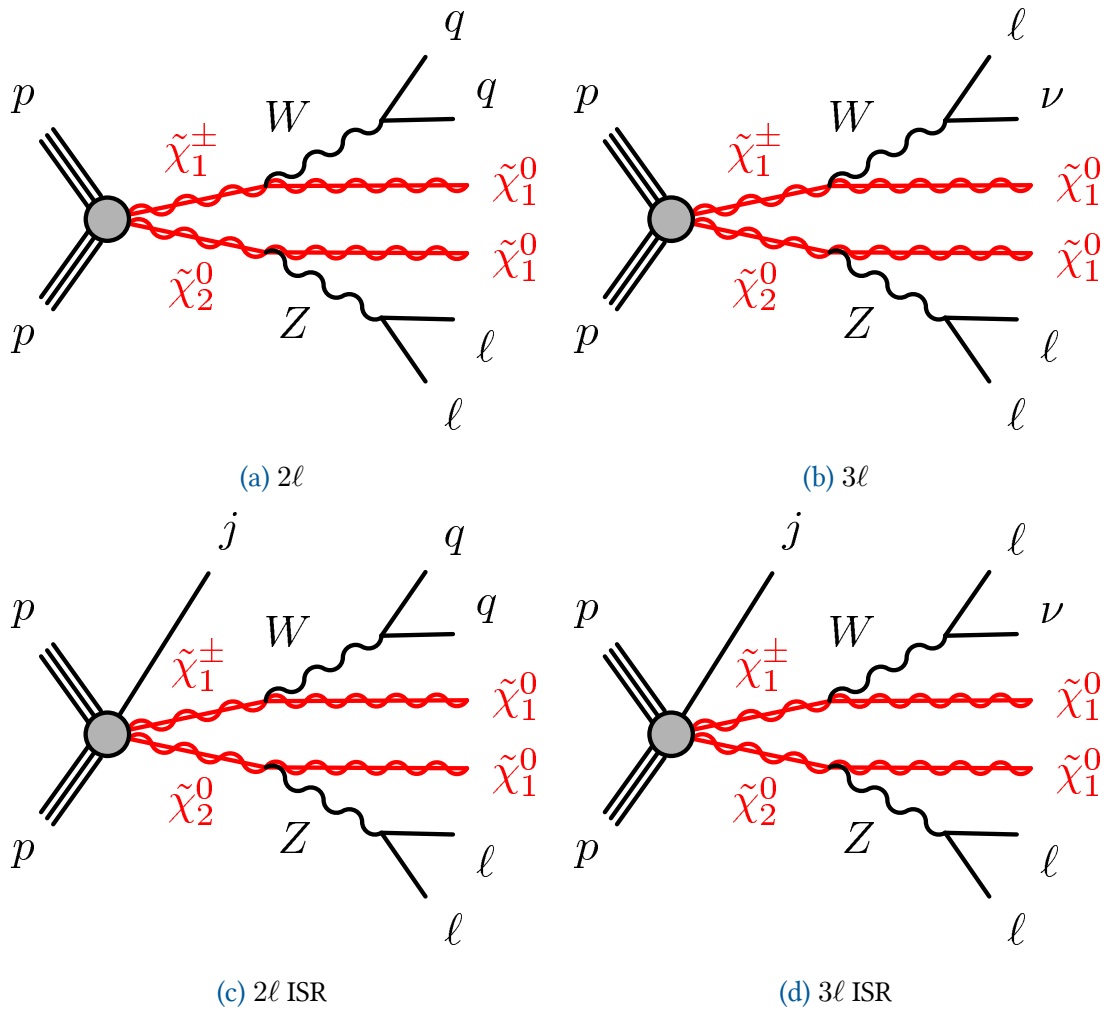

(a) 2ℓ (b) 3ℓ

(c) 2ℓ ISR (d) 3ℓ ISR

Figure 4.2: We sere signal models based on the W decaying either leptonically or hadronically, as well as the presence of initial state radiation. This naturally creates 2ℓ and 3ℓ signals, and ISR and non-ISR signals [65].

4.2 Analysis Overview

We define our analysis region parameter space in Figure 4.3. On the x axis we have the mass of the degenerate sparticles $\tilde{\chi}_1^\pm/\tilde{\chi}_2^0$. The y axis corresponds to the mass of the LSP

$\tilde{\chi}_1^0$. The cross-hatched shaded region from 100 GeV diagonally is the region where $\tilde{\chi}_1^0$ is the lightest supersymmetric particle. The dashed diagonal line from $(0, 100)$ defines the area where $\tilde{\chi}_1^\pm/\tilde{\chi}_2^0$ can decay to an on-shell Z boson and the LSP. We define four regions of interest; low-mass, ISR, intermediate-mass and high-mass. The low-mass region and the ISR region are orthogonal based purely on jet multiplicity requirements, but target the same mass space. This analysis is a follow up from a previous result [65], and only considers the ISR and low-mass regions. The intermediate and high-mass regions are not considered here.

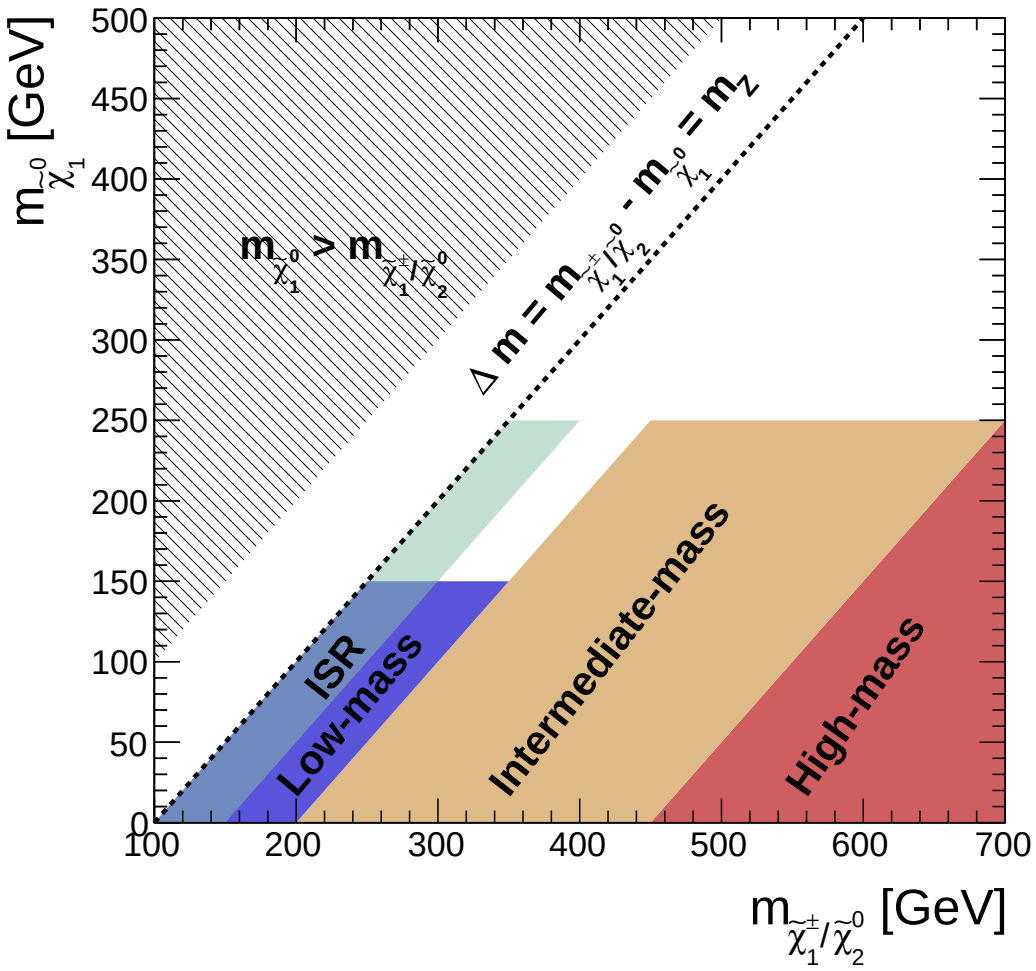

Figure 4.3: Schematic of the analysis design [65].

4.3 Recursive Jigsaw Reconstruction Implementation

The recursive jigsaw reconstruction technique (RJR) is an approach which allows us to resolve combinatoric and kinematic ambiguities of any production or decay topology

[66]. The RJR technique resolves ambiguities by first assuming a decay topology and then by applying assumptions about the unknown degrees of freedom in that topology. We apply these assumptions with algorithms we call *jigsaw rules*. By applying these rules to an unconstrained final state, we can extract values for the unknown degrees of freedom. Once each unknown degree of freedom has a constraint, we have a four-vector corresponding to each final state object. Taking these four-vectors, we can then use relativistic kinematics to recursively boost to intermediate states between the production and final states. Using this technique, we can create a natural basis of variables for a given topology, leveraging this information allows us to define new selection criteria.

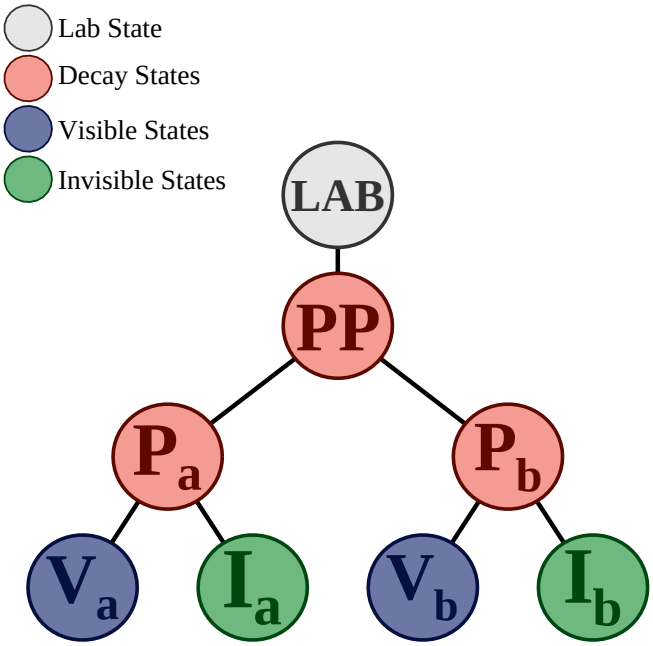

Figure 4.4: A recursive jigsaw generic decay tree.

The electroweak signal model we target is one such example of an unconstrained decay topology. In the case of $\tilde{\chi}_1^{\pm}\tilde{\chi}_2^0$, we have two lightest, stable neutralinos which carry a significant proportion of the momentum and energy, thus leaving the visible sector of the decay unconstrained. By applying the RJR technique, we can define a basis of variables to define Signal Regions (SRs).

4.3.1 Standard Approach

Applying RJR requires an assumption of the decay topology called a decay tree; we show an example of a generic tree in Figure 4.4. We split the decay tree into four states; the "Lab State" denoted with grey, the "Decay States" denoted with red, the "Visible states" denoted with blue, the invisible states denoted in green. The lab state (LAB) corresponds to the lab frame, the decay states (PP, P_a, P_b) correspond to intermediate states, the visible states (V_a, V_b) and invisible states (I_a, I_b) which correspond to observed and unobserved states. Visible states are the most straightforward; where they correspond to

measured particles — leptons and jets. By making an assumption about the invisible particles and the topology of the event, we can break the E_T^{miss} vector into I_a and I_b. For the visible states, we assign particles or groups of particles to a corresponding frame. The four-momentum of the frame corresponds to its constituent particle's four momenta.

Examples of the possible assumptions are that the invisible particle's mass is zero, or that the rapidity of the visible system is equal to that of the invisible system. We also need to take into account the intermediate particles and whether or not they are off-shell. We show a schematic breakdown of the RJR approach in Figure 4.5. In Figure 4.6 we show a schematic view of the scalar summation of n visible particles and m invisible particles in a generic event. In Figure 4.7 we show a schematic view of the vector summation of n visible particles and m invisible particles in a generic event.

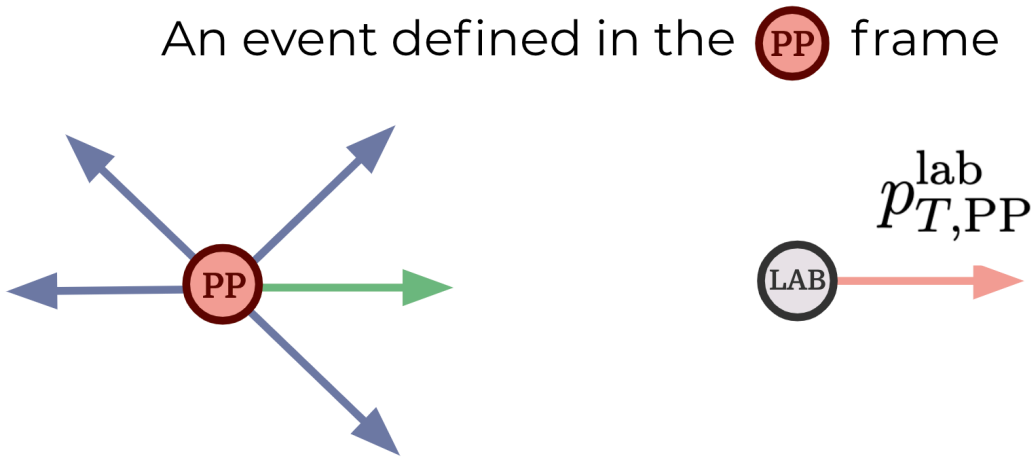

Figure 4.5: A schematic view of a typical event in an RJR approach. On the left, we have n visible objects denoted by the light-purple colour. These visible objects are tracks, leptons, jets or composite objects. We denote the invisible system, with light-green. Typically an event has more than one source of missing momentum, but we cannot resolve the individual contributions to this measured quantity; thus we illustrate $I_A + I_B$.

The main group of variables used in our search are the so-called *hemisphere* variables which are denoted with H. Here, *Hemisphere* refers to each branch of the decay tree. Hemisphere variables are constructed in a given frame with different combinations of visible and invisible momenta.

$$H_{n,m}^{F} = \sum_{i}^{n} |\vec{p}_{\text{vis},i}^{\,F}| + \sum_{j}^{F} |\vec{p}_{\text{inv},j}^{\,F}|. \tag{4.1}$$

The H variables are labelled with a superscript F and two subscripts n and m. The F denotes the rest frame the hemisphere variable is calculated in, n is the number of groups the visible objects are partitioned into, and m represents the number of groups the invisible particles are separated into. If the subscript T is used then it indicates that only transverse momenta of the particles enter into the calculation of the hemisphere

variable.

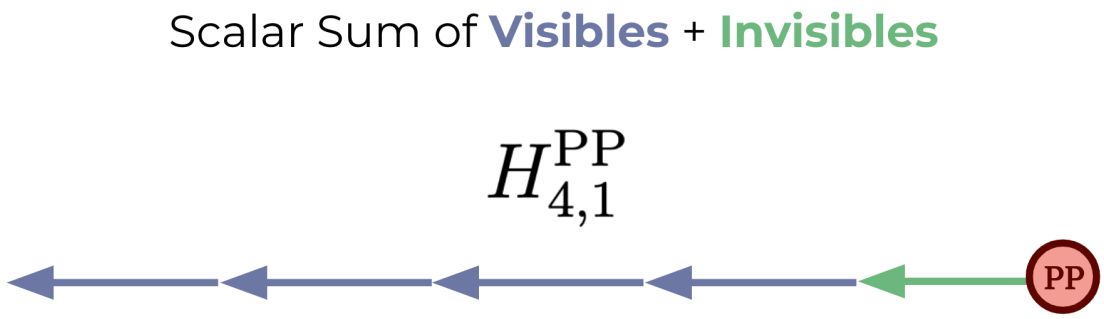

Figure 4.6: A schematic view of the scalar summation of n visible particles of a generic event. In this approach, we take the absolute magnitude of each objects momentum and add those to the absolute value of the invisible system's momentum. This quantity gives us an idea of the energy scale involved in a given parton–parton interaction.

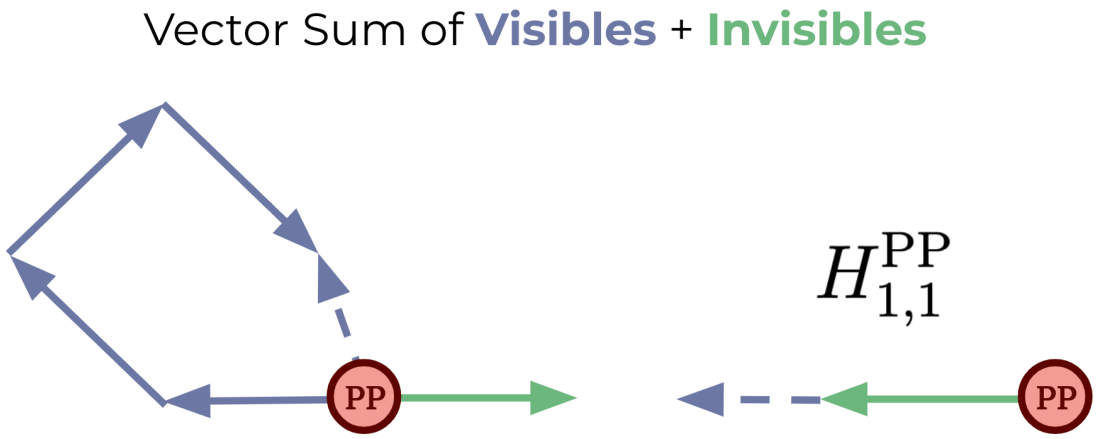

Figure 4.7: A schematic view of the vector summation of n visible particles of a generic event. In this approach, we add all momenta of all n visible particles, and then take the absolute value of that sum. We add this sum to the invisible systems momentum magnitude. This quantity is similar to twice the value of the missing transverse energy. When we take the ratio between the vector and the scalar quantities, we get a variable sensitive to the initial boosts of parent objects, and thus the geometry of the decay.

4.3.2 ISR Approach

The second approach we utilise is for events with at least one high-p_T jet from an initial state radiation (ISR) system. Such events need not have significant amounts of $E_{\mathrm{T}}^{\mathrm{miss}}$. In order to target an ISR topology, we use a different decay tree, as shown in Figure 4.8. This tree is more straight forward than the generic tree approach but provides some powerful variables for discrimination.

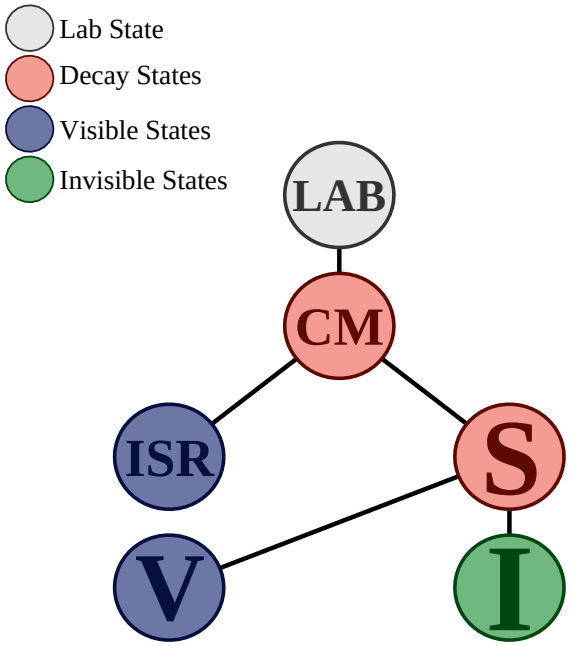

Figure 4.8: The recursive jigsaw ISR decay tree [65].

Similarly to the generic case, the ISR decay tree is split into lab state, decay states, visible states, and invisible states. The ISR decay tree introduces the **CM** *Centre-of-Mass* frame, the **ISR** frame and the system frame **S**, which corresponds to the hard-scatter of the underlying signal process. We use all visible and invisible objects to determine where the jets are assigned using mass minimisation of the ISR system and the sparticle system. We show a schematic view of the ISR system in Figure 4.9. In the ISR approach, given we use only the transverse components of the E^{miss}, we only use the transverse components of all other input objects.

We take the $E_{\text{T}}^{\text{miss}}$ and assign it to the invisible system I. We take all leptons and assign these to the visible system V. The full set of jets is denoted with J_{all}. The jets are not yet assigned to a frame. In order to assign the jets to either the **ISR** or **S** we take all two-group combinations of jets denoted J_a and J_b. The set of all jets is given as $J_{\text{all}} = \{j_1, j_2, j_3, \ldots j_n\}$.

We choose the jet assignment to **ISR** and **S** based on the combination which has the minimum mass for J_a and J_b:

$$\{J_{\text{ISR}}, J_{\text{S}} | \min_{\forall a,b} [M(J_{\text{ISR},a}) + M(J_{\text{S},b})]\}, \tag{4.2}$$

where a and b denote any two-group combination of jets.

Having defined **ISR**, **V** and **I** we can boost to any frame in the decay tree. We now give examples of ISR decay tree variables.

$p_{\text{T,ISR}}^{\text{CM}}$ is the momentum of the **ISR** system in the **CM** frame. The magnitude of the vector

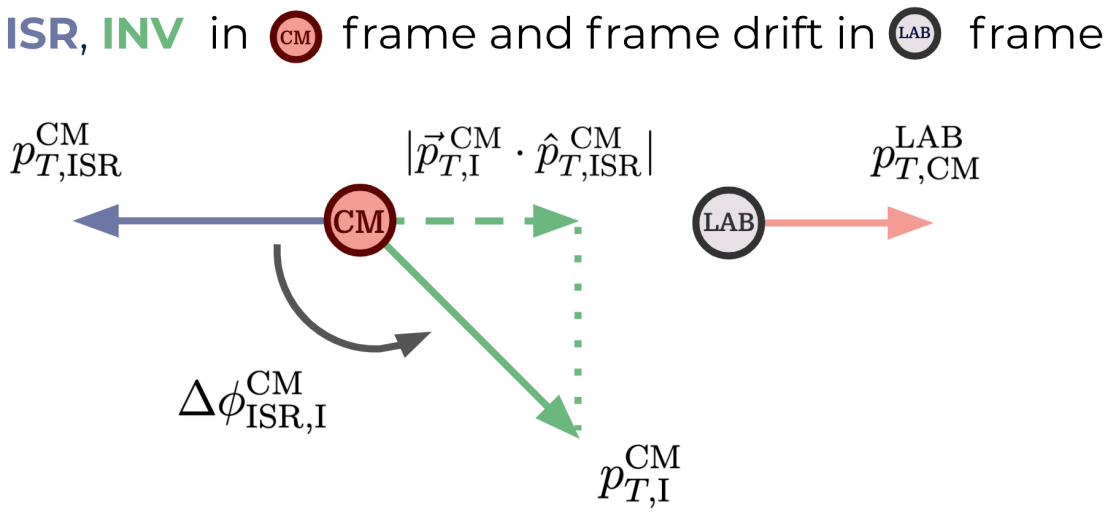

Figure 4.9: A schematic view of the ISR system. We define this approach in the centre-of-mass frame. We define the momentum of the ISR system, the momentum of the invisible system, the azimuthal angle between the ISR and the invisible system, as well as the LAB frame drift of the CM frame.

sum of the **I** system in the **CM** frame is denoted as $p_{T,\mathrm{I}}^{\mathrm{CM}}$. This variable corresponds to the missing transverse momentum without the ISR recoil. The momentum of the **CM** frame, measured in the **LAB** frame, is given by $p_{\mathrm{T}}^{\mathrm{CM}}$. Small values of $p_{\mathrm{T}}^{\mathrm{CM}}$ correspond to situations where we have correct assignment and an initial total transverse momentum of zero. Given the imperfections of assignment, low values of $p_{\mathrm{T}}^{\mathrm{CM}}$ correspond to a well described system. The next variable described in this approach is R_{ISR} which is given by:

$$R_{\mathrm{ISR}} = \frac{|\vec{p}_{\mathrm{T,I}}^{\,\mathrm{CM}} \cdot \hat{p}_{\mathrm{T,ISR}}^{\,\mathrm{CM}}|}{|\vec{p}_{\mathrm{T,ISR}}^{\,\mathrm{CM}}|}, \tag{4.3}$$

where we take the dot product of the **I** system 3-vector and the direction of the **ISR** system 3-vector, divided by the **ISR** system momentum.

R_{ISR} is an estimate of $m_{\tilde{\chi}_1^0}/m_{\tilde{\chi}_2^0/\tilde{\chi}_1^\pm}$. The quantity corresponds to the amount of momentum carried by the invisible system being attributed to the ISR kick in units of the ISR boost. As $p_{\mathrm{T,ISR}}^{\mathrm{CM}}$ gets larger it becomes increasingly difficult for backgrounds to have a large R_{ISR}. The final ISR variable we highlight is $\Delta\phi_{\mathrm{ISR,I}}^{\mathrm{CM}}$ which is the azimuthal opening angle between the **ISR** system and the invisible system in the **CM** frame. In Figure 4.10 we summarise the ISR variables in use in the analysis.

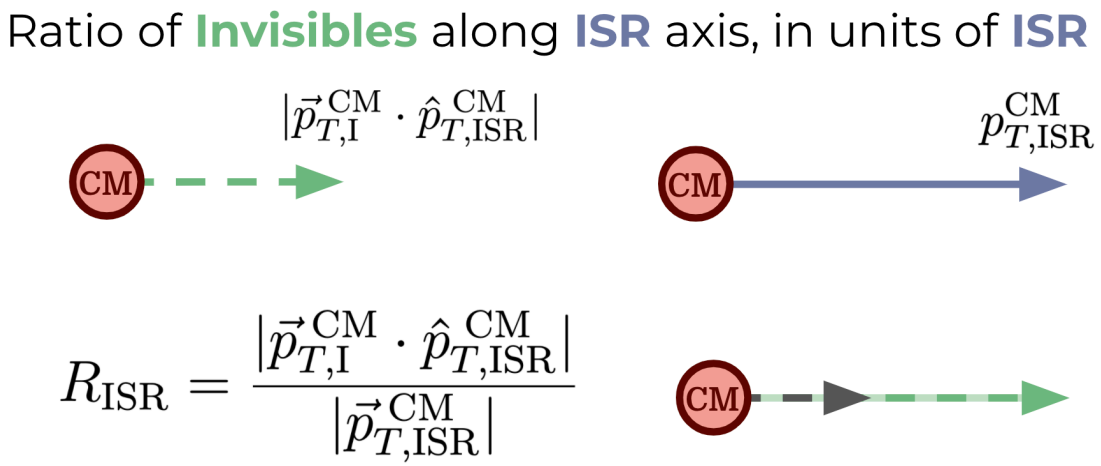

Figure 4.10: A schematic of the projection of the **INV** system onto the ISR boost-axis, in units of the ISR system momentum. This defines R_{ISR} which is a very useful variable for ISR scenarios.

4.4 Technical Setup

The dataset used in this analysis was collected by the ATLAS detector during run-II operations. We show the delivered luminosity of the ATLAS dataset between 2011 and 2018 in Figure 4.11a. The peak luminosity in 2015–2016, 2017 and 2018 was measured to be $5.2\times10^{33}\ \mathrm{cm^{-2}s^{-1}}$, $1.37\times10^{34}\ \mathrm{cm^{-2}s^{-1}}$, and $2.1\times10^{33}\ \mathrm{cm^{-2}s^{-1}}$, respectively [57, 58]. In Figure 4.11b, we show the luminosity weighted distribution of the average number of interactions per crossing for the full run-II proton–proton collision data at $\sqrt{s} = 13$ TeV centre-of-mass energy [57]. The average pileup is broken down in terms of individual years and the average pileup over the full run-II dataset is overlaid. The average number of pileup events in 2015 was $\langle\mu\rangle = 14$ and by 2017 increased to $\langle\mu\rangle = 37.8$, by 2018 the average pileup decreased to $\langle\mu\rangle = 36.1$ due to luminosity levelling [57].

In Figure 4.12, we show the evolution of the ATLAS total integrated luminosity as a function of time over run-II [57]. We see during run-II the LHC delivered 156 $\mathrm{fb^{-1}}$ of proton–proton collisions, while the ATLAS detector recorded 147 $\mathrm{fb^{-1}}$ [57]. Upon applying beam, detector, and data-quality criteria, the ATLAS experiment had a good-for-physics dataset of 139 $\mathrm{fb^{-1}}$ [57].

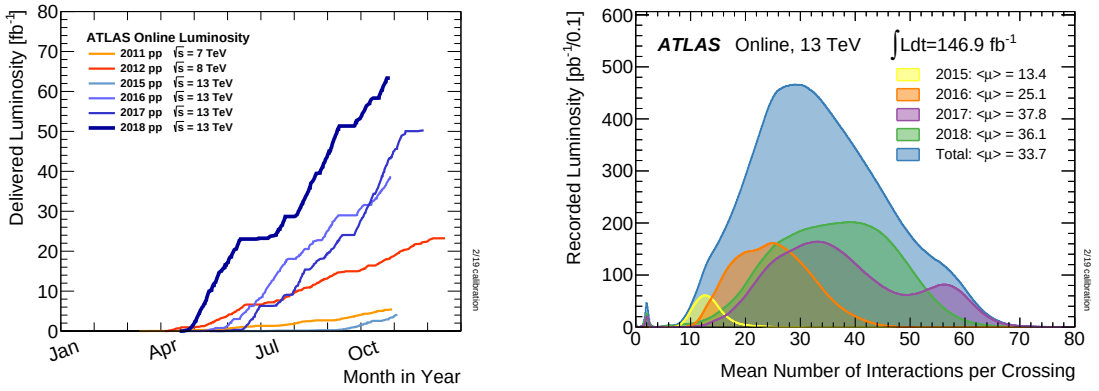

(a) Delivered luminosity

(b) Pileup

Figure 4.11: The delivered integrated luminosity and pileup distributions for the ATLAS experiment during run-II operations [57].

The simulation of background processes requires an understanding of the detector response, geometry, and object reconstruction definitions, as well as the aforementioned pileup conditions. We describe the object reconstruction methods in Section 4.5. In our analysis, for each background, we chose the MC generator which models the given background best. Once we have generated and simulated the MC, we validate them against the run-II dataset to confirm the agreement between the two; this is done in Section 4.8. We will now summarise the MC generators chosen for each background process, as well as the signal process choices.

In this electroweak analysis we use a set of MC background samples and signal samples to optimize the selection criteria. The MC generators are summarised in Table 4.1.

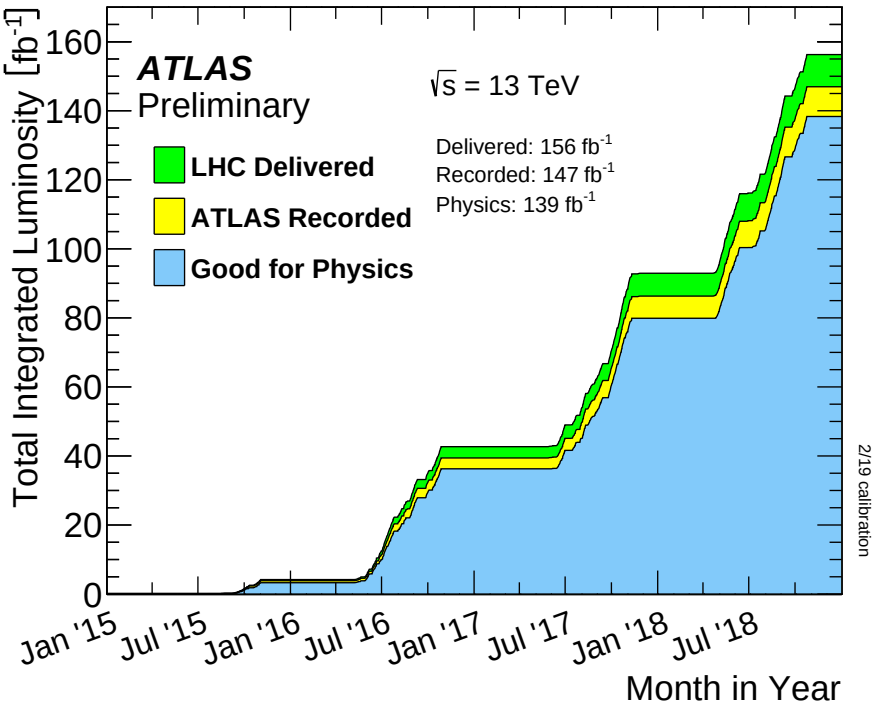

Figure 4.12: Breakdown of the total integrated luminosity of the ATLAS dataset [57].

Table 4.1: The SUSY signals and the Standard Model background MC samples used in this search. The generators, the order in α_s of cross-section calculations used for yield normalization, PDF sets, parton showers and parameter tunes used for the underlying event are shown.

Physics process	Generator	Cross-section normalization	PDF set	Parton shower	Tune
SUSY processes	MADGRAPH v2.2.3	NLO+NLL	NNPDF2.3LO	PYTHIA 8.186	A14
$Z/\gamma^*(\to \ell\bar{\ell})$ + jets	SHERPA 2.2.1	NNLO	NNPDF3.0NNLO	SHERPA	SHERPA default
γ + jets	SHERPA 2.1.1	LO	CT10	SHERPA	SHERPA default
$H(\to \tau\tau)$, $H(\to WW)$	POWHEG-BOX v2	NLO	CTEQ6L1	PYTHIA 8.186	A14
HW, HZ	MG5_aMC@NLO 2.2.2	NLO	NNPDF2.3LO	PYTHIA 8.186	A14
$t\bar{t}+H$	MG5_aMC@NLO 2.2.2	NLO	CTEQ6L1	HERWIG 2.7.1	A14
$t\bar{t}$	POWHEG-BOX v2	NNLO+NNLL	CT10	PYTHIA 6.428	Perugia2012
Single top (Wt-channel)	POWHEG-BOX v2	NNLO+NNLL	CT10	PYTHIA 6.428	Perugia2012
Single top (s-channel)	POWHEG-BOX v2	NLO	CT10	PYTHIA 6.428	Perugia2012
Single top (t-channel)	POWHEG-BOX v1	NLO	CT10f4	PYTHIA 6.428	Perugia2012
Single top (Zt-channel)	MG5_aMC@NLO 2.2.1	LO	CTEQ6L1	PYTHIA 6.428	Perugia2012
$t\bar{t}+W/WW$	MG5_aMC@NLO 2.2.2	NLO	NNPDF2.3LO	PYTHIA 8.186	A14
$t\bar{t}+Z$	MG5_aMC@NLO 2.2.3	NLO	NNPDF2.3LO	PYTHIA 8.186	A14
WW, WZ, ZZ	SHERPA 2.2.1	NLO	NNPDF30NNLO	SHERPA	SHERPA default
$V\gamma$	SHERPA 2.1.1	LO	CT10	SHERPA	SHERPA default
Triboson	SHERPA 2.2.1	NLO	NNPDF30NNLO	SHERPA	SHERPA default

The production of Z bosons in association with jets [67] was performed with the SHERPA 2.2.1 generator [68]. The NNPDF3.0NNLO [69] parton distribution function (PDF) was used in conjunction with dedicated parton shower tuning developed by the SHERPA authors. The matrix elements (ME) were calculated for up to two partons at next-to-

leading order (NLO) and with up to two additional partons at leading order (LO) using the Comix [70] and Open Loops [71] matrix-element generators, and merged with the Sherpa parton shower (PS) [72] using the ME+PS@NLO prescription [73]. We use the data-driven ABCD technique to estimate Z/γ^*+jets contributions in the Signal Regions (SRs) and Z/γ^*+jets MC in higher statistics regions, γ+jets events were generated at LO with up to four additional partons using the Sherpa 2.1.1 generator with CT10 [74] PDF set. We describe the ABCD technique generically in Section 4.7, and for our specific analysis we describe it in Section 4.13.

The Powheg-Box v2 [75] generator was used for the generation of $t\bar{t}$ and single top-quark processes in the Wt- and s-channels [76], while t-channel single-top production was modeled using Powheg-Box v1 [77]. For the latter process, the decay of the top quark was simulated using MadSpin [78] preserving all spin correlations. For all processes the CT10 [74] PDF set was used for the matrix element, while the parton shower, fragmentation, and the underlying event were generated using Pythia 6.428 [79] with the CTEQ6L1 [80] PDF set and a set of tuned parameters called the Perugia 2012 tune [81]. The top-quark mass in all samples was set to 172.5 GeV. The $t\bar{t}$ and the Wt-channel single-top events were normalized to cross-sections calculated at next-to-next-to-leading-order plus next-to-next-to-leading-logarithm (NNLO+NNLL) [82–85] accuracy, while s- and t-channel single-top-quark events were normalized to the NLO cross-sections [86, 87]. The production of Zt events was generated with the MG5_aMC@NLO 2.2.1 [88] generator at LO with the CTEQ6L1 PDF set.

The MG5_aMC@NLO 2.2.2 (2.2.3 for $t\bar{t}$ + Z/γ^*) generator at LO, interfaced to the Pythia 8.186 [89] parton-shower model, was used for the generation of $t\bar{t}$ + EW processes ($t\bar{t}$ + $W/Z/WW$) [90], with up to two ($t\bar{t}$+W, $t\bar{t}$+$Z(\to \nu\nu/qq)$), one ($t\bar{t}$+$Z(\to \ell\ell)$) or no ($t\bar{t}+WW$) extra partons included in the matrix element. The events were normalized to their respective NLO cross-sections [91, 92]. Collectively these top processes are refered to as "Top Other".

Diboson processes (WW, WZ, ZZ) [93] were simulated using the Sherpa 2.2.1 generator and contain off-shell contributions. For processes with four charged leptons (4ℓ), three charged leptons and a neutrino (3ℓ+1ν) or two charged leptons and two neutrinos (2ℓ+2ν), the matrix elements contain all diagrams with four electroweak couplings, and were calculated for up to one (4ℓ, 2ℓ+2ν) or no extra partons (3ℓ+1ν) at NLO. All diboson samples were also simulated with up to three additional partons at LO using the Comix and OpenLoops matrix-element generators, and were merged with the Sherpa parton shower using the ME+PS@NLO prescription. The diboson samples were normalized to their NLO cross-sections [94, 95]. Additional MC simulation samples of events with a leptonically decaying vector boson and photon, $V\gamma$, where $V = W, Z$ were generated at LO using Sherpa 2.1.1 [68]. Matrix elements including all diagrams with three electroweak couplings were calculated with up to three partons at LO and merged with the Sherpa parton shower [96] according to the ME+PS@LO prescription [97]. The CT10 PDF set is used in conjunction with dedicated parton shower tuning developed by the Sherpa authors.

Triboson processes (WWW, WWZ, WZZ and ZZZ) were simulated with the SHERPA 2.2.1 generator with matrix elements calculated at LO with up to one additional parton. The triboson events were normalized to their LO cross-sections [98].

Higgs boson production processes, including gluon–gluon fusion, associated vector boson production, VH,[1], and vector-boson fusion, VBF, were generated using POWHEGV2 [76] + PYTHIA8.186 and normalized to cross-sections calculated at NNLO with soft gluon emission effects added at NNLL accuracy, whilst $t\bar{t}H$ events were produced using AMC@NLO 2.2.2 + HERWIG 2.7.1 [99] and normalized to the NLO cross-section [100]. All samples assume a Higgs boson mass of 125 GeV.

The MC signal samples were generated from leading-order matrix elements with up to two extra partons using MADGRAPH v2.2.3 [101] interfaced to PYTHIA version 8.186, with the A14 parameter tune [102], for the modeling of the SUSY decay chain, parton showering, hadronization and the description of the underlying event. Parton luminosities were provided by the NNPDF23LO PDF set [74]. Jet–parton matching follows the CKKW–L prescription [103], with a matching scale set to one quarter of the $\tilde{\chi}_1^{\pm}/\tilde{\chi}_2^0$ mass. Signal cross-sections were calculated at NLO in the strong coupling constant, with soft gluon emission effects added at next-to-leading-logarithm (NLL) accuracy [104–108]. The nominal cross-section and the uncertainty were taken from an envelope of cross-section predictions using different PDF sets and factorization and renormalization scales, as described in Ref. [109].

4.5 Object Reconstruction and Identification

The definitions of the objects used are described in this section. The objects used in the ATLAS experiment are defined by comparison between MC and Data. These definitions are general and not specific to this analysis.

The reconstructed primary vertex of the event is required to be consistent with the luminous region and to have at least two associated tracks with $p_T > 400$ MeV. When more than one such vertex is found, the vertex with the largest $\sum p_T^2$ of the associated tracks is chosen.

Two different classes of reconstructed lepton candidates (electrons or muons) are used in the analysis, labeled baseline and high-purity in the following. When selecting samples for the search, events must contain a minimum of two baseline electrons or muons.

Baseline muon candidates are formed by combining information from the muon spectrometer and ID as described in Reference [110], must pass the *medium* identification requirements defined therein, and have $p_{\mathrm{T}} > 10$ GeV and $|\eta| < 2.7$. High-purity muon candidates must additionally have $|\eta| < 2.4$, the significance of the transverse impact parameter relative to the primary vertex $|d_0^{\mathrm{PV}}|/\sigma(d_0^{\mathrm{PV}}) < 3$, and the longitudinal impact

[1] The letter V represents the W or Z gauge boson.

parameter relative to the primary vertex $|z_0^{\mathrm{PV}}\sin\theta| < 0.5$ mm. Furthermore, high-purity candidates must satisfy the *GradientLoose* isolation requirements described in Reference [110], which rely on tracking-based and calorimeter-based variables and implement a set of η- and p_T-dependent criteria. The highest-p_T(leading) high-purity muon is also required to have $p_T > 25$ GeV. The baseline and signal lepton identification criteria for muons are summarised in Table 4.2. Baseline electron candidates are reconstructed

Table 4.2: Summary of the muon selection criteria. The signal selection requirements are applied in addition to the baseline selection criteria, and take place after overlap removal.

Category	Acceptance	PID Quality	Isolation	Impact Parameter
Baseline Muon	$p_T > 10$ GeV $\lvert\eta^{\mathrm{clust}}\rvert < 2.40$	`Medium`	-	$\lvert z_0\sin\theta\rvert < 0.5$ mm
Signal Muon	$p_T > 10$ GeV $\lvert\eta^{\mathrm{clust}}\rvert < 2.40$	`Medium`	`FixedCutTight`	$\lvert z_0\sin\theta\rvert < 0.5$ mm $\lvert d_0/\sigma_{d_0}\rvert < 3$

from an isolated electromagnetic calorimeter energy deposit matched to an ID track. They are required to have $p_{\mathrm{T}} > 10$ GeV, $|\eta| < 2.47$, and to satisfy a set of quality criteria similar to the *Loose* likelihood-based identification criteria described in Reference [111], but including a requirement of a B-layer hit. High-purity electron candidates additionally must satisfy *MediumLH* selection criteria described in Reference [111]. They are also required to have $|d_0^{\mathrm{PV}}|/\sigma(d_0^{\mathrm{PV}}) < 5$, $|z_0^{\mathrm{PV}}\sin\theta| < 0.5$ mm, and to satisfy isolation requirements that are the same as those applied to high-purity muons [111]. The leading high-purity electron is also required to have $p_T > 25$ GeV. The baseline and signal lepton identification criteria for muons are summarised in Table 4.3.

Table 4.3: Summary of the electron selection criteria. The signal selection requirements are applied in addition to the baseline selection criteria, and take place after overlap removal.

Category	Acceptance	PID Quality	Isolation	Impact Parameter
Baseline Electron	$p_T > 10$ GeV $\lvert\eta^{\mathrm{clust}}\rvert < 2.47$	`LooseAndBLayerLLH`	- -	$\lvert z_0\sin\theta\rvert < 0.5$ mm
Signal Electron	$p_T > 10$ GeV $\lvert\eta^{\mathrm{clust}}\rvert < 2.47$	`LLHMedium`	`FixedCutTight`	$\lvert z_0\sin\theta\rvert < 0.5$ mm $\lvert d_0/\sigma_{d_0}\rvert < 5$

Jet candidates are reconstructed using the anti-k_t jet clustering algorithm [112–114] with a jet radius parameter of 0.4 starting from clusters of calorimeter cells [115]. The jets are corrected for energy from pileup using the method described in Reference [116]: a contribution equal to the product of the jet area and the median energy density of the event is subtracted from the jet energy [117]. Further corrections, referred to as the jet energy scale corrections, are derived from MC simulation and data and are used to calibrate the average energies of jets to the scale of their constituent particles [118]. In order to reduce the number of jets originating from pileup, a significant fraction of the

tracks associated with each jet must have an origin compatible with the primary vertex, as defined by the jet vertex tagger (JVT) output [119]. Only corrected jet candidates with $p_{\mathrm{T}} > 20$ GeV and $|\eta| < 4.5$ are retained. High-purity jets are defined with the tighter requirement $|\eta| < 2.4$. The chosen requirement corresponds to the *Medium* working point of the JVT and is only applied to jets with $p_T < 60$ GeV and $|\eta| < 2.4$.

An algorithm based on boosted decision trees, MV2c10 [120, 121], is used to identify jets containing a b-hadron (b-jets), with an operating point corresponding to an efficiency of 77% per b-jet, and rejection factors of 134 for light-quark and gluon jets and 6 for charm jets [121], for reconstructed jets with $p_{\mathrm{T}} > 20$ GeV and $|\eta| < 2.5$ in simulated $t\bar{t}$ events. Candidate b-tagged jets are required to have $p_{\mathrm{T}} > 20$ GeV and $|\eta| < 2.4$. The baseline and signal identification criteria for jets, as well as b-tagging criteria are summarised in Table 4.4.

Table 4.4: Summary of the jet and b-jet selection criteria. The signal selection requirements are applied in addition to basline requirements. Signal b-jet selection is in addition to the signal requirements. These requirements take place after overlap removal.

Category	Collection	Acceptance	JVT	b-tagger Algorithm	Efficiency
Baseline jet	`AntiKt4EMTopo`	$p_T > 20$ GeV, $\|\eta\| < 4.5$	-	-	-
Signal jet	`AntiKt4EMTopo`	$p_T > 20$ GeV, $\|\eta\| < 2.4$	$\|\mathrm{JVT}\| > 0.59^*$	-	-
Signal b-jet	`AntiKt4EMTopo`	$p_T > 20$ GeV, $\|\eta\| < 2.4$	$\|\mathrm{JVT}\| > 0.59^*$	`MV2c10`	77%

After the selection requirements described above, ambiguities between candidate jets with $|\eta| < 4.5$ and baseline leptons are resolved as follows:

1. Any electron sharing an ID track with a muon is removed.
2. If a b-tagged jet (identified using the 85% efficiency working point of the MV2c10 algorithm) is within $\Delta R \equiv \sqrt{(\Delta y)^2 + (\Delta\phi)^2} = 0.2$ of an electron candidate, the electron is rejected, as it is likely to originate from a semileptonic b-hadron decay; otherwise, if a non-b-tagged jet is within $\Delta R = 0.2$ of an electron candidate then the electron is kept and the jet is discarded as it is likely to be due to the electron-induced shower.
3. Electrons within $\Delta R = 0.4$ of a remaining jet candidate axis are discarded, to suppress electrons from semileptonic decays of c- and b-hadrons.
4. Jets with fewer than three associated tracks that have a nearby muon that carries a significant fraction of the transverse momentum of the jet ($p_T^{\mu} > 0.7 \sum p_T^{\text{jet tracks}}$, where p_T^{μ} and $p_T^{\text{jet tracks}}$ are the transverse momenta of the muon and the tracks associated with the jet, respectively) are discarded either if the candidate muon is within $\Delta R = 0.2$ of the jet axis or if the muon is matched to a track associated with the jet.
5. Muons within $\Delta R = 0.4$ of a remaining jet candidate are discarded to suppress muons from semi-leptonic decays of c- and b-hadrons.

The events used by the searches described in this paper are selected using high-purity leptons and jets with a trigger logic that accepts events with either two electrons, two muons or an electron plus a muon. We summarise the triggers used for each data-taking period in Table 4.5.

Table 4.5: The triggers used for each year of data-taking at the ATLAS experiment. These triggers are all dilepton triggers and split based on lepton flavour composition. In general we require very loose likelihood requirements for lepton identification, and do not apply selections on the transverse impact parameters. Different years have different triggers due to different data-taking conditions.

Year	ee trigger	$\mu\mu$ trigger	$e\mu$ trigger
2015	`2e12_lhloose_L12EM10VH`	`2mu10`	`e17_lhloose_mu14`
2016	`2e17_lhvloose_nod0`	`mu22_mu8noL1` or `2mu14`	`e17_lhloose_nod0_mu14` or `e7_lhmedium_nod0_mu24`
2017	`2e17_lhvloose_nod0` or `2e24_lhvloose_nod0`	`mu22_mu8noL1` or `2mu14`	`e17_lhloose_nod0_mu14` or `e7_lhmedium_nod0_mu24`
2018	`2e17_lhvloose_nod0` or `2e24_lhvloose_nod0`	`e17_lhloose_nod0_mu14` or `2mu14` or	`mu22_mu8noL1` or `e7_lhmedium_no0_mu24`

The measurement of the missing transverse momentum vector $\vec{P}_{\mathrm{T}}^{\mathrm{miss}}$ (and its magnitude E_T^{miss}) is based on the calibrated transverse momenta of all electron, photon, muon, and jet candidates, as well as all tracks originating from the primary vertex, and not associated with such objects [122]. The missing transverse momentum is defined as the negative of the vector sum of these object momenta.

4.6 Fakes Matrix Method

MC generators can model production and decay of physics processes well, though it is significantly more challenging to model detector response and the subsequent reconstruction of physics objects. Given object reconstruction is based on detector response, one underlying particle can produce a detector response which looks like another. In situations where one particle is reconstructed incorrectly as another, we call that falsely reconstructed object a *fake*. Collectively, events which fake their way into passing selection criteria are known as *fakes*. Given it is challenging to model detector response, instead of using the individual MC samples to model the fakes contributions, we use the data from the run-II dataset. The approach we use to create this fakes estimation sample is the data-driven matrix method.

The matrix method works by taking events with at least two-lepton selection. We then select at least two leptons with which to apply the matrix method. In the case of a three-lepton selection, we chose the two softest leptons. From the selected events, we classify leptons into two groups. The first group are leptons which pass baseline (Loose) lepton criteria. The second group are leptons which pass signal (Tight) lepton criteria. We then

determine the probabilities that a given lepton is fake or real, given they are members of each group. The baseline and signal lepton identification criteria for electrons and muons are summarised in Table 4.3 and Table 4.2 respectively. We now explain the matrix method approach.

Let T denote leptons passing the tight identification criteria and L denote leptons that at least pass the loose criteria. Any event which is in L is known as *inclusive loose*. Leptons passing loose but **not** tight are called *exclusive loose*, we denote these as l. For our estimation, we only consider events which have two inclusive loose leptons, and we order the leptons based on p_T. We denote the number of events with two inclusive loose leptons as N_{LL}.

We then categorise the two leptons into two different groups; these are inclusive loose or exclusive loose. Categorising leptons in this way gives the total event four classifications, these are: $\{T, T\}$, $\{T, l\}$, $\{l,\ T\}$ and $\{l,\ l\}$. In the notation, where $\{a,\ b\}$ is the lepton pair, we take a to be the highest momentum lepton and b to be the second highest momentum lepton (sub-leading) lepton. We denote the number of events in each classification as N_{TT}, N_{Tl}, N_{lT}, and N_{ll}.

We want to classify an event based on real and fake leptons present. Categorising a lepton as either tight or exclusive loose does not tell us whether or not a lepton is a *real* or *fake* lepton. We create groups for events with real and fake leptons. These groups are $\{R, R\}$, $\{R, F\}$, $\{F, R\}$ and $\{F, F\}$, where R denotes a real lepton and F denotes a fake lepton. We break down the total number of inclusive loose events into the number of real and fake leptons. Ultimately we want to solve for the real and fake leptons. The total number of inclusive loose leptons is, therefore, equal to:

$$N_{LL} = N_{LL}^{RR} + N_{LL}^{RF} + N_{LL}^{FR} + N_{LL}^{FF}. \tag{4.4}$$

We want to relate the T and l categorisation to the real–fake categorisation. To do this, we require the probability of a T lepton being real or fake, and the probability of a l lepton being real or fake. We take r to be the probability that a real lepton passes the loose identification criteria and also passes the tight criteria. We take f to be the probability a fake lepton passes loose and also passes tight.

In general r and f are functions of a lepton's momentum and pseudorapidity, as well as its flavour. This means we need a 2D map for electrons and muons with momentum and pseudorapidity dependence. Mathematically we can generalise this as $r_i(p_T,\ \eta,\ e/\mu)$, and $f_i(p_T,\ \eta,\ e/\mu)$, where $i = 1, 2$ and is p_T ordered.

We know from simulation that fake leptons have several origins, so we can further breakdown the fake leptons in terms of their origin; light-flavoured jet decay (LF), heavy-flavoured hadrons (HF) and electron conversions (CO). We take the different fake rates into account by perfoming a weighted averaged:

$$f_{\text{total}}(p_T, \eta) = \sum_{i=\text{LF,HF,CO}} f_i(p_T, \eta) w_i(p_T, \eta), \tag{4.5}$$

where f_i is the fake rate of the given component and w_i is the relative contribution of each fake type. We extract weights in signal-like regions.

Taking all we have discussed thus far, we can write the relationship between lepton identification and its real/fake categorisation in the following way:

$$\begin{bmatrix} N_{TT} \\ N_{Tl} \\ N_{lT} \\ N_{ll} \end{bmatrix} = \begin{bmatrix} r_1 r_2 & r_1 f_2 & f_1 r_2 & f_1 f_2 \\ r_1(1-r_1) & r_1(1-f_2) & f_1(1-r_2) & f_1(1-f_2) \\ (1-r_1)r_2 & (1-r_1)f_2 & (1-f_1)r_2 & (1-f_1)f_2 \\ (1-r_1)(1-r_2) & (1-r_1)(1-f_2) & (1-f_1)(1-r_2) & (1-f_1)(1-f_2) \end{bmatrix} \begin{bmatrix} N_{LL}^{RR} \\ N_{LL}^{RF} \\ N_{LL}^{FR} \\ N_{LL}^{FF} \end{bmatrix}. \tag{4.6}$$

We invert this equation to cast the relationship between the two categories in terms of real and fake leptons. This gives us the four equations,

$$N_{LL}^{RR} = (1-f_1)(1-f_2)N_{TT} - f_2(1-f_1)N_{Tl} - f_1(1-f_2)N_{lT} + f_1 f_2 N_{ll}, \tag{4.7}$$
$$N_{LL}^{RF} = -(1-f_1)(1-r_2)N_{TT} + r_2(1-f_1)N_{Tl} + f_1(1-r_2)N_{lT} + f_1 r_2 N_{ll}, \tag{4.8}$$
$$N_{LL}^{FR} = -(1-f_2)(1-r_1)N_{TT} + f_2(1-r_1)N_{lT} + r_1(r-f_2)N_{Tl} + f_2 r_1 N_{ll}, \tag{4.9}$$
$$N_{LL}^{FF} = (1-r_1)(1-r_2)N_{TT} - r_2(1-r_1)N_{Tl} - r_1(1-r_2)N_{lT} + r_1 r_2 N_{ll}. \tag{4.10}$$

These four equations given the expected number of events with two, one, and zero real leptons for events with two inclusive loose leptons. We trigger on dilepton events with two tight leptons. In order to translate the inclusive loose estimates shown in Equation 4.10, we need to multiply by the appropriate efficiencies. This gives us:

$$N_{TT}^{RR} = r_1 r_2 N_{LL}^{RR}, \tag{4.11}$$
$$N_{TT}^{RF} = r_1 f_2 N_{LL}^{RF}, \tag{4.12}$$
$$N_{TT}^{FR} = f_1 r_2 N_{LL}^{FR}, \tag{4.13}$$
$$N_{TT}^{FF} = f_1 f_2 N_{LL}^{FF}. \tag{4.14}$$

. The total number of events for a dilepton triggered data sample is written as,

$$N_{TT} = N_{TT}^{RR} + N_{TT}^{RF} + N_{TT}^{FR} + N_{TT}^{FF}, \tag{4.15}$$

we can apply the matrix method to get an appropriate weighting for a given event. The result is a data-driven estimation for the fakes contribution in a given region. Here reala nd fake are solved for, but loose and tight are known from data.

4.7 Z/γ^*+jets Estimation Methods

When using an MC generator, we want to model a given background process appropriately. In the case of our Z/γ^*+jets background estimation, we use Sherpa 2.2.1 as our MC generator. Sherpa 2.2.1 is an MC generator which has a known feature that tails of distributions have positive and negative large weighted events. In order to counteract this, in regions with low statistics, such as our SRs, we estimate the Z/γ^*+jets

background using a data-driven approach. We have already explored one data-driven estimation technique in the matrix method; we will now outline a second known as the ABCD method.

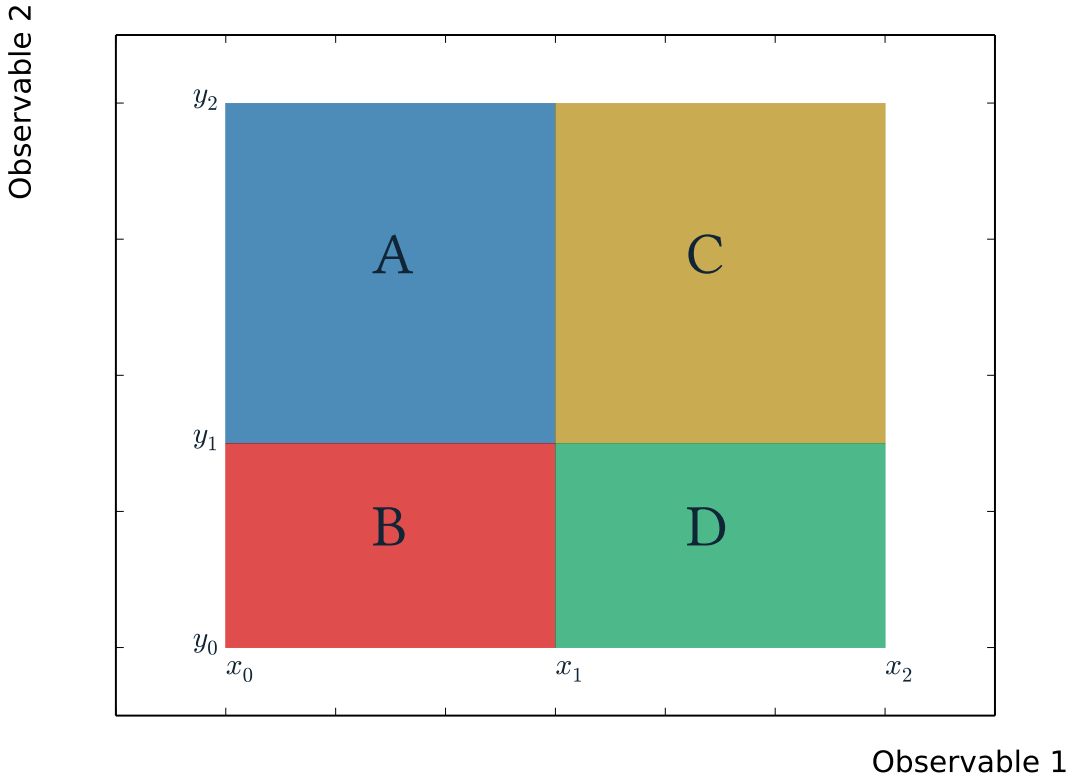

Figure 4.13: ABCD generic approach overview.

ABCD Method

We can apply the ABCD method to any estimate any background provided we meet certain conditions. For our case, we apply it to Z/γ^*+jets background, and replace Z/γ^*+jets MC with our data-driven estimation method. In order to apply the ABCD method we first need to define a region to apply it to. For our purposes we call this region **C**. We then need to find two variables which are used to define region **C** and we need to relax or broaden those selections. This defines a 2D plane. In order to apply the ABCD method we need variables to be uncorrelated with respect to one another, for the Z/γ^*+jets background. Once we have an uncorrelated plane we define regions **A**, **B** and **D** which are typically defined by inverting the selections of region **C**. In observable 1 we break down the range into boundaries defined by x_0, x_1 and x_2 where observable 2 is broken down between y_0, y_1 and y_2. We provide a general schematic of the ABCD method in Figure 4.13, and we show the region definitions in Table 4.6. Once we have defined our regions we must calculate a data-driven Z/γ^*+jets estimate. In order to do

Table 4.6: Generic region definitions for ABCD method.

Region	other criteria	x	y
A	all other criteria	$\in (x_0, x_1)$	$\in (y_1, y_2)$
B	all other criteria	$\in (x_0, x_0)$	$\in (y_0, y_1)$
C	all other criteria	$\in (x_1, x_2)$	$\in (y_1, y_2)$
D	all other criteria	$\in (x_1, x_2)$	$\in (y_0, y_1)$

this, we must take the number of events in data in the given region and subtract from it an estimate of all contributions of all other backgrounds — excluding Z/γ^*+jets. This acts as an estimate of what proportion of the number of events in data corresponding to Z/γ^*+jets. Mathematically this is equivilent to,

$$N_i = D_i - M_i^{\text{non } Z+\text{jets}}, \tag{4.16}$$

where i =A, B, or D. Here D_i and $M_i^{\text{non } Z+\text{jets}}$ are the number of events of the data and MC contributions in region i. Given the events in the regions are uncorrelated with respect to one another in the two variables selected, we can relate the number of events in each region to one another via:

$$\frac{N_A}{N_B} = \frac{N_C}{N_D}. \tag{4.17}$$

We rearrange to get a data-driven estimate for our SR,

$$N_C = N_D \times \frac{N_A}{N_B}, \tag{4.18}$$

We implement the estimation of Z/γ^*+jets in a simultaneous fit. By performing a simultaneous fit, we are allowing the estimate in each region to float to fit the data. The estimate in a given region is a free parameter and denoted as μ_i. We define the value of the fit parameter of the Z/γ^*+jets estimate to be 1.0 events so μ_C corresponds to the final fitted Z/γ^*+jets estimate, i.e $N_C = \mu_C \times 1.0$. Next, we express the estimates of Z/γ^*+jets in regions A, B and D in terms of efficiency factors from region C giving us:

$$\mu_A = \mu_C \times \epsilon_A \tag{4.19}$$

$$\mu_D = \mu_C \times \epsilon_D. \tag{4.20}$$

Given Equation 4.18, we write the estimate for region B as:

$$\mu_B = \mu_C \times \epsilon_A \times \epsilon_D. \tag{4.21}$$

m_{jj} Sideband Fit

We require an alternative approach to estimating Z/γ^*+jets in the SR, which will allow us to cross check our estimate. While the ABCD method uses a purely data-driven approach, the m_{jj} sideband fit method uses a data-driven approach for determining the Z/γ^*+jets estimate in a m_{jj} sideband region (SB) and then uses Z/γ^*+jets MC to determine the *shape factor* between that SB and the SR. Here Z denotes Z/γ^*+jets.

The first step of the m_{jj} sideband fit method is to define the SR and the SB regions. As is the case in the ABCD method, we get a data-driven estimate of the Z/γ^*+jets estimate in the sideband:

$$N_{Z,\mathrm{DD}}^{\mathrm{SB}} = N_{\mathrm{Data}}^{\mathrm{SB}} - N_{\mathrm{MC}}^{\text{non } Z\text{+jets,SB}} \tag{4.22}$$

We then calculate the estimate in the SR by multiplying the SB data-driven estimate by a shape factor calculated from MC. The shape factor is defined as:

$$R^{\mathrm{shape}} = \frac{N_Z^{\mathrm{SR,MC}}}{N_Z^{\mathrm{SB}}}, \tag{4.23}$$

which when multiplied by the estimate of Z/γ^*+jets in the SB gives us the data-driven estimate in the SR:

$$N_{Z,\mathrm{DD}}^{\mathrm{SR}} = N_{Z,\mathrm{DD}}^{\mathrm{SB}} \times R^{\mathrm{shape}}. \tag{4.24}$$

Typical sources of systematic uncertainty in this method come from the variation of the ABCD region boundaries. Sources of uncertainty from experimental or theoretical sources can also be implemented and propogated to the final estimates.

4.8 MC Validation

We have described the run-II dataset that we will be utilising in this analysis. We then described our approach to modelling that dataset, namely by splitting the modelling into different background processes.

To validate our modelling of two-lepton selections for events with at least two jets, we split the validation into RJ2ℓA with exactly two jets and into RJ2ℓB, which requires at least two jets. Here RJ2ℓB is contained within RJ2ℓA, though has a different recursive jigsaw treatment. We also require an opposite-sign same-flavour with a dilepton invariant mass with 10 GeV of the Z boson mass, we call this an on-Z selection, or merely say it is consistent with the Z boson mass. Similarly, we select for a W boson decaying hadronically such that there is a jet pair that has an invariant mass within 20 GeV of the W mass. The definition of these preselection regions is shown in Table 4.7.

To validate our modelling of three-lepton selections for events with all jet multiplicities,

Table 4.7: The two-lepton preselection regions defined to validate our MC modelling of the run-II ATLAS dataset.

Region	Selection	N_{Jets}	$p_T^{\ell_1}$ [GeV]	$p_T^{\ell_2}$ [GeV]	$p_T^{j_1}$ [GeV]	$p_T^{j_2}$ [GeV]	$m_{\ell\ell}/M_Z$ [GeV]	m_{jj}/M_J [GeV]
RJ2ℓA	$l^{\pm}l^{\mp}$	$= 2$	> 25	> 25	> 30	> 30	$\in [80, 100]$	$\in [60, 100]$
RJ2ℓB	$l^{\pm}l^{\mp}$	$>= 2$	> 25	> 25	> 30	> 30	$\in [80, 100]$	$\in [60, 100]$

we split the validation into an inclusive jet-multiplicity region, RJ3ℓA which requires an opposite-sign same-sign lepton pair with an invariant mass consistent with the Z mass. The definition of these preselection regions is shown in Table 4.8.

Table 4.8: The three-lepton preselection regions defined to validate our MC modelling of the run-II ATLAS dataset.

Region	Selection	N_{Jets}	$p_T^{\ell_1}$ [GeV]	$p_T^{\ell_2}$ [GeV]	$p_T^{\ell_3}$ [GeV]	$m_{\ell\ell}$ [GeV]	m_T^W [GeV]
RJ3ℓA	$\ell^{\pm}\ell^{\mp}\ell$	$>= 0$	> 25	> 25	> 20	$\in [75, 105]$	> 50
RJ3ℓB	$\ell^{\pm}\ell^{\mp}\ell$	> 0	> 25	> 25	> 20	$\in [75, 105]$	> 50

Preselection Validation

In Figures 4.14 and 4.15 we show the histogram of the transverse momentum of each lepton. Each plot is split into two sub-plots; the primary and the ratio plot. In the top left of the primary plot, we have the centre-of-mass energy 13 TeV, the integrated luminosity of the dataset presented in the plot and the plotted selection criteria summarised by region name. The x axis corresponds to the leading lepton, the sub-leading lepton, or the sub-sub-leading lepton, the y axis is often the number of entries per the width of the binning; in this case 25 GeV. The y axis is often on a logarithmic scale; this allows us to see the shape of background components with different orders of magnitude. In the situation where the regions have fewer events, we typically change the y axis scale to linear. In our analysis we show the CR, VR and SRs using a linear scale.

We show the data as black circles, with vertical bars to represent the errors, typically Poisson errors. We then use the different MC samples as outlined in Section 4.4. We use the matrix method estimation for the fakes backgrounds, and despite using a data-driven technique for our Z/γ^*+jets estimate for our signal region selections, for the purposes of preselection validation we use the Sherpa 2.2.1 generator.

We represent the backgrounds in the *stacked* histogram; each background has a different colour; $t\bar{t}$ is orange; single top (tX) is salmon-orange; top other is crimson red; Z/γ^*+jets is green; diboson is light blue, Triboson is dark blue; V+gamma, where V is either W or Z, is shown in teal; Higgs is pale-yellow; Drell–Yan is bright-green, and fakes is shown in charcoal grey. We denote the signal, which corresponds to the $\tilde{\chi}_1^{\pm}/\tilde{\chi}_2^0/\tilde{\chi}_1^0 = (200, 100)$ GeV point, with a solid red line. The bottom plot is the ratio plot which shows the "Data/SM". We calculate this by taking the data yield per bin and divides the yield by the

summed yield of all backgrounds (SM) in that bin; we represent this with black circle markers. The red line in the ratio plot shows perfect agreement. The dashed blue line shows the average Data/SM for the region.

In both Figure 4.14 and 4.15 we see that in each case the lepton transverse momenta are in agreement between the MC and the observed number of events. This gives us confidence for using these MC samples for our more specific analysis selections.

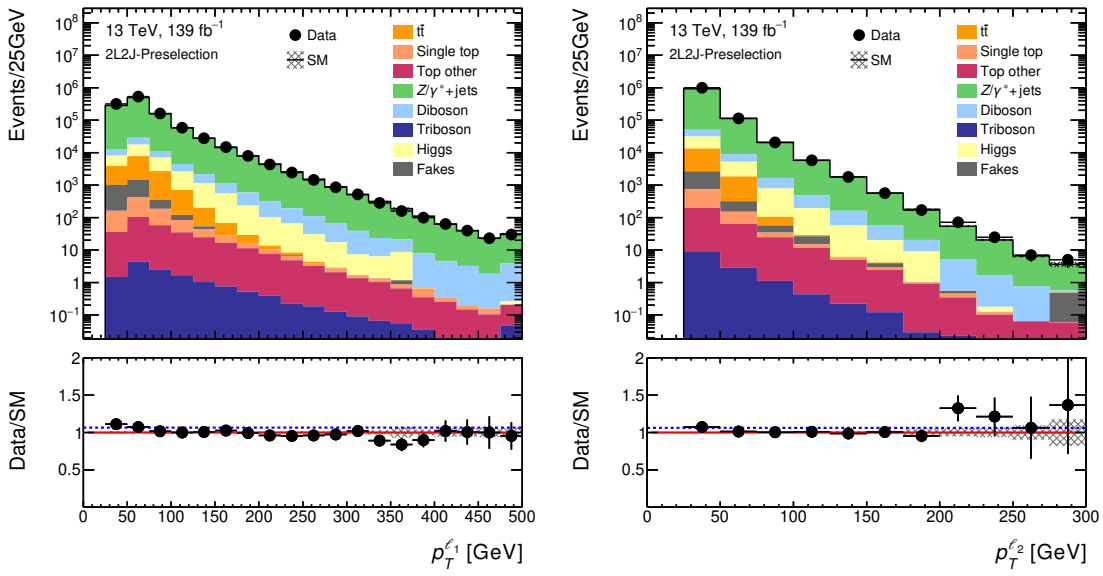

(a) Leading lepton (b) Sub-leading lepton

Figure 4.14: The lepton p_T modelling for preselection validation regions for RJ2ℓA.

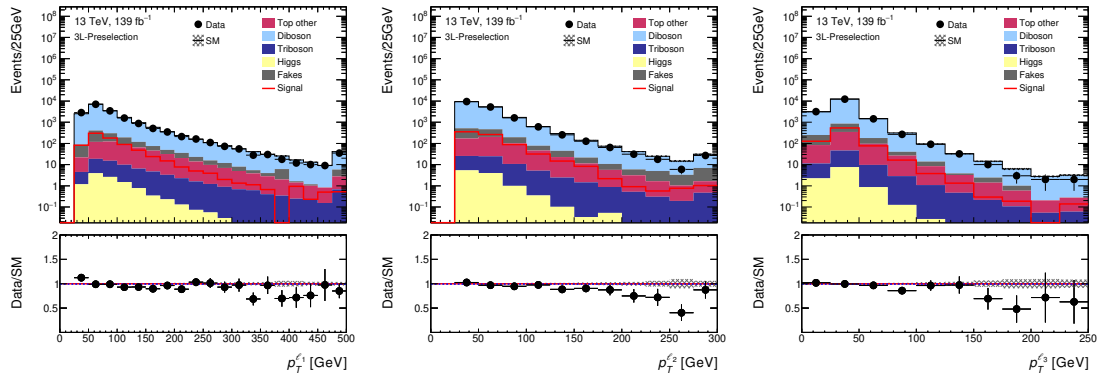

(a) Leading lepton (b) Sub-sub-leading lepton (c) Sub-sub-leading lepton

Figure 4.15: The lepton p_T modelling for preselection validation regions for RJ3ℓA.

4.9 Systematic Uncertainties

There are several uncertainties considered on a measurement at the ATLAS experiment. We split the uncertainties into experimental and theoretical sources; they are included in a given measurement by way of a profile likelihood fit, which we implement in HistFitter [123].

Typically during the development stage of an analysis, we calculate normalisation factors by hand and manually propagate them to the SR yields. Once we have a well-defined analysis and a fixed procedure, we move from this manual approach to a simultaneous fit procedure which accounts for correlations between different regions. This section defines the regions which we use in the fitting procedure and defines the likelihood function, the test statistic and the method with which we extract a signal strength parameter μ. The signal strength is the ratio between the measured cross-section and the SM expectation.

The statistical fit of the analysis involves the use of a likelihood function $\mathcal{L}(\mu, \theta|\mathcal{N})$, which is a function of the strength parameter μ and the set of nuisance parameters $\theta = \{\theta_a, \theta_b, \dots\}$ given a set of event yields $\mathbf{N} = \{N_A, N_B, \dots\}$. For our purposes θ and $\mathcal{N}$ are known quantities, with μ being the variable we wish to extract. By using a *profiled likelihood test statistic* (q_μ) we can test the background-only versus the background-and-signal hypotheses, and thus extract an allowed range for our signal strength μ. The test statistic is defined by:

$$q(\mu) = -2\ln\left(\frac{\mathcal{L}(\mu,\theta)}{\mathcal{L}_{\max}}\right)|_{\theta=\hat{\theta}(\mu)}. \tag{4.25}$$

This function is also written as q_μ and the argument of the natural logarithm sometimes being denoted as Λ. The denominator $\mathcal{L}_{\max}$ is maximized under all possible values of μ and θ, the μ which maximises the denominator is denoted $\hat{\mu}$. The numerator $\mathcal{L}(\mu, \theta)$ is maximised for a specific μ over all θ. The θ which maximise $\mathcal{L}(\mu, \theta)$ are called $\hat{\theta}_\mu$. The background only probability, $p(\mu = 0)$ is defined as the probability to obtain $q(\mu = 0)$ larger than the observed $q(\mu)$. Due to Wilk's theorem we can assume $-2\ln(\Lambda(\mu))$ follows a χ^2 distribution [124]. Local significance is defined as the one-sided tail of the Gaussian distribution:

$$Z_0 = \sqrt{2}\mathrm{erf}^{-1}(1 - 2p_0). \tag{4.26}$$

To compute the exclusion regions we use a modified frequentist method known as CL_S [124].

Experimental Systematics

We include the experimental sources of uncertainty from jet energy scale and resolution, the modelling of the missing transverse energy, effects of pileup, as well as the

lepton reconstruction efficiency, the b-tagging efficiency, the lepton energy scale, energy resolution and in the modelling of the trigger itself [110, 111, 116–119, 121, 122, 125]. Using a combination of simulation and data samples, we calculate the jet energy scale and jet energy resolution uncertainties by measuring the jet response balance in multijet, Z/γ+jets events [118]. To calculate the systematic uncertainty on the missing transverse energy, we must propagate the uncertainties from the visible objects, as well as the soft-term resolution and scale, through to the final estimate [122]. We assign systematic uncertainties to the matrix method fakes estimate by accounting for the variation of the sample between the SRs and CRs.

Theory Systematics

Our ability to calculate quantities from the SM faces various limitations. These limitations can include assumptions about particle's mass and couplings. Reducing the sources of uncertainty due to these limitations is a difficult task, one which requires both theorists and experimentalists working in consultation. In Chapter 3 Equation 3.10, we introduced the inclusive $pp \to X$ cross-section. In Equation 3.10, we have written the $pp \to X$ cross-section implicity to all orders, we can instead choose to write it in a way to emphasise the different orders to the perturbative expansion, giving us:

$$\sigma^{(n)} = \mathrm{PDF}(x_1, \mu_F) \otimes \mathrm{PDF}(x_2, \mu_F) \otimes \hat{\sigma}^{(n)}(x_1, x_2, \mu_R), \tag{4.27}$$

where x_1, x_2 are the momentum fraction of a given parton involved in an interaction, μ_F is called the factorisation scale, and μ_R is the renormalisation scale, and where:

$$\hat{\sigma}^{(n)} = \hat{\sigma}^{(0)} + \alpha_s^1 \hat{\sigma}^{(1)} + \cdots + + \alpha_s^n \hat{\sigma}^{(n)} + \mathcal{O}(\alpha_S^{n+1}). \tag{4.28}$$

The PDFs we use are estimated by assuming a functional form for the parton content of the proton at a given scale Q in GeV. The Dokshitzer-Gribov-Lipatov-Altarelli-Parisi (DGLAP) evolution equations are then used to estimate the PDFs at different energy scales, with fractions of those scales given by z. This is given by:

$$\frac{d\mathrm{PDF}(x, Q^2)}{d \log Q^2} = P(\alpha_s, z)\mathrm{PDF}(x/z, Q^2), \tag{4.29}$$

with:

$$P(\alpha_s, z) = \alpha_s P^{LO} + \alpha_S^2 P^{NLO} + \ldots, \tag{4.30}$$

here $P(\alpha_s, z)$ corresponds to the the parton fractions.

The strong coupling α_s is also determined experimentally and is quoted at the scale $Q = m_Z$. There are three main sources of uncertainty in perturbative QCD calculations. The first is due to missing higher orders in the perturbative expansion of the partonic cross-section. The usual way to estimate them is to perform scale variations. We do this

by varying renormalisation (μ_R) and factorisation (μ_F) scales upward and downward by a factor of two. We do this in a pairwise fashion:

$$\{\mu_R, \mu_F\} \times \{0.5, 0.5\}, \{1, 0.5\}, \{0.5, 1\}, \{1, 1\}, \{2, 1\}, \{1, 2\}, \{2, 2\}. \tag{4.31}$$

Performing these variations gives us an estimate for $\mathcal{O}(\alpha_s^{n+1})$.

The second source of uncertainty is choice of PDF, the uncertainty on the functional form used in the PDF fits, and missing higher-order uncertainties on the DGLAP evolution equations. The third uncertainty source is from α_s — the measured value of the strong coupling constant quoted at the scale of the Z mass. To quote the value of α_s for a given scale, we use RGEs; truncated to a given order. There are two sources of uncertainty for the RGEs the experimental errors and the RGE truncation. To parameterise these uncertainties, we calculate different PDFs which correspond to different values of α_s. These uncertainties propagate through to the calculation of hadronic cross-sections.

We determine the upper and lower uncertainties by calculating the minimum and maximum variations for each of the three types of uncertainty. If the nominal does not lay between the upper and lower variations, then we take the maximal difference as a symmetric uncertainty.

4.10 Signal Region Definitions

In this section we will introduce the 2ℓ and 3ℓ SRs. We will outline the Recursive Jigsaw Reconstruction approaches for both 2ℓ and 3ℓ, as well as the region selections, and finally the background contributions. In order to not bias the analysis we implement a blinding strategy. We do not look at the observed number of events in the SRs until all background estimation techniques and sources of systematic errors are finalised. Furthermore, we also performed a partial unblinding of the dataset using only the 2015 and 2016 subset of the dataset.

Two-Lepton Standard Signal Region

We show the RJR decay tree used in the two-lepton selections of this analysis in Figure 4.16. We have assume $\tilde{\chi}_1^{\pm}\tilde{\chi}_2^0$ production, followed by the decay of $\tilde{\chi}_1^{\pm}$ into a W boson and LSP. The W boson in the 2ℓ analysis is specified to decay hadronically, the $\tilde{\chi}_2^0$ decays into a Z boson and a second LSP, the Z boson subsequently decays leptonically. The definition of the decay tree gives us access to the RJR basis of variables.

The first SR we describe targets the signal process in Figure 4.2a, given this signal does not have ISR present, and targets the low-mass region, we call this region SR2ℓ_Low, and by contrast to the ISR regions, we refer to it as the "standard" SR. We first apply preselection criteria, we require exactly two leptons and exactly two jets. The minimum

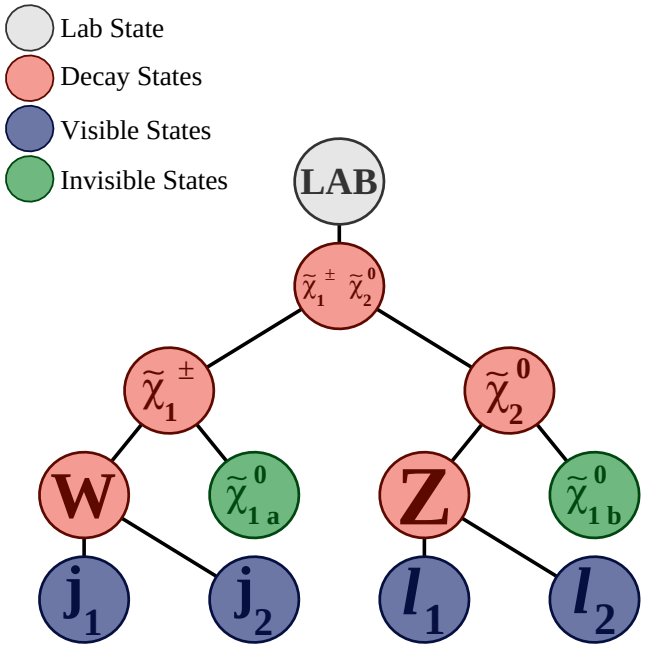

Figure 4.16: RJR Topologies 2ℓ and 3ℓ.

momentum for the leptons is 25 GeV ($p_{\mathrm{T}}^{\ell} > 25$ GeV), the minimum momentum of each jet is 30 GeV ($p_{\mathrm{T}}^{j} > 30$ GeV). We expect the signal to have two jets with an invariant mass near the W mass, thus $m_{jj} \in (60, 100)$ GeV, the two leptons present should have an invariant mass approximately near the Z mass, i.e. $m_{\ell\ell} \in (80, 100)$ GeV.

In what follows, we describe the RJR variables we choose for 2ℓ standard optimisation. We begin with:

$$H_{4,1}^{\mathrm{PP}} = |\vec{p}_{\ell_1}^{\,\mathrm{PP}}| + |\vec{p}_{\ell_2}^{\,\mathrm{PP}}| + |\vec{p}_{j_1}^{\,\mathrm{PP}}| + |\vec{p}_{j_2}^{\,\mathrm{PP}}| + |\vec{p}_{\mathrm{inv}}^{\,\mathrm{PP}}|, \tag{4.32}$$

which is the scalar sum of all visible object momenta plus the invisible system momentum. We demand that $H_{4,1}^{\mathrm{PP}} > 400$ GeV. We then have the transverse version, $H_{T\,4,1}^{\mathrm{PP}}$ which is defined as,

$$H_{T\,4,1}^{\mathrm{PP}} = |\vec{p}_{T,\ell_1}^{\,\mathrm{PP}}| + |\vec{p}_{T,\ell_2}^{\,\mathrm{PP}}| + |\vec{p}_{T,j_1}^{\,\mathrm{PP}}| + |\vec{p}_{T,j_2}^{\,\mathrm{PP}}| + |\vec{p}_{T,\mathrm{inv}}^{\,\mathrm{PP}}|. \tag{4.33}$$

The variable $H_{1,1}^{\mathrm{PP}}$ is the vectorial sum of the visible objects plus the magnitude of the invisible system, it is defined as:

$$H_{1,1}^{\mathrm{PP}} = \left(|\vec{p}_{\ell_1} + \vec{p}_{\ell_2} + \vec{p}_{j_1} + \vec{p}_{j_2}| + |\vec{p}_{\mathrm{inv}}|\right)^{\mathrm{PP}}. \tag{4.34}$$

We construct a ratio of $H_{1,1}^{\mathrm{PP}}$ and $H_{4,1}^{\mathrm{PP}}$, which is the amount of momentum stored in the transverse plane. In our selections we demand,

$$H_{1,1}^{\mathrm{PP}} / H_{4,1}^{\mathrm{PP}} \in (0.35, 0.60). \tag{4.35}$$

We then have the hemisphere specific variables, $H_{1,1}^{\mathrm{Pa}}$, $H_{1,1}^{\mathrm{Pb}}$, $H_{2,1}^{\mathrm{Pa}}$ and $H_{2,1}^{\mathrm{Pb}}$. These hemisphere specific variables only take objects from their respective hemisphere a or b. The vector-sum hemisphere variables give a scale of how collimated a hemisphere's children are. The different hemisphere variables are defined as:

$$H_{1,1}^{\mathrm{Pa}} = \left(|\vec{p}^{\,j_1} + \vec{p}^{\,j_1}| + |\vec{p}_{\mathrm{inv}}|\right)^{\mathrm{Pa}}, \tag{4.36}$$

$$H_{1,1}^{\mathrm{Pb}} = \left(|\vec{p}^{\,\ell_1} + \vec{p}^{\,\ell_1}| + |\vec{p}_{\mathrm{inv}}|\right)^{\mathrm{Pb}}. \tag{4.37}$$

The scalar-sum type hemisphere variables give a scale of the overall momentum of each branch, and are defined as:

$$H_{2,1}^{\mathrm{Pa}} = \left(|\vec{p}^{\,j_1}| + |\vec{p}^{\,j_1}| + |\vec{p}_{\mathrm{inv}}|\right)^{\mathrm{Pa}}, \tag{4.38}$$

$$H_{2,1}^{\mathrm{Pb}} = \left(|\vec{p}^{\,\ell_1}| + |\vec{p}^{\,\ell_1}| + |\vec{p}_{\mathrm{inv}}|\right)^{\mathrm{Pb}}. \tag{4.39}$$

We construct a ratio which gives us a measure of how much momentum is in one hemisphere versus another. The hemisphere which has the smallest value of $H_{1,1}^{\mathrm{X}}$ corresponds to the hemisphere which is least collimated. The hemisphere with the smallest value of $H_{2,1}^{\mathrm{X}}$ corresponds to the hemisphere with the smaller momentum scale. The ratio between $\min\left(H_{1,1}^{\mathrm{Pa}}, H_{1,1}^{\mathrm{Pb}}\right)$ and $\min\left(H_{2,1}^{\mathrm{Pa}}, H_{2,1}^{\mathrm{Pb}}\right)$ is maximised when the invisble momentum vector and visible momentum vector are collimated in each hemisphere. The ratio is minimised when one hemisphere has a large fraction of the momentum and the second hemisphere objects decay at rest.

Another variable of interest is the momentum of the lab frame, in units of the total momentum of the visible objects, invisible objects and the PP frame. The smaller the value, the better the lab frame has been approximated. This variable is refered to as R_{P_T} which mathematically is written in the form:

$$R_{P_T} = \frac{p_{T,\mathrm{PP}}^{\mathrm{LAB}}}{p_{T,\mathrm{PP}}^{\mathrm{LAB}} + H_{T\ 4,1}^{\mathrm{PP}}}. \tag{4.40}$$

We want the opening angle, $\Delta\phi_V^P$, of the parent frames to be sufficiently wide.

We do not want the missing transverse momentum to predominantly originate from jet mismeasurement. In order to minimise the likelihood of the missing transverse momentum originating from jet mis-measurement, we require,

$$\min \Delta\phi(j_{1,2}, p_T^{\mathrm{miss}}) > 2.4 \tag{4.41}$$

We summarise the above selection criteria for SR2ℓ_Low in Tables 4.9 and 4.10.

Table 4.9: Preselection criteria for the 2ℓ standard decay tree SR. The variables are defined in the text.

Region	n_{leptons}	n_{jets}	$n_{b\text{-tag}}$	$p_T^{\ell_1,\ell_2}$ [GeV]	$p_T^{j_1,j_2}$ [GeV]	$m_{\ell\ell}$ [GeV]	m_{jj} [GeV]
SR2ℓ_Low	$= 2$	$= 2$	$= 0$	> 25	> 30	$\in (80, 100)$	$\in (70, 90)$

Table 4.10: Selection criteria for the 2ℓ standard decay tree SR. The variables are defined in the text.

Region	$H_{4,1}^{\text{PP}}$ [GeV]	$H_{1,1}^{\text{PP}}$ [GeV]	R_{p_T}	$\frac{H_{1,1}^{\text{PP}}}{H_{4,1}^{\text{PP}}}$	$\min\Delta\phi(j_{1,2}, \vec{P}_{\text{T}}^{\text{miss}})$
SR2ℓ_Low	> 400	< 0.05	$\in (0.35, 0.60)$	> 2.4	

2ℓ ISR Signal Region

The next SR we detail targets the signal process in Figure 4.2c. Given that this signal process has ISR radiation present, we refer to this signal region as SR2ℓ_ISR. This signal process requires the use of the RJR ISR decay tree in Figure 4.8. The basic preselection

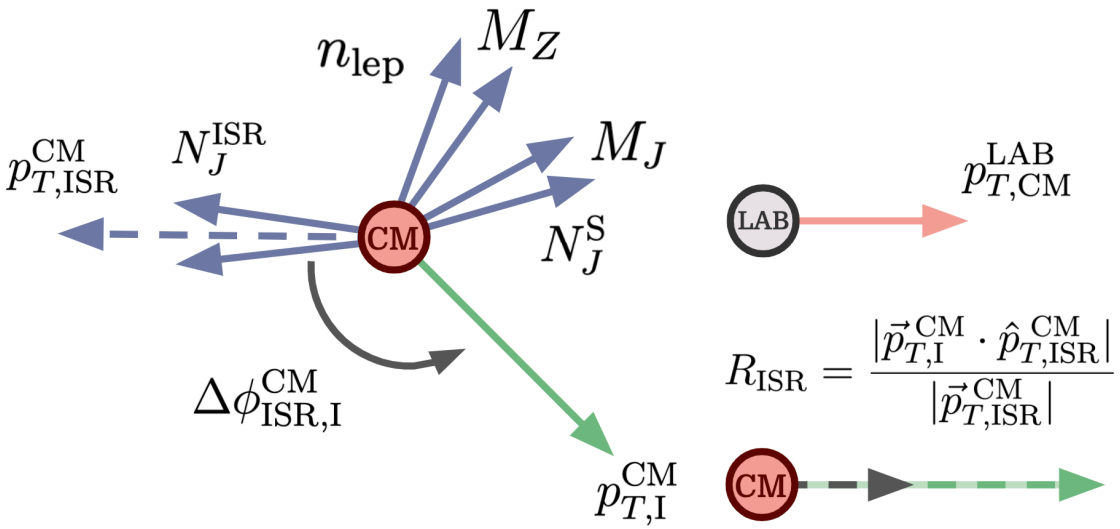

Figure 4.17: The RJR ISR decay tree.

we apply is to the jets and the leptons. We require that there are exactly two leptons. We require a jet multiplicity of either three or four jets. We require $p_T^{\ell} > 25$ GeV and $p_T^{j} > 30$ GeV. We require zero b-tagged jets, and that of the three or four jets at least 1 of the jets is assigned to the ISR system, and that exactly two jets are assigned to the S system.

The S frame contains the objects assigned in the topology of the signal process. There is a Z frame. We take the mass of this frame to be M_Z and require that it be on the Z peak

with $M_Z \in (80, 100)$. We take the invariant mass of all jets assigned in the S system M_J, and we require this be around the W mass $M_J \in (50, 110)$. The ISR system must have sufficiently hard momentum ($p_{T,\text{ISR}}^{\text{CM}} > 100$ GeV), and we want the invisible system to be hard also ($p_{T,\text{I}}^{\text{CM}} > 100$ GeV). We want the ISR boost to contribute to the amount of invisible momentum, we do this by requiring the opening angle between ISR and I must be sufficiently back-to-back in the CM frame; $\Delta\phi_{\text{ISR,I}}^{\text{CM}} > 2.8$, meaning the ISR system can generate the missing transverse energy through a boost. We require a sufficient amount of the invisible system's momentum in the CM frame to originate from an ISR boost; this is selected with $R_{\text{ISR}} \in (0.4, 0.75)$. Finally, we require that this topological tree sufficiently fits the given event by demanding $p_T^{\text{CM}} < 20$ GeV. The selection criteria for SR2ℓ_ISR are summarised in Tables 4.11 and 4.12.

Table 4.11: Preselection criteria for the 2ℓ ISR decay tree SR. The variables are defined in the text.

Region	n_{leptons}	$N_{\text{jet}}^{\text{ISR}}$	$N_{\text{jet}}^{\text{S}}$	n_{jets}	$n_{b\text{-tag}}$	$p_T^{\ell_1,\ell_2}$ [GeV]	$p_T^{j_1,j_2}$ [GeV]
SR2ℓ_ISR	$= 2$	≥ 1	$= 2$	$\in [3, 4]$	$= 0$	> 25	> 30

Table 4.12: Selection criteria for the 2ℓ ISR decay tree SR. The variables are defined in the text.

Region	m_Z [GeV]	m_J [GeV]	$\Delta\phi_{\text{ISR,I}}^{\text{CM}}$	R_{ISR}	$p_{\text{T ISR}}^{\text{CM}}$ [GeV]	$p_{\text{T I}}^{\text{CM}}$ [GeV]	p_{T}^{CM} [GeV]
SR2ℓ_ISR	$\in (80, 100)$	$\in (50, 110)$	> 2.8	$\in (0.4, 0.75)$	> 180	> 100	< 20

3ℓ Standard Signal Region

We have laid much groundwork to explain and explore our RJR analysis approach for the 2ℓ selections. Similarly to the 2ℓ analysis, we will split our approach into a standard approach and an ISR approach. There will be similarities of approach between 2ℓ and the 3ℓ analysis, but a key difference is that there are fewer SM backgrounds to three-lepton signals.

The next SR we detail targets the signal process in Figure 4.2b, it targets the low-mass region, and so its called SR3ℓ_Low. We show the 3ℓ RJR decay tree in Figure 4.18. We have $\tilde{\chi}_1^{\pm}\tilde{\chi}_2^0$ production, followed by the decay of $\tilde{\chi}_1^{\pm}$ into a W boson and LSP. The W boson in the 3ℓ analysis is specified to decay leptonically. The $\tilde{\chi}_2^0$ decays into a Z boson and a second LSP followed by the Z boson decaying leptonically. As there are two sources of missing transverse momentum in the decay tree, we do not have the ability to discern the W boson from the $\tilde{\chi}_1^{\pm}$; for this reason we have no dedicated W boson frame.

The definition of the 3ℓ decay tree gives us access to an RJR basis of variables, but this basis of variables is different to those defined in the 2ℓ analysis. To define SR3ℓ_Low, we apply some preselection criteria to define the boundaries of our object selection. Firstly,

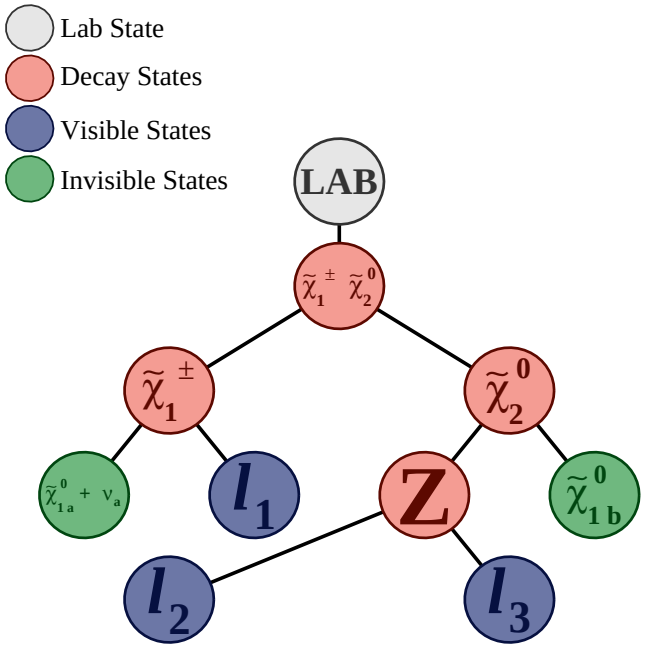

Figure 4.18: RJR standard decay tree for 3ℓ Analysis.

we require exactly three leptons and zero jets. We also require that there are zero b-tagged jets. The minimum momentum of the three leptons is $p_T^{\ell_1} > 60$ GeV for the leading lepton, $p_T^{\ell_2} > 40$ GeV for the sub-leading lepton, and $p_T^{\ell_3} > 30$ GeV for the sub-sub-leading lepton. The preselection criteria are summarised in Table 4.13.

Table 4.13: Preselection criteria for the 3ℓ standard decay tree SR. The variables are defined in the text.

Region	n_{leptons}	n_{jets}	$n_{b\text{-tag}}$	$p_T^{\ell_1}$ [GeV]	$p_T^{\ell_2}$ [GeV]	$p_T^{\ell_3}$ [GeV]	$m_{\ell\ell}$ [GeV]
SR3ℓ_Low	$= 3$	$= 0$	$= 0$	> 60	> 40	> 30	$\in (75, 105)$

The RJR variables we choose for 3ℓ standard optimisation share similarities with the 2ℓ selections. Clearly, the decay tree is different and so the quantities we extract must be also. The first variable we introduce for the 3ℓ standard approach is $H_{3,1}^{\text{PP}}$, mathematically given by:

$$H_{3,1}^{\text{PP}} = |\vec{p}_{\ell_1}^{\,\text{PP}}| + |\vec{p}_{\ell_2}^{\,\text{PP}}| + |\vec{p}_{\ell_3}^{\,\text{PP}}| + |\vec{p}_{\text{inv}}^{\,\text{PP}}|, \tag{4.42}$$

which is the scalar sum of all visible object momenta plus the invisible system momentum. We demand that $H_{3,1}^{\text{PP}} > 250$ GeV. The transverse version of this variable $H_{T\,3,1}^{\text{PP}}$ is defined as:

$$H_{T\,3,1}^{\text{PP}} = |\vec{p}_{T,\ell_1}^{\,\text{PP}}| + |\vec{p}_{T,\ell_2}^{\,\text{PP}}| + |\vec{p}_{T,\ell_3}^{\,\text{PP}}| + |\vec{p}_{T,\text{inv}}^{\,\text{PP}}|. \tag{4.43}$$

The analogous variables for the 2ℓ analysis are $H_{4,1}^{\text{PP}}$ and $H_{T\,4,1}^{\text{PP}}$. We take $H_{T\,3,1}^{\text{PP}}$ and $H_{3,1}^{\text{PP}}$

and construct a ratio between the two, this ratio is a measure of the proportion of the momentum of the event being held in the transverse plane. The selection we make on this quantity is:

$$H_{T\,3,1}^{\mathrm{PP}}/H_{3,1}^{\mathrm{PP}} > 0.75. \tag{4.44}$$

As both quantities are being evaluated in the same reference frame this quantity very naturally has a strict kinematic endpoint at $H_{T\,3,1}^{\mathrm{PP}}/H_{3,1}^{\mathrm{PP}} = 1.0$. The selection criteria for SR3ℓ_Low are summarised in Table 4.14.

Table 4.14: Selection criteria for the 3ℓ standard decay tree SR. The variables are defined in the text.

Region	m_{T}^{W} [GeV]	$H_{3,1}^{\mathrm{PP}}$ [GeV]	$\frac{p_{\mathrm{T\,PP}}^{\mathrm{lab}}}{p_{\mathrm{T\,PP}}^{\mathrm{lab}}+H_{\mathrm{T}\,3,1}^{\mathrm{PP}}}$	$\frac{H_{\mathrm{T}\,3,1}^{\mathrm{PP}}}{H_{3,1}^{\mathrm{PP}}}$	$\frac{H_{1,1}^{\mathrm{P_b}}}{H_{2,1}^{\mathrm{P_b}}}$
SR3ℓ_Low	> 100	> 250	< 0.05	> 0.9	–

3ℓ ISR Signal Region

The next SR targets the signal process in Figure 4.2d, which requires ISR jets. The SR is called SR3ℓ_ISR, and utilises the RJR ISR decay tree in Figure 4.8. We now detail the

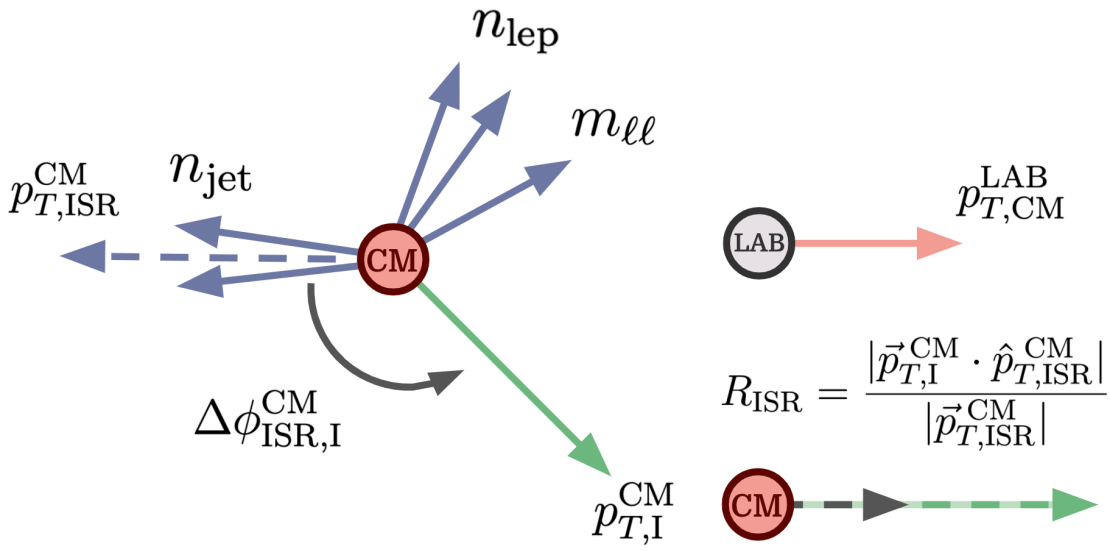

Figure 4.19: RJR ISR variable summaries.

preselection for SR3ℓ_ISR. We require that there are exactly three leptons. We permit either one, two or three jets. The lepton momenta must obey $p_T^{\ell_1} > 25$ GeV, $p_T^{\ell_2} > 25$ GeV and $p_T^{\ell_3} > 20$ GeV, and the jet momenta must obey $p_T^{j} > 30$ GeV, with no jet tagged as a b-jet. We require that at least one of the $\in (1, 3)$ jets be assigned to the ISR system,

if it is not assigned to the ISR system then it is an observer jet, and does not take part in the decay tree. The preselection criteria for SR3ℓ_ISR are summarised in Table 4.15.

Table 4.15: Preselection criteria for the 3ℓ ISR decay tree SR. The variables are defined in the text.

Region	n_{leptons}	n_{jets}	$n_{b\text{-tag}}$	$p_T^{\ell_1}$ [GeV]	$p_T^{\ell_2}$ [GeV]	$p_T^{\ell_3}$ [GeV]
SR3ℓ_ISR	$= 3$	$\in [1, 3]$	$= 0$	> 25	> 25	> 20

The S frame here contains the generic 3ℓ SR. As there are three leptons there is an ambiguity as to how we assign them within the decay tree. We take the lepton pairs with the smallest invariant mass, and we assign those to the Z boson. After assigning leptons to the Z frame, we demand $m_{\ell\ell} \in (75, 105)$. We require that the ISR system has a sufficiently hard momentum: $p_{T,ISR}^{CM} > 100$ GeV. We require $p_{T,\text{I}}^{CM} > 80$ GeV. We require the opening angle between **ISR** and **I** to be sufficiently back-to-back in the CM frame; $\Delta\phi_{ISR,I}^{CM} > 2.0$. We require a sufficient amount of the invisible system's momentum in the CM frame to originate from an ISR boost; this is selected with $R_{\text{ISR}} \in (0.55, 1.0)$. We require that this topological tree sufficiently fits the given event by implementing $p_T^{\text{CM}} < 25$ GeV. The selection criteria for SR3ℓ_Low are summarised in Table 4.16.

Table 4.16: Selection criteria for the 3ℓ ISR decay tree SR. The variables are defined in the text.

Region	$m_{\ell\ell}$ [GeV]	m_{T}^{W} [GeV]	$\Delta\phi_{\text{ISR,I}}^{\text{CM}}$	R_{ISR}	$p_{\text{T ISR}}^{\text{CM}}$ [GeV]	$p_{\text{T I}}^{\text{CM}}$ [GeV]	p_{T}^{CM} [GeV]
SR3ℓ_ISR	$\in (75, 105)$	> 100	> 2.0	$\in (0.55, 1.0)$	> 100	> 80	< 25

Signal Region Breakdowns

In order to define the analysis approach, we looked at the dominant SM processes in the four SRs. We first outline the 2ℓ SRs, with the background decompositions for SR2ℓ_Low and SR2ℓ_ISR shown in Table 4.17. In these tables we see the background contribution from all SM background contributions. Most background components are generated with MC, as was detailed in Section 4.4. The Z/γ^*+jets contributions in the two SRs have a very low number of entries in the MC sample, and events with incredibly large weights and sources of uncertainty. Large weights and low numbers of events in our analysis regions leads to lack of statistical power in the Z/γ^*+jets modelling, and for this reason, we instead choose to develop a data-driven estimate for the Z/γ^*+jets instead of using MC. The other dominant backgrounds are diboson, and $t\bar{t}$ and single top production processes. We use a control region (CR)–validation region (VR) approach to control for these backgrounds.

SR3ℓ_Low and SR3ℓ_ISR background breakdowns are shown in Table 4.18. The three-lepton SRs are significantly more straight forward than the 2ℓ SRs, where we see the ma-

jor dominant background is diboson production, with no other significant backgrounds. We use a CR, VR approach to control for the diboson backgrounds.

Table 4.17: The expected estimate for SR2ℓ_Low and SR2ℓ_ISR. All expectations include experimental systematics except the Z/γ^*+jets estimate.

Full run-II	SR2ℓ_Low	SR2ℓ_ISR
Total exp. SM events	59 ± 18	40 ± 6
MC exp. Higgs events	$0.35^{+0.69}_{-0.35}$	$0.01^{+0.01}_{-0.01}$
MC exp. Triboson events	$0.06^{+0.09}_{-0.06}$	$0.05^{+0.06}_{-0.05}$
MC exp. Diboson events	12 ± 2.26	11 ± 5
MC exp. Top other events	0.06 ± 0.02	0.51 ± 0.36
MC exp. $t\bar{t}$ events	3.9 ± 1.9	9.9 ± 3.6
MC exp. Single top events	$0.76^{+0.77}_{-0.76}$	$0.03^{+0.14}_{-0.03}$
DD. Fakes events	$0.01^{+0.09}_{-0.01}$	0.68 ± 0.17
MC exp. Z/γ^*+jets events	42 ± 17	18 ± 2

Table 4.18: The expected estimate for SR3ℓ_Low and SR3ℓ_ISR. All expectations include full systematics.

Full run-II	SR3ℓ_Low	SR3ℓ_ISR
Total exp. SM events	53 ± 3	19 ± 2
MC exp. Diboson events	51 ± 3	17 ± 2
MC exp. Higgs events	$0.00^{+0.00}_{-0.00}$	$0.01^{+0.01}_{-0.01}$
MC exp. Triboson events	0.71 ± 0.68	$0.33^{+0.41}_{-0.33}$
MC exp. Top other events	$0.05^{+0.08}_{-0.05}$	$0.41^{+0.63}_{-0.41}$
DD exp. Fakes events	1.4 ± 0.4	0.8 ± 0.2

4.11 Fakes Validation

The four SR definitions have now been defined for our analysis. In Figure 4.14 we validated our MC and data-driven fakes estimations for preselection regions. We must now validate our backgrounds in a region of parameter space closer to the SRs.

4.11.1 2ℓ Fakes Validation

In this section, we validate both light ($n_b = 0$) and heavy ($n_b \neq 0$) sources of fakes. To validate the two types of fakes present in our analysis, we define four regions close to SR2ℓ_Low and SR2ℓ_ISR. The VRs for SR2ℓ_Low are VR2ℓ_LF and VR2ℓ_HF, and the VRs for SR2ℓ_ISR are VR2ℓ_ISR-LF and VR2ℓ_ISR-HF. The only difference between light fakes' and heavy fakes' selections is the b-tag selection requirement.

In Table 4.19 we show the definitions for the two fakes VRs for the standard approach. We remove the m_{jj} selection, we remove the R_{P_T} selection and we remove the $\min\Delta\phi$ selection. The most significant modification with respect to the SR is the inversion of the $m_{\ell\ell}$ requirement. In Table 4.20 we show the definitions for the two fakes VRs for the ISR approach. For this approach we remove the M_J requirements, as well as p_T^{CM} and R_{ISR}. We then invert the M_Z requirement.

In Table 4.21, we show the yields for all four fakes VRs. Each row corresponds to a different background component which all sum up to the total estimated SM expectation. In this table, we confirm that the fakes comprise a high purity for each region. These fake VRs also show agreement between data and MC, though with MC trending larger than the observed number of events in these regions.

In Figures 4.20 – 4.23 we show that for leading and sub-leading lepton momentum, we have appropriate modelling in the fakes VRs. We note the trend of the number of observed events being lower than the SM expectation, but highlight the lack of a top or diboson normalisation estimate in these plots.

Table 4.19: The selection criteria for the standard fakes VRs. There is VR2ℓ-LF is the VR for light fakes, and VR2ℓ-HF is the VR for heavy fakes. The standard SR is quoted again for direct comparison and for ease of demonstrating orthogonality.

Region	Selection	N_{Jets}	N_b	p_T^ℓ	p_T^j	$m_{\ell\ell}$	m_{jj}	$H_{4,1}^{\mathrm{PP}}$	$H_{1,1}^{\mathrm{PP}}/H_{4,1}^{\mathrm{PP}}$	$\frac{p_{\mathrm{T\ PP}}^{\mathrm{lab}}}{p_{\mathrm{T\ PP}}^{\mathrm{lab}}+H_{\mathrm{T}\ 4,1}^{\mathrm{PP}}}$	$\min\Delta\phi(j_1/j_2, p_T^{\mathrm{miss}})$
SR2ℓ_Low	$\ell^\pm\ell^\mp$	$= 2$	0	> 25	> 30	$\in (80, 100)$	$\in (50, 110)$	> 400	$\in (0.35, 0.6)$	< 0.05	> 2.4
VR2ℓ-LF	$\ell^\pm\ell^\mp$	> 2	0	> 25	> 30	$\notin [80, 100]$	–	> 400	$\in (0.35, 0.6)$	–	–
VR2ℓ-HF	$\ell^\pm\ell^\mp$	> 2	1	> 25	> 30	$\notin [80, 100]$	–	> 400	$\in (0.35, 0.6)$	–	–

4.11.2 3ℓ Fakes Validation

Similarly to the 2ℓ fakes validation, we validate both light and heavy sources of fakes for both the standard region definitions and the ISR region definitions. To validate the

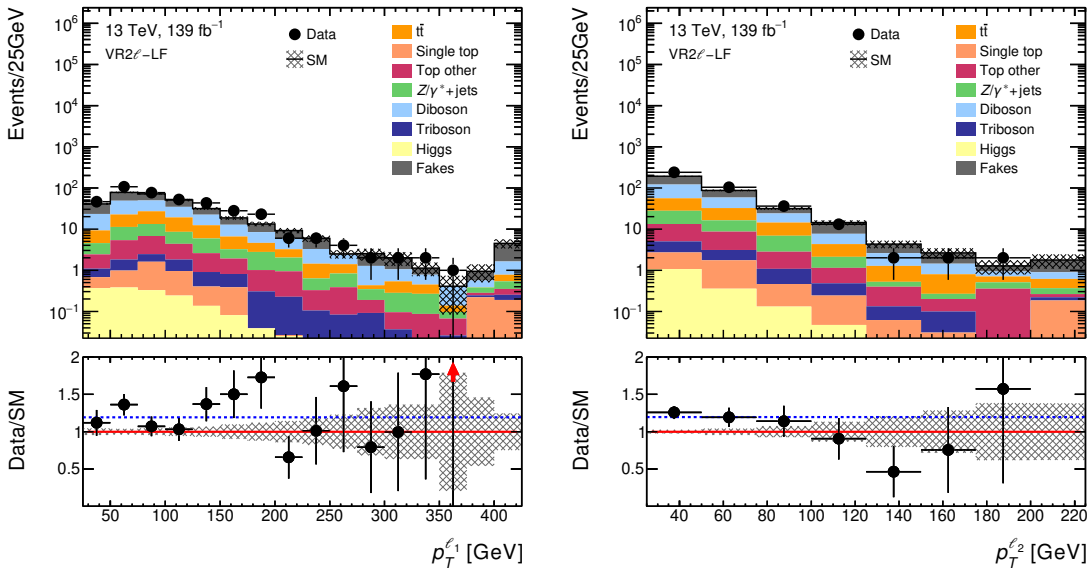

(a) Leading lepton (b) Sub-leading lepton

Figure 4.20: Validation of lepton momenta in VR2ℓ-LF. In (a) and (b) the lepton momentum is well modelled. There are no sources of systematic uncertainty included.

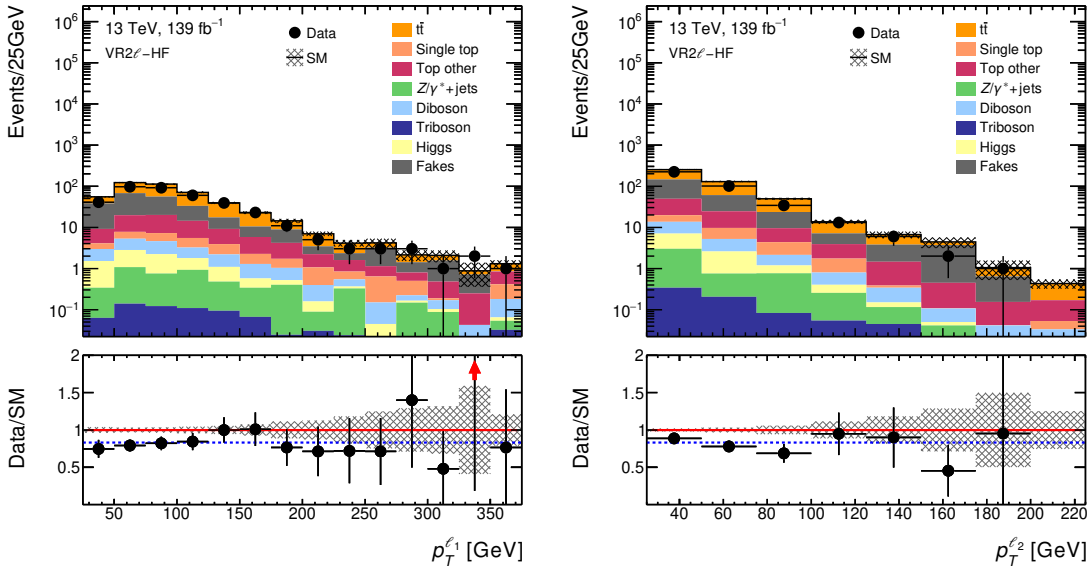

(a) Leading lepton (b) Sub-leading lepton

Figure 4.21: Validation of lepton momenta in VR2ℓ-LF. In (a) and (b) the lepton momentum is well modelled. Uncertainties are statistical only.

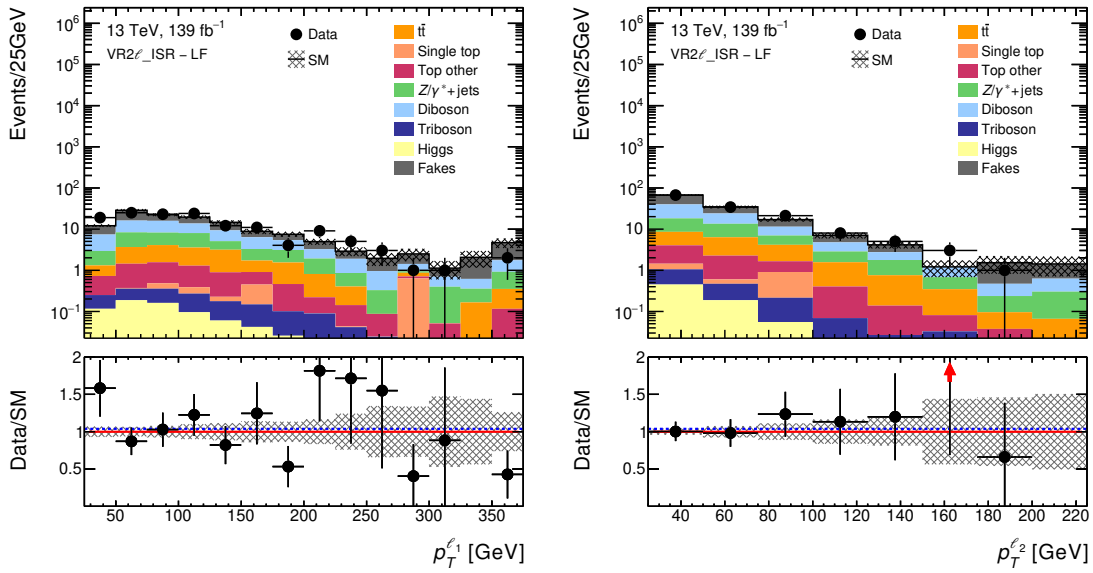

(a) Leading lepton (b) Sub-leading lepton

Figure 4.22: Validation of lepton momenta in VR2ℓ_ISR-LF. In (a) and (b) the lepton momentum is well modelled. Uncertainties are statistical only.

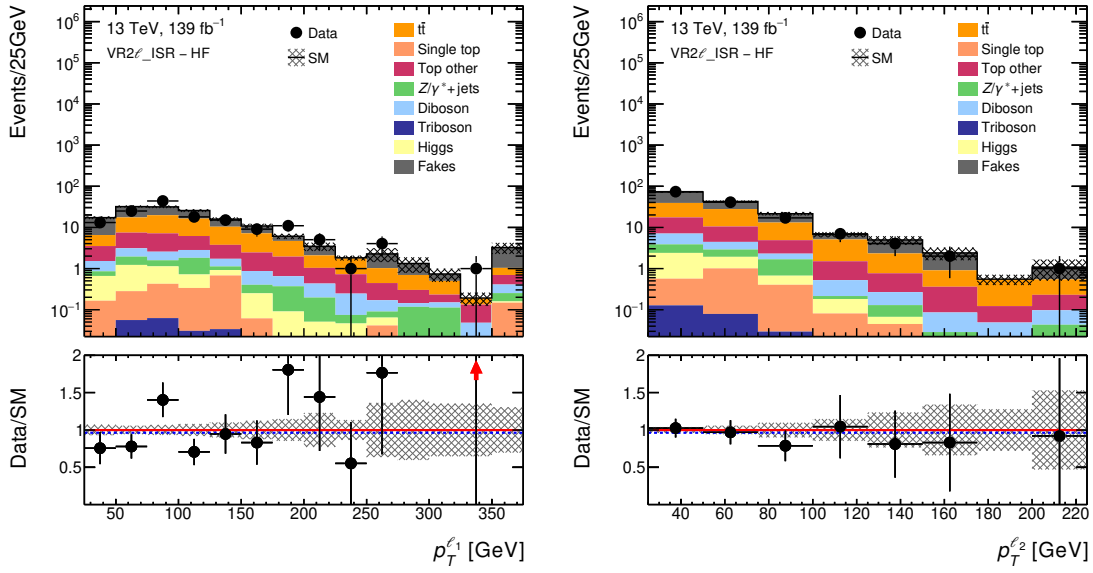

(a) Leading lepton (b) Sub-leading lepton

Figure 4.23: Validation of lepton momenta in VR2ℓ_ISR-HF. In (a) and (b) the lepton momentum is well modelled. Uncertainties are statistical only.

Table 4.20: The selection criteria for the ISR fakes VRs. There is VR2ℓ_ISR-LF is the VR for light fakes, and VR2ℓ_ISR-HF is the VR for heavy fakes. The ISR SR is quoted again for direct comparison and for ease of demonstrating orthogonality.

Region	Selection	N_{Jets}	N_{S}	N_{ISR}	N_b	p_T^ℓ	p_T^j	m_Z	M_J	P_T^{ISR}	P_T^{I}	P_T^{CM}	$\Delta\phi_{\text{ISR}}^{\text{I}}$	R_{ISR}
SR2ℓ_ISR	$\ell^\pm\ell^\mp$	$\in [3,4]$	≥ 1	$= 2$	$= 0$	> 25	> 30	$\in (80,100)$	$\in (50,110)$	> 180	> 100	< 20	> 2.8	$\in (0.4,0.75)$
VR2ℓ_ISR-LF	$\ell^\pm\ell^\mp$	> 2	2	> 1	0	> 25	> 30	$\notin [80,100]$	–	> 180	> 50	–	> 2	–
VR2ℓ_ISR-HF	$\ell^\pm\ell^\mp$	> 2	2	> 1	1	> 25	> 30	$\notin [80,100]$	–	> 180	> 50	–	> 2	–

Table 4.21: Fake validation region yields. Split into light flavour and heavy flavour for both the standard regions and ISR regions.

Full run-II	VR2ℓ-LF	VR2ℓ-HF	VR2ℓ_ISR-LF	VR2ℓ_ISR-HF
Observed events	398 ± 20	381 ± 20	139 ± 12	146 ± 12
MC exp. SM events	348 ± 7	467 ± 8	134 ± 5	151 ± 5
MC exp. Z/γ^*+jets events	28 ± 2	4.2 ± 0.7	23 ± 2	3.6 ± 0.6
MC exp. Top other events	16.9 ± 0.6	54 ± 1	5.5 ± 0.2	21.1 ± 0.7
MC exp. Higgs events	1.6 ± 0.2	6.0 ± 0.4	0.72 ± 0.04	3.2 ± 0.2
MC exp. Diboson events	119 ± 1	12.0 ± 0.3	39.9 ± 0.5	5.9 ± 0.2
MC exp. Triboson events	4.7 ± 0.2	0.74 ± 0.07	1.16 ± 0.08	0.31 ± 0.04
MC exp. Single top events	3.9 ± 0.9	14 ± 2	1.2 ± 0.6	1.8 ± 0.5
MC exp. $t\bar{t}$ events	57 ± 2	219 ± 3	13.2 ± 0.8	53 ± 2
DD exp. Fakes events	117 ± 6	156 ± 6	49 ± 4	62 ± 4

two types of fakes present in our analysis, we define four regions close to SR3ℓ_Low and SR3ℓ_ISR. The VRs for SR3ℓ_Low are VR3ℓ-LF and VR3ℓ-HF, and the VRs for SR3ℓ_ISR are VR3ℓ_ISR-LF and VR3ℓ_ISR-HF.

In Table 4.22, we show the definitions for the two standard fakes VRs. In Table 4.23, we show the definitions for the two ISR fakes VRs. The total background yields for these regions are shown in Table 4.24, and the modelling for each of these VRs can be found in Figures 4.24–4.27.

In the VR for light fakes, shown in Figure 4.24, we see a significant contribution from the diboson background. We found that it was challenging to separate the diboson events from the non-prompt fake events, and so we opted to find a region with the largest fake contribution that was similar to the SR selection criteria. In general, the modelling between expectation and observed number of events is good.

Shown in Figure 4.25, the heavy flavour fakes VR, we see high purity of non-prompt fakes, as well as good modelling for the leading and sub-leading lepton momenta.

In the two ISR fakes VRs we have a similar situation to the standard fakes VRs. The standard VRs have large amounts of diboson, but the ISR regions have large amounts of fakes. Both regions have good agreement between expectation and observed numbers of events.

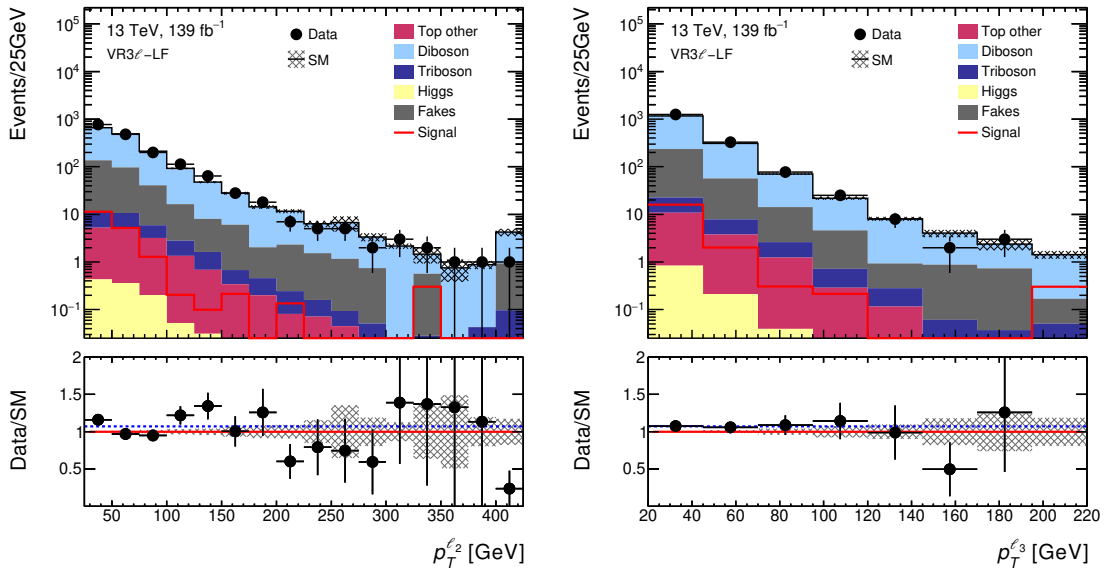

(a) Sub-leading lepton (b) Sub-sub-leading lepton

Figure 4.24: Validation of lepton momenta in VR3ℓ-LF. In (a) the sub-leading lepton momentum is well modelled. In (b) the sub-sub-leading lepton is well modelled.

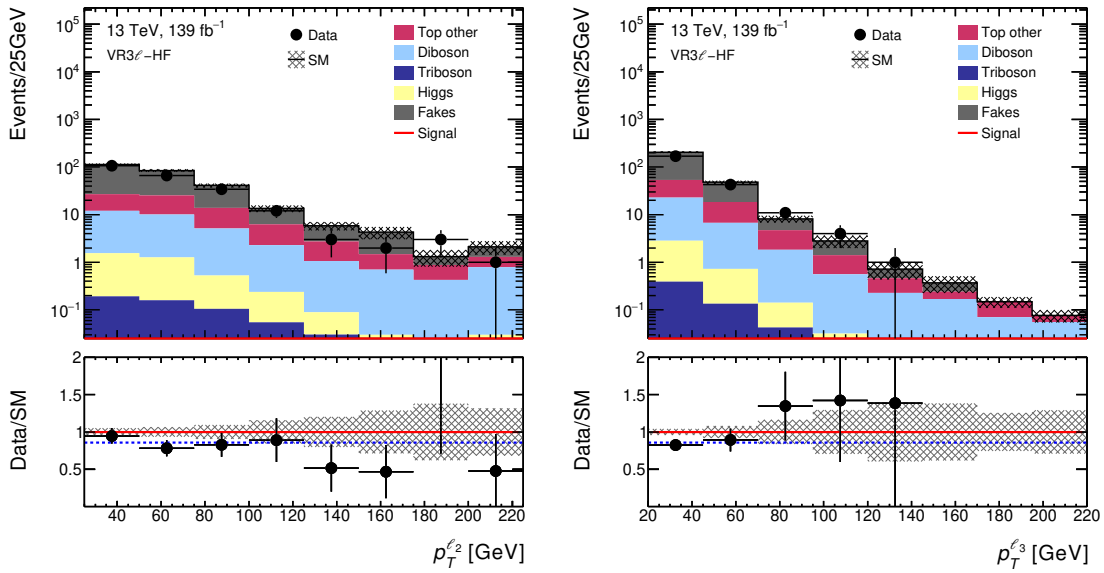

(a) Sub-leading lepton (b) Sub-sub-leading lepton

Figure 4.25: Validation of lepton momenta in VR3ℓ-HF. In (a) the sub-leading lepton momentum is well modelled. In (b) the sub-sub-leading lepton is well modelled.

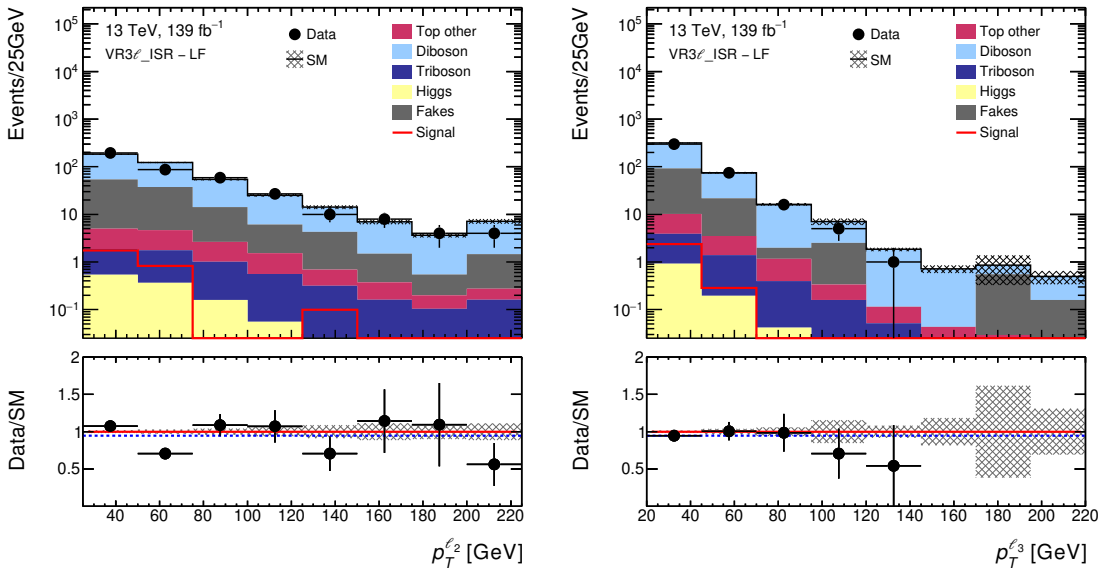

(a) Sub-leading lepton (b) Sub-sub-leading lepton

Figure 4.26: Validation of lepton momenta in VR3ℓ_ISR-LF. In (a) the sub-leading lepton momentum is well modelled. In (b) the sub-sub-leading lepton is well modelled.

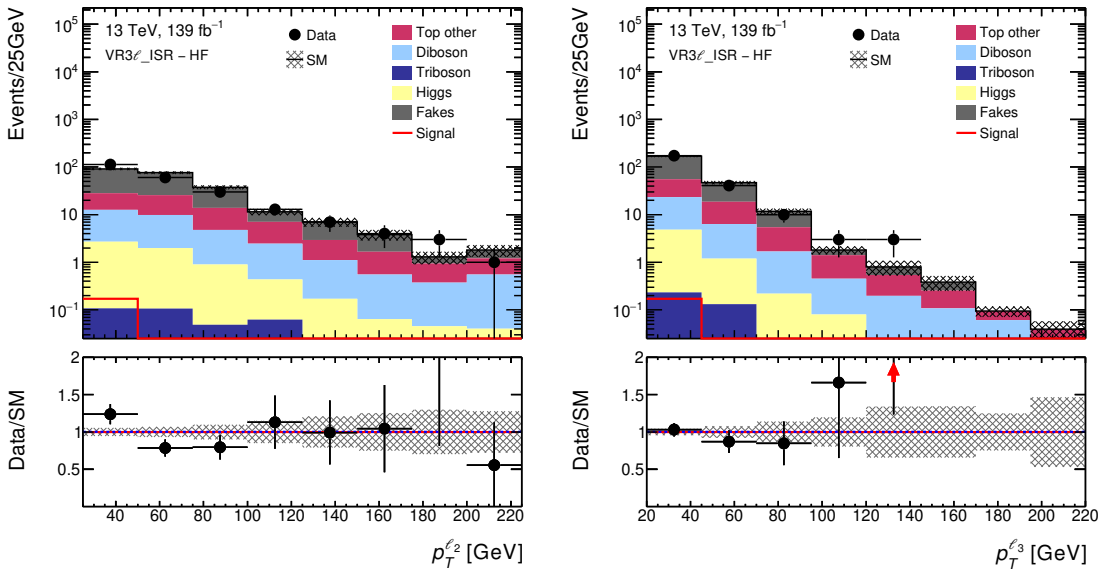

(a) Sub-leading lepton (b) Sub-sub-leading lepton

Figure 4.27: Validation of lepton momenta in VR3ℓ_ISR-HF. In (a) the sub-leading lepton momentum is well modelled. In (b) the sub-sub-leading lepton is well modelled.

Table 4.22: The selection criteria for the standard fake VRs. All selections are for OSSF leptons.

Selection	$m_{\ell\ell}$	$p_T^{\ell_i}$[GeV]	n_J^{20}	n_b	m_T^W	$H_{3,1}^{\mathrm{PP}}$
VR3ℓ-LF	$\notin [75, 105]$	$25, 25, 20$	$\in (0, 3)$	0	> 50	> 150
VR3ℓ-HF	$\notin [75, 105]$	$25, 25, 20$	$\in (1, 3)$	1	> 50	> 150

Table 4.23: The selection criteria for the ISR fakes VRs. All selections are for OSSF leptons.

Selection	$m_{\ell\ell}$	$p_T^{\ell_i}$[GeV]	n_J^{20}	n_b	$p_{T\mathrm{I}}^{\mathrm{CM}}$	$p_{T\mathrm{ISR}}^{\mathrm{CM}}$ [GeV]	$\Delta\phi_{\mathrm{ISR,I}}$	R_{ISR}
VR3ℓ_ISR_LF	$\notin [75, 105]$	$25, 25, 20$	$\in (0, 3)$	0	> 50	> 50	> 1.5	$\in (0, 1)$
VR3ℓ_ISR_HF	$\notin [75, 105]$	$25, 25, 20$	$\in (1, 3)$	1	–	> 100	> 1.5	$\in (0, 1)$

4.12 Background Estimation

To be confident in the background composition of the four SRs, we must control and validate each background component. We outline the MC generators used for the SRs in Table 4.1. In the case of SR2ℓ_Low and SR2ℓ_ISR the dominant backgrounds are Z/γ^*+jets, diboson and $t\bar{t}$. In the case of our 3ℓ SRs, the dominant background is diboson only. As has been stated before, the Z/γ^*+jets estimate in the two 2ℓ SRs is a data-driven estimate, which we validate against a separate MC driven approach. We now describe our control and validation approach for these major backgrounds.

In Figure 4.28, we show a schematic overview of the HistFitter analysis design strategy employed by this analysis [123]. On the x and y axis is a variable of choice describing some aspect of an event. We see we have three SRs defined in the schematic; SR1, SR2 and SR3. Each SR has different background compositions, and each background which contributes significantly requires a dedicated CR. A requirement of the CRs is to be close to the parameter space defined by the SR, and to have a high purity in a desired background component. Given these two are held, we define a *normalisation factor* for the given CR which is defined:

$$\beta^i = \frac{D_i^{\mathrm{est}}}{N_i^{\mathrm{MC}}} \tag{4.45}$$

where $D^{\mathrm{est}\ i} = D - \sum_j^{\mathrm{non}\ i} N_j^{\mathrm{MC}}$ is the number of events in data in the CR, $\sum_j N_j^{\mathrm{MC,non}\ i}$ is the summation of all background estimates which do not correspond to the controlled background (i). N_i^{MC} is the estimate of the controlled background using MC. A normalisation factor close to 1 is desirable, but deviations are acceptable if the origin is understood. Validation regions have the normalisation factors, β^i, applied to each background i. If the modelling is good in the VRs, then we will apply the normalisation factors to the SRs.

Table 4.24: The three-lepton fakes VRs for both standard and ISR regions. The uncertainties include statistics only.

Full run-II	VR3ℓ-LF	VR3ℓ-HF	VR3ℓ_ISR_LF	VR3ℓ_ISR_HF
Observed events	1697	228	395	231
Total exp. SM events	1680 ± 17	268 ± 13	440 ± 7	233 ± 12
MC exp. Diboson events	1371 ± 10	31 ± 1	321 ± 4	28 ± 1
MC exp. Triboson events	13.2 ± 0.5	0.45 ± 0.02	3.8 ± 0.2	0.26 ± 0.01
MC exp. Top other events	15 ± 1	47 ± 2	9.5 ± 0.4	50 ± 3
DD exp. Fakes events	279 ± 11	187 ± 10	104 ± 4	149 ± 8

4.12.1 2ℓ Control Region Definitions

To control the diboson and $t\bar{t}$ background compositions in SR2ℓ_Low and SR2ℓ_ISR, we require four separate regions. These regions are labelled CR2ℓ-VV, CR2ℓ_ISR-VV, CR2ℓ-Top and CR2ℓ_ISR-Top. We will outline our diboson approach and then our top approach.

The diboson approach is defined by the difficulty of isolating Z/γ^*+jets and diboson backgrounds. The reason for the difficulty arises from the fact that both backgrounds have the same final state. The decay pathway for Z/γ^*+jets is $Z/\gamma^* + jj \rightarrow (\ell\ell)jj$ and for diboson we have $Z(W) \rightarrow \ell\ell(jj)$. We get around the Z/γ^*+jets contamination by look at three, and four, lepton events instead of two. Typically in order to study the diboson modelling, we look at the decay pathway $Z(W) \rightarrow \ell\ell(jj)$, which is typical of the topology we are looking for in our signal. Instead, we look at different diboson topologies, specifically $ZZ \rightarrow \ell\ell(\ell\ell)$ or $WZ \rightarrow \ell\nu\ell\ell$.

We are only able to use the two-lepton RJR decay tree once we have a consistent interpretation for three and four lepton events. Our approach is to find the OSSF lepton pair closest to the Z mass, and for the two-lepton decay tree, we treat these as the two leptons. We take the third and fourth lepton, and we assign them to the invisible system, which is equivalent to adding the four-vector(s) of the extra leptons to $\vec{E}_T^{\text{miss}}$. Once this approach is applied, we calculate all RJR quantities in the same fashion as always.

Table 4.25: Preselection criteria for the standard decay tree 2ℓ SR and the associated CRs and VRs. The variables are defined in the text.

Region	n_{leptons}	n_{jets}	$n_{b\text{-tag}}$	$p_T^{\ell_1,\ell_2}$ [GeV]	$p_T^{j_1,j_2}$ [GeV]	$m_{\ell\ell}$ [GeV]	m_{jj} [GeV]	m_{T}^W [GeV]
CR2ℓ-VV	$\in [3,4]$	≥ 2	=0	> 25	> 30	$\in (80,100)$	> 20	$\in (70,100)$ if $n_{\text{leptons}} = 3$
CR2ℓ-Top	$= 2$	≥ 2	=1	> 25	> 30	$\in (20,80)$ or > 100	$\in (40,250)$	– –
VR2ℓ-VV	$= 2$	≥ 2	=0	> 25	> 30	$\in (80,100)$	$\in (40,70)$ or $\in (90,500)$	– –
VR2ℓ-Top	$= 2$	≥ 2	=1	> 25	> 30	$\in (80,100)$	$\in (40,250)$	–
SR2ℓ_Low	$= 2$	$= 2$	$= 0$	> 25	> 30	$\in (80,100)$	$\in (70,90)$	–

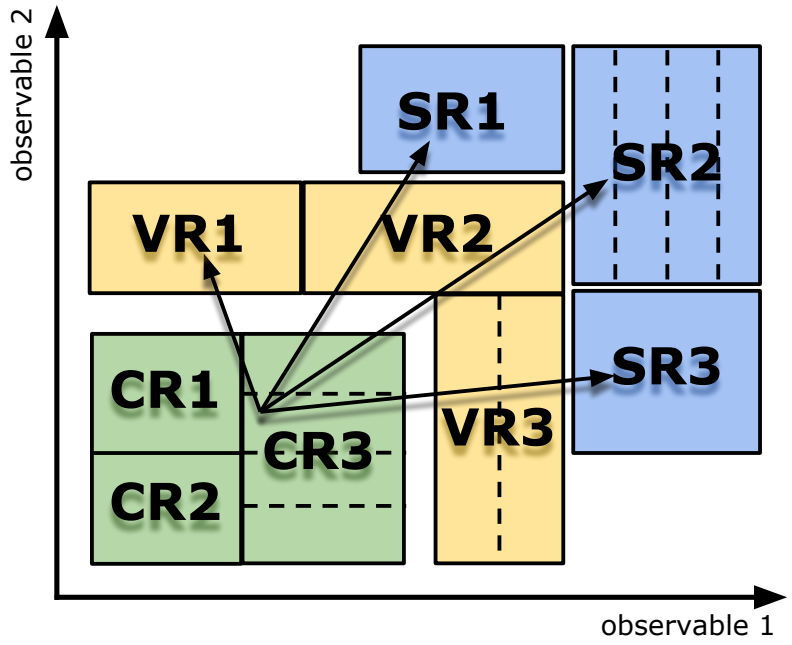

Figure 4.28: A schematic view of an analysis strategy with multiple CR, VR and SRs. All regions can have single- or multiple bins, as illustrated by the dashed lines. The extrapolation from the CR to the SRs is verified in the VRs [123].

Table 4.26: Selection criteria for the standard decay tree 2ℓ SR and the associated CRs and VRs. The variables are defined in the text

Region	$H_{4,1}^{\mathrm{PP}}$ [GeV]	$H_{1,1}^{\mathrm{PP}}$ [GeV]	$\frac{p_{\mathrm{T\,PP}}^{\mathrm{lab}}}{p_{\mathrm{T\,PP}}^{\mathrm{lab}}+H_{\mathrm{T\,4,1}}^{\mathrm{PP}}}$	$\frac{\min(H_{1,1}^{\mathrm{Pa}},H_{1,1}^{\mathrm{Pb}})}{\min(H_{2,1}^{\mathrm{Pa}},H_{2,1}^{\mathrm{Pb}})}$	$\frac{H_{1,1}^{\mathrm{PP}}}{H_{4,1}^{\mathrm{PP}}}$	$\Delta\phi_{\mathrm{V}}^{\mathrm{P}}$	$\min\Delta\phi(j_1/j_2,\vec{P}_{\mathrm{T}}^{\mathrm{miss}})$
CR2ℓ-VV	> 200	–	< 0.05	> 0.2	–	$\in (0.3, 2.8)$	–
CR2ℓ-Top	> 400	–	< 0.05	> 0.5	–	$\in (0.3, 2.8)$	–
VR2ℓ-VV	> 400	> 250	< 0.05	$\in (0.4, 0.8)$	–	$\in (0.3, 2.8)$	–
VR2ℓ-Top	> 400	–	< 0.05	> 0.5	–	$\in (0.3, 2.8)$	–
SR2ℓ_Low	> 400	–	< 0.05	–	$\in (0.35, 0.60)$	–	> 2.4

Table 4.27: Preselection criteria for the ISR-decay-tree 2ℓ SR and the associated CRs and VRs. The variables are defined in the text.

Region	n_{leptons}	$N_{\mathrm{jet}}^{\mathrm{ISR}}$	$N_{\mathrm{jet}}^{\mathrm{S}}$	n_{jets}	$n_{b\text{-tag}}$	$p_T^{\ell_1,\ell_2}$ [GeV]	$p_T^{j_1,j_2}$ [GeV]
CR2ℓ_ISR-VV	$\in [3, 4]$	≥ 1	≥ 2	> 2	$= 0$	> 25	> 30
CR2ℓ_ISR-Top	$= 2$	≥ 1	$= 2$	$\in [3, 4]$	$= 1$	> 25	> 30
VR2ℓ_ISR-VV	$\in [3, 4]$	≥ 1	≥ 2	≥ 3	$= 0$	> 25	> 20
VR2ℓ_ISR-Top	$= 2$	≥ 1	$= 2$	$\in [3, 4]$	$= 1$	> 25	> 30
SR2ℓ_ISR	$= 2$	≥ 1	$= 2$	$\in [3, 4]$	$= 0$	> 25	> 30

The standard diboson CR requires either three or four leptons and at least two jets. We shift the m_{jj} selection from $m_{jj} \in (70, 90)$ GeV to $m_{jj} > 20$ GeV and if the number of leptons is three, then we require $m_T^W \in (70, 100)$. We loosen $H_{4,1}^{\mathrm{PP}}$ from $H_{4,1}^{\mathrm{PP}} > 400$ GeV to $H_{4,1}^{\mathrm{PP}} > 200$ GeV. We then apply two selection criteria which the SR does not apply, these are $\min(H_{1,1}^{\mathrm{Pa}}, H_{1,1}^{\mathrm{Pb}})/\min(H_{2,1}^{\mathrm{Pa}}, H_{2,1}^{\mathrm{Pb}}) > 0.2$ and $\Delta\phi_V^P \in (0.3, 2.8)$. These are all selections which define the standard diboson CR. The lepton multiplicity is the selection

Table 4.28: Selection criteria for the ISR-decay-tree 2ℓ SR and the associated CRs and VRs. The variables are defined in the text.

Region	m_Z [GeV]	m_J [GeV]	$\Delta\phi^{\mathrm{CM}}_{\mathrm{ISR,I}}$	R_{ISR}	$p^{\mathrm{CM}}_{\mathrm{T\,ISR}}$ [GeV]	$p^{\mathrm{CM}}_{\mathrm{T\,I}}$ [GeV]	$p^{\mathrm{CM}}_{\mathrm{T}}$ [GeV]
CR2ℓ_ISR-VV	$\in (80, 100)$	> 20	> 2.0	$\in (0.0, 0.5)$	> 50	> 50	< 30
CR2ℓ_ISR-Top	$\in (50, 200)$	$\in (50, 200)$	> 2.8	$\in (0.4, 0.75)$	> 180	> 100	< 20
VR2ℓ_ISR-VV	$\in (20, 80)$ or > 100	> 20	> 2.0	$\in (0.0, 1.0)$	> 70	> 70	< 30
VR2ℓ_ISR-Top	$\in (50, 200)$	$\in (50, 200)$	> 2.8	$\in (0.4, 0.75)$	> 180	> 100	> 20
SR2ℓ_ISR	$\in (80, 100)$	$\in (50, 110)$	> 2.8	$\in (0.4, 0.75)$	> 180	> 100	< 20

which imposes orthogonality between the CR and the SR. The leading and sub-leading lepton transverse momenta are shown in Figure 4.29. We see the lepton momenta are both well modelled.

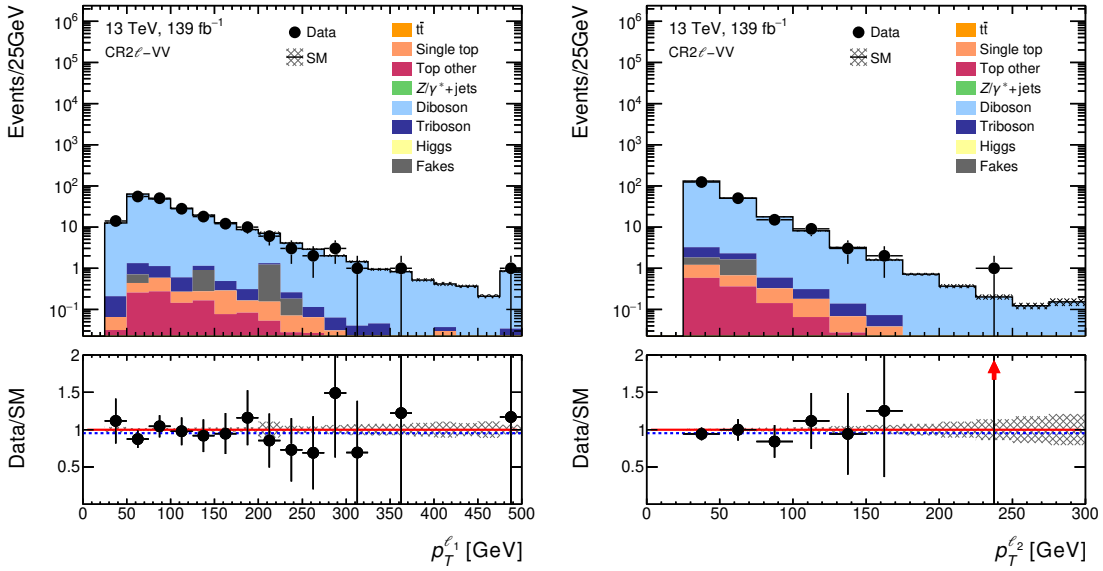

(a) Leading lepton (b) Sub-leading lepton

Figure 4.29: Validation of lepton momenta in CR2ℓ-VV. In (a) the leading lepton momentum is well modelled. In (b) the sub-leading lepton is well modelled.

The standard top CR requires exactly two leptons and at least two jets. Unlike the SR which vetos b-tagged jets, the CR requires a single b-tagged jet. We loosen the m_{jj} requirement to $m_{jj} \in (40, 250)$. We keep $H^{\mathrm{PP}}_{4,1} > 400$ GeV and we apply similar selection criteria to the CR, $\min(H^{\mathrm{Pa}}_{1,1}, H^{\mathrm{Pb}}_{1,1})/\min(H^{\mathrm{Pa}}_{2,1}, H^{\mathrm{Pb}}_{2,1}) > 0.5$ and $\Delta\phi^{P}_{V} \in (0.3, 2.8)$. Both standard diboson and top CRs are summarised in Table 4.25 and Table 4.26. The leading and sub-leading lepton transverse momenta are shown in Figure 4.30, and we see the expectations and observed number of events for the lepton momentum are in agreement.

The ISR diboson CR requires three or four leptons with at least three jets. We require at least one of the three jets to be assigned to the ISR system ($N_{\mathrm{ISR}} \geq 1$) and at least two

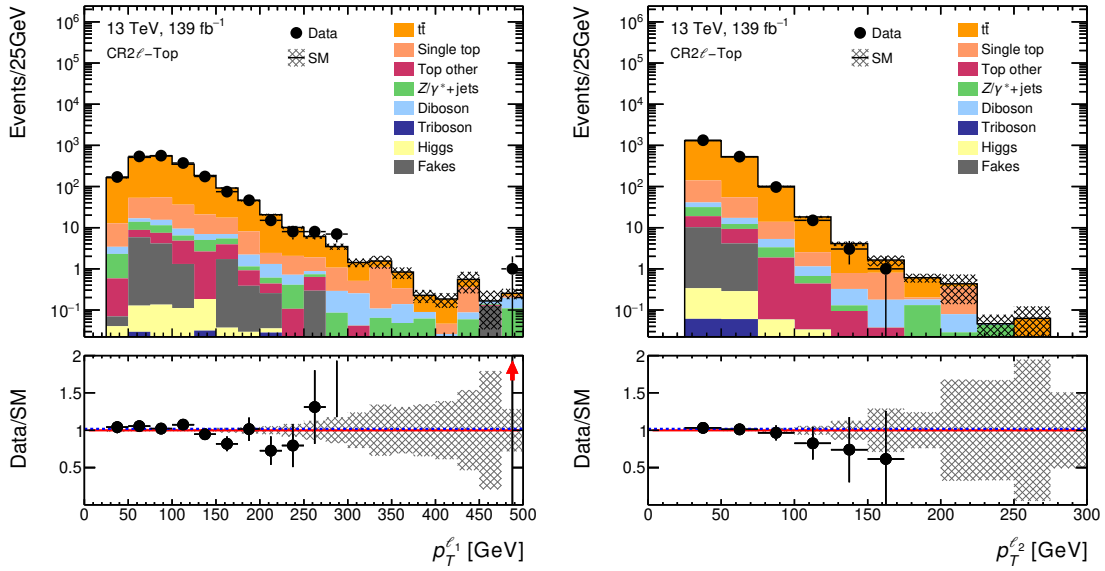

(a) Leading lepton (b) Sub-leading lepton

Figure 4.30: Validation of lepton momenta in CR2ℓ-Top. In (a) the leading lepton momentum and in (b) the sub-leading lepton.

jets to be assigned to the sparticle system($N_{\mathrm{S}} \geq 2$). We keep the m_Z requirement and we shift the m_J requirement to $m_J > 20$ GeV. The angle between the ISR system and the invisible system in the CM frame is loosened to $\Delta\phi^{\mathrm{CM}}_{\mathrm{ISR,I}} > 2.0$ We shift R_{ISR} from $R_{\mathrm{ISR}} \in (0.4, 0.75)$ to $R_{\mathrm{ISR}} \in (0.0, 0.5)$. We reduce the minimum momentum of the ISR system from $p^{\mathrm{CM}}_{T,\mathrm{ISR}} > 100$ GeV to $p^{\mathrm{CM}}_{T,\mathrm{ISR}} > 50$ GeV. We reduce the minimum momentum of the CM system from $p^{\mathrm{CM}}_{T,\mathrm{I}} > 100$ GeV to $p^{\mathrm{CM}}_{T,\mathrm{I}} > 50$ GeV. We loosen the requirement on well constructed topological trees by shifting $p^{\mathrm{CM}}_T < 20$ GeV to $p^{\mathrm{CM}}_T < 30$ GeV. The leading and sub-leading lepton transverse momenta are shown in Figure 4.31, again, we see the lepton's momenta SM predictions agree well with the observed number of events for each bin.

The ISR top CR requires exactly two leptons, with either three or four jets. We require two or three jets to be assigned to the ISR system ($N^{\mathrm{ISR}}_{jet} \in [1, 2]$) and exactly two jets to be assigned to the sparticle system ($N^{\mathrm{S}}_{jet} = 2$). We require a single b-tagged jet. We loosen the M_Z requirement to $M_Z \in (50, 200)$ and loosen the M_J requirement to $M_J \in (50, 200)$. We keep all other selections fixed. Both ISR diboson and top CRs are summarised in Table 4.27 and Table 4.28. The leading and sub-leading lepton transverse momenta are shown in Figure 4.32.

Further modelling for all CRs is shown in Figures 4.37–4.40, here we show modelling of variables with which we defined SRs and CRs. In general we see good modelling for all regions. The plots for the modelling of variables do not incldue the systematic sources of uncertainty, which are detailed in Table 4.42.

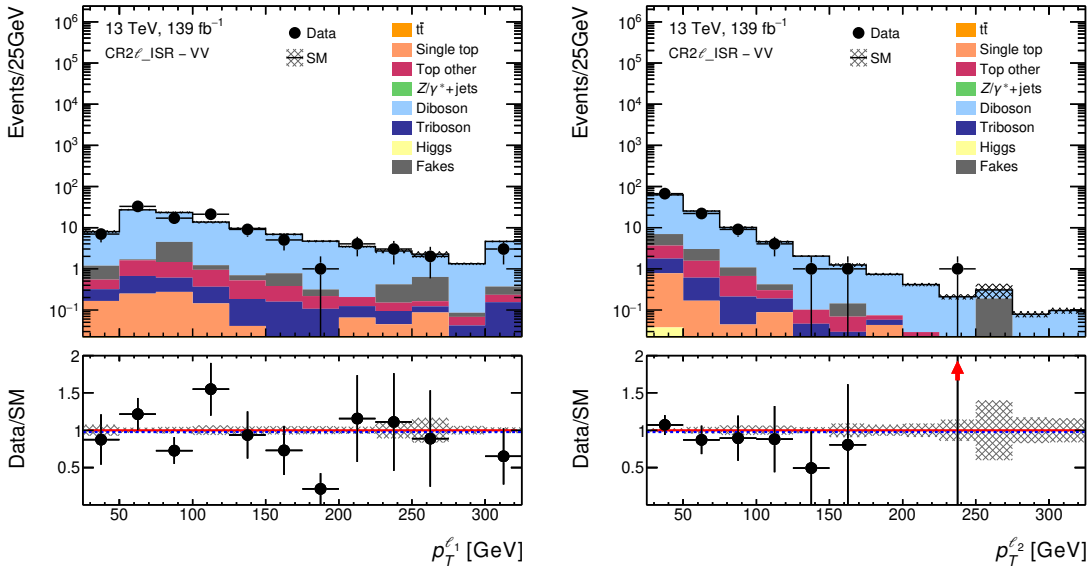

(a) Leading lepton (b) Sub-leading lepton

Figure 4.31: Validation of lepton momenta in CR2ℓ_ISR-VV. In (a) we show the leading lepton momentum and in (b) the sub-leading lepton momentum is shown.

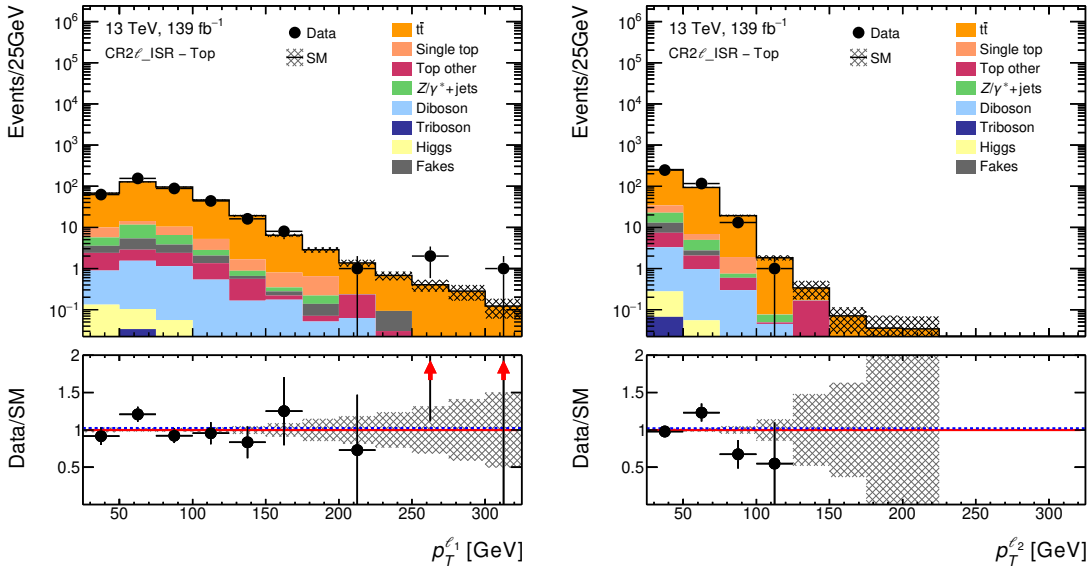

(a) Leading lepton (b) Sub-leading lepton

Figure 4.32: Validation of lepton momenta in CR2ℓ_ISR-Top. In (a) the leading lepton momentum is well modelled. In (b) the sub-leading lepton is well modelled.

2ℓ Validation Region Definitions

To validate SR2ℓ_Low and SR2ℓ_ISR, we define four VRs, labelled VR2ℓ-VV, VR2ℓ_ISR-VV, VR2ℓ-Top, and VR2ℓ_ISR-Top. Once we apply the normalisation factors, we look at

the agreement in yield of the full run-II data set versus our background estimations. We also confirm that the shape of variables is acceptable.

We first define the VRs. The standard diboson VR, VR2ℓ-VV, requires exactly two leptons with an invariant mass being roughly equal to the Z boson's mass, $m_{\ell\ell} \in (80, 100)$ GeV. We require two or more jets with an invariant mass in the range $m_{jj} \in (40, 70) \cup (90, 500)$ GeV. We keep $H_{4,1}^{\mathrm{PP}}$ and $p_{T,\mathrm{PP}}^{\mathrm{lab}}/(p_{T,\mathrm{PP}}^{\mathrm{lab}} + H_{T\,4,1}^{\mathrm{PP}})$ identical to SR2ℓ_Low, and remove $H_{1,1}^{\mathrm{PP}}/H_{4,1}^{\mathrm{PP}}$ as well as $\min \Delta\phi(j_{1(2)}, p_T^{\mathrm{miss}})$. Unlike the SR we require the selection $H_{1,1}^{\mathrm{PP}} > 250$ GeV, $\min(H_{1,1}^{\mathrm{P_{a(b)}}})/\min(H_{2,1}^{\mathrm{P_{a(b)}}}) \in (0.4, 0.8)$ and $\Delta\phi_V^P \in (0.3, 2.8)$. The leading and sub-leading lepton transverse momenta are shown in Figure 4.33.

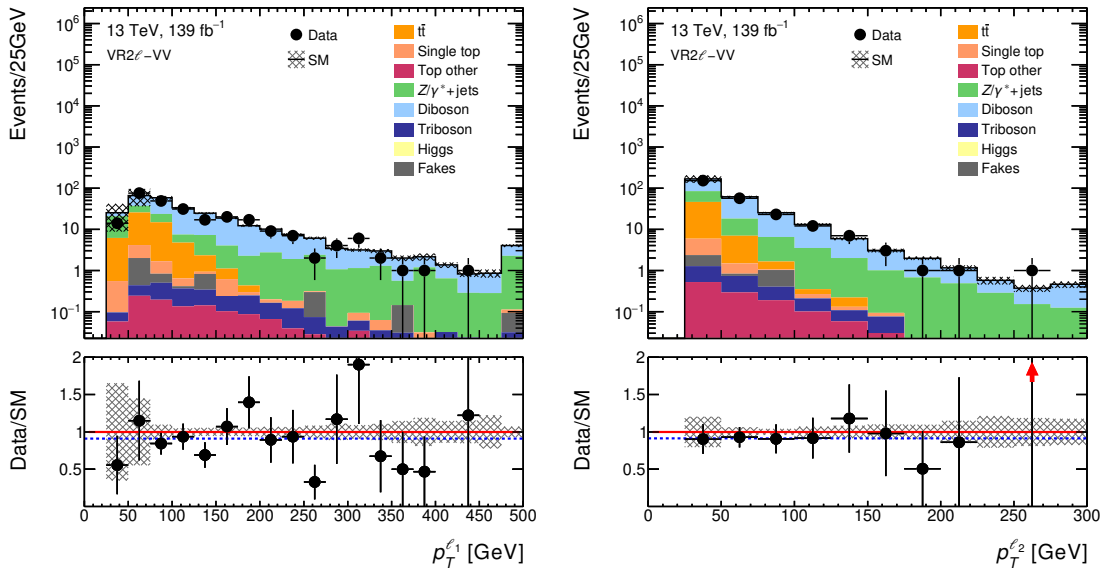

(a) Leading lepton (b) Sub-leading lepton

Figure 4.33: Validation of lepton momenta in VR2ℓ-VV. In (a) the leading lepton momentum is well modelled. In (b) the sub-leading lepton is well modelled.

The standard top VR, VR2ℓ-Top, requires exactly two leptons with invariant mass away from the Z boson's mass, $m_{\ell\ell} \in (20, 80) \cup (100, \infty)$ GeV. We require at least two jets with an invariant mass $m_{jj} \in (40, 250)$ GeV. We require at least one of the jets to be b-tagged. Similarly to VR2ℓ-VV we remove $H_{1,1}^{\mathrm{PP}}/H_{4,1}^{\mathrm{PP}}$ as well as $\min \Delta\phi(j_i, p_T^{\mathrm{miss}})$, we also apply $\min(H_{1,1}^{\mathrm{Pa}}, H_{1,1}^{\mathrm{Pb}})/\min(H_{2,1}^{\mathrm{Pa}}, H_{2,1}^{\mathrm{Pb}}) > 0.5$ and $\Delta\phi_V^P \in (0.3, 2.8)$. The leading and sub-leading lepton transverse momenta are shown in Figure 4.34.

The ISR diboson VR, VR2ℓ_ISR-VV, requires either three or four leptons. We require at least three jets with at least one being assigned to the ISR system and at least two assigned to the sparticle system. We require $M_Z \in (20, 80) \cup (100, \infty)$ GeV and $M_J > 20$ GeV. We loosen $\Delta\phi_{\mathrm{ISR,I}}^{\mathrm{CM}}$ to $\Delta\phi_{\mathrm{ISR,I}}^{\mathrm{CM}} > 2.0$. We loosen R_{ISR} to all kinematically allowable values $R_{\mathrm{ISR}} \in (0, 1)$. We loosen $p_{T,\mathrm{ISR}}^{\mathrm{CM}}$, $p_{T,\mathrm{I}}^{\mathrm{CM}}$ and p_T^{CM} to $p_{T,\mathrm{ISR}}^{\mathrm{CM}} > 70$ GeV, $p_{T,\mathrm{I}}^{\mathrm{CM}} > 70$ GeV and $p_T^{\mathrm{CM}} < 30$ GeV. The leading and sub-leading lepton transverse momenta are shown in Figure 4.35.

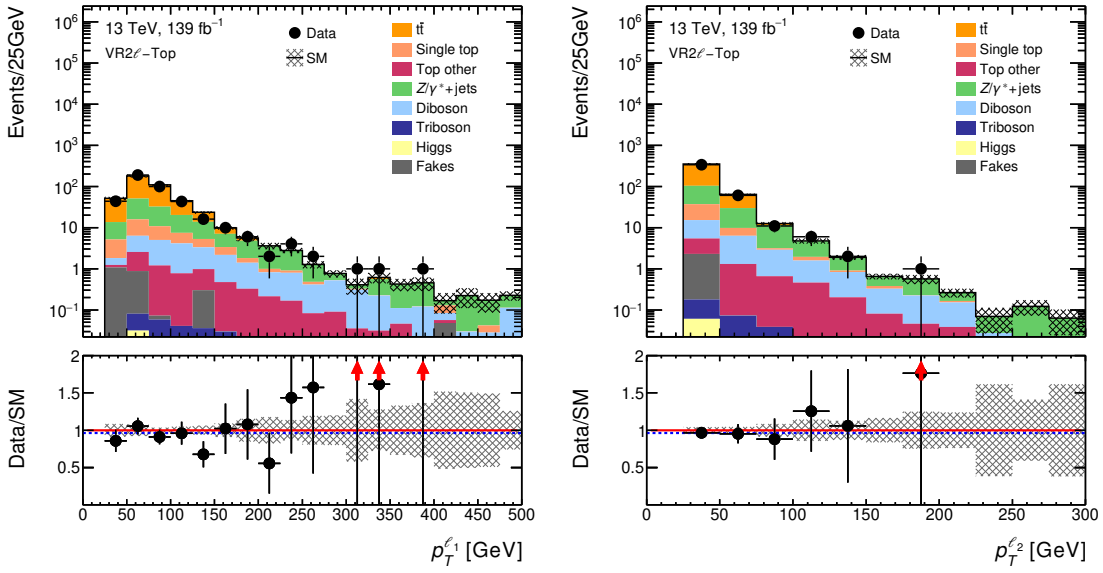

(a) Leading lepton (b) Sub-leading lepton

Figure 4.34: Validation of lepton momenta in VR2ℓ-Top. In (a) we show the leading lepton momentum. In (b) the sub-leading lepton is shown.

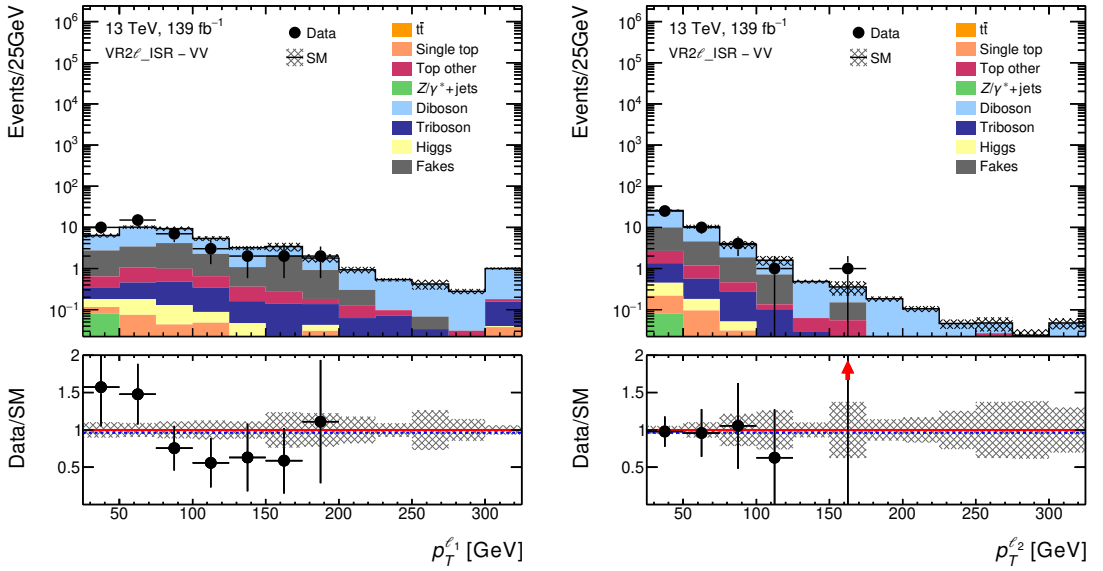

(a) Leading lepton (b) Sub-leading lepton

Figure 4.35: Validation of lepton momenta in VR2ℓ_ISR-VV. In (a), we show the leading lepton momentum and in (b) the sub-leading lepton is shown.

The ISR top VR, VR2ℓ_ISR-Top, requires exactly two leptons with either three or four jets; of those jets we require at least one assigned to the ISR system and exactly two in the sparticle system with at least one b-tagged jet. We require $M_Z \in (50, 200)$ GeV, $M_J \in (50, 200)$ GeV and we keep $\Delta\phi^{\mathrm{CM}}_{\mathrm{ISR,I}}$, R_{ISR}, $p^{\mathrm{CM}}_{T,\mathrm{ISR}}$ and $p^{\mathrm{CM}}_{T,\mathrm{I}}$ identical to SR2ℓ_ISR.

We invert p_T^{CM} from $p_T^{\mathrm{CM}} < 20$ GeV to $p_T^{\mathrm{CM}} > 20$ GeV. The leading and sub-leading lepton transverse momenta are shown in Figure 4.36.

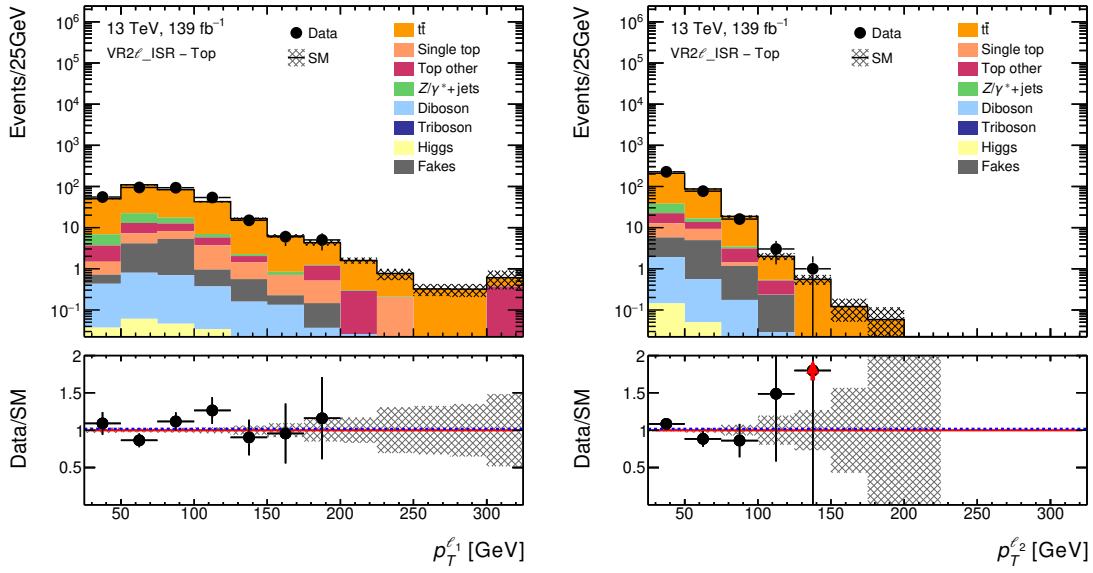

(a) Leading lepton (b) Sub-leading lepton

Figure 4.36: Validation of lepton momenta in VR2ℓ_ISR-Top. In (a) the leading lepton momentum is well modelled. In (b) the sub-leading lepton is well modelled.

The region breakdowns for all eight CRs and VRs are summarised in Table 4.29 and Table 4.30. We see that for each of the four CRs, the purity in the primary background is very high. We see that the full run-II dataset and the MC are in good agreement with Data/MC. This shows us that these variables are modelled both in the expected number of events and the shapes. The modelling of the four CRs is shown in Figures 4.37 to Figure 4.40.

Table 4.29 and Table 4.30, demonstrate that the application of the normalisation factors in the VRs produces good agreement between the observed events and the background estimations. Furthermore, we see that the VR modelling is excellent — even before the application of the normalisation factors, as shown in Figure 4.41–4.44.

4.12.2 3ℓ Control and Validation Region Definitions

In Section 4.10 and 4.10, we have defined the 3ℓ standard and ISR SR, and we have determined the SM expectations for the regions. To control and validate the background composition of the 3ℓ SRs, we will use an identical approach to the 2ℓ section of the analysis. Unlike the 2ℓ SRs which are dominated by diboson, $t\bar{t}$, and Z/γ^*+jets; the 3ℓ SRs are only dominated by diboson background contributions. The number of SM processes which produce three-lepton multiplicities is much less than two-lepton final states, and therefore we find a very diboson pure selection. Given the purity of the background contributions, we will only have diboson CRs, these will be called CR3ℓ-VV and

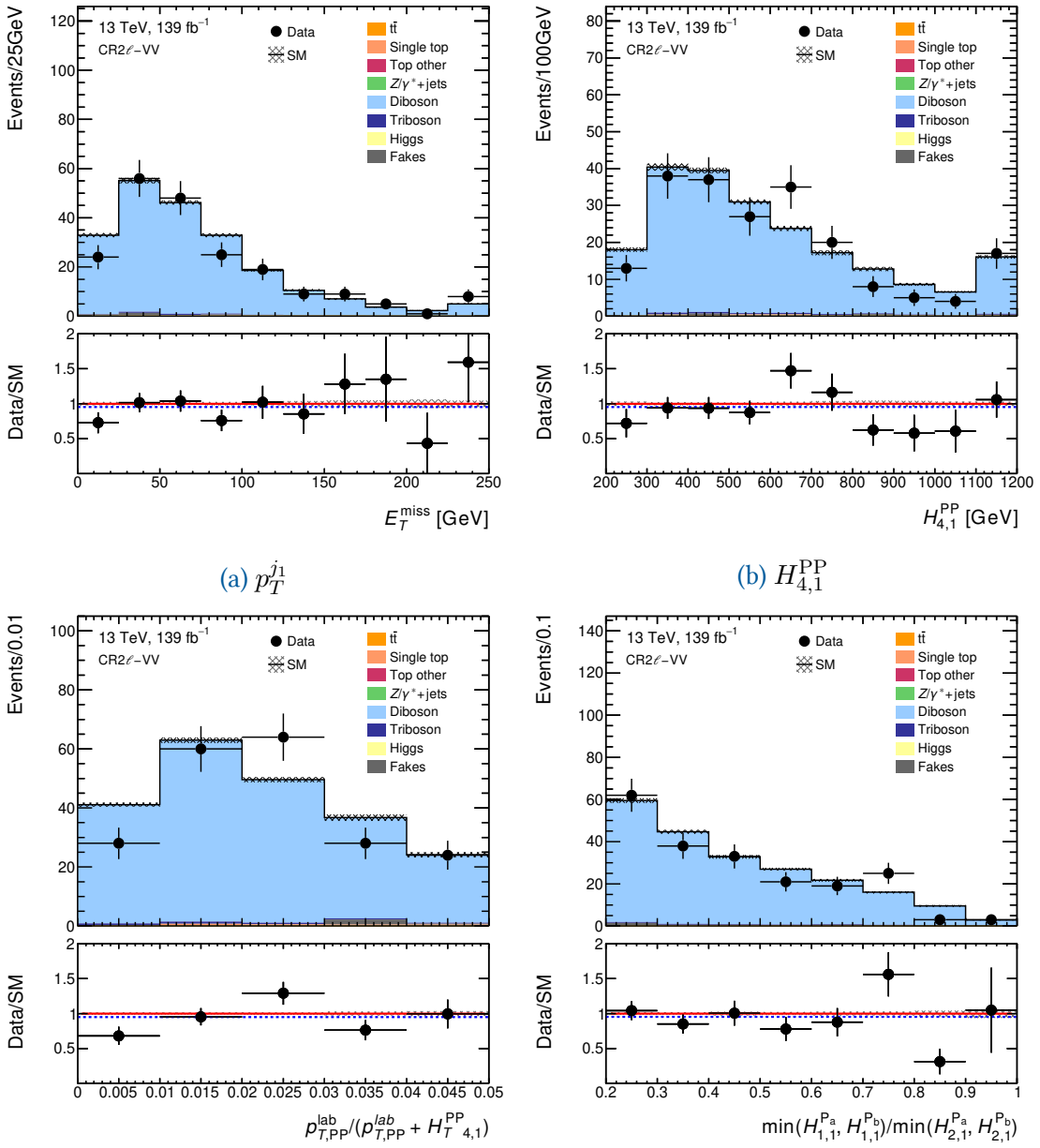

(a) $p_T^{j_1}$ (b) $H_{4,1}^{\mathrm{PP}}$

(c) R_{pT} (d) $\min(H_{1,1}^{\mathrm{Pa}}, H_{1,1}^{\mathrm{Pb}})/\min(H_{2,1}^{\mathrm{Pa}}, H_{2,1}^{\mathrm{Pb}})$

Figure 4.37: CR2ℓ-VV: Modelling for $p_T^{j_1}$ in (a). We show $H_{4,1}^{\mathrm{PP}}$ in (b). In (c) we show R_{pT}. In (d) we show $\min(H_{1,1}^{\mathrm{Pa}}, H_{1,1}^{\mathrm{Pb}})/\min(H_{2,1}^{\mathrm{Pa}}, H_{2,1}^{\mathrm{Pb}})$.

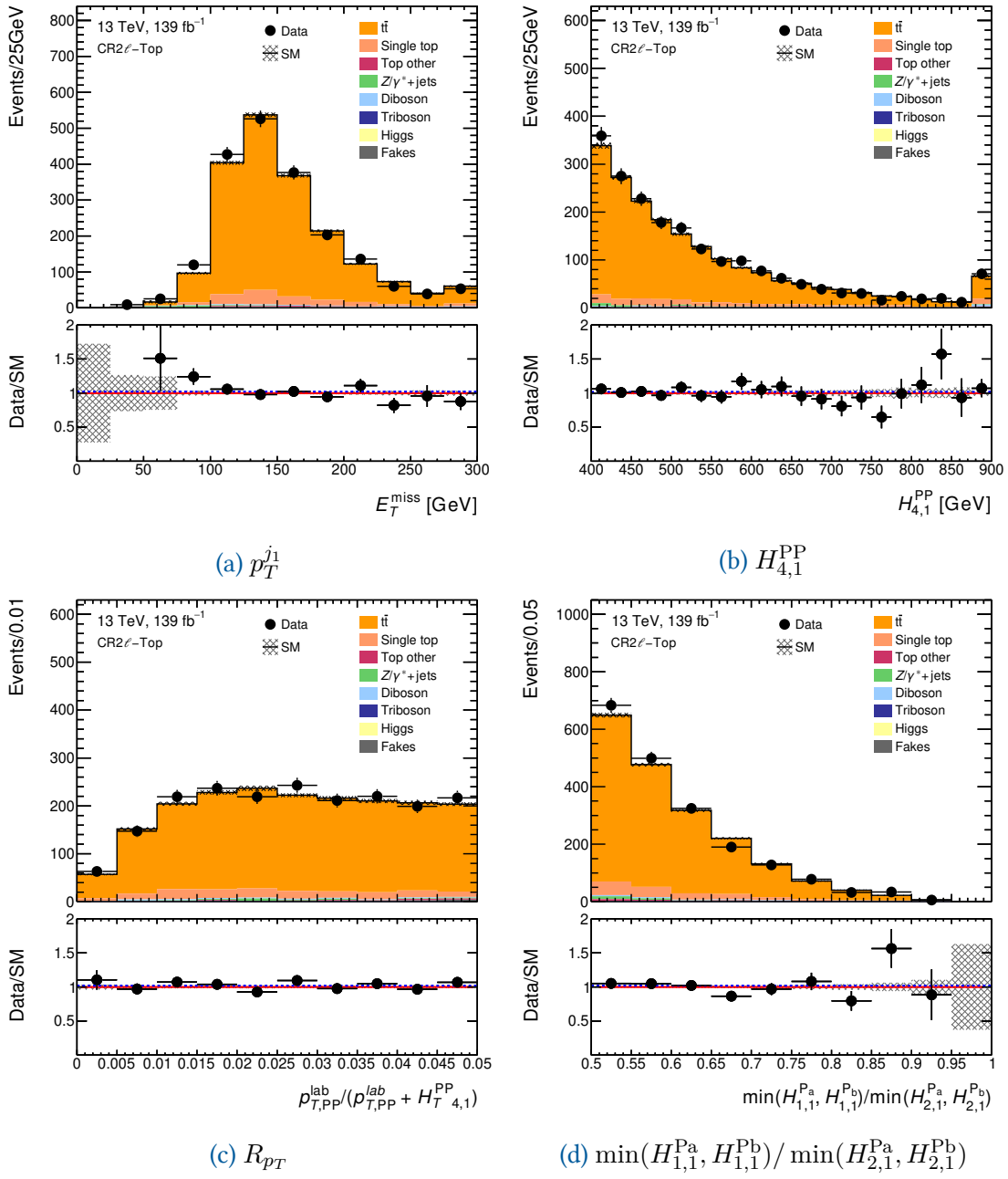

(a) $p_T^{j_1}$ (b) $H_{4,1}^{\mathrm{PP}}$

(c) R_{p_T} (d) $\min(H_{1,1}^{\mathrm{Pa}}, H_{1,1}^{\mathrm{Pb}})/\min(H_{2,1}^{\mathrm{Pa}}, H_{2,1}^{\mathrm{Pb}})$

Figure 4.38: CR2ℓ-Top: Modelling for $p_T^{j_1}$ in (a). We show $H_{4,1}^{\mathrm{PP}}$ in (b). In (c) we show R_{p_T}. In (d) we show $\min(H_{1,1}^{\mathrm{Pa}}, H_{1,1}^{\mathrm{Pb}})/\min(H_{2,1}^{\mathrm{Pa}}, H_{2,1}^{\mathrm{Pb}})$.

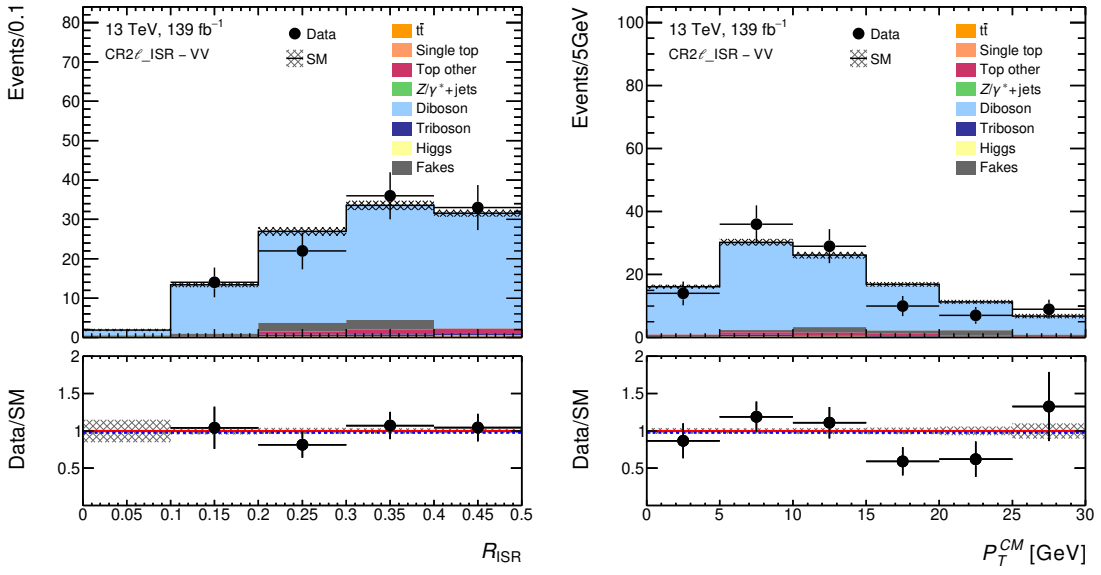

(a) R_{ISR}

(b) P_T^{CM}

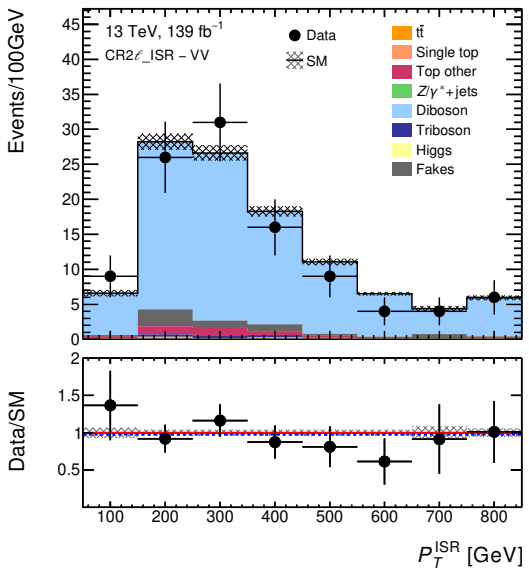

(c) P_T^{ISR}

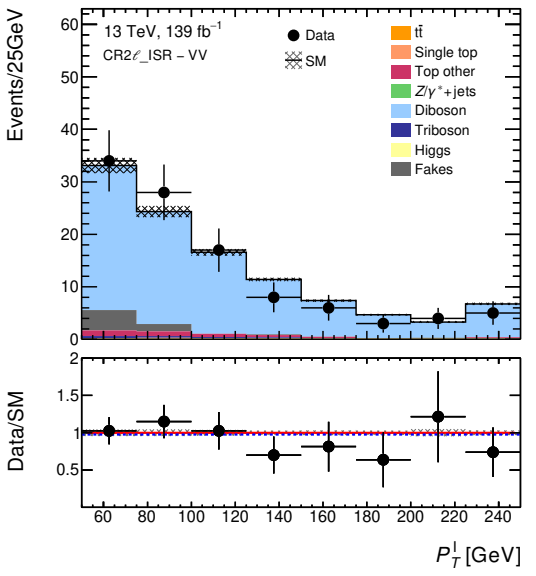

(d) P_T^{I}

Figure 4.39: CR2ℓ_ISR-VV: Modelling for R_{ISR} in (a). We show P_T^{CM} in (b). In (c) we show P_T^{ISR}. In (d) we show P_T^{I}.

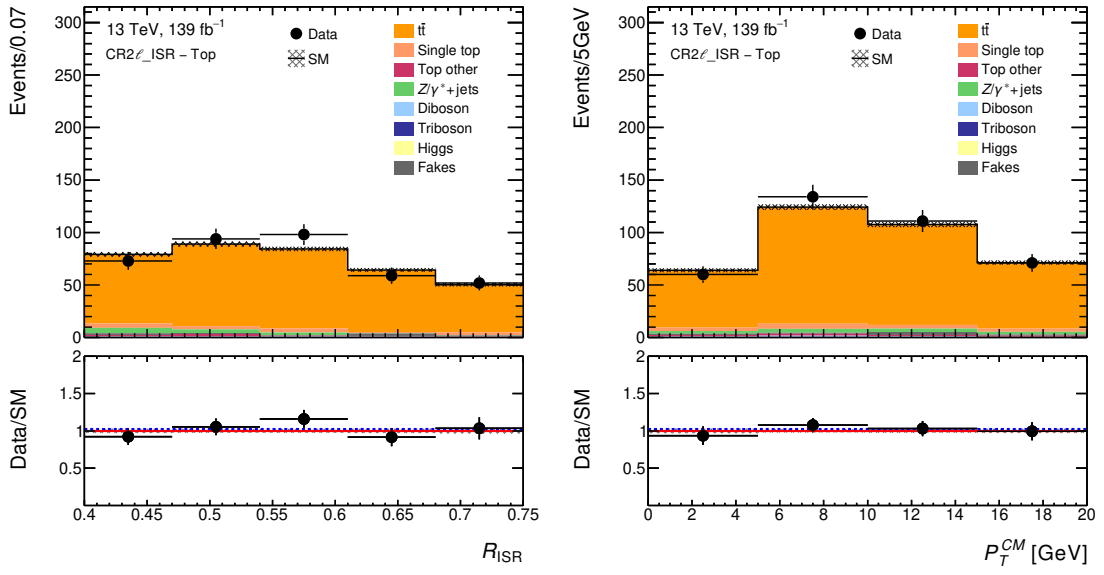

(a) R_{ISR}

(b) P_T^{CM}

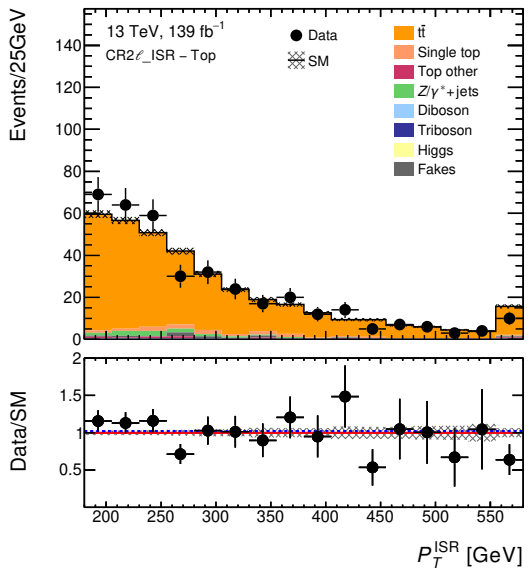

(c) P_T^{ISR}

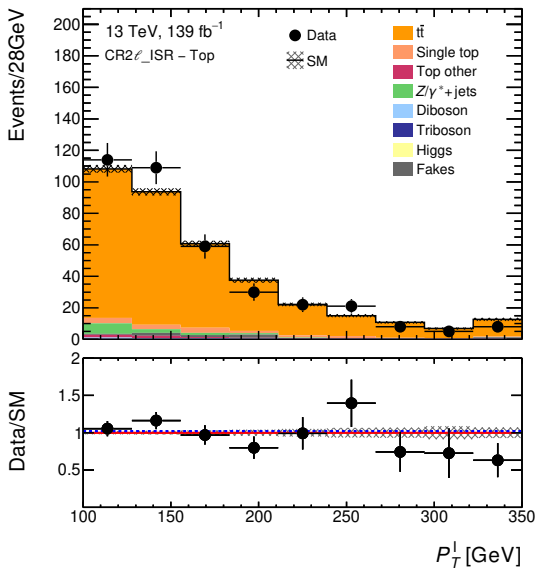

(d) P_T^{I}

Figure 4.40: CR2ℓ_ISR-Top: Modelling for R_{ISR} in (a). We show P_T^{CM} in (b). In (c) we show P_T^{ISR}. In (d) we show P_T^{I}.

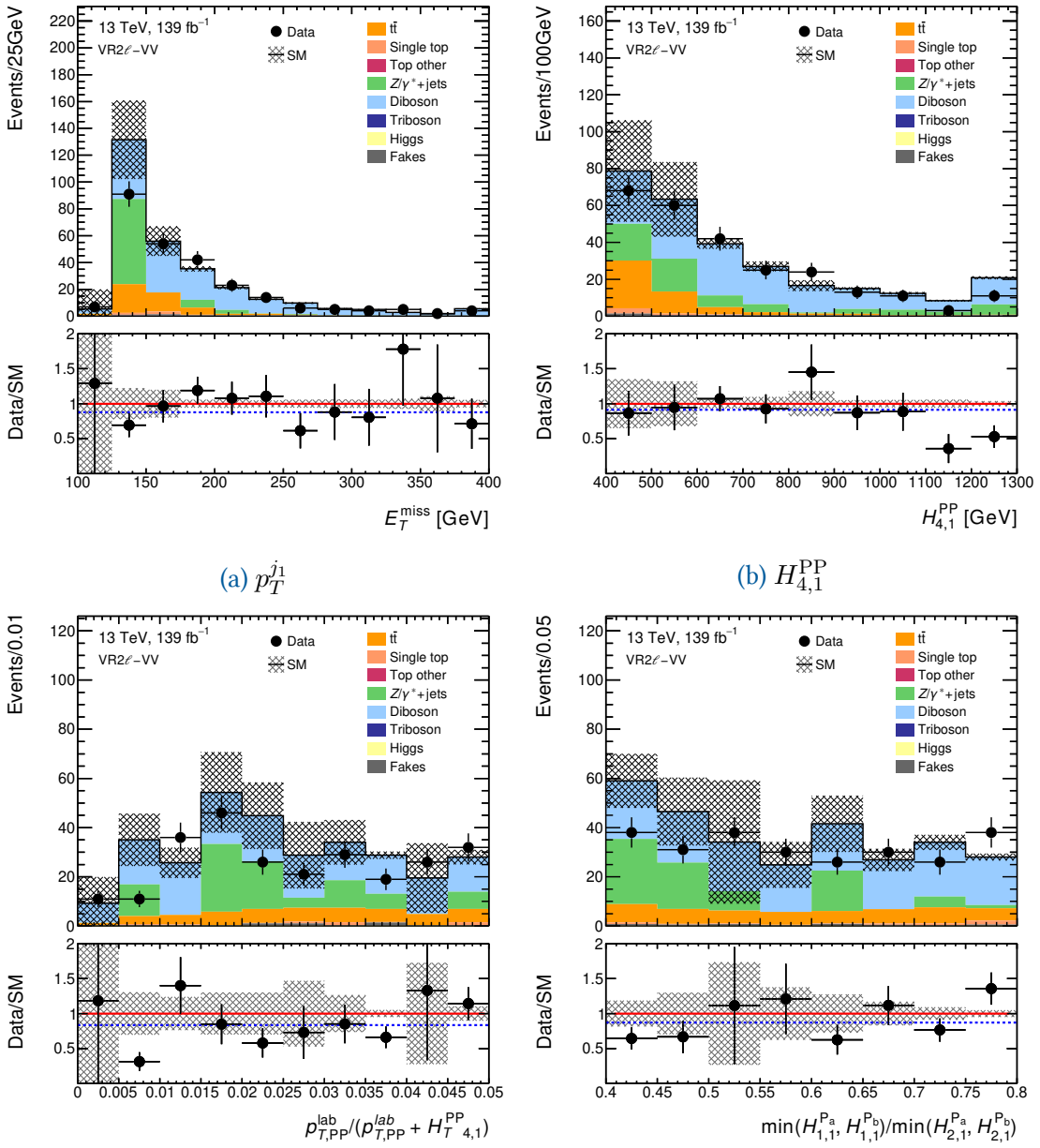

(a) $p_T^{j_1}$ (b) $H_{4,1}^{\text{PP}}$

(c) R_{pT} (d) $\min(H_{1,1}^{\text{Pa}}, H_{1,1}^{\text{Pb}})/\min(H_{2,1}^{\text{Pa}}, H_{2,1}^{\text{Pb}})$

Figure 4.41: VR2ℓ-VV: Modelling for $p_T^{j_1}$ in (a). We show $H_{4,1}^{\text{PP}}$ in (b). In (c) we show R_{pT}. In (d) we show $\min(H_{1,1}^{\text{Pa}}, H_{1,1}^{\text{Pb}})/\min(H_{2,1}^{\text{Pa}}, H_{2,1}^{\text{Pb}})$.

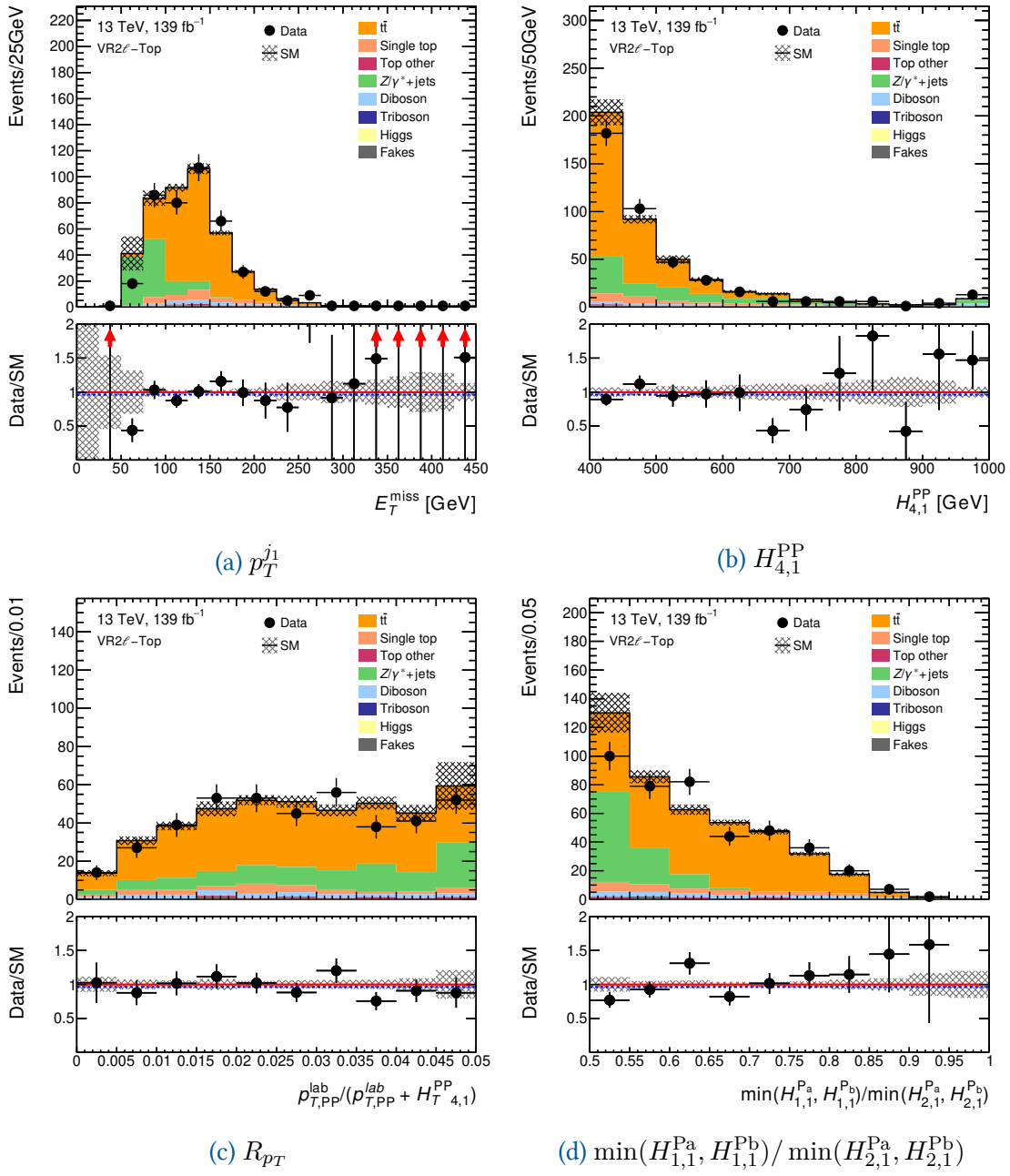

(a) $p_T^{j_1}$ (b) $H_{4,1}^{\text{PP}}$

(c) R_{pT} (d) $\min(H_{1,1}^{\text{Pa}}, H_{1,1}^{\text{Pb}})/\min(H_{2,1}^{\text{Pa}}, H_{2,1}^{\text{Pb}})$

Figure 4.42: VR2ℓ-Top: Modelling for $p_T^{j_1}$ in (a). We show $H_{4,1}^{\text{PP}}$ in (b). In (c) we show R_{p_T}. In (d) we show $\min(H_{1,1}^{\text{Pa}}, H_{1,1}^{\text{Pb}})/\min(H_{2,1}^{\text{Pa}}, H_{2,1}^{\text{Pb}})$.

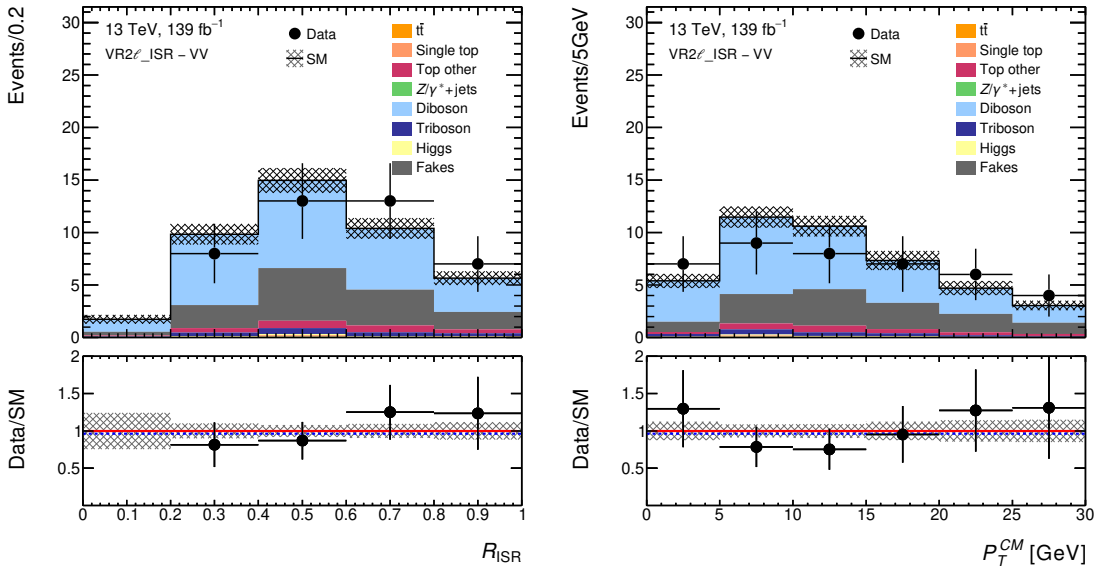

(a) R_{ISR}

(b) P_T^{CM}

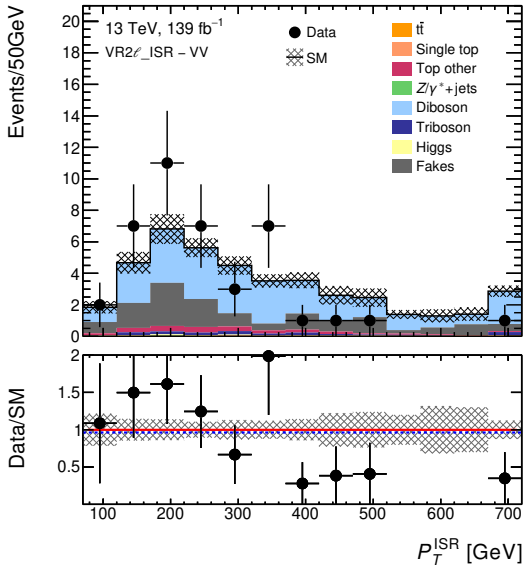

(c) P_T^{ISR}

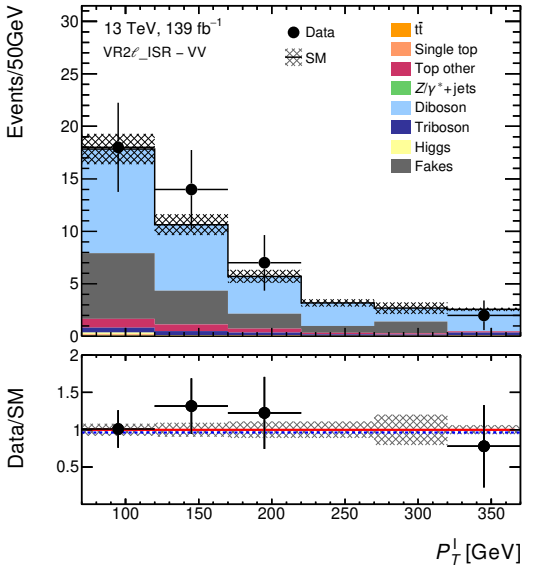

(d) P_T^{I}

Figure 4.43: VR2ℓ_ISR-VV: Modelling for R_{ISR} in (a). We show P_T^{CM} in (b). In (c) we show P_T^{ISR}. In (d) we show P_T^{I}.

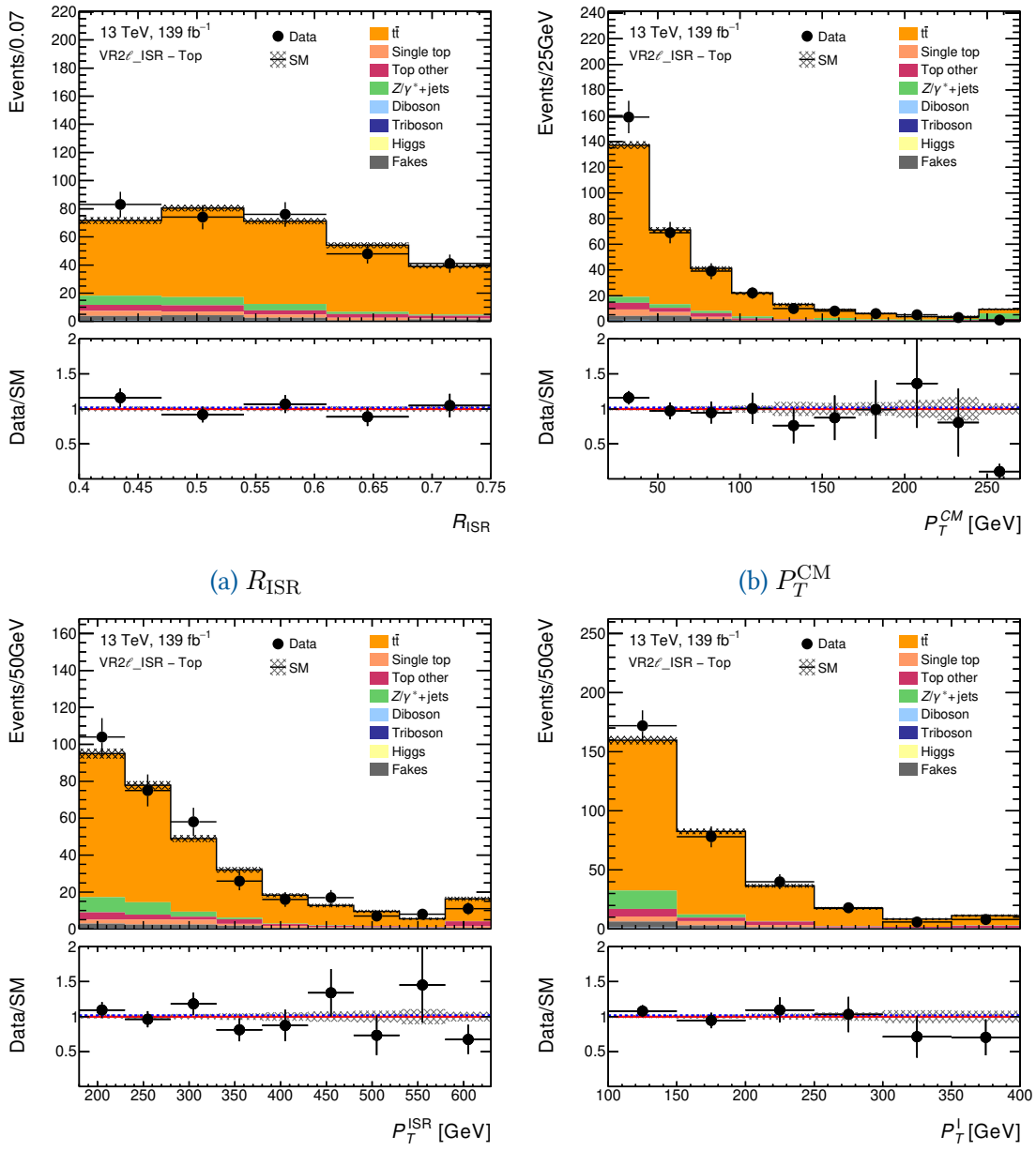

(a) R_{ISR}

(b) P_T^{CM}

(c) P_T^{ISR}

(d) P_T^{I}

Figure 4.44: VR2ℓ_ISR-Top: Modelling for R_{ISR} in (a). We show P_T^{CM} in (b). In (c) we show P_T^{ISR}. In (d) we show P_T^{I}.

Table 4.29: Standard tree CRs and VRs. All sources of systematics are included. All CRs are simultaneously fit for normalisation factors. Z/γ^*+jets is estimated from MC.

Full run-II	CR2ℓ_VV	CR2ℓ_TOP	VR2ℓ_VV	VR2ℓ_TOP
Observed events	186	1975	257	418
Fitted SM events	186 ± 14	1975 ± 44	286 ± 37	435 ± 24
Fitted Higgs events	$0.01^{+0.01}_{-0.01}$	$0.57^{+1.20}_{-0.57}$	$0.01^{+0.06}_{-0.01}$	$0.07^{+0.15}_{-0.07}$
Fitted Triboson events	2^{+3}_{-2}	0.07 ± 0.04	$1.3^{+1.5}_{-1.3}$	$0.3^{+0.3}_{-0.3}$
Fitted Diboson events	181 ± 14	18 ± 3	166 ± 26	20 ± 3
Fitted Top other events	0.8 ± 0.4	17 ± 3	1.2 ± 0.7	6.0 ± 3.0
Fitted $t\bar{t}$ events	0.00 ± 0.00	1756 ± 42	48 ± 6	278 ± 14
Fitted Single top events	$0.7^{+0.9}_{-0.7}$	152 ± 4	4 ± 2	26 ± 9
Fitted Fakes events	1.2 ± 0.9	13 ± 7	1.6 ± 0.8	2 ± 1
Fitted Z/γ^*+jets events	0.00 ± 0.00	18 ± 1	64 ± 8	104 ± 6
Total exp. SM events	209 ± 3	2027 ± 20	308 ± 37	446 ± 23
MC exp. Higgs events	$0.01^{+0.01}_{-0.01}$	$0.6^{+1.2}_{-0.6}$	$0.01^{+0.06}_{-0.01}$	$0.07^{+0.15}_{-0.07}$
MC exp. Triboson events	$2.1^{+2.7}_{-2.1}$	0.07 ± 0.05	$1.3^{+1.5}_{-1.3}$	$0.3^{+0.3}_{-0.3}$
MC exp. Diboson events	204 ± 2	20 ± 3	187 ± 24	22 ± 3
MC exp. Top other events	0.8 ± 0.4	16 ± 3	1.0 ± 0.6	5.9 ± 3.0
MC exp. $t\bar{t}$ events	0.00 ± 0.00	1802 ± 16	49 ± 7	286 ± 13
MC exp. Single top events	$0.7^{+1.0}_{-0.7}$	156 ± 1	5 ± 2	27 ± 9
DD exp. Fakes events	1.0 ± 0.9	13 ± 7	1.6 ± 0.8	2 ± 1
MC exp. Z/γ^*+jets events	0.00 ± 0.00	18.0 ± 0.70	64 ± 8	104 ± 6

CR3ℓ_ISR-VV. The corresponding VRs will be VR3ℓ-VV and V3ℓ_ISR-VV.

The leading lepton must have a $p_T^{\ell_1} > 60$ GeV, the sub-leading lepton must have $p_T^{\ell_2} > 40$ GeV and the sub-sub-leading lepton must have a transverse momentum of $p_T^{\ell_3} > 30$ GeV. We require that there be no jets above 20 GeV and no b-tagged jets. We define the preselections for the standard SR in Tables 4.31.

The ISR regions are made orthogonal to the standard regions by requiring at least one jet. Given the ISR regions require at least one jet, we can use the RJR ISR decay tree. As with the standard regions, we first define the preselection and then define the SR, CR and VRs.

Unlike the standard regions, the ISR region preselections differ slightly between the SRs and the others. The SR requires at least three leptons, which must be greater than 25 GeV, 25 GeV and 20 GeV respectively and we require between 1 and 3 jets. We require that zero of the jets are b-tagged, and unlike the SR we allow the CRs and VR events to contain more than three jets. We summarise the preselection criteria for the CR3ℓ_ISR-VV, VR3ℓ_ISR-VV, and SR3ℓ_ISR in Table 4.32.

Table 4.30: ISR tree CRs and VRs. All sources of systematic and statistical uncertainty are included. All CRs are simultaneously fit for normalisation factors. Z/γ^*+jets is estimated from MC.

Full run-II	CR2ℓ_ISR_VV	CR2ℓ_ISR_TOP	VR2ℓ_ISR_VV	VR2ℓ_ISR_TOP
Fitted SM events	111 ± 11	376 ± 19	43 ± 4	328 ± 42
Fitted Higgs events	$0.05^{+0.10}_{-0.05}$	$0.3^{+0.5}_{-0.3}$	$0.4^{+0.7}_{-0.4}$	$0.2^{+0.3}_{-0.2}$
Fitted Triboson events	$2.0^{+2.6}_{-2.0}$	$0.04^{+0.06}_{-0.04}$	2.0 ± 0.5	0.02 ± 0.01
Fitted Diboson events	99 ± 11	4.3 ± 0.7	26 ± 3	2.5 ± 0.5
Fitted Top other events	3.6 ± 1.6	5.8 ± 3.0	2.2 ± 1.0	16 ± 7
Fitted $t\bar{t}$ events	0.00 ± 0.00	332 ± 19	0.00 ± 0.00	267 ± 41
Fitted Single top events	$0.7^{+1.5}_{-0.7}$	15.0 ± 0.9	$0.2^{+0.5}_{-0.2}$	11 ± 5
Fitted Fakes events	5.3 ± 1.8	6.1 ± 1.6	12.6 ± 2.0	9.4 ± 2.1
Fitted Z/γ^*+jets events	0.00 ± 0.00	12.5 ± 0.5	0.09 ± 0.01	20.0 ± 0.9
Total exp. SM events	135 ± 3	445 ± 8	50 ± 3	384 ± 44
MC exp. Higgs events	$0.05^{+0.10}_{-0.05}$	$0.3^{+0.5}_{-0.3}$	$0.4^{+0.7}_{-0.4}$	$0.2^{+0.3}_{-0.2}$
MC exp. Triboson events	$2.0^{+2.6}_{-2.0}$	$0.04^{+0.06}_{-0.04}$	2.0 ± 0.5	0.02 ± 0.01
MC exp. Diboson events	123 ± 2	5.4 ± 0.8	32 ± 1	3.2 ± 0.5
MC exp. Top other events	3.6 ± 1.6	5.8 ± 2.6	2.3 ± 1.0	16 ± 7
MC exp. $t\bar{t}$ events	0.00 ± 0.00	397 ± 7	0.00 ± 0.00	320 ± 44
MC exp. Single top events	$0.8^{+1.8}_{-0.8}$	17.9 ± 0.3	$0.2^{+0.7}_{-0.2}$	14 ± 6
DD exp. Fakes events	5.3 ± 1.8	6.0 ± 1.9	13 ± 2	9 ± 2
MC exp. Z/γ^*+jets events	0.00 ± 0.00	12 ± 1	0.09 ± 0.01	20.0 ± 0.9

Table 4.31: Preselection criteria for the 3ℓ CR, VR, and SR with the standard decay tree. The variables are defined in the text.

Region	n_{leptons}	n_{jets}	$n_{b\text{-tag}}$	$p_T^{\ell_1}$ [GeV]	$p_T^{\ell_2}$ [GeV]	$p_T^{\ell_3}$ [GeV]
CR3ℓ-VV	$= 3$	0	$= 0$	> 60	> 40	> 30
VR3ℓ-VV	$= 3$	0	$= 0$	> 60	> 40	> 30
SR3ℓ_Low	$= 3$	$= 0$	$= 0$	> 60	> 40	> 30

Table 4.32: Preselection criteria for the 3ℓ CR, VR, and SR with the ISR decay tree. The variables are defined in the text.

Region	n_{leptons}	n_{jets}	$n_{b\text{-tag}}$	$p_T^{\ell_1}$ [GeV]	$p_T^{\ell_2}$ [GeV]	$p_T^{\ell_3}$ [GeV]
CR3ℓ_ISR-VV	$= 3$	≥ 1	$= 0$	> 25	> 25	> 20
VR3ℓ_ISR-VV	$= 3$	≥ 1	$= 0$	> 25	> 25	> 20
SR3ℓ_ISR	$= 3$	$\in [1, 3]$	$= 0$	> 25	> 25	> 20

Our CR for SR3ℓ_Low is CR3ℓ-VV and for this region the preselections are identical to the SR preselections as shown in Table 4.31. The selection criteria for the diboson CR differs only in a few places, the key difference being a shift of m_T^W from 100 GeV in the SR - to $\in (0, 70)$ GeV in the CR. We also loosen R_{p_T} from < 0.05 to < 0.2 and we loosen $H_{1,1}^{\text{P}_\text{b}}/H_{2,1}^{\text{P}_\text{b}}$ from 0.9 to 0.75.

Table 4.33: Selection criteria for the 3ℓ CR, VR, and SR with the standard decay tree. The variables are defined in the text.

Region	$m_{\ell\ell}$ [GeV]	m_{T}^{W} [GeV]	$H_{3,1}^{\mathrm{PP}}$ [GeV]	$\frac{p_{\mathrm{T\ PP}}^{\mathrm{lab}}}{p_{\mathrm{T\ PP}}^{\mathrm{lab}}+H_{\mathrm{T}\ 3,1}^{\mathrm{PP}}}$	$\frac{H_{\mathrm{T}\ 3,1}^{\mathrm{PP}}}{H_{3,1}^{\mathrm{PP}}}$	$\frac{H_{1,1}^{\mathrm{Pb}}}{H_{2,1}^{\mathrm{Pb}}}$
CR3ℓ-VV	$\in (75, 105)$	$\in (0, 70)$	> 250	< 0.2	> 0.75	–
VR3ℓ-VV	$\in (75, 105)$	$\in (70, 100)$	> 250	< 0.2	> 0.75	–
SR3ℓ_Low	$\in (75, 105)$	> 100	> 250	< 0.05	> 0.9	–

Table 4.34: Selection criteria for the 3ℓ CR, VR, and SR with the ISR decay tree. The variables are defined in the text.

Region	$m_{\ell\ell}$ [GeV]	m_{T}^{W} [GeV]	$\Delta\phi_{\mathrm{ISR,I}}^{\mathrm{CM}}$	R_{ISR}	$p_{\mathrm{T\ ISR}}^{\mathrm{CM}}$ [GeV]	$p_{\mathrm{T\ I}}^{\mathrm{CM}}$ [GeV]	$p_{\mathrm{T}}^{\mathrm{CM}}$ [GeV]
CR3ℓ_ISR-VV	$\in (75, 105)$	< 100	> 2.0	$\in (0.55, 1.0)$	> 80	> 60	< 25
VR3ℓ_ISR-VV	$\in (75, 105)$	> 60	> 2.0	$\in (0.55, 1.0)$	> 80	> 60	> 25
SR3ℓ_ISR	$\in (75, 105)$	> 100	> 2.0	$\in (0.55, 1.0)$	> 100	> 80	< 25

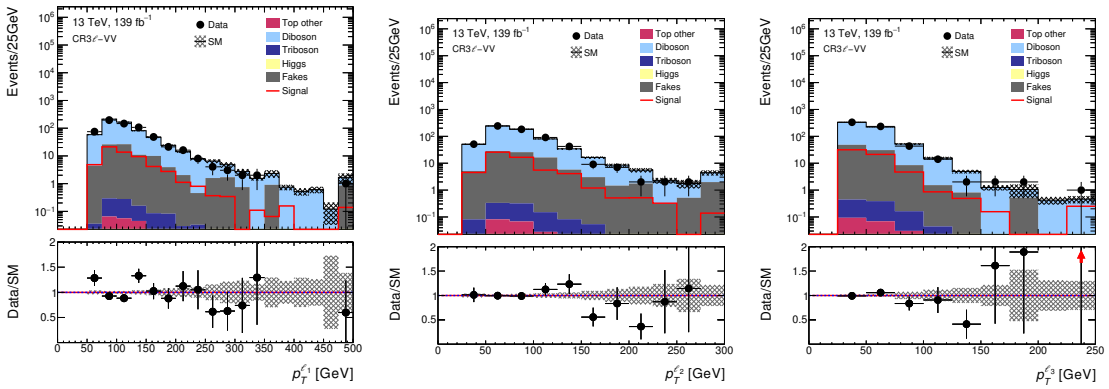

(a) Leading lepton (b) Sub-leading lepton (c) Sub-sub-leading lepton

Figure 4.45: Validation of lepton momenta in CR3ℓ-VV. In (a) we show the leading lepton momentum. In (b) we show the sub-leading lepton. In (c) we see the sub-sub-leading lepton momentum is well modelled.

The CR selections are defined by inverting m_T^W to < 100 GeV. We keep $\Delta\phi_{\mathrm{ISR},I} > 2.0$ fixed. We keep R_{ISR} fixed. We loosen the ISR momentum requirement to $p_{\mathrm{ISR,T}}^{\mathrm{CM}} > 80$ GeV and loosen the invisible system momentum requirement giving $p_{\mathrm{I,T}}^{\mathrm{CM}} > 60$ GeV. We keep p_T^{CM} fixed.

The VR for SR3ℓ_Low is VR3ℓ-VV and for this region the preselections are identical to the SR preselections as shown in Table 4.31. The key variable differences from CR3ℓ-VV are shifting $m_T^W \in (0, 70)$ GeV to $m_T^W \in (70, 100)$ GeV and again loosening R_{p_T} and $H_{1,1}^{\mathrm{Pb}}/H_{2,1}^{\mathrm{Pb}}$ to the same values as the CR. The VR selections are defined by loosening m_T^W to > 60 GeV. We keep $\Delta\phi_{\mathrm{ISR},I} > 2.0$ fixed. We keep R_{ISR} fixed. We loosen the ISR momentum requirement to $p_{\mathrm{ISR,T}}^{\mathrm{CM}} > 80$ GeV and loosen the invisible system momentum requirement to $p_{\mathrm{I,T}}^{\mathrm{CM}} > 60$ GeV, we invert the CM frame momentum giving $p_T^{\mathrm{CM}} >$

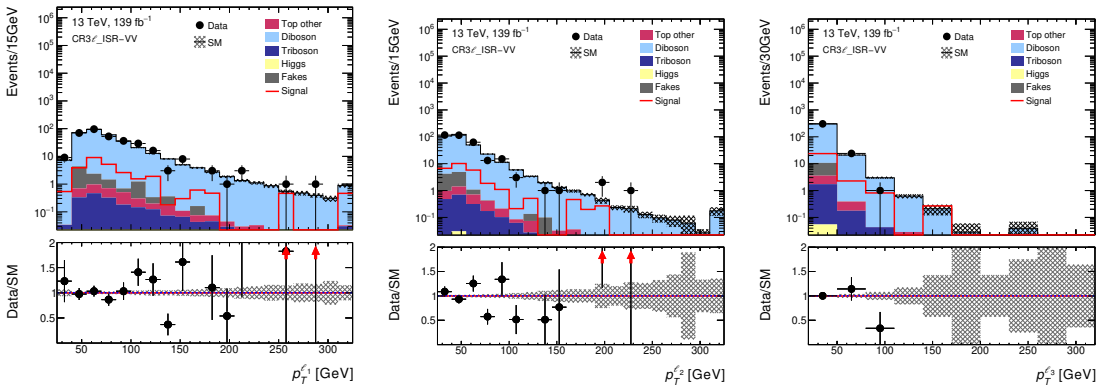

(a) Leading lepton (b) Sub-leading lepton (c) Sub-sub-leading lepton

Figure 4.46: Validation of lepton momenta in CR3ℓ_ISR-VV. In (a) we show the leading lepton momentum. In (b) we show the sub-leading lepton momentum. In (c) we show the sub-sub-leading lepton momentum.

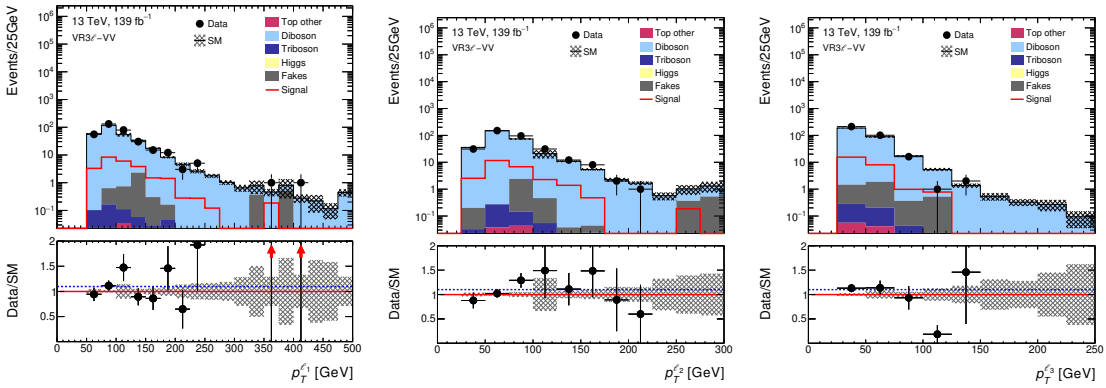

(a) Leading lepton (b) Sub-leading lepton (c) Sub-sub-leading lepton

Figure 4.47: Validation of lepton momenta in VR3ℓ-VV. In (a) we show the leading lepton momentum. In (b) we show the sub-leading lepton momentum. In (c) we show the sub-sub-leading lepton momentum.

25 GeV. All our CRs and VRs for our standard approach are summarised in Table 4.33, with all our ISR CRs and VRs being summarised in Table 4.34. The transverse momenta are summarised for these regions in Figures 4.45–4.48. We see good p_T modelling for all three leptons in both CRs.

The region breakdowns for all two CRs and VRs are summarised in Table 4.35. We see that for the two CRs, the purity in the primary background is very high. The observed number of events and total SM expectation are in agreement, with the Data/SM being approximately 1. We break down the full run-II dataset

We look not only at the agreement between the overall yields but also at the bin-by-bin agreement between the observed number of events and the SM expectation we can determine the general modelling for each variable. The modelling of the two CRs is

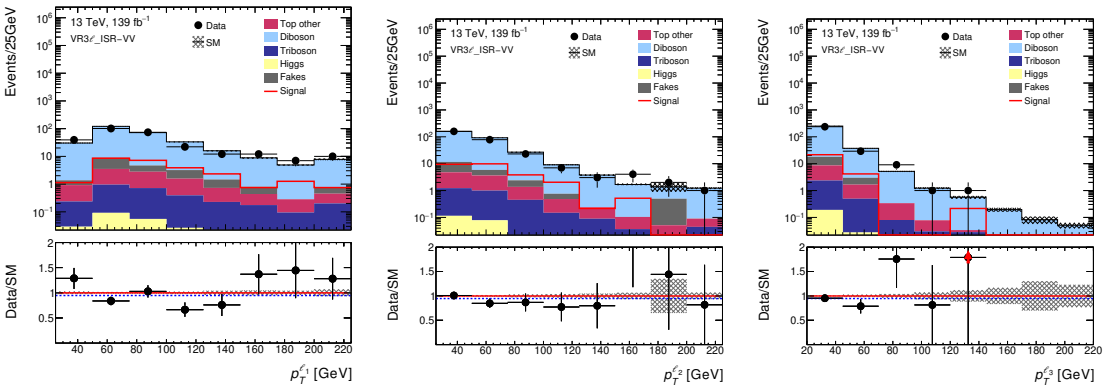

(a) Leading lepton (b) Sub-leading lepton (c) Sub-sub-leading lepton

Figure 4.48: Validation of lepton momenta in VR3ℓ_ISR-VV. In (a) the leading lepton momentum is well modelled. In (b) the sub-leading lepton is well modelled. In (c) we see the sub-sub-leading lepton momentum is well modelled.

shown in Figures 4.49–Figure 4.50.

We extract a normalisation factor for each region, and we see in Table 4.35 that the VRs have agreement between our SM expectation and the observed number of events. Furthermore, we see that the VR modelling is excellent, as shown in Figure 4.51–4.52.

Table 4.35: The full run-II region breakdowns for the 3ℓ CRs and VRs. Uncertainties include statistical and systematic components. We see closure consistent with 1 for the VRs.

Full run-II	CR3ℓ-VV	VR3ℓ-VV	CR3ℓ_ISR_VV	VR3ℓ_ISR_VV
Observed events	629	331	328	277
Fitted SM events	629 ± 25	300 ± 29	328	277
Fitted Diboson events	540 ± 36	296 ± 29	319 ± 18	273 ± 48
Fitted Triboson events	0.48 ± 0.06	0.24 ± 0.05	0.17 ± 0.07	0.35 ± 0.09
Fitted Top other events	$0.21 \pm 0.$	0.10 ± 0.05	2.1 ± 1.0	7.7 ± 3.5
Fitted Fakes events	88 ± 25	3.7 ± 0.2	7.1 ± 1.9	10.6 ± 3.3
Total exp. SM events	674 ± 26	324 ± 22	353 ± 4	313 ± 49
MC exp. Diboson events	584 ± 8	321 ± 22	343 ± 3	295 ± 49
MC exp. Triboson events	0.48 ± 0.06	0.24 ± 0.05	0.17 ± 0.07	0.4 ± 0.1
MC exp. Top other events	0.21 ± 0.09	0.10 ± 0.05	2.0 ± 1.0	7.7 ± 3.6
DD exp. Fakes events	88 ± 25	3.7 ± 0.2	7.1 ± 1.9	10 ± 3

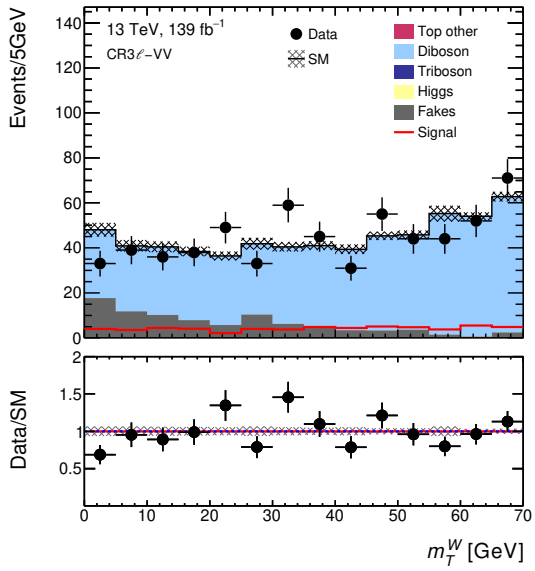

(a) m_T^W

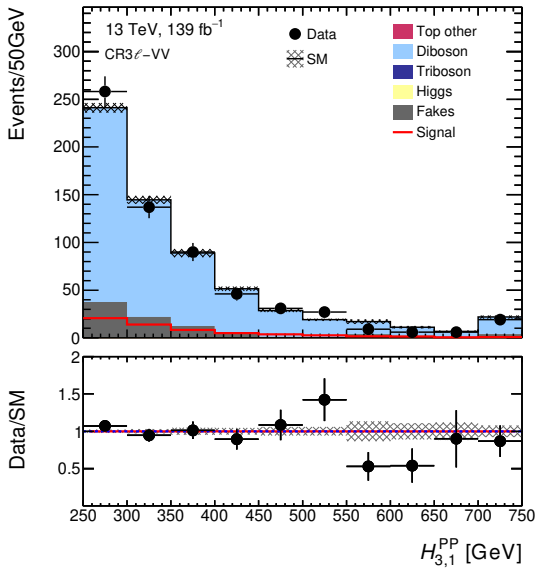

(b) $H_{3,1}^{\mathrm{PP}}$

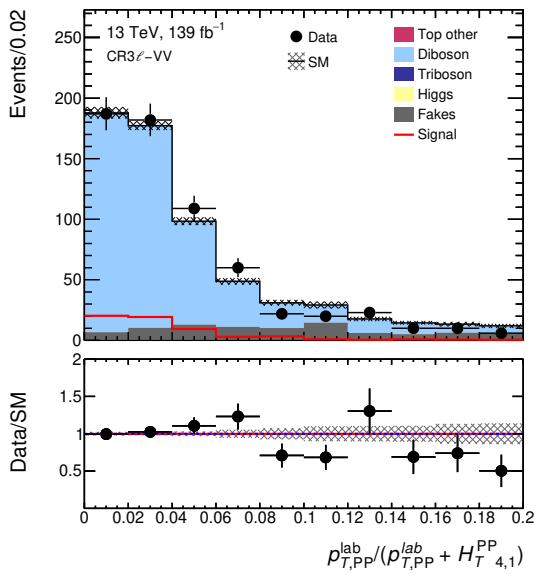

(c) R_{p_T}

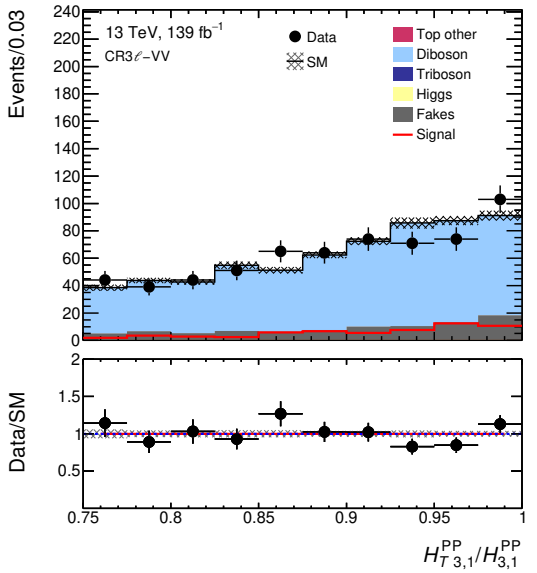

(d) $H_{1,1}^{\mathrm{PP}}/H_{3,1}^{\mathrm{PP}}$

Figure 4.49: CR3ℓ-VV: Modelling for (a) m_T^W, (b) $H_{3,1}^{\mathrm{PP}}$, (c) R_{p_T} and (d) $H_{T\ 3,1}^{\mathrm{PP}}/H_{3,1}^{\mathrm{PP}}$.

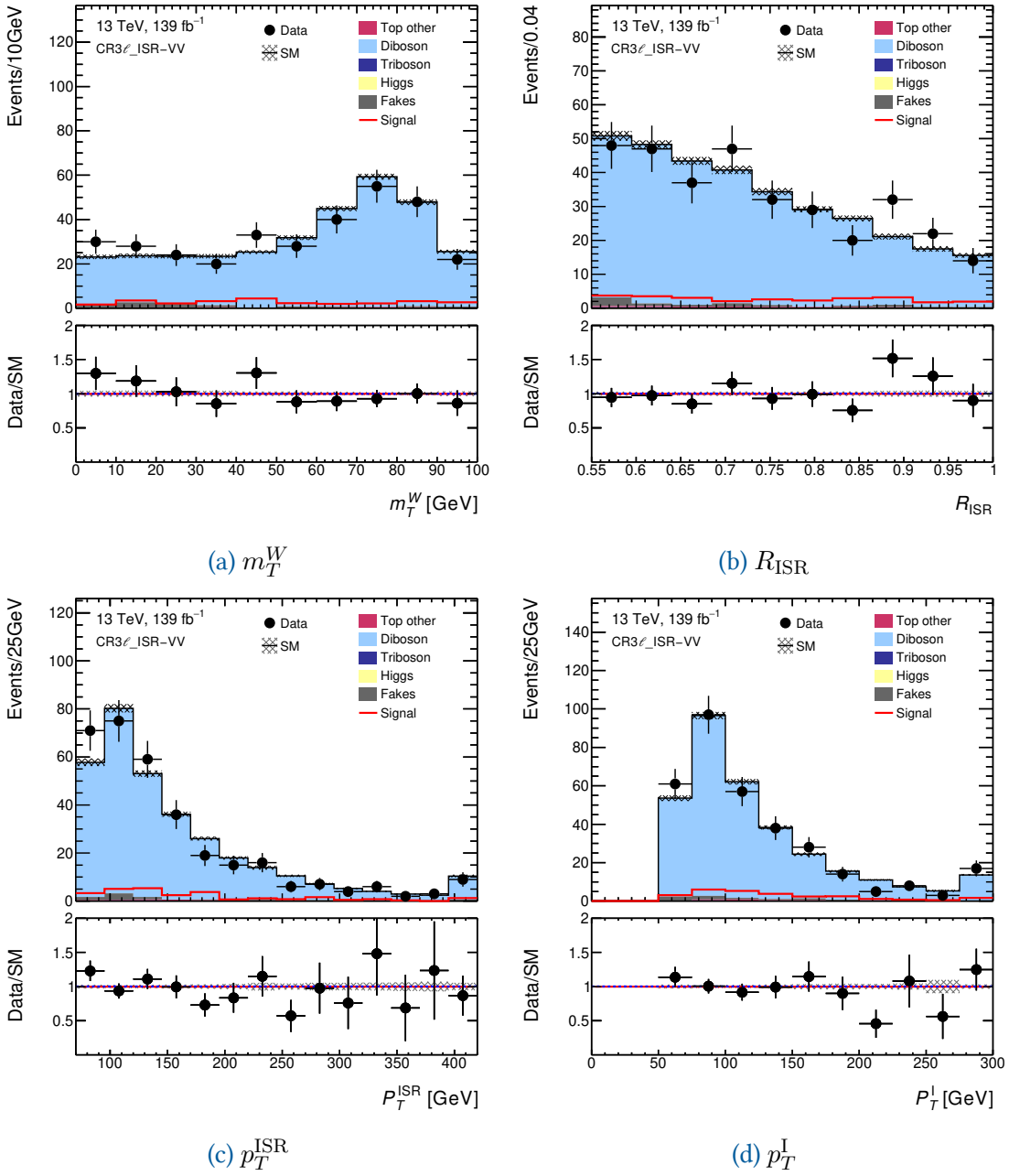

(a) m_T^W (b) R_{ISR}

(c) p_T^{ISR} (d) p_T^{I}

Figure 4.50: CR3ℓ_ISR-VV: Modelling for (a) m_T^W, (b) R_{ISR}, (c) p_T^{ISR} and (d) P_T^{I}.

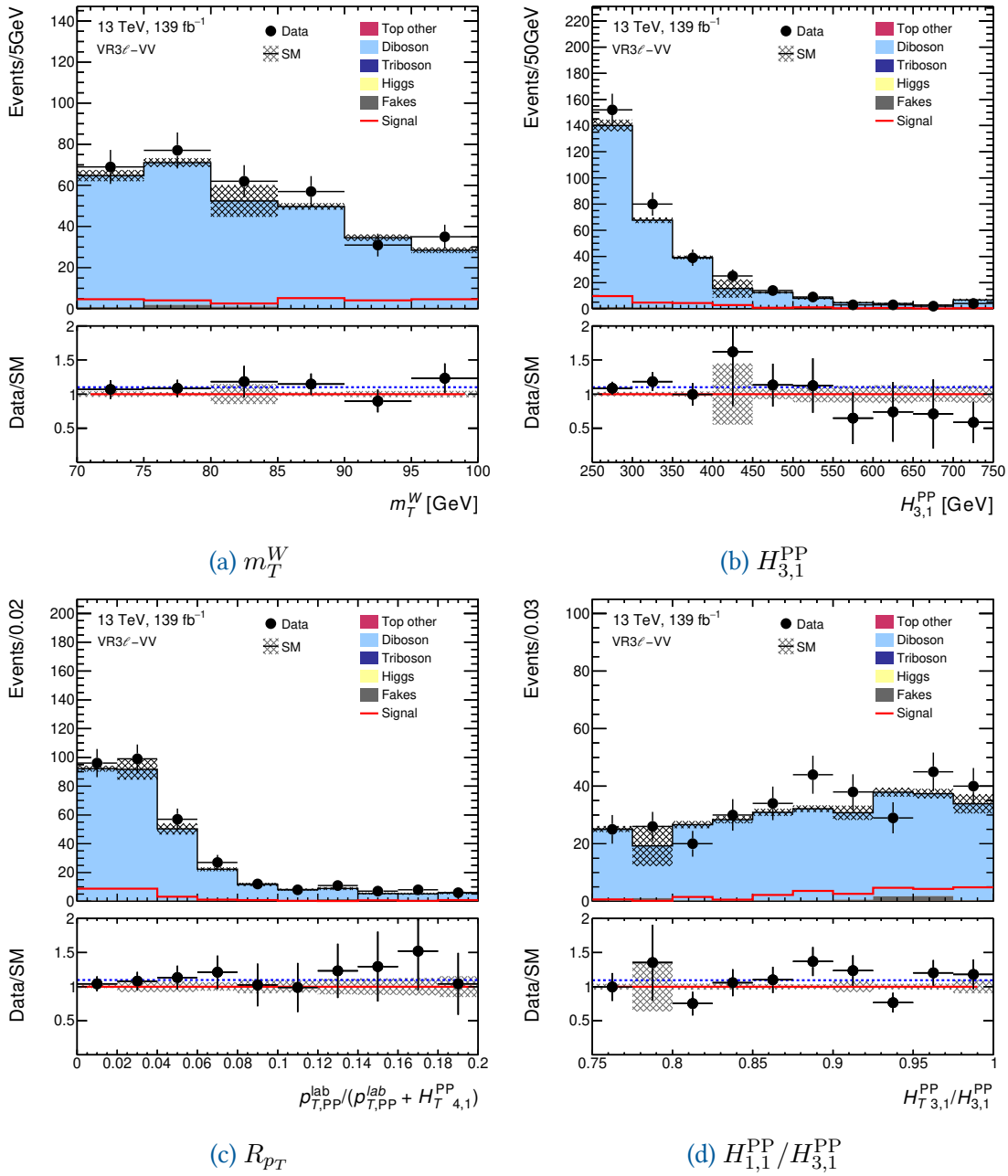

(a) m_T^W (b) $H_{3,1}^{\mathrm{PP}}$

(c) R_{p_T} (d) $H_{1,1}^{\mathrm{PP}}/H_{3,1}^{\mathrm{PP}}$

Figure 4.51: VR3ℓ-VV: Modelling for (a) m_T^W, (b) $H_{3,1}^{\mathrm{PP}}$, (c) R_{p_T} and (d) $H_{T\ 3,1}^{\mathrm{PP}}/H_{3,1}^{\mathrm{PP}}$.

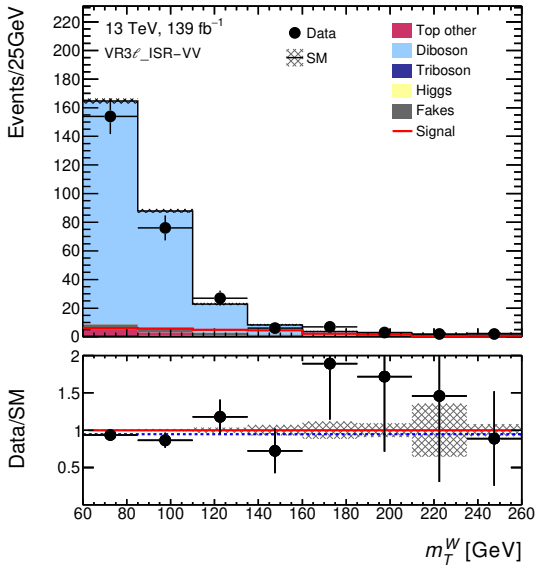

(a) m_T^W

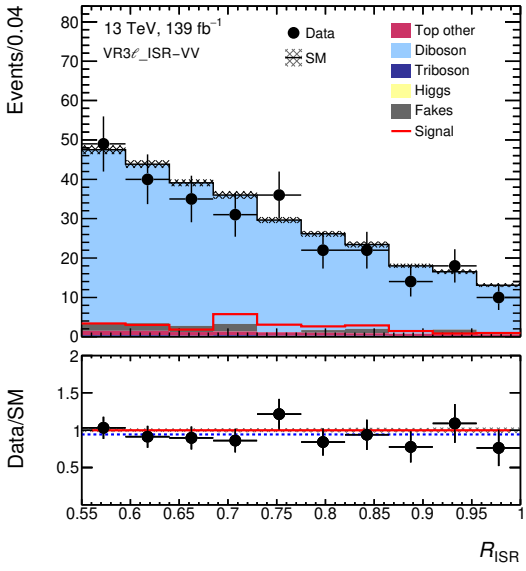

(b) R_{ISR}

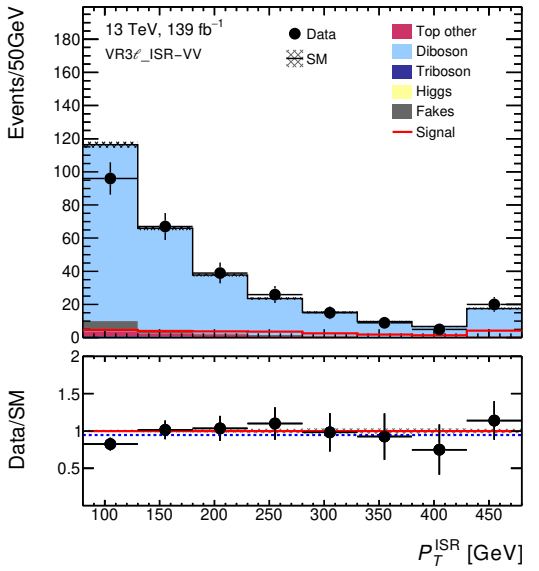

(c) p_T^{ISR}

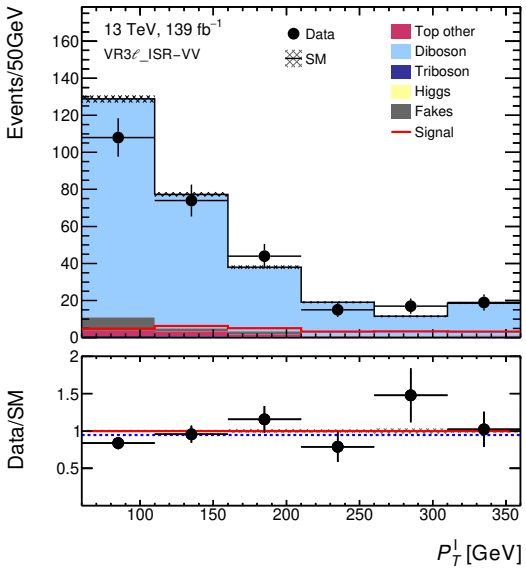

(d) p_T^{I}

Figure 4.52: VR3ℓ_ISR-VV: Modelling for (a) m_T^W, (b) R_{ISR}, (c) p_T^{ISR} and (d) P_T^{I}.

4.13 ABCD Z/γ^*+jets Estimation

This section outlines our estimation of the 2ℓ background Z/γ^*+jets. We have outlined our method to control and validate all other backgrounds present within SR2ℓ_Low and SR2ℓ_ISR. As has been stated, due to the presence of large positively and negatively weighted events in the SRs, we cannot use the SHERPA 2.2.1 MC generator for Z/γ^*+jets estimation for SR2ℓ_Low or SR2ℓ_ISR. For this reason, we employ the ABCD method as outlined in Section 4.7. We will again describe each step our methodology, specific to each SR.

4.13.1 SR2ℓ_Low Z/γ^*+jets Estimation

When applying the ABCD method, we first require a region to apply it to, in the case of the standard approach, this is SR2ℓ_Low. The second step in the process is to define the ABCD plane by removing two separate variable selections which define SR2ℓ_Low. The two variables we choose to define the ABCD plane are m_{jj} and $H_{1,1}^{\mathrm{PP}}/H_{4,1}^{\mathrm{PP}}$. The 2D distributions Z/γ^*+jets for these variables are shown in Figure 4.53a. The correlation factor between m_{jj} and $H_{1,1}^{\mathrm{PP}}/H_{4,1}^{\mathrm{PP}}$ for Z/γ^*+jets events is -0.06. Given the correlation factor is close to zero, we move forward and define the ABCD plane.

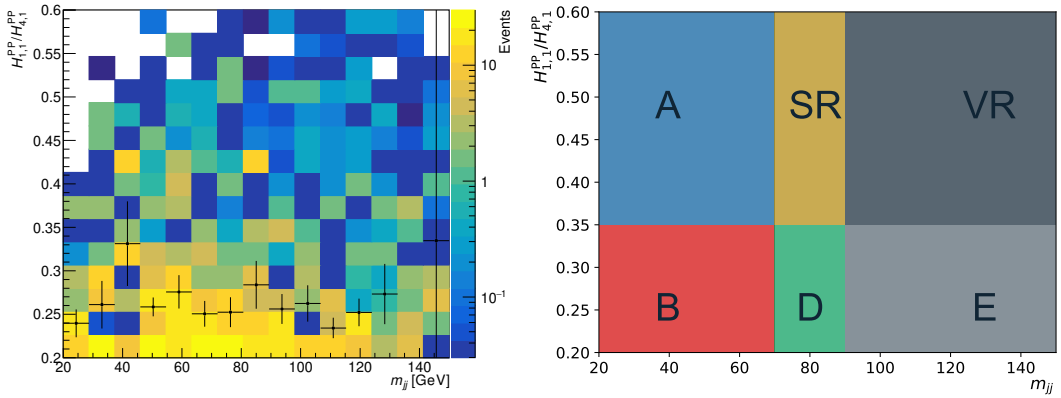

(a) Z/γ^*+jets correlations. (b) ABCD 2D plane.

Figure 4.53: The ABCD regions for SR2ℓ_Low Z/γ^*+jets estimate. In (a), the black dots are a profile of each vertical slice. In (b), we have the regions labelled for the method.

Unlike in Section 4.7, we will have more than four regions defined. When calculating an estimate for the Z/γ^*+jets background, we want to have an internal validation step. In order to perform this validation we need to define two extra regions VR and E. Each region we define is determined by inverting either m_{jj} or $H_{1,1}^{\mathrm{PP}}/H_{4,1}^{\mathrm{PP}}$ as defined for the SR. Region A is defined for low m_{jj} and nominal $H_{1,1}^{\mathrm{PP}}/H_{4,1}^{\mathrm{PP}}$, region B is defined for low m_{jj} and low $H_{1,1}^{\mathrm{PP}}/H_{4,1}^{\mathrm{PP}}$, region D is defined for nominal m_{jj} and low $H_{1,1}^{\mathrm{PP}}/H_{4,1}^{\mathrm{PP}}$, region

E is defined for high m_{jj} and low $H_{1,1}^{\text{PP}}/H_{4,1}^{\text{PP}}$ and region VR is defined for high m_{jj} and nominal $H_{1,1}^{\text{PP}}/H_{4,1}^{\text{PP}}$. We summarise these regions in Figure 4.53b and Table 4.36.

Table 4.36: SR2ℓ_Low ABCD selection criteria for m_{jj} and $H_{1,1}^{\text{PP}}/H_{4,1}^{\text{PP}}$ variables.

Region	m_{jj}	$H_{1,1}^{\text{PP}}/H_{4,1}^{\text{PP}}$
SR	$\in (70, 90)$	$\in (0.35, 0.60)$
A	$\in (20, 70)$	$\in (0.35, 0.60)$
B	$\in (20, 70)$	$\in (0.20, 0.35)$
D	$\in (70, 90)$	$\in (0.20, 0.35)$
E	$\in (90, 150)$	$\in (0.20, 0.35)$
VR	$\in (90, 150)$	$\in (0.35, 0.60)$

In Table 4.37 we summarise the background estimates in the regions defined for SR2ℓ_Low, region A, region B and region D. All estimates include not only statistical uncertainties but also systematic uncertainties from experimental sources. The pre-fit Z/γ^*+jets contribution is not present as we do not use the MC estimate; instead, we use the data-driven fit approach. The efficiency factors between the different regions dominate the contribution to the Z/γ^*+jets uncertainty. Given we vary all regions simultaneously, and given the Z/γ^*+jets estimates are proportional to the efficiency factors, we expect to see strong correlations between the estimates. For each region, we have appropriately high purities in Z/γ^*+jets, and minimal uncertainties on non-dominant backgrounds.

We show the cross-validation of the ABCD estimate in Table 4.38, where we compare the ABCD, the m_{jj} sideband fit method and also the MC estimate itself. What we find is that both the ABCD and m_{jj} sideband fit have very similar estimates, but that the ABCD estimate has a smaller uncertainty.

4.13.2 SR2ℓ_ISR Z/γ^*+jets Estimation

When applying the ABCD method to SR2ℓ_ISR, we must approach things a little differently compared to the standard approach. Unlike the standard approach, the ISR approach only uses RJR variables to define the selections. In the ISR approach we choose to use M_J and $P_{T,I}^{CM}$. Here M_J is the mass of the jet system within the sparticle system of the ISR decay tree and $P_{T,I}^{CM}$ is the momentum of the invisible system in the centre of mass frame. We make this selection by comparing all variables which define SR2ℓ_ISR, and M_J and $P_{T,I}^{CM}$ produce the least correlated 2D distribution in Z/γ^*+jets. We show the 2D distribution of these two variables in Figure 4.54a, here, we see that the two variables have a correlation factor of 0.03, and this correlation factor is perfectly acceptable in order to apply the ABCD method.

The ISR SR is defined for $P_{T,I}^{CM} > 100$ GeV and $M_J \in (50, 110)$ GeV, and thus it is unbounded in the $P_{T,I}^{CM}$ dimension. The six regions we define here are region A, defined for low M_J and high $P_{T,I}^{CM}$; region B, defined for low M_J and low $P_{T,I}^{CM}$; region D, defined

Table 4.37: The full run-II ABCD Z/γ^*+jets estimation for SR2ℓ_Low, A, B, and D. We show the pre-fit yields in the bottom section of the table. The pre-fits do not include the Z/γ^*+jets MC as we do not use it in the fit. The total non-Z/γ^*+jets background is shown - instead of the prefit total exp. MC for the SM. We do this as we do not use the Z/γ^*+jets MC, and only have an estimate after this fit procedure.

Full run-II	SR2ℓ_Low	A	B	D
Observed events	–	123	1185	359
Fitted SM events	–	123.00 ± 10.96	1184.97 ± 35.25	358.99 ± 18.70
Fitted Higgs events	–	0.21 ± 0.02	1.17 ± 0.78	$0.30^{+1.24}_{-0.30}$
Fitted Triboson events	–	$0.03^{+0.04}_{-0.03}$	$0.01^{+0.01}_{-0.01}$	$0.04^{+0.07}_{-0.04}$
Fitted Diboson events	–	16.64 ± 2.54	11.32 ± 3.70	8.71 ± 3.01
Fitted Top other events	–	0.01 ± 0.01	0.00 ± 0.00	$0.02^{+0.03}_{-0.02}$
Fitted $t\bar{t}$ events	–	4.62 ± 1.21	0.67 ± 0.61	$0.44^{+0.65}_{-0.44}$
Fitted Single top events	–	1.15 ± 0.58	$0.59^{+1.01}_{-0.59}$	$0.26^{+0.53}_{-0.26}$
Fitted Fakes events	–	1.80 ± 0.64	5.27 ± 4.07	3.31 ± 1.74
Fitted Z/γ^*+jets events	29.23 ± 7.58	98.54 ± 11.37	1165.94 ± 36.03	345.91 ± 19.22
Total exp. SM events	–	26.72 ± 3.08	20.50 ± 7.94	14.21 ± 5.90
MC exp. Higgs events	–	0.21 ± 0.02	1.17 ± 0.79	$0.30^{+1.25}_{-0.30}$
MC exp. Triboson events	–	$0.03^{+0.04}_{-0.03}$	$0.01^{+0.01}_{-0.01}$	$0.04^{+0.07}_{-0.04}$
MC exp. Diboson events	–	18.75 ± 2.36	12.76 ± 4.01	9.82 ± 3.27
MC exp. Top other events	–	0.01 ± 0.01	0.00 ± 0.00	$0.02^{+0.03}_{-0.02}$
MC exp. $t\bar{t}$ events	–	4.74 ± 1.25	0.68 ± 0.63	$0.45^{+0.67}_{-0.45}$
MC exp. Single top events	–	1.18 ± 0.60	$0.61^{+1.05}_{-0.61}$	$0.26^{+0.55}_{-0.26}$
DD exp. Fakes events	–	1.80 ± 0.65	5.27 ± 4.11	3.31 ± 1.75
MC exp. Z/γ^*+jets events	–	–	–	–

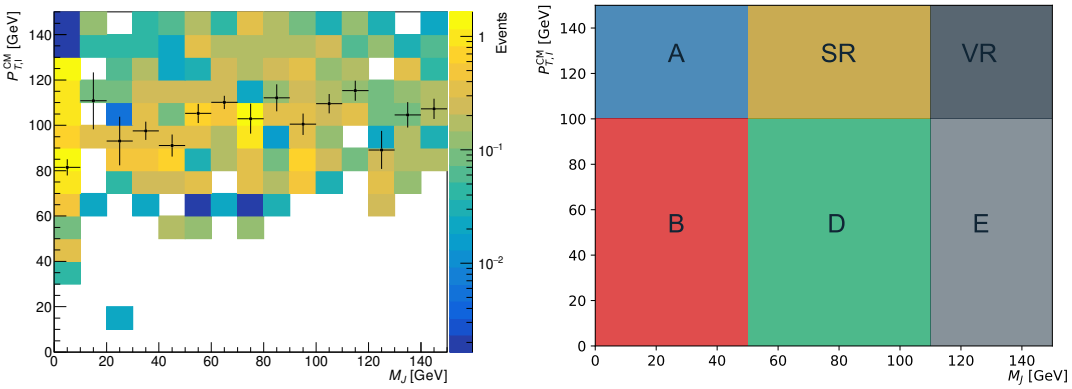

(a) Z/γ^*+jets correlations. (b) ABCD 2D plane.

Figure 4.54: The plane defining our ABCD regions for SR2ℓ_ISR Z/γ^*+jets estimate. In the left plot the black dots are a profile of each vertical slice. In the right plot we have the regions labelled for the method.

Table 4.38: The full run-II SR2ℓ_Low Z/γ^*+jets background estimations. We compare three different methods to estimate this background. The first is the MC, the second is the m_{jj} sideband fit method, which uses Z/γ^*+jets MC and the final is the ABCD method which is independent of the Z/γ^*+jets MC and is instead data driven. We see agreement between the three estimation methods.

Region	Estimate (Stat.+Sys.)
$N_{\text{ABCD}}^{Z+\text{jets}}$	29.23 ± 7.58
$N_{m_{jj}}^{Z+\text{jets}}$	28.14 ± 17.3
$N_{\text{MC}}^{Z+\text{jets}}$	42.20 ± 17.23

for nominal M_J and low $P_{T,I}^{CM}$; region E, defined for high M_J and low $P_{T,I}^{CM}$ and region VR, defined for high M_J and high $P_{T,I}^{CM}$. These six regions are shown in Figure 4.54b and Table 4.39. Note, A-VR refers to the combination of the regions, and not the subtraction.

Table 4.39: SR2ℓ_ISR ABCD selection criteria for m_{jj} and $H_{1,1}^{\text{PP}}/H_{4,1}^{\text{PP}}$ variables.

Region	m_J	$P_{T,I}^{CM}$
A_{ISR}	$\in (0, 50)$	> 100
B_{ISR}	$\in (0, 50)$	< 100
D_{ISR}	$\in (50, 110)$	< 100
E_{ISR}	$\in (110, 130)$	< 100
VR_{ISR}	$\in (110, 130)$	> 100
SR2ℓ_ISR	$\in (50, 110)$	> 100

In Table 4.40 we summarise the region breakdown of background estimates for SR2ℓ_ISR, region A, region B and region D. Just as with the estimate for SR2ℓ_Low we find that the Z/γ^*+jets contribution in these regions is appropriately high.

We show the cross-validation of the ISR ABCD estimate in Table 4.41, where we compare the ABCD, the m_{jj} sideband fit method, and also the MC estimate itself. What we find is that both the ABCD and m_{jj} sideband fit have very similar nominal values for the estimate, but that the ABCD estimate has a preferable uncertainty due to being entirely data-driven.

Table 4.40: The full run-II ABCD Z/γ^*+jets estimation for SR2ℓ_ISR and ABCD regions. We show the pre-fit yields in the bottom section of the table. The pre-fits do not include the Z/γ^*+jets MC as we do not use it in the fit. The total non-Z/γ^*+jets background is shown - instead of the prefit total exp. MC for the SM. We do this as we do not use the Z/γ^*+jets MC, and only have an estimate after this fit procedure.

Full run-II	SR2ℓ_ISR	A-VR	B-E	D
Observed events	–	42	32	22
Fitted bkg events	–	42 ± 6	32 ± 6	22 ± 5
Fitted Higgs events	–	$0.01^{+0.01}_{-0.01}$	$0.00^{+0.00}_{-0.00}$	$0.00^{+0.00}_{-0.00}$
Fitted Triboson events	–	$0.09^{+0.11}_{-0.09}$	$0.01^{+0.02}_{-0.01}$	$0.01^{+0.01}_{-0.01}$
Fitted Diboson events	–	13 ± 2	1.7 ± 0.6	1.3 ± 1.2
Fitted Top other events	–	0.11 ± 0.06	$0.01^{+0.02}_{-0.01}$	0.00 ± 0.00
Fitted $t\bar{t}$ events	–	10.0 ± 2.3	1.5 ± 0.8	0.8 ± 0.4
Fitted Single top events	–	$1.1^{+1.7}_{-1.1}$	$0.3^{+0.7}_{-0.3}$	0.00 ± 0.00
Fitted Fakes events	–	0.00 ± 0.00	0.7 ± 0.2	0.00 ± 0.00
Fitted Z/γ^*+jets events	13 ± 8	18 ± 8	28 ± 6	10 ± 5
Total exp. SM events	–	29 ± 4	5.0 ± 2.0	3 ± 2
MC exp. Higgs events	–	$0.01^{+0.01}_{-0.01}$	$0.00^{+0.00}_{-0.00}$	$0.00^{+0.00}_{-0.00}$
MC exp. Triboson events	–	$0.09^{+0.11}_{-0.09}$	$0.01^{+0.02}_{-0.01}$	$0.01^{+0.01}_{-0.01}$
MC exp. Diboson events	–	16 ± 1	2.1 ± 0.7	1.7 ± 1.4
MC exp. Top other events	–	0.11 ± 0.06	$0.01^{+0.02}_{-0.01}$	0.00 ± 0.00
MC exp. $t\bar{t}$ events	–	12 ± 3	1.8 ± 0.9	1.0 ± 0.5
MC exp. Single top events	–	$1.23^{+2.0}_{-1.3}$	$0.3^{+0.9}_{-0.3}$	0.00 ± 0.00
DD exp. Fakes events	–	0.00 ± 0.00	0.7 ± 0.2	0.00 ± 0.00
MC exp. Z/γ^*+jets events	–	–	–	–

Table 4.41: The full run-II SR2ℓ_ISR Z/γ^*+jets background estimations. We compare three different methods to estimate this background. The first is the MC, the second is the m_{jj} sideband fit method, which uses Z/γ^*+jets MC and the final is the ABCD method which is independent of the Z/γ^*+jets MC and is instead data-driven. We see agreement with the three separate methods. The uncertainty on the MC is purely statistical.

Region	Estimate (Stat.+Sys.)
$N^{Z+\text{jets}}_{\text{ABCD}}$	13.19 ± 7.70
$N^{Z+\text{jets}}_{m_{jj}}$	13.37 ± 18.27
$N^{Z+\text{jets}}_{\text{MC}}$ (Stat. only)	17.57 ± 1.82

Table 4.42: Summary of the main sources of systematic uncertainties and their impact (in %) on the SM background prediction in each of the 2ℓ and 3ℓ SRs. The total systematic can be different from the sum in quadrature of individual uncertainties due to the correlations between them resulting from the fit to the data.

Signal Region	SR2ℓ_Low	SR2ℓ_ISR	SR3ℓ_Low	SR3ℓ_ISR
Total uncertainty [%]	20	28	9	25
Z/γ^*+jets data-driven estimate	16	24	–	–
VV theoretical uncertainties	4	13	3	25
Top theoretical uncertainties	2	8	–	–
MC statistical uncertainties	15	18	14	24
VV fitted normalisation	2	3	7	21
$t\bar{t}$ fitted normalisation	< 1	2	–	–
Fakes leptons	< 1	< 1	< 1	< 1
Jet energy resolution	6	2	2	13
Jet energy scale	2	< 1	3	< 1
E_T^{miss}	2	4	4	3
Lepton reconstruction/identification	< 1	2	3	2

4.14 Results

We have fully validated our background estimation methods for each of the four SRs in our analysis. In this section we will fully summarise the finalised background estimations, as well as breakdown the uncertainties contributing to our estimates. Once we have detailed our systematics breakdown we will then detail the observed events in these regions.

In each of our regions we summarise the contribution to the uncertainties in 11 separate categories. These categories include: Z/γ^*+jets data-driven estimate, VV theoretical uncertainties, top theoretical uncertainties, MC statistical uncertainties, VV fitted normalisation, $t\bar{t}$ fitted normalisation, fake leptons, jet energy resolution, jet energy scale, E_T^{miss}, and lepton reconstruction or identification. The sources of uncertainty are summarised in Table 4.42, and the total uncertainties for each SR are 20%, 28%, 9%, and 15% for SR2ℓ_Low, SR2ℓ_ISR, SR3ℓ_Low, and SR3ℓ_ISR, respectively. The major source of uncertainty in the two 2ℓ SRs comes from the Z/γ^*+jets data-driven estimates. In the case of SR2ℓ_Low, this uncertainty corresponds to 16% of the total estimated background, whereas for SR2ℓ_ISR corresponds to 24% of the total estimated background. The major uncertainty for the 3ℓ signal regions MC statistical uncertainties for SR3ℓ_Low and an equal contribution from VV theoretical uncertainties, MC statistical uncertainties, and VV fitted normalisation, for SR3ℓ_ISR. Typically the uncertainties on the ISR SRs are greater than those in the standard SRs, and this is larger due to the theory uncertainties being larger for those regions.

We now summarise the results of each of our four SRs, including all statistical and systematic sources of uncertainty. In SR2ℓ_Low, we predict a total SM estimate of

44.85 ± 8.91, and we observe 41 events. In SR2ℓ_ISR, we predict a total SM estimate of 31.71 ± 8.95, and we observe 33 events. The summary for both 2ℓ regions is found in Table 4.43.

Table 4.43: The full run-II total background estimate for SR2ℓ_Low and SR2ℓ_ISR including all experimental systematics

Full run-II	SR2ℓ_Low	SR2ℓ_ISR
Observed events	41	33
Fitted SM events	45 ± 9	32 ± 9
Fitted Higgs events	$0.4^{+0.7}_{-0.4}$	$0.01^{+0.01}_{-0.01}$
Fitted Triboson events	$0.06^{+0.09}_{-0.06}$	$0.05^{+0.06}_{-0.05}$
Fitted Diboson events	11 ± 2	9.0 ± 4.2
Fitted Top other events	0.06 ± 0.02	0.5 ± 0.4
Fitted $t\bar{t}$ events	3.8 ± 1.8	8.3 ± 3.1
Fitted Single top events	$0.7^{+0.8}_{-0.7}$	$0.03^{+0.12}_{-0.03}$
Fitted Fakes events	$0.01^{+0.09}_{-0.01}$	0.7 ± 0.2
Fitted Z/γ^*+jets events	29 ± 8	13 ± 8
Total exp. non-Z/γ^*+jets events	17 ± 4	22 ± 6
MC exp. Higgs events	$0.4^{+0.7}_{-0.4}$	$0.01^{+0.01}_{-0.01}$
MC exp. Triboson events	$0.06^{+0.09}_{-0.06}$	$0.05^{+0.06}_{-0.05}$
MC exp. Diboson events	12 ± 2	11 ± 5
MC exp. Top other events	0.06 ± 0.02	0.5 ± 0.4
MC exp. $t\bar{t}$ events	4 ± 2	10 ± 4
MC exp. Single top events	$0.8^{+0.8}_{-0.8}$	$0.03^{+0.14}_{-0.03}$
DD exp. Fakes events	$0.01^{+0.09}_{-0.01}$	0.7 ± 0.2
MC exp. Z/γ^*+jets events	–	–

In SR3ℓ_Low, we predicted a total SM background estimation of 48.96 ± 4.36 and an observed number of events of 53. In SR3ℓ_ISR, we predicted a total SM background estimation of 17.41 ± 2.03 with a total number of observed events of 25. We show the full background estimation summary for these regions in Table 4.44.

4.14.1 Signal Region Modelling

We summarise the modelling for each SR in Figures 4.55–4.58. In all distributions we apply the normalisation factors, and in the case of the 2ℓ SRs we use the Z/γ^*+jets MC and normalise to our ABCD estimates. We first look at SR2ℓ_Low for which we see agreement within large uncertainties. Next, we look at SR2ℓ_ISR, where we see great agreement between the observed number of events and the MC, we also see good agreement in the overall modelling. For SR3ℓ_Low and SR3ℓ_ISR we predict smaller MC uncertainties, and good agreement between the observed events and the SM expectations.

Table 4.44: The full run-II total background estimate for SR3ℓ_Low and SR3ℓ_ISR including all experimental systematics

Full run-II	SR3ℓ_Low	SR3ℓ_ISR
Observed events	53	25
Fitted SM events	49 ± 14	17 ± 4
Fitted Diboson events	47 ± 14	16 ± 4
Fitted Triboson events	0.40 ± 0.07	$0.14^{+0.04}_{-0.04}$
Fitted Top other events	$0.05^{+0.03}_{-0.03}$	$0.4^{+0.2}_{-0.2}$
Fitted Fakes events	1.4 ± 0.4	0.8 ± 0.3
Total exp. SM events	52 ± 15	19 ± 4
MC exp. Diboson events	51 ± 15	17 ± 4
MC exp. Triboson events	0.40 ± 0.07	$0.14^{+0.04}_{-0.04}$
MC exp. Top other events	$0.05^{+0.03}_{-0.03}$	$0.4^{+0.2}_{-0.2}$
DD exp. Fakes events	1.4 ± 0.4	0.8 ± 0.3

SR3ℓ_ISR has good overall agreement with the SM expectation, we observe more events than the SM prediction.

4.14.2 Model Independent Limits

We take the expected estimates and directly compare to the observed number of events to set model-independent limits on possible signal contributions to these regions. In Table 4.45, we show the model-independent limits for all SRs in this analysis.

In this table we show the 95% CL upper limits on the visible cross-section ($\langle\epsilon\sigma\rangle^{95}_{\text{obs}}$) for a model-independent signal, the 95% CL upper limits on the number of signal events (S^{95}_{obs}), the 95% CL upper limit on the number of signal events given the expected number of background events (S^{95}_{exp}). We also show the CL_b value and the p-value for a background-only hypothesis.

In SR2ℓ_Low, we found that the observed number of events was consistent with the background estimation, with a p-value of 0.69, corresponding to a Z-score of -0.49σ. In SR2ℓ_ISR, we found that the observed number of events was consistent with the background estimation, with a p-value of 0.53, corresponding to a Z-score of -0.07σ.

For SR3ℓ_Low, we found that the observed number of events and the SM background estimation were in good agreement, with a p-value of 0.66, which corresponds to a Z-score of 0.41σ. For SR3ℓ_ISR, we found the observed number of events and the background estimation to be in agreement, with a p-value of 0.08, which corresponded to a Z-score of 1.42σ.

Finally, the 95% CLs upper limit of the visible cross-sections $\langle\epsilon\sigma\rangle^{95}_{\text{obs}}$[fb], of any signal

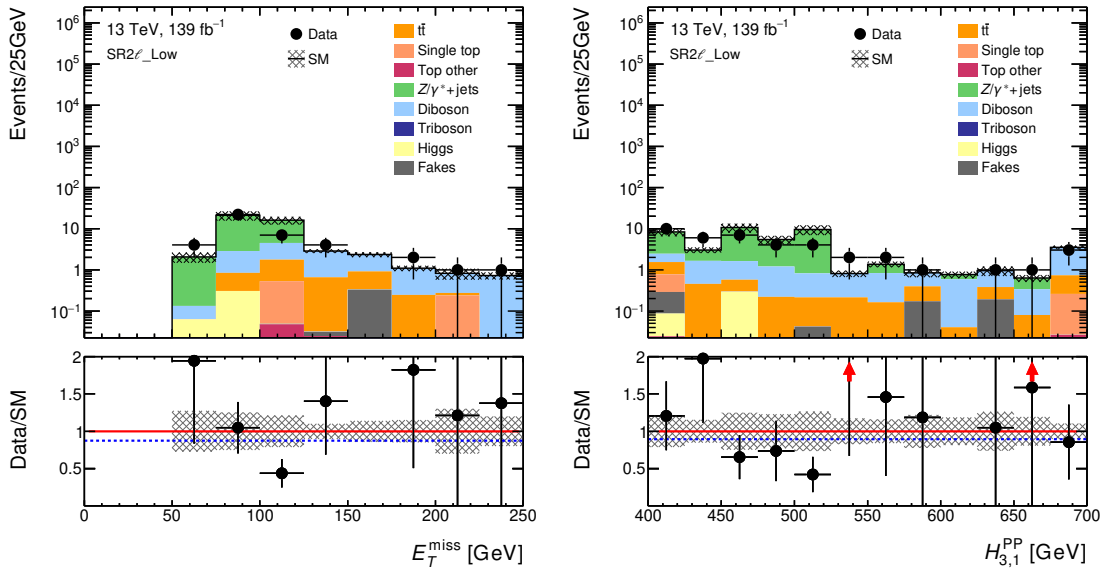

(a) E_T^{miss} (b) $H_{4,1}^{\text{PP}}$

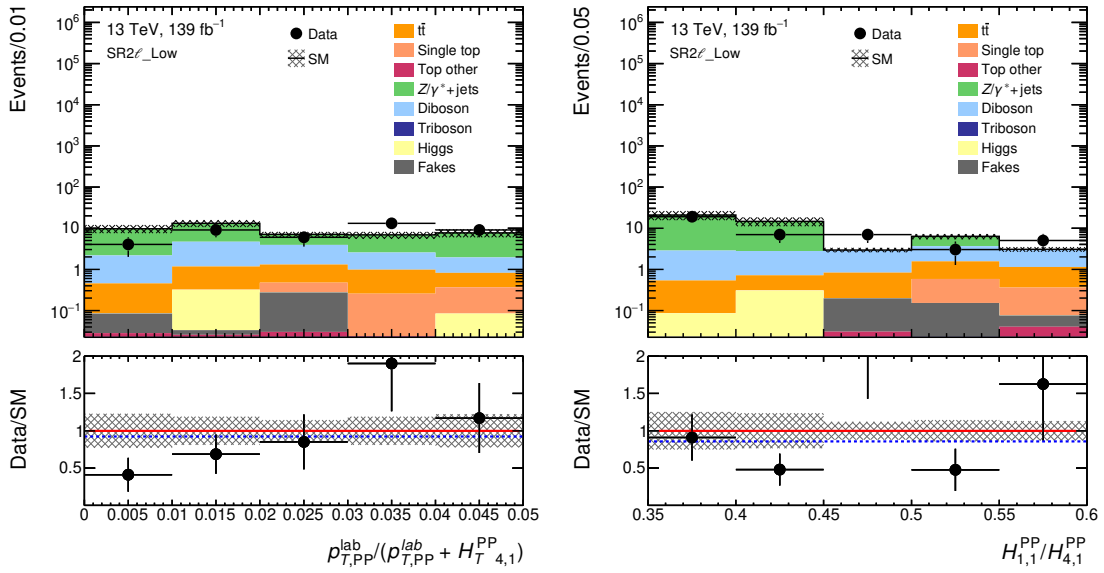

(c) R_{p_T} (d) $H_{1,1}^{\text{PP}}/H_{4,1}^{\text{PP}}$

Figure 4.55: SR2ℓ_Low: Modelling for (a) E_T^{miss}, (b) $H_{4,1}^{\text{PP}}$, (c) R_{p_T} and (d) $H_{1,1}^{\text{PP}}/H_{4,1}^{\text{PP}}$.

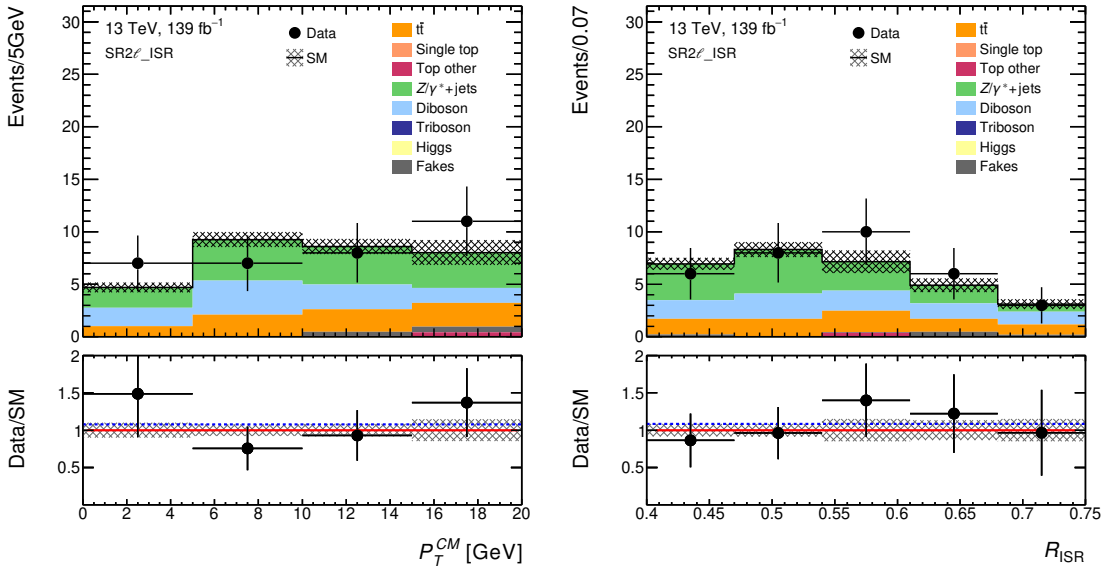

(a) E_T^{miss} (b) R_{ISR}

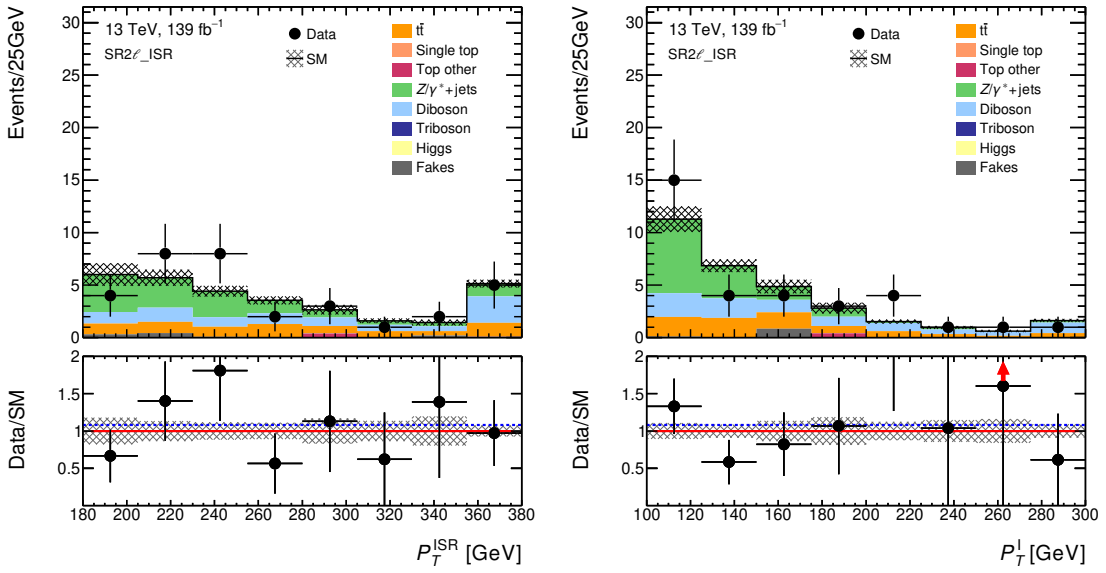

(c) p_T^{ISR} (d) P_T^I

Figure 4.56: SR2ℓ_ISR: Modelling for (a) P_T^{CM}, (b) R_{ISR}, (c) p_T^{ISR} and (d) P_T^{I}.

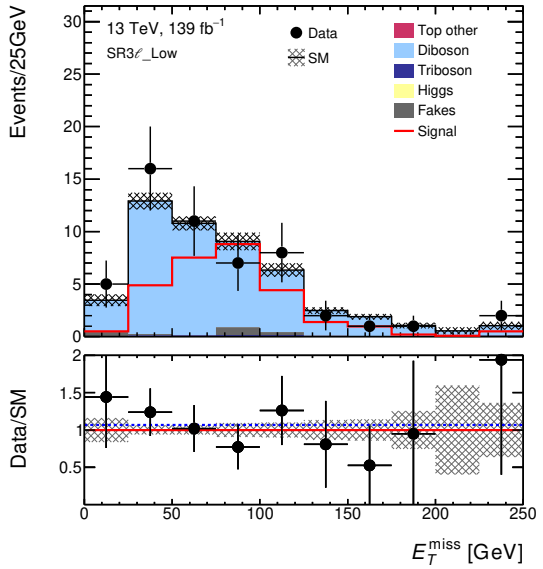

(a) E_T^{miss}

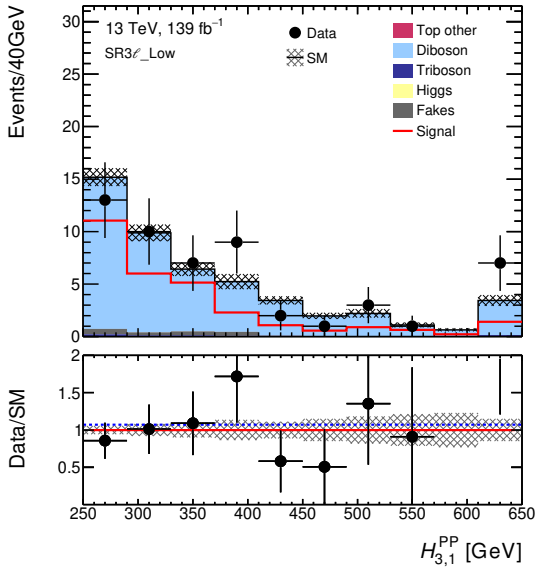

(b) $H_{3,1}^{\text{PP}}$

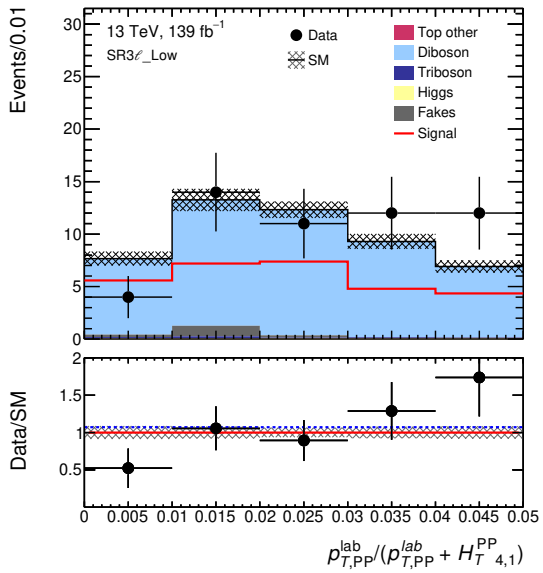

(c) R_{p_T}

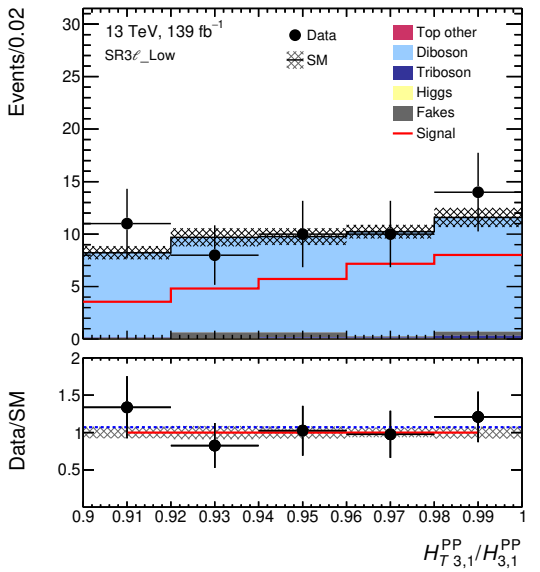

(d) $H_{T\ 3,1}^{\text{PP}}/H_{3,1}^{\text{PP}}$

Figure 4.57: SR3ℓ_Low: Modelling for (a) E_T^{miss}, (b) $p_T^{\ell_1}$, (c) R_{p_T} and (d) $H_{1,1}^{\text{PP}}/H_{4,1}^{\text{PP}}$.

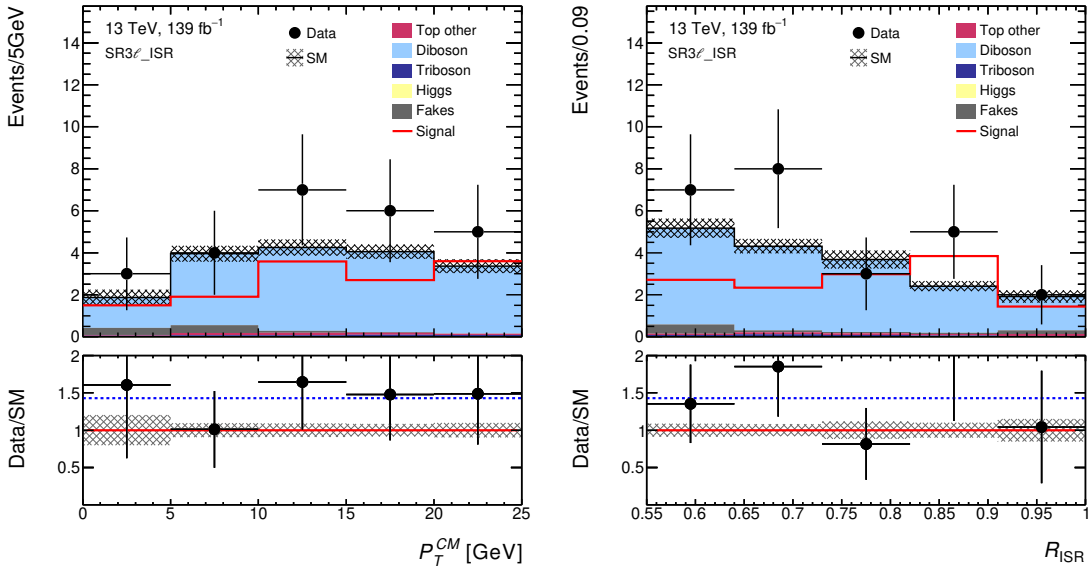

(a) p_T^{CM}

(b) R_{ISR}

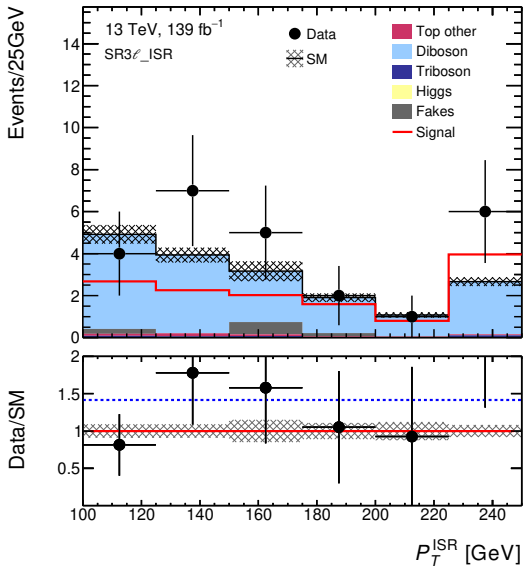

(c) p_T^{ISR}

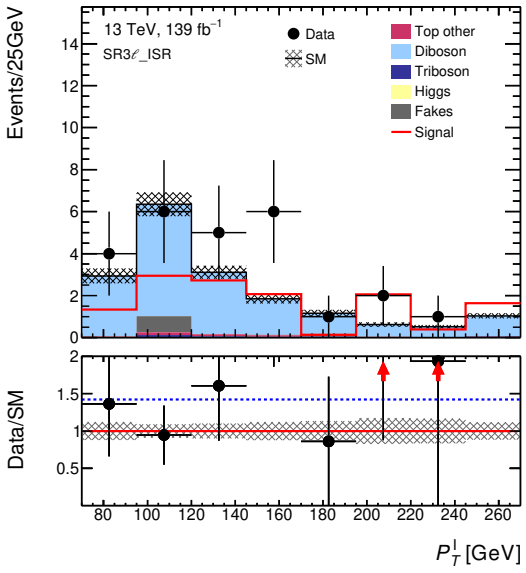

(d) P_T^I

Figure 4.58: SR3ℓ_ISR: Modelling for (a) p_T^{CM}, (b) R_{ISR}, (c) p_T^{ISR} and (d) P_T^{I}.

present within our SRs are 0.15, 0.17, 0.15, and 0.09 for SR2ℓ_Low, SR2ℓ_ISR, SR3ℓ_Low, and SR3L_ISR, respectively.

Table 4.45: Left to right: 95% CL upper limits on the visible cross-section ($\langle\epsilon\sigma\rangle^{95}_{\text{obs}}$) and on the number of signal events (S^{95}_{obs}). The third column (S^{95}_{exp}) shows the 95% CL upper limit on the number of signal events, given the expected number (and $\pm 1\sigma$ excursions on the expectation) of background events. The last two columns indicate the CL_B value, i.e. the confidence level observed for the background-only hypothesis, and the discovery p-value ($p(s=0)$).

Signal channel	$\langle\epsilon\sigma\rangle^{95}_{\text{obs}}$[fb]	S^{95}_{obs}	S^{95}_{exp}	CL_B	$p(s=0)$	Z
SR2ℓ_Low	0.15	21.4	$21.0^{+5.6}_{-7.7}$	0.31	0.69	(-0.49)
SR2ℓ_ISR	0.17	23.3	$22.5^{+1.6}_{-4.0}$	0.47	0.53	(-0.07)
SR3ℓ_Low	0.15	21.1	$21.1^{+5.0}_{-3.0}$	0.59	0.66	(0.41)
SR3ℓ_ISR	0.09	13.0	$11.2^{+4.5}_{-2.6}$	0.92	0.08	(1.42)

Chapter 5

Measurement of the Higgs Boson Production Cross-sections

In this chapter, we provide an overview of the discovery of the Higgs boson and then detail our run-II effort to measure the Higgs boson gluon–gluon fusion and vector boson fusion production cross-sections via the $H \to WW^* \to e\nu\mu\nu$ decay channel. We outline the data-driven technique used to estimate the b-tagging efficiency from data. We also provide an overview of the statistical combination of run-II Higgs boson measurements.

5.1 The Discovery of the Higgs Boson

In 2012 a neutral spin-0 boson consistent with the SM Higgs boson was observed. The ATLAS [124] and CMS [126] collaborations observed the particle had production and decay modes consistent with SM predictions. The ATLAS experiment discovery relied on the statistical combination of multiple search channels. Different channels have different cross-sections, backgrounds, and Higgs mass resolutions, as well as varying sensitivities. The $H \to ZZ^* \to 4\ell$ and $H \to \gamma\gamma$ channels have low cross-sections, with smaller backgrounds and overall higher mass resolutions; whereas the $H \to WW^* \to \ell\nu\ell\nu$ decay channel has a larger cross-section with high sensitivity, with poor mass resolution.

The statistical combination of the $\sqrt{s} = 7$ TeV and $\sqrt{s} = 8$ TeV datasets incorporated the $H \to ZZ^*$ channel, $H \to \gamma\gamma$ channel, and the $H \to WW^*$ channels. The statistical combination of these measurements resulted in a global combined significance of 5.1σ. Assuming $m_H = 126$ GeV, the signal estimate relative to SM expectation (signal strength) for the $H \to ZZ^*$ channel was found to be $\mu = 1.2 \pm 0.6$, the $H \to \gamma\gamma$ channel was $\mu = 1.8 \pm 0.5$ and the $H \to WW^*$ channel corresponded to $\mu = 1.3 \pm 0.5$. The statistical combination of these signal strengths resulted in $\mu = 1.4 \pm 0.3$. This measurement corresponds to a discovery of a neutral scalar particle with a mass of $126.0 \pm 0.4(\text{stat}) \pm 0.4(\text{sys})$ GeV. The combined measurement between ATLAS and CMS produced a signal strength of $1.09 \pm 0.007(\text{stat}) \pm 0.08(\text{syst})$ [128].

5.2 Overview of Run-II Approach

In this section, we will outline our run-II $H \to WW^* \to e\nu\mu\nu$ analysis using the 36.1 fb^{-1} proton–proton dataset. The goal of the analysis was to measure the inclusive Higgs boson production cross-section. The production pathways considered include gluon–

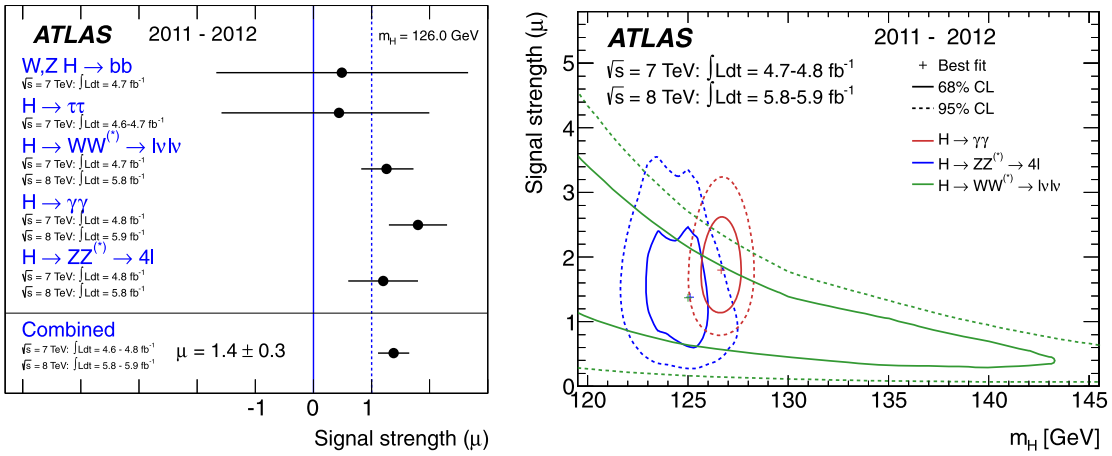

(a) Final state breakdown (b) Mass resolution

Figure 5.1: The combined Higgs signal strength measurements as of 2012 [127], for $m_H = 126$ GeV. In (a) the signal strength is broken down based on Higgs final states. In (b) the mass resolution of the signal strength for different Higgs final states is shown [127].

gluon fusion (ggF) and vector boson fusion (VBF). We show the two leading order Feynman diagrams for the ggF and VBF production processes in Figure 5.2.

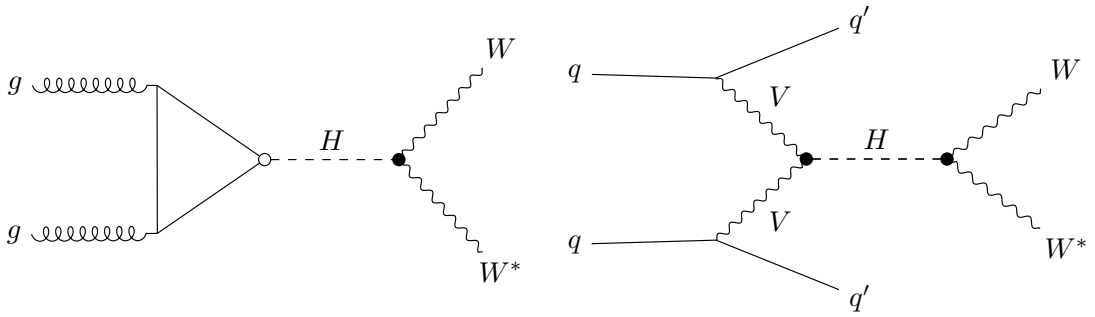

(a) Gluon–gluon fusion. (b) Vector boson fusion.

Figure 5.2: Diagrams for the leading production modes; (a) ggF and (b) VBF. Here we mark the VVH couplings with solid circle verticies and the qqH couplings with empty circles. The particle label "V" refers to a W/Z boson.

The decay pathway we target is $H \to WW^* \to e\nu\mu\nu$, and this is reflected in the design of the analysis. Looking back in Chapter 1, in Table 1.3, the decay process $H \to WW^*$ has the second-highest branching ratio of the Higgs to the SM products. The favourable branching ratio coupled with the favourable decay kinematics of $H \to WW^*$ provided us with the most precise method of measuring the inclusive Higgs boson production cross-sections [128].

Signal and Background Monte Carlo Simulation

The signal and the background MC simulation for each signal and background process description is outlined in [124]. The matrix element generator, PDF sets, underlying event, parton shower model, and prediction order are all summarised in Table 5.1.

Table 5.1: A summary of the MC used in the Higgs measurement [124].

Process	Matrix Element	PDF set	UEPS model	Prediction Order for total cross-section
ggF H	Powheg-Box v2 NNLOPS	PDF4LHC15 NNLO	Pythia 8	N^3LO QCD + NLO EW
VBF H	Powheg-Box v2	PDF4LHC15 NLO	Pythia 8	NNLO QCD + NLO EW
VH	Powheg-Box v2	PDF4LHC15 NLO	Pythia 8	NNLO QCD + NLO EW
$qq \to WW$	Sherpa 2.2.2	NNPDF3.0NNLO	Sherpa 2.2.2	NLO
$qq \to WW$	Sherpa 2.1.1	CT10	Sherpa 2.1	NLO
$WZ/V\gamma^*ZZ$	Sherpa 2.1	CT10	Sherpa 2.1	NLO
$V\gamma$	Sherpa 2.2.2	NNPDF3.0NNLO	Sherpa 2.2.2	NLO
$t\bar{t}$	Powheg-Box v2	NNPDF3.0NLO	Pythia 8	NNLO+NNLL
Wt	Powheg-Box v1	CT10	Pythia 6.428	NLO
Z/γ^*	Sherpa 2.1.1	NNPDF3.0NNLO	Sherpa 2.2.1	NNLO

5.3 Object Reconstruction

Events in this analysis are triggered using single-lepton triggers and a dilepton $e-\mu$ trigger. The lepton transverse momentum threshold ranges between 24 GeV and 26 GeV for single-electron triggers and between 20 GeV and 26 GeV for single-muon triggers, depending on the run period [129]. The $e-\mu$ trigger requires a minimum p_T threshold of 17 GeV for electrons and 14 GeV for muons.

The electrons and muons we use are the same as with those defined in Chapter 3. The jets we use for this analysis are also the same as with Chapter 3. If a reconstructed muon shares an inner detector track with an electron, then we reconstruct the muon, and the electron is removed. If leptons are within $\Delta R = 0.2$ of a reconstructed jet they are also removed. Electrons and muons, with transverse momentum p_T, are removed if they are within $\Delta R = \min(0.4, 0.04 + 10\ \text{GeV}p_T)$ of the axis of any surviving jet.

The missing transverse momentum uses standard definitions of E_T^{miss}, though it was found during the optimisation that p_T^{miss}, using the tracks associated with the jets instead of the calorimeter-measured jets, performs better in terms of background rejection [130], and therefore we use p_T^{miss}.

5.4 Signal Region Definitions

In terms of defining our analysis strategy, the most important categorisation of events is the number of $p_T > 30$ GeV jets present within an event. When targetting the ggF signal mode we look at 0 and 1-jet events. and for VBF production we look at events with at least two jets with $p_T > 30$ GeV. The N_j distribution is shown in Figure 5.3.

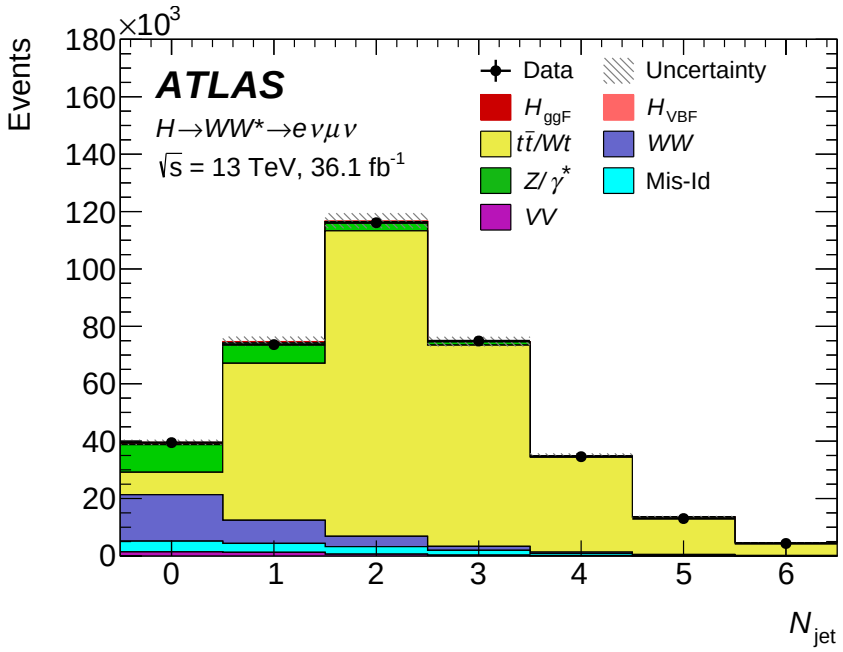

Figure 5.3: The jet multiplicty distribution under preselection criteria. Uncertainties include both statistical and systematic sources [131].

Our SRs are defined to maximise sensitivity to our ggF and VBF signal simulations. The background contributions for the different jet multiplicities vary significantly and motivate the analysis to be binned in N_J; we show this in Figure 5.3. We first make preselections to event-clean. We then apply selections oriented at rejecting background. We then apply selections aimed at selecting for the $H \to WW^* \to e\nu\mu\nu$ topology, and finally, we define the variable which we will extract a background-only significance from, using a simultaneous statistical fit.

For all our regions, we apply loose preslection criteria, such as requiring two isolated, different-flavour leptons ($\ell =$ e or μ) with opposite charge. We require the leading lepton momentum to be $p_T^{\text{lead}} > 22$ GeV and sub-leading transverse momentum of $p_T^{\text{sublead}} > 15$ GeV. We require $m_{\ell\ell} > 10$ GeV to reduce the contribution of Drell–Yan backgrounds, and in $N_J = 0$ and 1 we require $p_T^{\text{miss}} > 20$ GeV.

To reduce background contributions, the $N_J = 0$ SR requires that the azimuthal angle between the dilepton pair and the missing transverse energy $\Delta\phi(\ell\ell, E_T^{\text{miss}})$ to be greater than $\pi/2$, which reduces the contribution of missing transverse energy originating from

lepton mismeasurement. We also require the dilepton system's transverse momentum ($p_T^{\ell\ell}$) to be greater than 30 GeV, which reduces the contribution of Z/γ^*.

The $N_J = 1$ SR selects on $\max(m_T^{\ell_0}, m_T^{\ell_1})$ where,

$$m_T^{\ell_i} = \sqrt{2p_T^{\ell_i} \cdot E_T^{\text{miss}} \cdot (1 - \cos\Delta\phi(\ell_i, E_T^{\text{miss}}))}, \tag{5.1}$$

where i is either the leading or sub-leading lepton. We also demand $m_{\tau\tau} < m_Z - 25$ GeV where $m_{\tau\tau}$ is calculated using the collinear approximation [132]. This selection vetos background from $Z \to \tau\tau$ production. The $N_J \geq 2$ SR applies only the b-jet veto and the $m_{\tau\tau}$ selections.

To select for the $H \to WW^* \to e\nu\mu\nu$ topology $N_J = 0$ and 1 we apply $m_{\ell\ell} < 55$ GeV and $\Delta\phi_{\ell\ell} < 1.8$. Whereas for the $N_J \geq 2$ selection, we apply a central jet veto and an outside lepton veto, this is because the VBF signal process is most likely to produce leptons within the pseudorapidty range. The $N_J = 0$ and 1 use a variable m_T for the simultaneous statistical fit, defined as:

$$m_T = \sqrt{(E_T^{\ell\ell} + E_T^{\text{miss}})^2 - |\mathbf{p}_T^{\ell\ell} + \mathbf{E}_T^{\text{miss}}|^2}, \tag{5.2}$$

where

$$E_T^{\ell\ell} = \sqrt{|\mathbf{p}_T^{\ell\ell}|^2 + m_{\ell\ell}^2}, \tag{5.3}$$

and $\mathbf{p}_T^{\ell\ell}$ is defined as the vector sum of the lepton transverse momenta. In the case of $N_J \geq 2$, we use a BDT output score as our fitting score. The details of the BDT procedure can be found in [124]

5.5 Background Estimation Method

To control the normalisation of the dominant backgrounds in the aforementioned SRs we define CRs. In these CRs, we use data to normalise the MC simulation predictions. In $N_J = 0$ the background contribution is dominated by Z/γ^*, top quark pair production, and non-resonant WW production.

The backgrounds in the $n_J = 1$ SR are dominated first by non-resonant WW production and second by top pair production. The WW contribution accounts for 42% of the total expected background, whereas top pair production accounts for approximately 36% of total expected background. The top pair production background contribution is approximately five times greater than that of the expected ggF and VBF signal contributions. In the WW CR, top pair production and non-resonant WW production both account for approximately 38% of the background contributions of the region. For $N_J \geq 2$ the dominant background is by far top quark pair production, followed by a small contribution from Z/γ^*.

Table 5.2: The $N_J = 1$ control region event selection criteria.

ggF $N_j = 1$	$m_{\ell\ell}$	$\Delta\phi_{\ell\ell}$	N_b	$m_{\tau\tau}$	$\max(m_T^l)$	p_T^{miss}	$p_T^{\ell\ell}$	m_τ	$n_{jet}^{\eta<2.5}$	n_L^{inside}
SR	< 55	< 1.8	$= 0$	$< m_Z - 25$	$> 50 > 20$	–	–	–		
CR-WW	> 80	-	=0	$< m_Z - 25$	> 50	–	–	–	–	–
				$> m_Z + 25$						
CR-Top	–	–	$= 1$	$< m_Z - 25$	> 50	–	–	–	–	–
CR-Z/γ^*	< 80	–	$= 0$	$> m_Z - 25$	> 50	–	–	–	–	–

We summarise the definitions of the CRs in Tables ?? - 5.3. We will summarise the $N_J = 1$ regions, in particular the $N_J = 1$ SR. We define three CRs for the $N_J = 1$ SR. These CRs correspond to the backgrounds Z/γ^*,WW and top quark pair production. The Z/γ^* CR is defined at preselection with the requirement that $m_{\ell\ell} < 80$ GeV, we require $N_b = 0$ and we require an inversion of $m_{\tau\tau}$. We keep $\max\left(m_T^l\right)$ unchanged from the SR definition. The WW CR is defined with $m_{\ell\ell} > 80$ GeV, with $N_b = 0$, we require that $m_{\tau\tau}$ be at least 25GeV more or less than m_Z and we keep $\max m_T^l$ fixed.

Table 5.3: The $N_J \geq 2$ VBF control region event selection criteria.

VBF $N_j \geq 2$	$m_{\ell\ell}$	$\Delta\phi_{\ell\ell}$	N_b	$m_{\tau\tau}$	$\max(m_T^l)$	p_T^{miss}	$p_T^{\ell\ell}$	m_τ	$n_{jet}^{\eta<2.5}$	n_L^{inside}
SR	–	–	$= 0$	$< m_Z - 25$	–	–	–	$= 0$	$= 0$	
Top	–	–	$= 1$	$< m_Z - 25$	–	–	–	–	$= 0$	$= 0$
Z/γ^*	< 80	–	$= 0$	$\in (m_Z - 25, m_Z + 25)$	–	–	–	–	$= 0$	$= 0$

5.5.1 Top Control Regions

To control the top pair production background in the SR we define a top CR. The top CR is defined after preselection criteria, where we require at least 1 b-tagged jet and a $m_T^W > 50$ GeV. To increase statistics, we do not apply topological cuts to the CR. Full region selections are defined in Table 5.2. The SR preselection and the CR background estimates can be related to the preselection background estimates with a b-tagging efficiency ϵ_{tag} or a b-veto efficiency ϵ_{veto} defined as:

$$N_{\text{SR}}^{\text{PRE}} = N^{\text{PRE}} \times \epsilon^{\text{veto}} \tag{5.4}$$

$$N_{\text{CR}} = N^{\text{PRE}} \times \epsilon^{\text{tag}}. \tag{5.5}$$

Here N_{CR} is the aforementioned top CR and $N_{\text{SR}}^{\text{PRE}}$ is the SR defined before topological cuts and orthogonal to the CR via a b-tag veto. The relationship between the two and their preselections is shown in Equation 5.5. We can write the estimate for the SR top background contribution in terms of the CR top background estimate and the efficiency of b-tagging in a $N_J = 1$ sample. To do so in the simplest way requires us to take

$\epsilon^{1j}_{\text{tag}} = 1 - \epsilon^{1j}_{\text{veto}}$. This expression is given via,

$$N^{\text{PRE}}_{\text{SR}} = N_{\text{CR}} \times \frac{\left(1 - \epsilon^{1j}_{\text{tag}}\right)}{\epsilon^{1j}_{\text{tag}}} \tag{5.6}$$

The error propogation for this expression is,

$$\sigma^2_{SR} = \left(\frac{1 - \epsilon^{1j}_{\text{tag}}}{\epsilon^{1j}_{\text{tag}}}\right)^2 \sigma^2_{N_{\text{CR}}} + \left(\frac{N_{CR}}{\epsilon^2}\right)^2 \sigma^2_{\epsilon} \tag{5.7}$$

If we rearrange Equation 5.7 to put it into relative error form then we get an expression showing us the relative error contributions from N_{CR} and $\epsilon^{1j}_{\text{tag}}$:

$$\left(\frac{\sigma_{SR}}{N_{SR}}\right)^2 = \left(\frac{\sigma_{N_{CR}}}{N_{CR}}\right)^2 + \frac{1}{(1 - \epsilon^{1j}_{\text{tag}})^2}\left(\frac{\sigma_{\epsilon}}{\epsilon}\right)^2. \tag{5.8}$$

This reveals a troublesome dependence on the b-tagging experimental systematic uncertainties which come from estimating $\epsilon^{1j}_{\text{tag}}$ from MC. The typical relative error of $\epsilon^{1j}_{\text{tag}}$ to b-tagging experimental systematics is approximately 5%. If we take indicative values of $N_{CR} = 18813 \pm 141$ and $\epsilon^{1j}_{\text{tag}} = 0.746 \pm 0.004$ then the uncertainties as small as 5% uncertainty in the CR top component leads to relative errors in the SR top estimate of approximately 20%.

5.5.2 Data-Driven *b*-jet Efficiency Extraction Method

To reduce the dependence of the b-tagging systematic on the SR top estimation, we estimate the b-tagging efficiency directly from data, and not from the MC. This lets us remove the explicit dependence on the b-tagging efficiency estimates — though we retain our implicit dependencies. To have a baseline we define the MC b-tagging efficiency in a one jet sample as:

$$\epsilon^{\text{MC}}_{\text{Tag}} = \frac{N_{\text{1j1b}}}{N_{\text{1j0b}} + N_{\text{1j1b}}}, \tag{5.9}$$

where N_X is the top pair production yield corresponding to the CR indicated. To extract a data-driven estimate of this efficiency we can use a tag and probe approach. To use a tag and probe approach, we will require a two jet CR sample. We define two new regions both with two jets required with either a one b-tag or two b-tag selection. The regions entering into our data-driven b-tagging estimate are summarised in Figure 5.4.

We label the efficiency of a b-tag selection in a two jet selection with $\epsilon^{\text{Data}}_{\text{2j}}$. We must first ensure that the modelling and the shape differences between the one jet and the two jet selections are appropriately similar. There are different choices that we can make when comparing the kinematic distributions in a tag and probe approach. The first method is to plot the kinematic distributions of only of the leading p_T jet. The second approach is

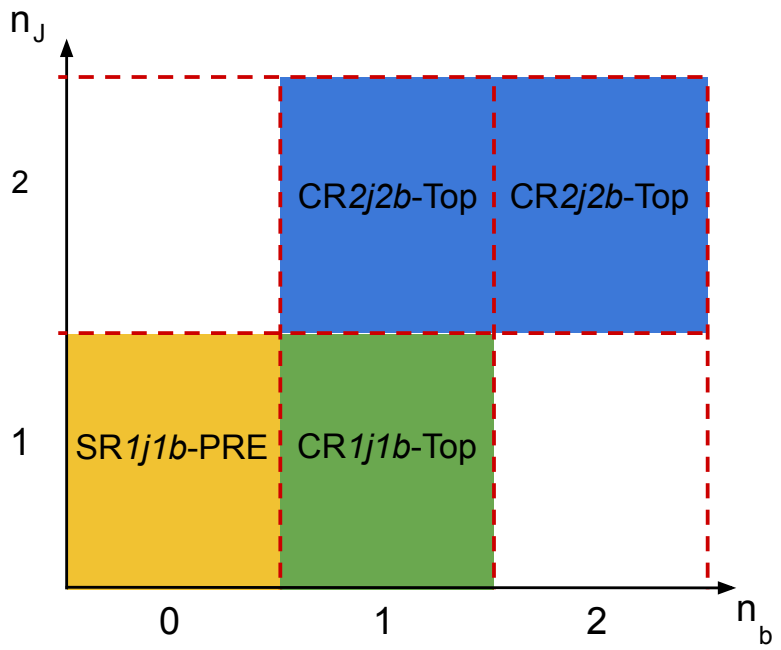

Figure 5.4: A summary of the jet and b-tag selection requirements for the top CRs and b-tagging efficiency CRs.

only to plot the distributions of the sub-leading jet, and the third approach is to select a jet in each selection randomly. We show the tag and probe approach in Figure 5.5.

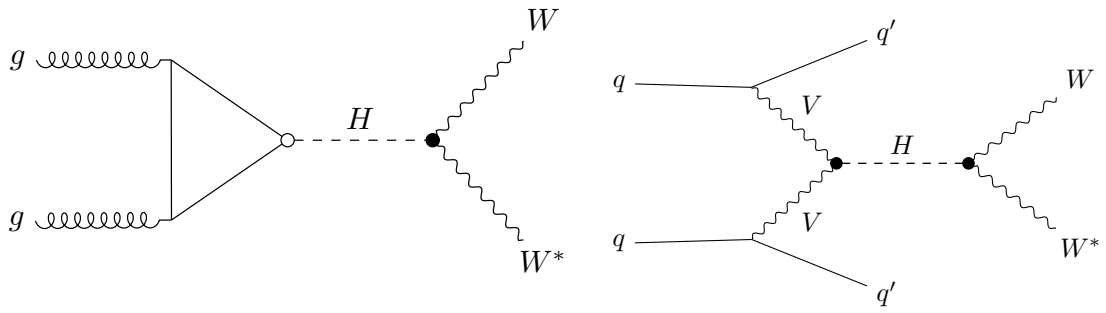

(a) Gluon–gluon fusion. (b) Vector boson fusion.

Figure 5.5: Top CR distributions of $t\bar{t}$ and Wt jet p_T in $n_j = 2$ (2j probe) events and $n_j = 1$ events. For each $n_j = 2$ event one of the two jets is chosen randomly and the p_T of that jet enters the distribution if the other jet is tagged. The left plot is for the run-I $\sqrt{s} = 8$ TeV dataset, and the right plot is for run-II 2015 MC. The distributions in both cases are similar with deviations only for low jet p_T.

Given the modelling is good in our control regions, we can then write the efficiency of

$\epsilon_{\mathrm{2j}}^{\mathrm{Data}}$ as:

$$\epsilon_{\mathrm{2j}}^{\mathrm{Data}} = \frac{N_{\mathrm{2j1b}}}{\frac{1}{2}N_{\mathrm{2j1b}} + N_{\mathrm{2j2b}}}. \tag{5.10}$$

We can relate this efficiency in a two jet selection in data to an estimate for the efficiency in a one jet selection with:

$$\epsilon_{1j}^{\mathrm{EST}} = \epsilon_{2j}^{\mathrm{Data}} \times f^{\mathrm{correction}} \qquad \text{where } f^{\mathrm{correction}} = \frac{\epsilon_{1j}^{\mathrm{MC}}}{\epsilon_{2j}^{\mathrm{MC}}}, \tag{5.11}$$

where $f^{\mathrm{correction}}$ is the term which accounts for kinematic deviations between the one jet and two jet selections. Given that the modelling is good in all CRs we can be confident that the deviation in this term is driven by the true underlying kinematics and not mismodelling.

To apply the data-driven b-tag extraction method we need the background information from four regions, the SR1j0b-PRE, CR1j1b-Top, CR2j1b-Top, and CR2j2b-Top regions.

Table 5.4: The yield breakdown for the different regions used for calculating the b-tagging efficiency. We show preselection of the SR and one top CR and two regions for b-tag efficiency extraction [131].

Region	SR1j0b-PRE	CR1j1b-Top	CR2j1b-Top	CR2j2b-Top
WW	6085.82 ± 22.80	319.79 ± 5.84	202.72 ± 4.38	9.95 ± 0.92
other VV	454.19 ± 10.50	30.84 ± 3.26	27.17 ± 2.36	1.26 ± 0.62
V+γ	307.94 ± 22.62	24.35 ± 6.59	21.19 ± 5.12	0.38 ± 0.29
Top	7359.65 ± 36.84	20263.98 ± 64.18	30060.93 ± 76.97	30502.72 ± 80.07
Z/γ^*	1305.75 ± 114.47	139.35 ± 23.60	110.43 ± 18.81	10.63 ± 5.60
VBF [125GeV]	$35.37.10 \pm 0.51$	2.10 ± 0.13	5.25 ± 0.21	0.16 ± 0.04
ggF [125GeV]	455.10 ± 4.62	26.23 ± 1.19	18.01 ± 1.01	1.51 ± 0.26
Total	16827.55 ± 129.68	21168.96 ± 72.94	30955.48 ± 84.46	30848.95 ± 84.40
Data	16737	20758	30678	329512
Data/SM	0.99 ± 0.01	0.98 ± 0.01	0.99 ± 0.01	0.96 ± 0.01
Top Purity	0.44	0.96	0.97	0.99

These regions have a top purity of 0.99 ± 0.01, 0.98 ± 0.01, 0.99 ± 0.01 and 0.96 ± 0.01 respectively. The Data/SM ratio for all regions is acceptable for all regions. The yields are summarised in Table 5.4 and the modelling for the leading jet in these regions is shown in Figures 5.6–5.8.

5.5.3 Signal Region Top Pair Production Estimation

The MC estimate for the b-taggin efficiency is $\epsilon_{1j}^{MC} = 0.736 \pm 0.003$, with the data-driven estimate being extracted to be $\epsilon_{1j}^{\mathrm{EST}} = 0.727 \pm 0.004$, with the b-tagging efficiency in data

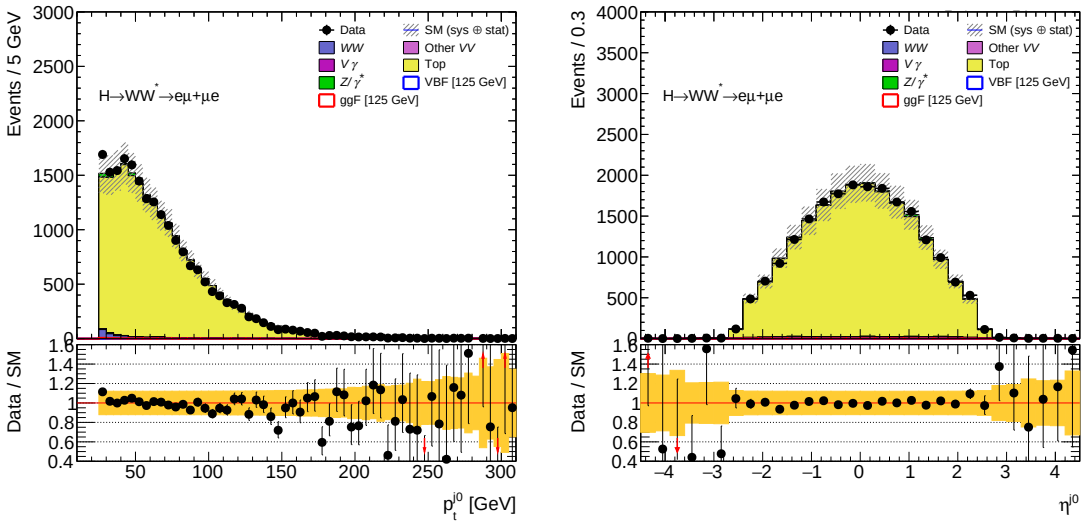

(a) CR1j1b-Top p_T (b) CR1j1b-Top p_T

Figure 5.6: We show the modelling for CR1j2b-Top. In (a) we show the leading jet p_T. In (b) we show the leading jet η.

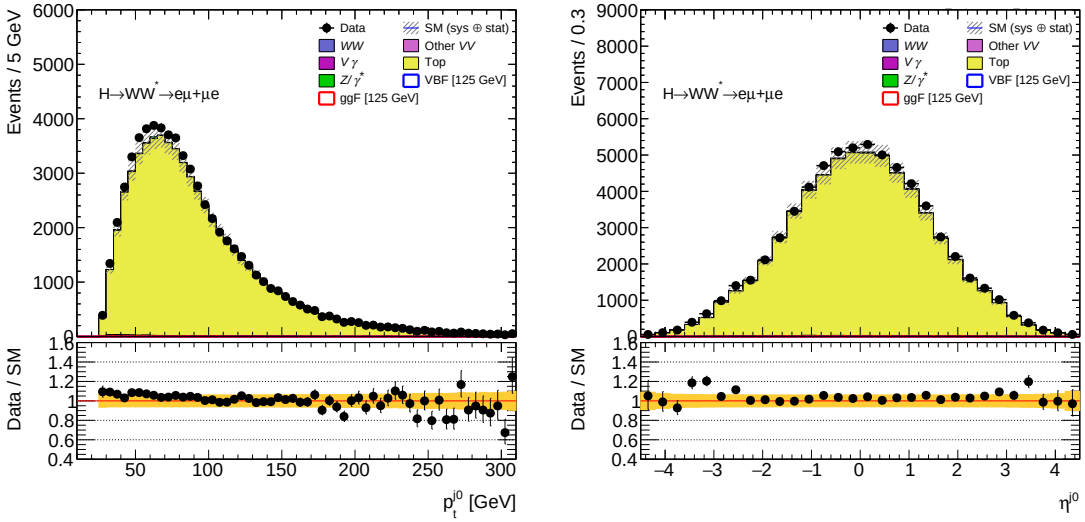

(a) CR2j1b-Top p_T (b) CR2j1b-Top p_T

Figure 5.7: We show the modelling for CR2j2b-Top. In (a) we show the leading jet p_T. In (b) we show the leading jet η.

being less than the MC prediciton. The overall top background normalisation factor is dependent on the b-tagging efficiency, and by more accurately measuring the b-tagging efficiency we can get a more accurate estimate in the SR.

Using the MC b-tagging efficiency ϵ_{1j}^{MC} we get a SR1j0b-PRE top contribution of $N_{1j0b} = 7360 \pm 37$. By instead using the data-driven estimate $\epsilon_{1j}^{\text{EST}}$ we estimate $N_{1j0b} = 7459 \pm 152$. The difference between these two methods corresponds to a total normalisation of 1.01 ± 0.02. We summarise the quantities used in these calculations in Table 5.5.

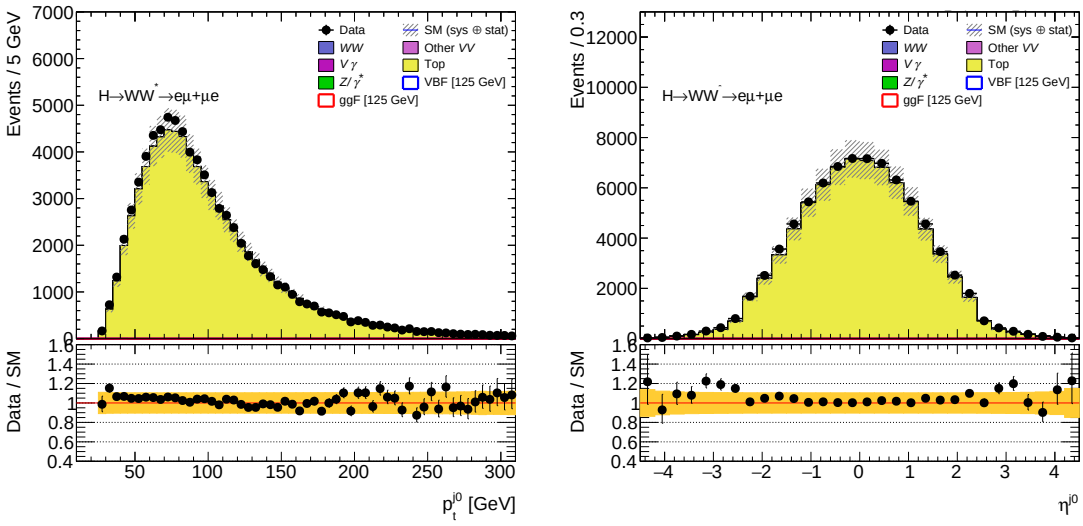

(a) CR2j2b-Top p_T (b) CR2j2b-Top p_T

Figure 5.8: We show the modelling for CR2j2b-Top. In (a) we show the leading jet p_T. In (b) we show the leading jet η.

Table 5.5: We summarise and compare the different estimates which enter into the b-tag efficiency calculation, for both run-I [124] and run-II. See text for description.

	Run-I $[e\mu + \mu e]$	Run-II $[e\mu + \mu e]$
$N_{\text{top}}^{\text{MC},1j0b}$	2000 ± 5	7360 ± 37
$N_{\text{top}}^{\text{EST},1j0b}$	2051 ± 49	7459 ± 152
$N_{\text{top}}^{\text{EST},1j1b}$	6083 ± 82	19853 ± 148
$\epsilon_{1j}^{\text{MC}}$	0.75 ± 0.14	0.736 ± 0.003
$\epsilon_{2j}^{\text{MC}}$	0.69 ± 0.04	0.6699 ± 0.0008
$\epsilon_{2j}^{\text{DATA}}$	0.69 ± 0.31	0.662 ± 0.002
$\epsilon_{1j}^{\text{EST}}$	N/A	0.727 ± 0.004
β_{tag}	1.03 ± 0.02	1.01 ± 0.02

Once we have the estimate in SR1j0b-PRE, we wish to apply the topological selections to make an estimate in the SR itself. To do this, we use the MC in SR1j0b-PRE and the SR and determine a transfer efficiency. The transfer efficiency for our regions is $\epsilon_{1j0b/\text{SR}} = 0.182 \pm 0.002$. Applying this efficiency takes us from an SR1j0b-PRE top estimate of 7459.25 ± 151.94 to an SR estimate of 1356 ± 32.

The effect associated with the primary b-tag efficiency was determined and is summarised in Table 5.6. In general, we see that the data-driven estimates are far less dependent on the critical b-tagging experimental systematic.

Table 5.6: Summary of the systematic uncertainty on the SR top background estimate due to the primary b-tag efficiency. The data-driven estimates produce improved uncertainties.

	Standard [% error]	Data Driven [% error]
$N_{\text{Top}}^{EST,1j0b}$	$+14.6/-12.0$	$+1.7/-1.8$
$\epsilon_{\text{1j0b/SR}}$	$+3.1/-2.8$	$+3.1/-2.8$
$N_{\text{Top}}^{\text{EST,SR}}$	$+18.2/-14.5$	$+4.9/-4.6$

5.6 Fit Method

We use a profile likelihood approach as outlined in Section 4.9. For this analysis, the likelihood function incorporates probability distributions for SRs, CRs, systematic uncertainties and MC statistics. The SR is modelled using Poisson function $f(N_{ib}|\dots)$ which is binned in n_j as well as in the fit variable itself (m_T). The CR is modelled using the Poisson functions $f(N_l|\Sigma_k\beta_k B_{kl})$ for CR l and background process k. The top CRs are treated slightly differently. The yield in CR$1j1b$-Top is used as the top quark pair production normalisation factor.

$$f(N_{\text{TOP}}^{\text{CR}}|\beta_{\text{top}}B_{\text{top}}^{\text{CR}} + B_{\text{other}}). \tag{5.12}$$

We then define β_{tag} to fit for the b-tagging efficiency. While controlling for b-tagging inefficiencies we must have an interplay between the SR top quark yields and the CRs. This is because events can propogate between them when the b-tagging efficiency is floated. The top background contribution is estimated by:

$$\begin{aligned} B_{\text{top}}^{\text{EST}} &= \beta B_{\text{top}}^{\text{MC}} \\ &= (1 + f_1 f_2) B_{\text{top}}^{\text{MC}} \\ &= B_{\text{top}}^{\text{MC}} + f_1 B_{\text{top}}^{1j1b} \\ &= B_{\text{top}}^{\text{MC}} + (1 - \beta_{\text{tag}}) B_{\text{top}}^{1j1b}, \end{aligned} \tag{5.13}$$

which is taken to be the top yield in the SR and WW CR Poisson functions. The CR$2j1b$-Top probability distribution function is taken to be:

$$P(2j1b) = f(N_{2j}^{1b}|\beta_{\text{top}}B_{\text{top}}^{1b} + \beta_{\text{top}}(1 - \beta_{\text{tag}})B_{\text{top}}^{2b} + B_{\text{other}}), \tag{5.14}$$

and the CR$2j2b$-Top probability distribution function is:

$$P(2j2b) = f(N_{2j}^{2b}|\beta_{\text{top}}\beta_{\text{tag}}B_{\text{top}}^{2b} + B_{\text{other}}). \tag{5.15}$$

The systematic uncertainties are implemented using Gaussian functions $g(\vartheta_t|\theta_t)$ for a source of uncertainty t. The MC statistics are incorprated with Poisson functions $f(\zeta_k)$ for k background processes.

5.7 Results

The results are generated after the simultaneous statistical fit and are inclusive of all systematic and experimental sources of uncertainty. In the SR for $n_J = 1$ we have $\beta_{WW} = 0.97 \pm 0.17$, $\beta_{top} = 0.98 \pm 0.08$, $\beta_{tag} = 1.014 \pm 0.021$ and $\beta_{Z/\gamma^*} = 0.90 \pm 0.12$. The normalisation factors for each of the three SRs are summarised in Table 5.7. The modelling for all CRs is acceptable, and is shown for all three of the CRs in Figure 5.9.

Table 5.7: Post-fit Normalisation Factors which scale the corresponding estimate yields in the SR. The WW background in the VBF SR uses an MC normalisation method. These normalisation factors incorporate both statistical and systematic uncertainties.

Fit NF	ggF $N_J = 0$	ggF $N_J = 1$	VBF $N_J \geq 2$
WW	1.06 ± 0.09	0.97 ± 0.17	–
Top	0.99 ± 0.17	0.98 ± 0.08	1.01 ± 0.01
b-tag	–	1.01 ± 0.02	–
Z/γ^*	0.84 ± 0.04	0.90 ± 0.12	0.93 ± 0.07

The total signal observed across all SRs is approximately 1000 events, and with the background and signal yields, we see agreement of both shape and yield with the expected SM behaviour. The post-fit SRs are shown in Table 5.8 and the $N_j \leq 1$ combination plot is shown in Figure 5.10, with the solid red representing the ggF $m_H = 125$ GeV $H \to WW^*$ signal model. The VBF signal model is also incorporated and is simultaneously fit in conjunction with the ggF component.

Table 5.8: The yield breakdown for the different SRs in the $H \to WW$ analyses. Uncertainties include both statistical and systematic sources [131].

Process	$N_J = 0$ ggF	$N_J = 1$ ggF	$N_J \geq 2$ VBF Inc BDT	$N_J \geq 2$ VBF BDT$\in (0.86, 1.0)$
ggF	639 ± 110	285 ± 51	42 ± 16	6 ± 3
VBF	7 ± 1	31 ± 2	28 ± 16	16 ± 6
WW	3016 ± 203	1053 ± 206	400 ± 60	11 ± 2
VV	333 ± 38	208 ± 32	70 ± 12	3 ± 1
Top	588 ± 130	1397 ± 179	1270 ± 80	14 ± 2
Mis-ID	447 ± 77	234 ± 49	90 ± 30	6 ± 2
Z/γ^*	27 ± 11	76 ± 24	280 ± 40	4 ± 1
Total	5067 ± 80	3296 ± 61	2170 ± 50	60 ± 10
Data	5089	3264	2164	60

The production cross-sections times branching ratios for $\sigma_{\text{ggF}} \cdot \mathcal{B}_{H\to WW^*}$ and $\sigma_{\text{VBF}} \cdot \mathcal{B}_{H\to WW^*}$ are extracted simultaneously. The gluon–gluon fusion component is measured to be:

$$\begin{aligned} \sigma_{\text{ggF}} \cdot \mathcal{B}_{H\to WW^*} &= 11.4^{+1.2}_{-1.1}(\text{stat.})^{+1.2}_{-1.1}(\text{theo. stat})^{+1.4}_{-1.3}(\text{exp syst.})\ \text{pb} \\ &= 11.4^{+2.2}_{-2.1}\ \text{pb}. \end{aligned} \tag{5.16}$$

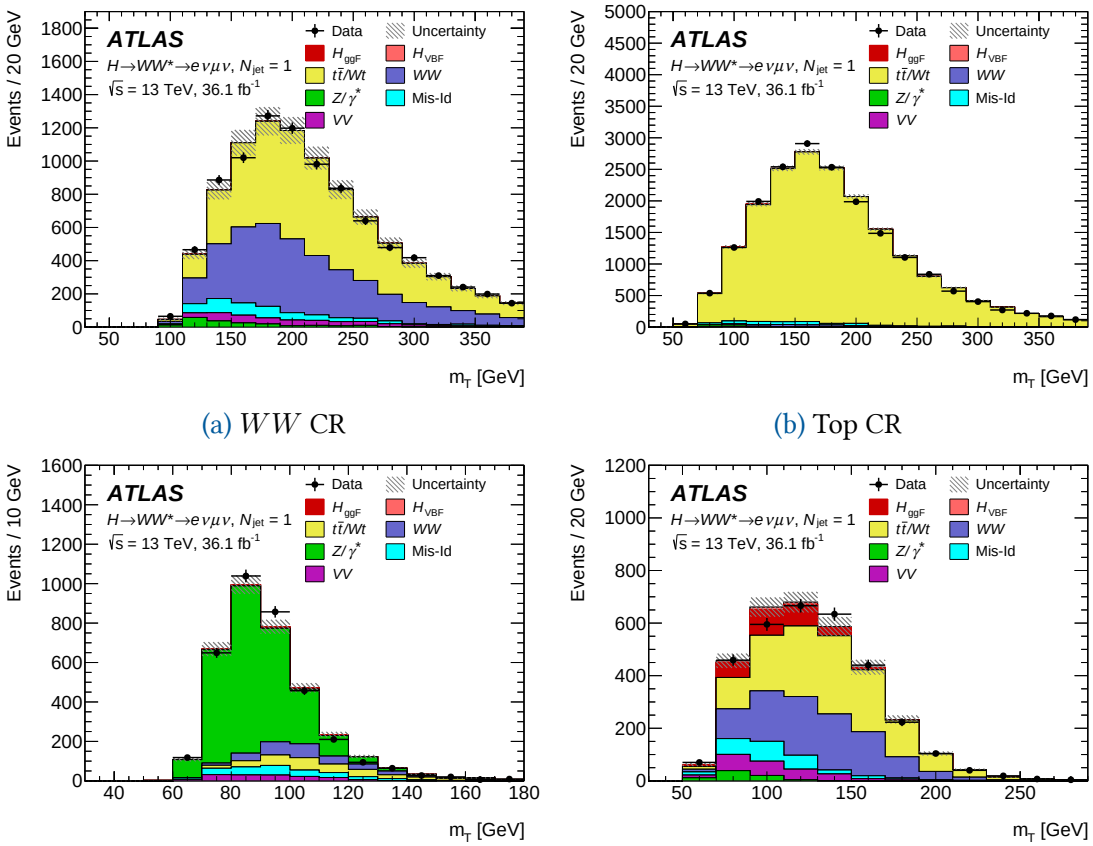

(a) WW CR

(b) Top CR

(c) Z+jets CR

(d) $N_J = 1$ SR

Figure 5.9: The CR and SRs for the $N_J = 1$ ggF selections. In (a) we have the WW CR. In (b) we have the top CR, (c) corresponds to the Z+jets CR and (d) shows the $N_J = 1$ SR [131].

The vector boson fusion component is measured to be:

$$\begin{aligned}\sigma_{\text{VBF}} \cdot \mathcal{B}_{H\to WW^*} &= 0.50^{+0.24}_{-0.22}(\text{stat.})^{+0.10}_{-0.10}(\text{theo. stat})^{+0.12}_{-0.13}(\text{exp syst.})\ \text{pb} \\ &= 0.50^{+0.29}_{-0.28}\ \text{pb}.\end{aligned} \tag{5.17}$$

The SM predictions are 10.4 ± 0.6 pb and 0.81 ± 0.02 pb for ggF and VBF [133] respectively.

We simultaneously fit the signal strength parameter μ for both ggF and VBF production, with a decay of $H \to WW^*$. The measurement of the ggF signal strength:

$$\mu_{\text{ggF}} = 1.10^{+0.10}_{-0.09}(\text{stat.})^{+0.13}_{-0.11}(\text{theo syst.})^{+0.14}_{-0.13}(\text{exp syst.}) \tag{5.18}$$

$$= 1.10^{+0.21}_{-0.20}. \tag{5.19}$$

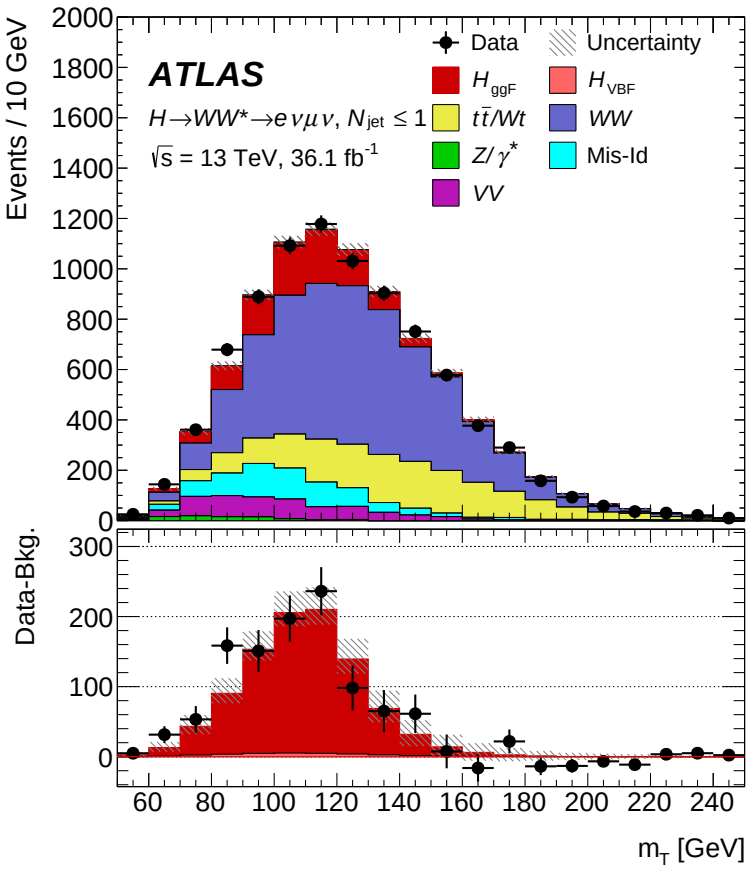

Figure 5.10: The $N_{\text{jet}} \leq 1$ combined SR distribution for m_{T}. We can see the necessity of the gluon-gluon fusion Higgs background and glimpses of the vector boson fusion components [131].

The VBF signal strength was measured to be:

$$\mu_{\text{VBF}} = 0.62^{+0.29}_{-0.27}(\text{stat.})^{+0.12}_{-0.13}(\text{theo syst.})^{+0.15}_{-0.15}(\text{exp syst.}) \quad (5.20)$$

$$= 0.62^{+0.36}_{-0.35}. \quad (5.21)$$

The contributions to the errors of this signal strength measurement have a variety of sources —- statistical, experiment, and theoretical, with different contributions to ggF and VBF, respectively. We break these down in Table 5.9. For the measured ggF cross-section, the MC statistics contributes 6% of the total error. The largest theoretical uncertainty is from non-resonant WW production, which also comes in at 6% with the largest experimental uncertainty being due to the modelling of pileup at 5%. We note that the b-tagging uncertainty is only contributing 4% to the total cross-section uncertainty - which is a big improvement given the huge dependency of this uncertainty using the MC estimated b-tagging systematic. The total relative uncertainty is 18% and the VBF cross-section measurement is dominated by data statistics, followed by MC statistics, and then theoretical uncertainties, which are driven by uncertainty in the ggF signal for $N_j \geq 2$ signal selections. The total uncertainty in the VBF cross-section measurement

is 57%.

Table 5.9: Breakdown of the main contributions to the total uncertainties on $\Delta\sigma_{\text{ggF}} \cdot \mathcal{B}_{H\to WW^*}$ and $\Delta\sigma_{\text{VBF}} \cdot \mathcal{B}_{H\to WW^*}$. The sources are grouped by origin. Correlations are incorporated in the combination of systematic sources [131].

Source	$\Delta\sigma_{\text{ggF}} \cdot \mathcal{B}_{H\to WW^*}$[%]	$\Delta\sigma_{\text{VBF}} \cdot \mathcal{B}_{H\to WW^*}$[%]
Data Statistics	10	46
CR Statistics	7	9
MC statistics	6	21
Theoretical uncertainties	10	19
ggF signal	5	13
VBF signal	< 1	4
WW	6	12
Top	5	5
Experimental uncertainties	8	9
b-tagging	4	6
Modelling of pile-up	5	2
Jet	2	2
Lepton	3	< 1
Misidentified leptons	6	9
Luminosity	3	3
SYS.+STAT.	18	57

Both the ggF and VBF signal strength measurements are compatible with SM prediction, with the observed ggF significance being 6.0σ and the VBF significance being 1.8σ [124].

5.8 Full Run-II Combined Results

The work outlined in the previous sections related specifically to the measurement of the inclusive Higgs boson production cross-section via the $H \to WW^* \to e\nu\mu\nu$ decay channel. Similar measurements of $\sigma_{\text{ggF,H}}$ and $\sigma_{\text{VBF,H}}$ can be made while studying each decay pathway available to the Higgs boson. In fact, this is exactly what was done during the run-I analyses as outlined in Section 5.1. In the run-II follow-up we can perform a similar combination of these measurements using all the individual analyses as they currently stand[134]. The combined result combines the results of $H \to \gamma\gamma$ (including $t\bar{t}H$, $H \to \gamma\gamma$), $H \to ZZ^* \to 4\ell$, VH, $H \to bb$ and $H \to \mu\mu$; using the data from 2015–2017, with the results from, $H \to WW^* \to e\nu\mu\nu$, $H \to \tau\tau$, $VBF\ H \to b\bar{b}$, $t\bar{t}H$, $H \to b\bar{b}$, and $t\bar{t}H$ multilepton, $H \to$ invisible, and off-shell $H \to ZZ^* \to 4\ell$ and $H \to ZZ^* \to 2\ell 2\nu$; using data from 2015–2016. The specific analyses and datasets are documented in Table 5.10. We summarise the ATLAS collaboration Higgs measurements in Figure 5.11. We summarise the production cross-sections normalised to SM values for Higgs boson production cross-sections from gluon–gluon fusion, vector

Table 5.10: A summary of the final states used in the combined Higgs measurement [134].

Analysis	Dataset	Integrated luminosity [fb^{-1}]
$H \to \gamma\gamma$ (including $t\bar{t}H$,$H \to \gamma\gamma$)	2015–2017	79.8
$H \to ZZ^* \to 4\ell$ (including $t\bar{t}H$,$H \to ZZ^* \to 4\ell$)	2015–2017	79.8
$VH,\ H \to bb$	2015–2017	79.8
$H \to \mu\mu$	2015–2017	79.8
$H \to WW^* \to e\nu\mu\nu$	2015–2016	36.1
$H \to \tau\tau$	2015–2016	36.1
VBF $H \to b\bar{b}$	2015–2016	24.5-30.6
$t\bar{t}H,\ H \to b\bar{b}$ and $t\bar{t}H$ multilepton	2015–2016	36.1
$H \to$ invisible	2015–2016	36.1
off-shell $H \to ZZ^* \to 4\ell$ and $H \to ZZ^* \to 2\ell 2\nu$	2015–2016	36.1

boson fusion, W Higgstrahlung, Z Higgstralung, and $t\bar{t}$ fusion and top Higgstrahlung. The normalised production cross-section for gluon–gluon fusion is $\sigma_{ggF}/\sigma_{ggF}^{SM} = 1.04 \pm 0.09$, the production cross-section for vector boson fusion $\sigma_{\text{VBF}}/\sigma_{\text{VBF}}^{SM} = 1.21^{+0.24}_{-0.22}$ we then have W Higgstrahlung $\sigma_{WH}/\sigma_{WH}^{SM} = 1.30^{+0.40}_{-0.38}$, Z Higgstrahlung $\sigma_{ZH}/\sigma_{ZH}^{SM} = 1.05^{+0.31}_{-0.29}$. $t\bar{t}$ fusion and top Higgstrahlung $\sigma_{t\bar{t}H+tH}/\sigma_{t\bar{t}H+tH}^{SM} = 1.21^{+0.26}_{-0.24}$.

In Figure 5.12, we can look at the correlations between σ_{ggF} and σ_{VBF} for $H \to \gamma\gamma$, $H \to ZZ$, $H \to WW$, $H \to \tau\tau$ individually, as well as the combined measurement. The SM prediction agrees within the 95% CLs interval of the combined measurement.

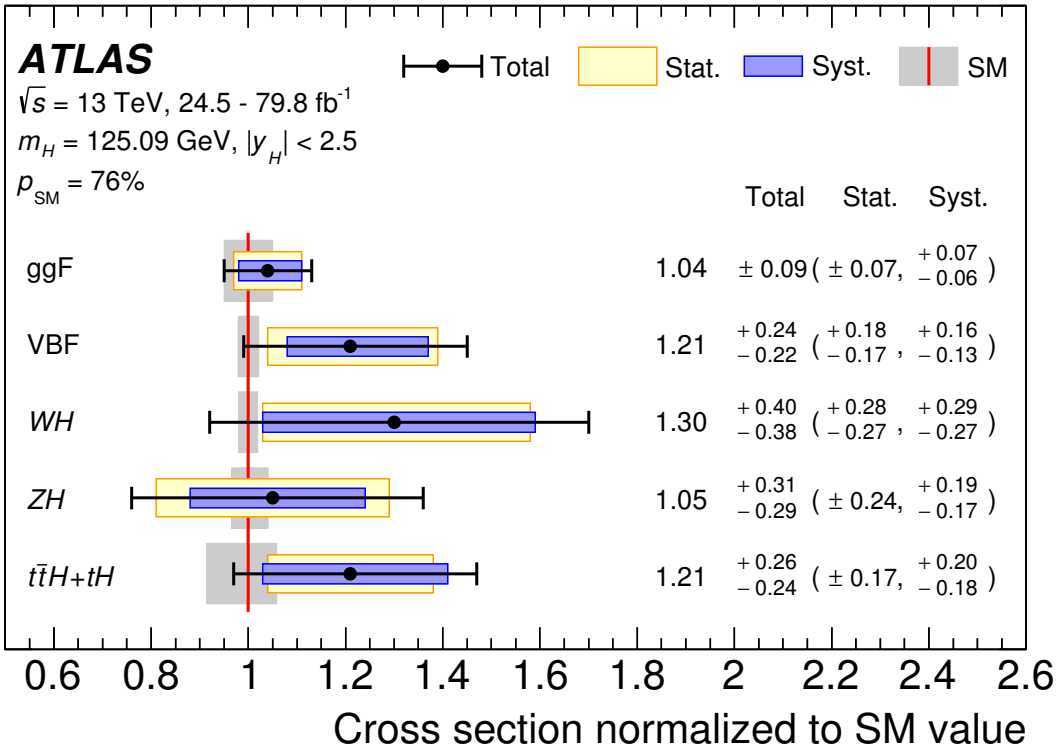

Figure 5.11: The cross-section normalised to SM value for different Higgs production pathways. These measurements come from a variety of datasets, detailed in [134]. The SM cross-section is shown in red. Detailed for each measurement is the statistical uncertainty, the systematic uncertainty and the total uncertainty. This allows us to determine if a measurement is statistics or systematics limited, and therefore which the most effective pathways for analysis development are. All cross-section measurements are consistent with the SM.

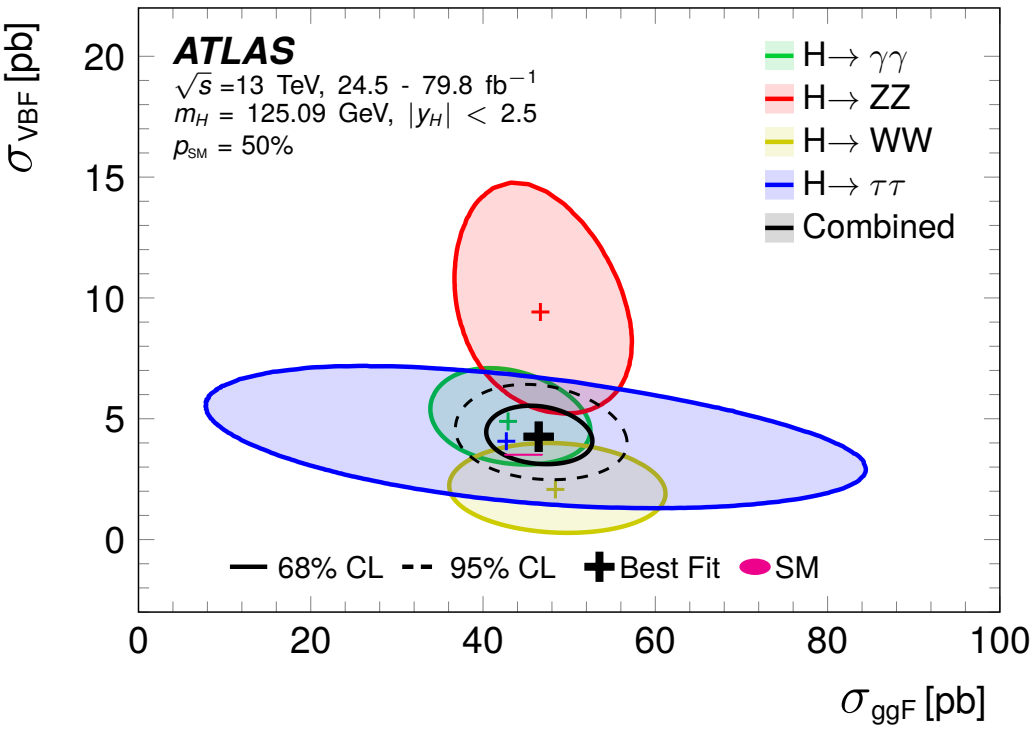

Figure 5.12: The summary of ggF and VBF Higgs production cross-sections as measured using different Higgs final states. For each measurement, the 68% CL is shown using a solid line, and the 95% CL, for the combined measurement is shown in a dotted line. The best fit for each measurement is shown with a cross. The combined measurement is shown in black, with the SM expectation being shown in magenta. The SM expectation is consistent with the combined 68% CL contour [134].

Chapter 6

FTK Fast Simulation

In this chapter, we describe our development and implementation of a fast simulation method for the ATLAS Fast Tracker project. The goal of this fast simulation project was to mitigate the CPU-intensive requirements of the full simulation of the Fast Tracker. First, we provide a general overview of the hardware of the Fast Tracker, then we provide an overview of the full simulation. Finally, we detail our methodology of parameterising the track parameter uncertainties. We call our methodology Fast Tracker fast simulation — FTKFastSim.

6.1 The Fast Tracker

The Fast Tracker (FTK) is a hardware-based solution to high multiplicity tracking difficulties. We provide a schematic of the FTK in Figure 6.1. The FTK takes in as input all pixel detector and SCT data and the outputs of the FTK is tracks. The FTK is located between the ATLAS readout drivers (RODs) and the readout system (ROS) and provides tracking information to the HLT for trigger decisions. In order for the FTK to operate

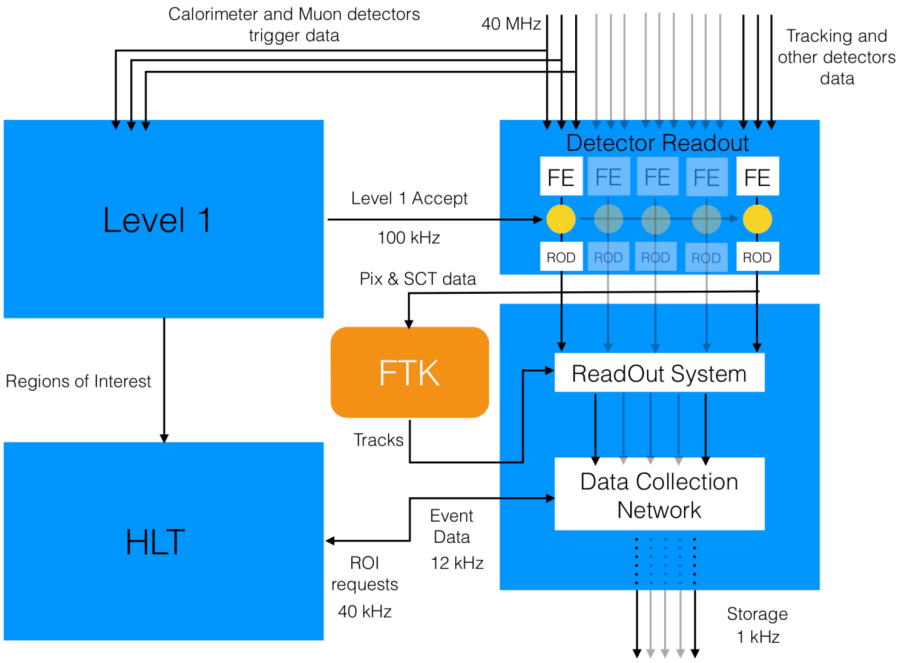

Figure 6.1: FTK trigger system overview [39].

in the high-speed environment provided by the LHC, we rely on five primary principles; parallelisation, reduction, elimination, simplification, and hardware. The first principle

is parallelising the problem; we do this by segmenting the pixel and SCT into $\eta - \phi$ space (*sounds destructive!*) and then separating this space into 64 bins; we refer to these bins as *towers*. We show the tower configurations in Figure 6.2. Seperating the detector into 64 bins allows us to parallelise the fitting procedure over multiple copies of identical hardware. The 64 towers have a degree of overlap while parallelising in order for ease of data access. In Figure 6.2, the red and blue rectangles highlight this data overlap

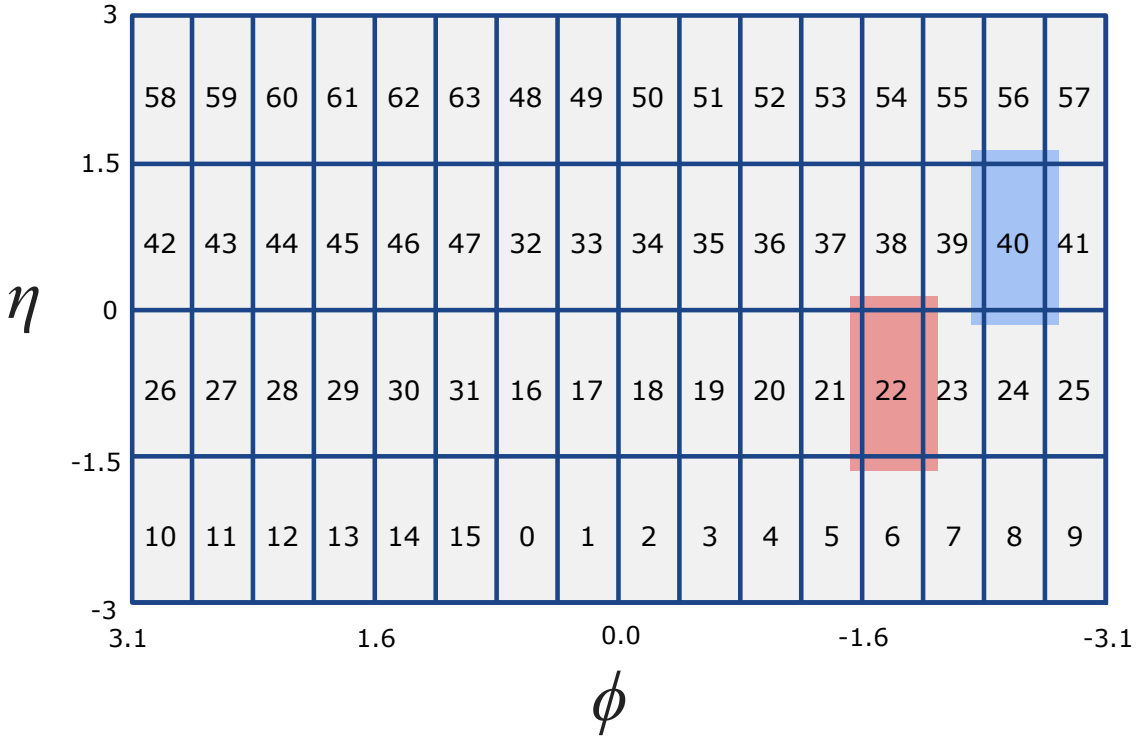

Figure 6.2: FTK tower map.

The second principle is *reduction* in the data volume. In order to operate under current run conditions, the amount of data passing through the FTK system must be reduced. In order to do this, we convert hits and clusters into coarse resolution regions known as superstrips. A schematic of the coarse resolution regions of space is shown in Figure 6.3. The individual rectangles are the coarse resolution superstrips, and the gold highlighted regions are areas which have measured a hit above some threshold.

The third principle is *elimination* of costly loops. The track finding algorithms are inherently computationally expensive, which requires many loops. In order to remove this constraint, the FTK precalculates superstrip configurations known as pattern banks; these patterns are then stored, where we can compare hit configurations later, upon measurement. We show a schematic of different pattern examples in Figure 6.4. The fourth principle is *simplification* of algorithms. Once we have the pattern bank match, we look at the higher resolution hits, where we now wish to fit for a track solution. The FTK uses a linearised fit method in conjunction with FPGAs in order to reduced the required time of this track fitting step. The tracking when done in this way can be completed in

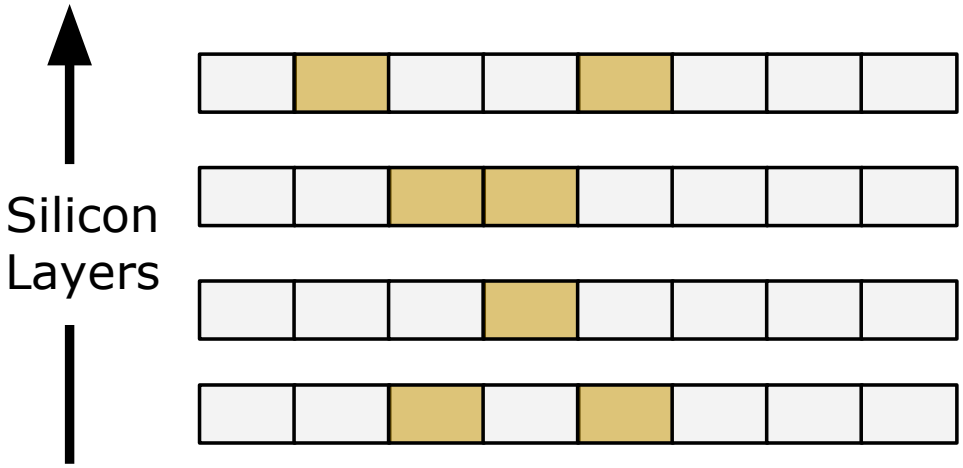

Figure 6.3: FTK superstrips and patterns.

5 picoseconds. The FTK achieves this lightening speed by calculating the phase-space of possible tracks (by minimising the χ^2), then using a linear approximation to calculate the tracks, where the linear approximation is dependent on the hit configuration. The FPGAs then multiply the hit coordinates extracted from the linear approximation by pre-calculated constants to get a χ^2. This χ^2 is calculated in the following way:

$$\chi_i = \sum_{j=1}^{N_c} S_{ij} x_j + h_i; i = 1, \ldots, N_\chi. \tag{6.1}$$

where The fifth and final principle is *hardware*.

6.2 FTK Hardware Overview

The FTK has the design goal of global tracking at a Level-1 trigger rate of 100 kHz and an instantaneous luminosity of 3×10^{34} $\mathrm{cm}^{-2}\mathrm{s}^{-1}$. The hardware functional schematic for the FTK is shown in Figure 6.5. The pixel and SCT data are transmitted from the Read Out Drivers (ROD) at 100 kHz and received by the Data Formatters (DF). The information parsed is clusters of pixel and SCT hits, where the clusters are defined as side-by-side or diagonally joined pixel or SCT hits. The DFs reorganise clusters into 64 $\eta - \phi$ space towers as illustrated in Figure 6.2.

We further split these towers into 16 ϕ bins and 4 η bins. Creating these zones in the $\eta - \phi$ space is problematic due to clusters overlapping with the tower boundaries; the solution to this is to allow overlap between these regions, as illustrated in Figure 6.2.

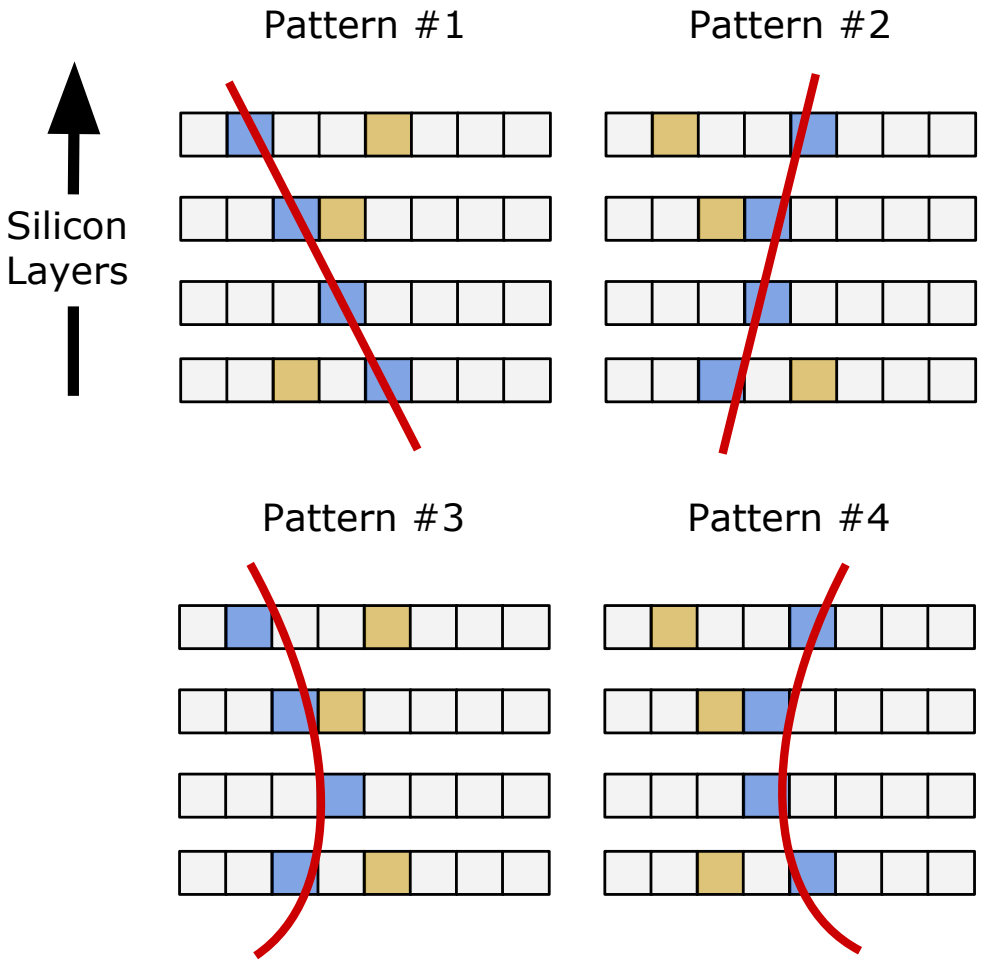

Figure 6.4: FTK patterns. Gold are all superstrips which have a hit in them. Blue are the superstrips which correspond to track solutions.

The overlap present in the ϕ boundaries is sufficient to cover the multiple scattering and track curvature uncertainties, and the resolution in η is sufficient to cover the beam's luminous region in the z-direction. The $\eta - \phi$ space clusters extend to a maximum of four pixels in the ϕ direction and five pixels in the z or r directions — depending on whether the cluster is in the endcap or barrel. Once the clusters have been organised into $\eta - \phi$ bins, each DF transmits 8 $\eta - \phi$ towers to the core crates, which contain the pattern recognition and track fitting hardware.

The Data Organiser (DO) then receives the clusters, where we convert from full resolution hits to coarse resolution superstrips. The superstrips are the core unit of our pattern recognition. The patterns are determined in advance using full ATLAS simulation with a single muon source and correspond to the possible superstrip combinations across eight silicon layers: the IBL, two outermost pixel layers, four axial and one stereo SCT layers. These pre-generated patterns are stored on Associative Memory (AM) boards and have unique identifiers known as a "road ID". The AM boards are massively parallel systems

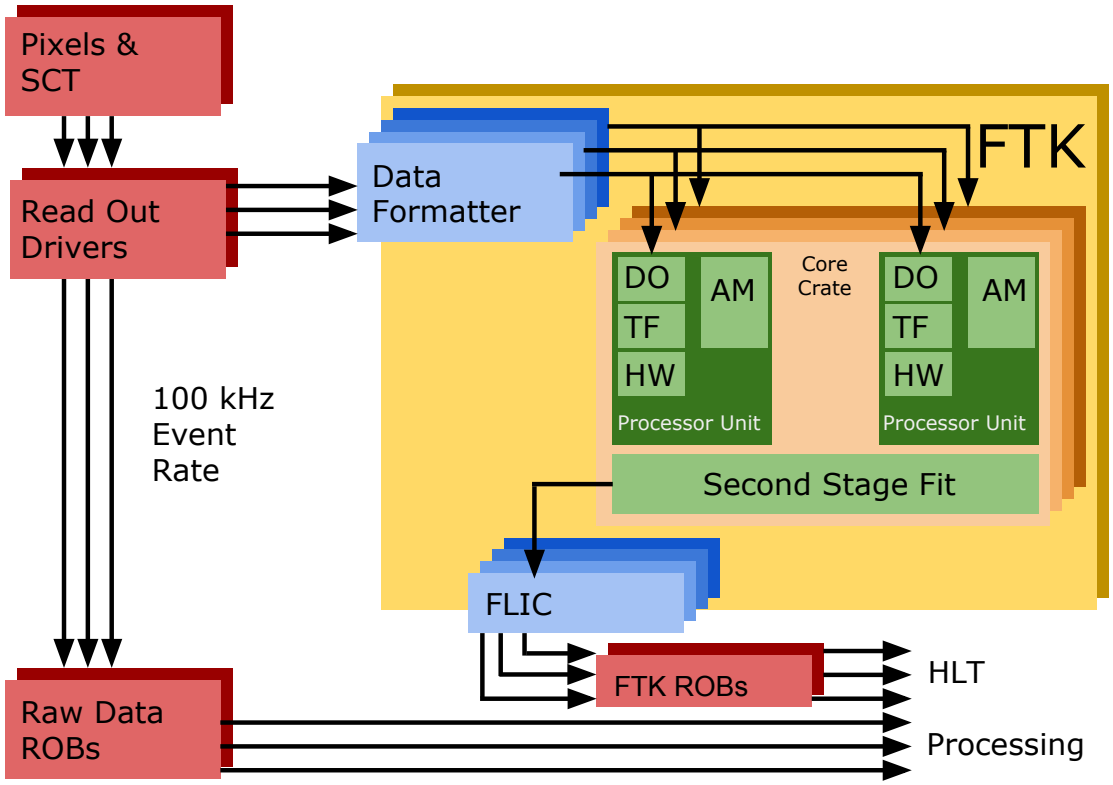

Figure 6.5: FTK hardware overview [39].

where each pattern has access to each hit nearly simultaneously; this allows the entire pattern matching process to be complete soon after the final hit enters the core crate, see Figure 6.5. Once we have a pattern match, the AM board communicates with the DO board requesting a pattern's full resolution information. The design of the DO then allows rapid access to this information.

Once a cluster of hits has an associated pattern, the Track Fitter (TF) receives a road ID from the DO. The TF then performs a linearised track fitting calculation to provide the track parameters. The TF can perform approximately 10^9 track fits per second. The Hit Warrior (HW) removes the duplicate tracks with predefined χ^2 criteria. The Second Stage Boards (SSB) extrapolate the 8-layer track to the 12 silicon layers present in the inner detector. The output of the SSB are tracks with their constituent hits, the χ^2, the helical track parameters, and the track quality. The SSB output tracks enter an FTK-to-Level2 Interface Crate (FLIC) which provides tracks to the HLT system.

6.3 FTK Full Simulation

The FTK full simulation, referred to herein as FTKFullSim, is implemented to emulate the logical functions of each FTK hardware component. FTKFullSim takes MC truth level track information and performs a full simulation of the FTK hardware system. The

output of the FTK simulation is trigger selection emulation. The DF board is simulated by dividing its function into two parts, the first being hardware clustering and the second being the transferring of hits to the relevant $\eta - \phi$ tower. The AM boards provide a massively parallel hardware system which can process each hit through approximately 1 billion patterns every 10 ns, and in order to store these patterns in the simulation, we require 35 GB of storage. This represents a massive hurdle to FTK simulation, as modern CPU architecture cannot simulate this functionality.

In order to approach this problem, we split the AM boards into two logical steps — road finding and track fitting. The road finding simulates the AM pattern-matching capabilities, including the retrieval of the superstrip address for each hit. The emulation of the TF completes after a block of events has been fully emulated. Differences between simulation and hardware have been studied and are negligible. In FTKFullSim the TF and SSB are both emulated together, with both 8-layer and 12-layer tracks being calculated simultaneously. The four excluded layers in the 8-layer fit by extrapolating from the 8-layer fit using a linear calculation. The fit coefficients required for simulation of the track fitting require 2 GB of storage space, and a GPU based approach runs approximately 1 million times slower than the FPGA hardware implementation. Unlike the hardware, the simulation can easily modify which of the 12 silicon layers can be used for pattern matching, which gives us the capability to perform optimisation studies.

A serious drawback of including the FTKFullSim into the ATLAS MC simulation is the significant increase of CPU usage, typically between 15-30%, bringing ATLAS simulation execution time to 300 s/event with the AM simulation taking approximately two-thirds of this time. Given track finding time is a function of track multiplicity, and scales with LHC luminosity, the track finding simulation time will only increase with future data-taking runs. The inevitable increase in track finding times necessitates the development of an alternative method to FTKFullSim, which is both faster and more memory efficient. Our solution to this problem is to develop a fast simulation approach, which emulates the track parameter resolutions of FTKFullSim via the use of a resolution lookup table.

6.4 FTK Fast Simulation

This section documents our work into parameterising the FTKFullSim track parameter uncertainties into a fast lookup table approach known as FTKFastSim. Our fast simulation approach begins by taking an ATLAS MC simulation which generates truth tracks as well as corresponding FTKFullSim tracks. In this simulation sample, there exists no one-to-one correspondence between truth tracks and FTKFullSim tracks due to the nature of the FTKFullSim pattern matching process. The FTKFastSim simply emulates track parameter resolutions, which are in the form of a lookup table for a given tracks properties. A general comparison between the FTKFullSim and FTKFastSim processes is shown in Figure 6.6.

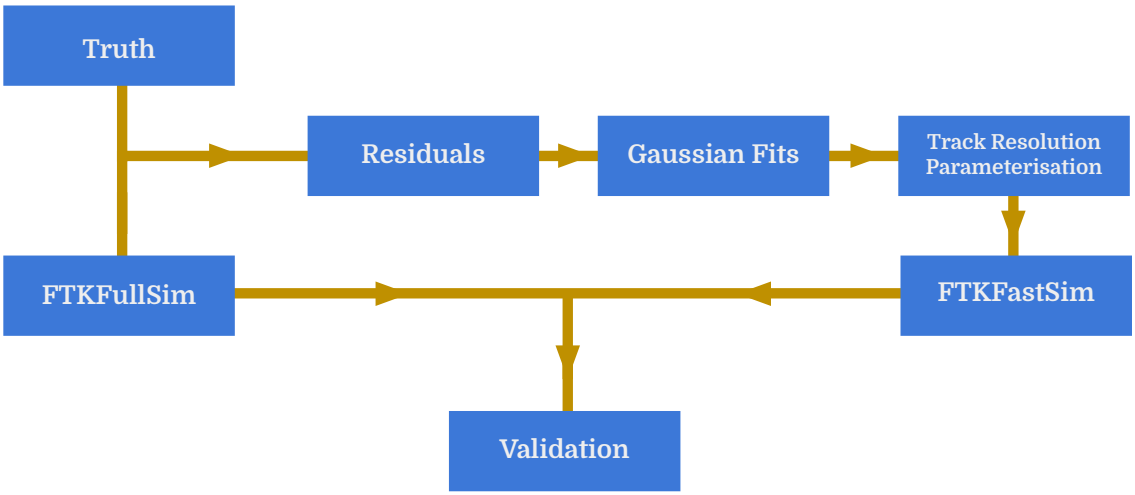

Figure 6.6: Schematic of FTKFullSim versus FTKFastSim, with Gaussian smearing occuring between.

6.4.1 Track Parameter Resolution

In the ATLAS detector the measurement of the impact parameter is primarily driven by the position resolution of the hits used to reconstruct a given track. In fact, the impact parameter resolutions are almost entirely driven by the first two measurement planes and can be approximated by [135]:

$$\sigma = \frac{r_1\sigma_2 \oplus r_2\sigma_1}{r_2 - r1} \oplus \frac{k_1 r_1}{p_T}, \tag{6.2}$$

here the $\oplus$ notation means *add in quadrature*. The position resolutions of the first and second measurement layers at r_1 and r_2 are σ_1 and σ_2. The second term $k_1 r_1/p_T$ is a term which encodes the RMS of the multiple scattering angle from the first plane onward.

For our purposes of creating FTKFastSim we can take Equation 6.2 and write it in the form:

$$\sigma = A(|\eta|, p_T) \oplus \frac{B(|\eta|, p_T)}{p_T}, \tag{6.3}$$

here $A(|\eta|)$ parameterises the intrinsic error of the track parameter and $B(|\eta|, p_T)$ accounts for errors associated with multiple scattering effects. We include the momentum dependence purely for generalising, though for all track parameters except the curvature, the constant B is purely a function of $|\eta|$ and has no momentum dependence. If we assume no correlation between the different sources of error we get the functional

form:

$$\sigma(|\eta|, p_T) = \sqrt{A(|\eta|, p_T)^2 + \left(\frac{B(|\eta|, p_T)}{p_T}\right)^2}. \tag{6.4}$$

On a track by track basis this resolution function cannot be directly calculated as the matrices $A(|\eta|, p_T)$ and $B(|\eta|, p_T)$ cannot be known. In order to tackle this problem we instead calculate the resolution function directly by taking track ensembles with similar kinematic properties. The first binning we choose is in $|\eta|$ where we choose to break the range into five bins. This gives us:

$$\sigma_i(p_T) = \sqrt{A_i^2(p_T) + \left(\frac{B_i(p_T)}{p_T}\right)^2}. \tag{6.5}$$

The second binning we choose is in the curvature of the tracks $1/2p_T$, where we break the range into 26 bins. This gives us:

$$\sigma_{ij} = \sqrt{A_i^2 + \left(\frac{B_{ij}}{p_T^j}\right)^2}. \tag{6.6}$$

The third binning we perform is in terms of whether a track has an IBL hit or not. The reason for this is driven by the IBL being the first possible plane of measurement, which largely determines the track parameter resolutions, as stated in Equation 6.2. In total this leaves us with 260 bins, broken down like so,

$$\{\eta_i \in (1, 5)\} \times \{1/2p_T \in (1, 26)\} \times \{\text{IBL} \in (0, 1)\}. \tag{6.7}$$

The FTKFastSim approach is visually shown in Figure 6.7, where each function corresponds to a specific pseudorapidity bin, and the resolutions are functions of the curvature.

6.4.2 Residuals and Gaussian Fits

For a given track with $|\eta|$, $1/2p_T$, and an IBL bit, we can calculate the resolution σ_{ij} for all $|\eta|$ and $1/2p_T$ bin combinations.

Our goal is to determine the resolution functions $\sigma(|\eta|, 1/2p_T)$ for the FTKFullSim, so that we can use them to parameterise the resolution and create an FTKFastSim. To determine these functional forms, we must first bin the MC truth events in terms of $|\eta|$. In order to determine the functional form we must calculate a resolution for tracks at each value of curvature involved, to do this we bin in $1/2p_T$.

We define two sets of tracks, the first being the truth level tracks, which provide us with exact knowledge of a particle's behaviour. The second set of tracks are reconstructed tracks from FTKFullSim. In order to get the FTKFullSim tracks, we pass the truth level

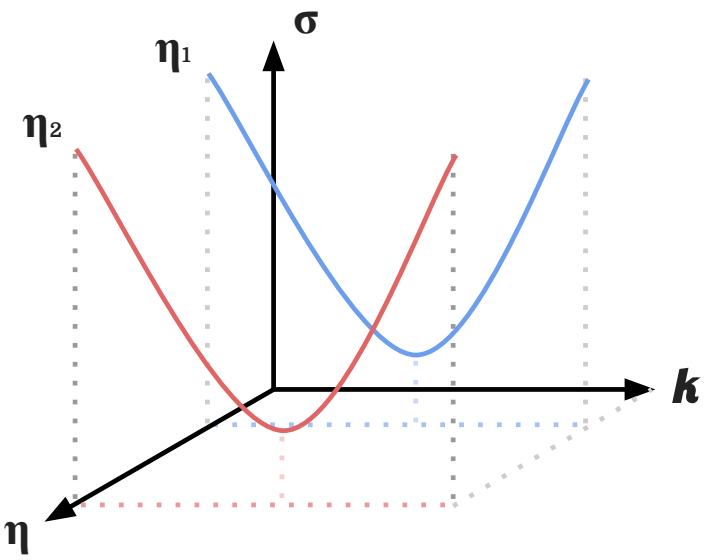

Figure 6.7: A schematic showing the FTKFastSim for a given track parameter resolution (σ) and IBL hit. We have three principal axes, the first being k, which here is the curvature of a given track. k is split into 26 different bins. The next axis is $|\eta|$, which is split into 5 separate bins. The third is the track parameter resolution σ. Equation 6.2 showed us we can write an error parameterisation in terms of a square root function for a fixed η, and varying k. The two functional forms correspond to different η binnings.

tracks through the FTKFullSim, producing a truth track–FTKFullSim track pair. Once we have the two populations of tracks, we can then compare them to one another to determine the resolution functions.

For each truth track and full simulation track pair and each track parameter P we calculate the following,

$$\Delta P = P_{\text{Full}} - P_{\text{Truth}}. \tag{6.8}$$

We then take this value and fill a histogram corresponding to the $|\eta|$ and $1/2p_T$ of the given truth track. Calculating this ensemble gives us the distribution in Figure 6.8. Once we have the residual distribution ΔP we fit a Gaussian to the distribution over the full range. The output of the Gaussian fit is a constant, N, a mean, μ, and a standard deviation of σ.

6.4.3 Track Resolution Parameterisation

For a fixed $|\eta|$ we calculate $\sigma_{\eta j}$ and then plot these together which gives us a proxy for $\sigma_\eta(1/2p_T)$. Figure 6.8 shows the distribution for tracks with $\eta \in (0, 0.5)$ and an IBL hit for track parameter d_0. We then fit these points $\sigma_\eta(1/2p_T)(\Delta P)$ with the square root

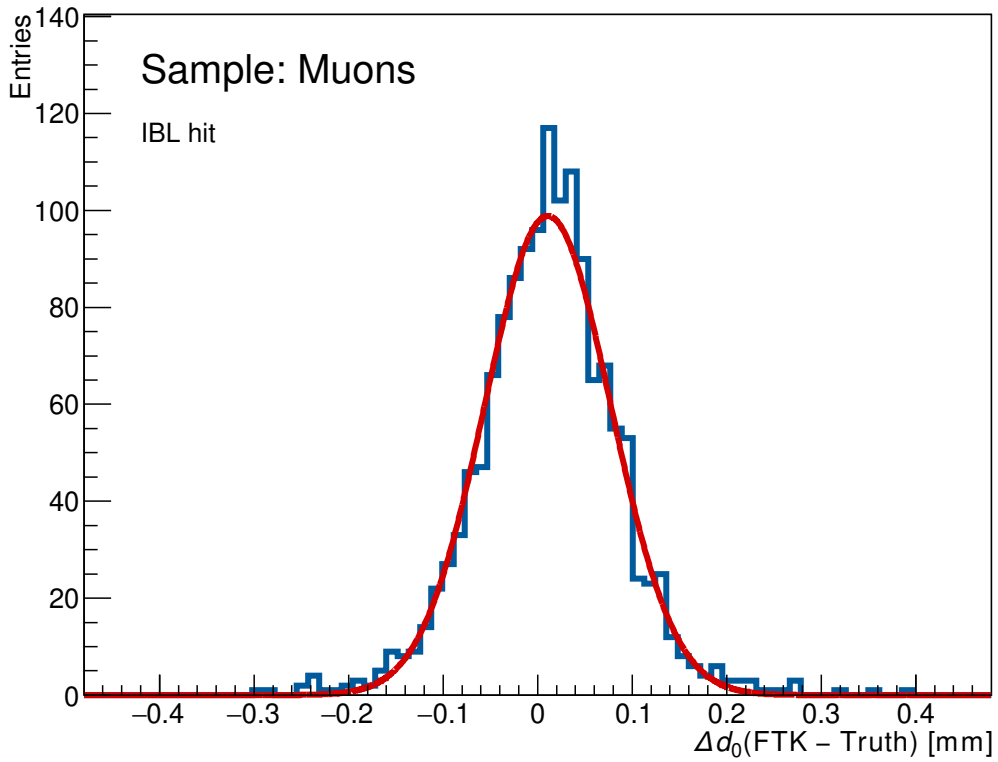

Figure 6.8: The Gaussian distribution for impact parameter d_0 with an IBL hit, $\eta \in (0, 0.5)$ and $1/2p_T \in (X1, X2)$

function:

$$\sigma_\eta(1/2p_T) = \sqrt{A + \frac{B}{p_T}}. \tag{6.9}$$

The output of the fit is constants A and B for a specific $|\eta|$ and IBL bit is shown in Figure 6.9

We generate a square root fit for each combination of η and IBL hits, and create a lookup table of A and B constants. This lookup table corresponds to the core implementation of the FTKFastSim. For a given measured track, we take its pseudorapidity η, and whether it has an IBL hit, and we reference the lookup table to retrieve A_{ij} and B_{ij}. The constants A_{ij} and B_{ij} give us the parameterisation of the resolution as a function of the track's curvature. This allows us to define a Gaussian with width equal to the resolution from our parameterisation. In order to determine the uncertainty of a given track parameter, it is then simply a matter of randomly sampling from the extracted Gaussian. Mathematically the fast simulation process is given by:

$$\mathrm{P}_{\mathrm{Fast}}(|\eta|, 1/2p_T) = \mathrm{P}_{\mathrm{Truth}} + \mathrm{G}_P(1, 0, \sigma(|\eta|, 1/2p_T)). \tag{6.10}$$

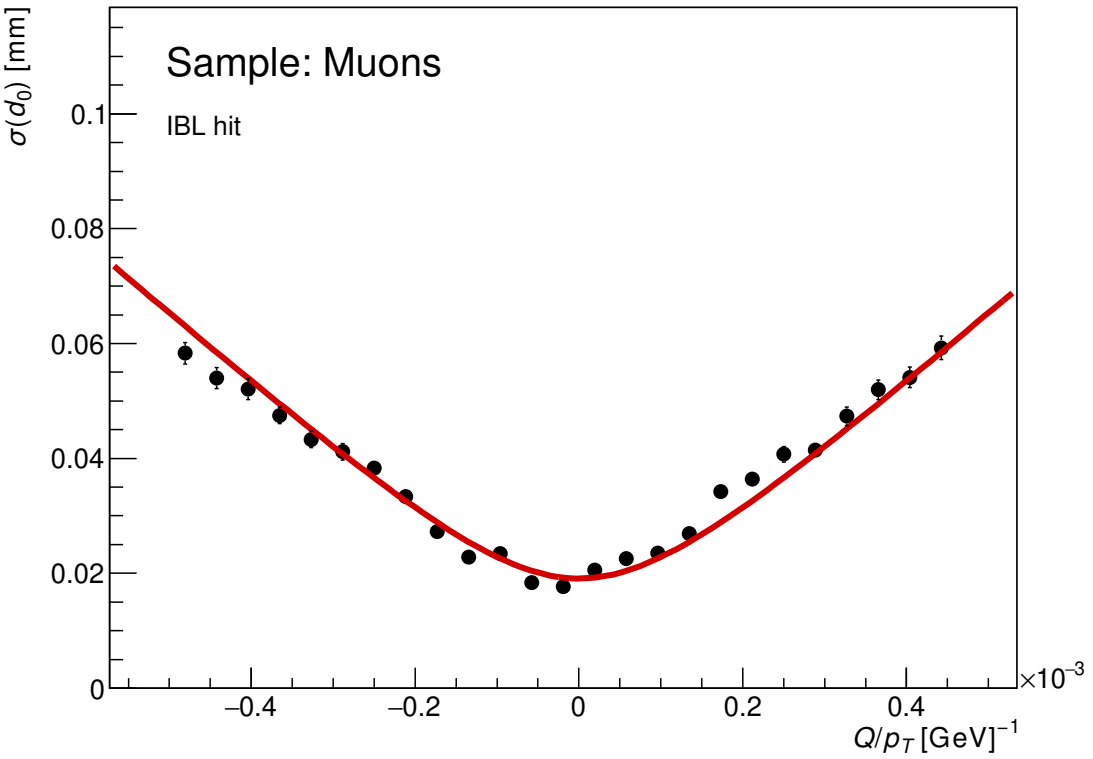

Figure 6.9: An example of a square root fit for the track parameter d_0 with a track having an IBL hit and $|\eta| < 0.5$. The individual black points correspond to resolution of the Gaussian distribution of all tracks which have an IBL hit in $|\eta| < 0.5$ as shown in Figure 6.8

6.4.4 Double Gaussian Case

It was found that different $|\eta|$, curvature and IBL hit combinations resulted in non-negligible tail fractions in the resolution distributions. The origin of these tail fractions was never explicitly determined, but we could include their presence in the resolution parameterisations. It was decided that we could parameterise these non-negligible tails with a second Gaussian contribution. The functional form of the Gaussian fit would therefore be modified, and go like:

$$\mathrm{DG} = G(N_1, \mu_1, \sigma_1) + G(N_2, \mu_2, \sigma_2). \tag{6.11}$$

The variance of a double Gaussian mixture is well understood and given by:

$$\sigma^2_{DG} = p_A\sigma^2_A + p_B\sigma^2_B + \left[p_A\mu^2_A + p_B\mu^2_B - (p_A\mu_A + p_B\mu_B)^2\right]. \tag{6.12}$$

Now, the goal of the track resolution parameterisation is to get a functional form of $\sigma_\eta(1/2p_T)$, which means all the terms which enter into the track resolution must have some known dependence on the curvature. Fortunately for us σ_A, σ_B and their asso-

ciated weights do have this property, but μ_A and μ_B do not have this property. It was decided to apply the constraint of $\mu_A = 0$ and $\mu_B = 0$, and this assumption was validated against truth MC. Making this assumption simplifies our track resolution parameterisation to:

$$\sigma^2_{DG} = p_A\sigma^2_A + p_B\sigma^2_B. \tag{6.13}$$

In order to make this parameterisation feasible we were required to fix the relative height of the tail Gaussian to the core Gaussian to approximately 11% - this choice was motivated by the vast majority of Gaussians naturally falling into this range, and for the stability of fits. By making this relative height assumption, we can normalise our track resolution parameterisation which gives us the value of the p_A and p_B.

When implementing the double Gaussian approach, we require two square root parameterisations. The first being the core Gaussian behaviour and the second being the tail Gaussian behaviour. All the other remaining steps are identical to the single Gaussian approach. The final form of the track parameter resolution smearing is given by:

$$\mathrm{P}_{\mathrm{Fast}} = \mathrm{P}_{\mathrm{Truth}} + \mathrm{DG}_P(1, 0, \sigma_{core}, 0.11, 0, \sigma_{tail}), \tag{6.14}$$

where the FTKFastSim track parameter resolution, $\mathrm{P}_{\mathrm{Fast}}$, is calculated by taking the truth-level value $\mathrm{P}_{\mathrm{Truth}}$, and smearing it by randomly sampling from the fitted double Gaussian, $\mathrm{DG}_P(1, 0, \sigma_{core}, 0.11, 0, \sigma_{tail})$.

6.5 Validation of FTK Fast Simulation

In order to validate FTKFastSim we compare the track resolution for each of the track parameters against FTKFullSim. In order to do this we take all tracks in the FTKFullSim sample, and we calculate the deviation from MC truth. The deviation is given by $\Delta\mathrm{P}_{\mathrm{Full}}$ and is given by:

$$\Delta\mathrm{P}_{\mathrm{Full}} = \mathrm{P}_{\mathrm{Full}} - \mathrm{P}_{\mathrm{Truth}} \tag{6.15}$$

The distribution of $\Delta\mathrm{P}_{\mathrm{Full}}$ gives us the resolution. In order to compare to FTKFastSim we compare the MC truth to a random sampling from the fitted double Gaussian which parameterises the resolution. This defines $\Delta\mathrm{P}_{\mathrm{Fast}}$ and is given by:

$$\Delta\mathrm{P}_{\mathrm{Fast}} = \mathrm{TP}_{\mathrm{Truth}} + DG(1, 0, \sigma_{\mathrm{core}}, 0.11, 0, \sigma_{\mathrm{tail}}). \tag{6.16}$$

The distributions of both simulation approaches are then directly compared for muon and pion samples separately.

The first track parameter we compare is d_0 which is shown in Figure 6.10. In Figure 6.10a, we have the muons and in Figure 6.10b we have the pion sample. For both distributions, we have $\Delta\mathrm{P}$ on the x-axis and number of tracks on the y axis. In the case of muons,

we can see good agreement for the core distribution; however, we see that FTKFastSim has a smaller resolution. In the case of pions, we see that FTKFullSim tends toward a positive bias of ΔP, which corresponds to FTKFullSim overestimating the d_0. This effect is not captured in FTKFastSim - which creates a bump feature around zero, this effect excluded; we see similar resolutions.

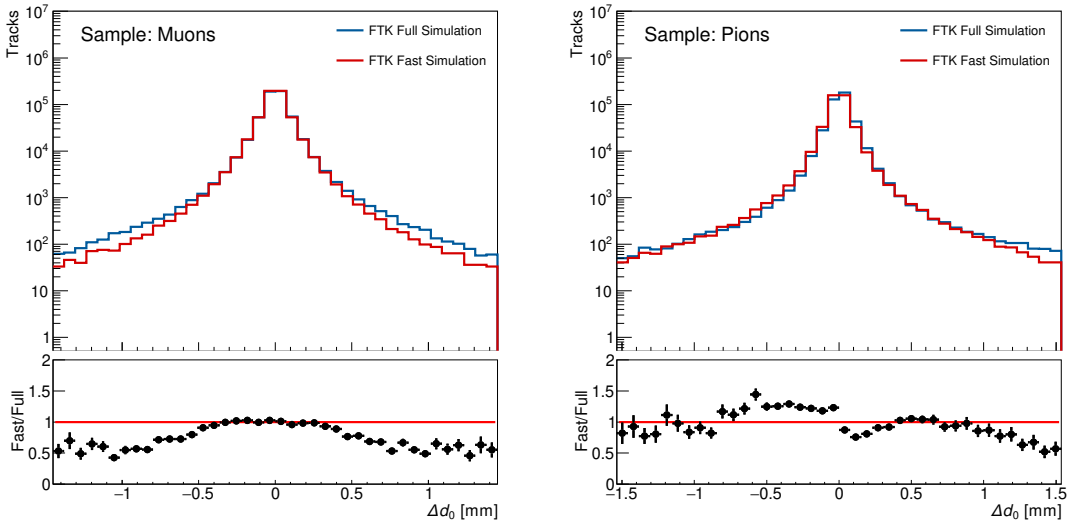

(a) Muon validation (b) Pion validation

Figure 6.10: d_0 FTKFullSim vs FTKFastSim comparison for (a) muons and (b) pions

The second track parameter to compare is z_0, which is shown in Figure 6.11. In the case of muons, we see good agreement across the board in both the core and tail regions, for pions; however, we see good agreement in the core region, but FTKFastSim produces smaller resolutions when compared with FTKFullSim.

Next is η as shown in Figure 6.12 which produces good agreement with muons, however for pions we see large deviations in the tails, where FTKFullSim has a smaller resolution compared to FTKFastSim. Next is ϕ as shown in Figure 6.13 which produces good agreement for muons and good agreement for pions in the core region, with disagreements in the tail regions for pions. This distribution indicates that FTKFullSim has larger deviations compared to truth than predicted. Finally, we have curvature, as shown in Figure 6.14 which has good agreement for muons and a distribution with disagreement in the tails for pions.

Overall we have shown that we can implement an FTK fast simulation approach which produces comparable track parameter resolutions, while taking a fraction of the time to simulate. The goals of this project were met, and this work will continue to play an important role in future hardware-based track-finding systems.

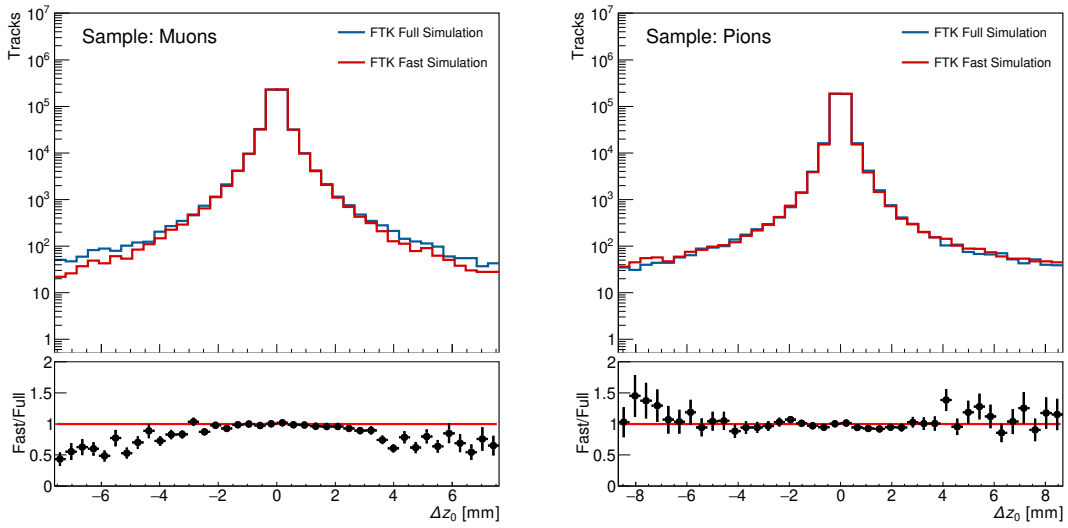

(a) Muon validation (b) Pion validation

Figure 6.11: z_0 FTKFullSim vs FTKFastSim comparison for (a) muons and (b) pions

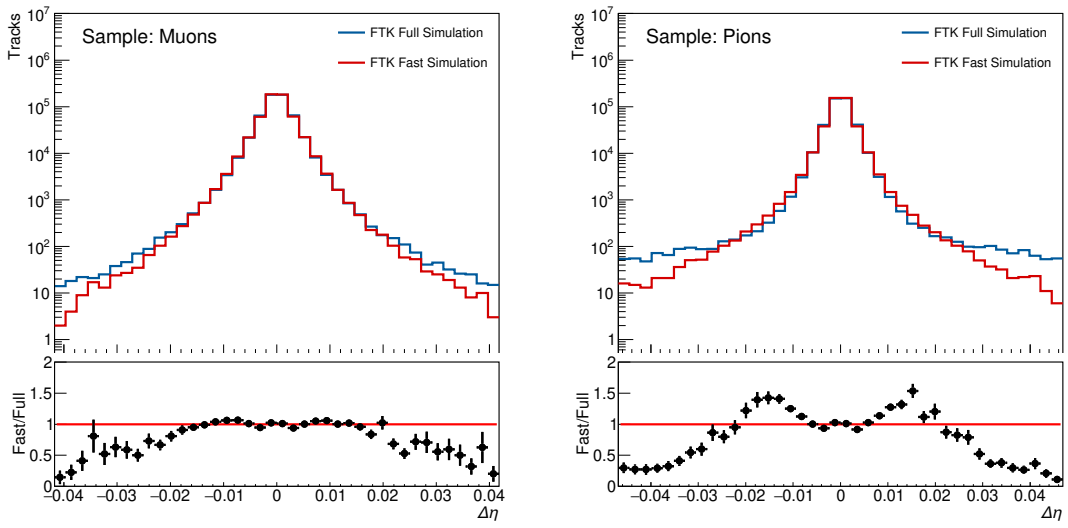

(a) Muon validation (b) Pion validation

Figure 6.12: η FTKFullSim vs FTKFastSim comparison for (a) muons and (b) pions

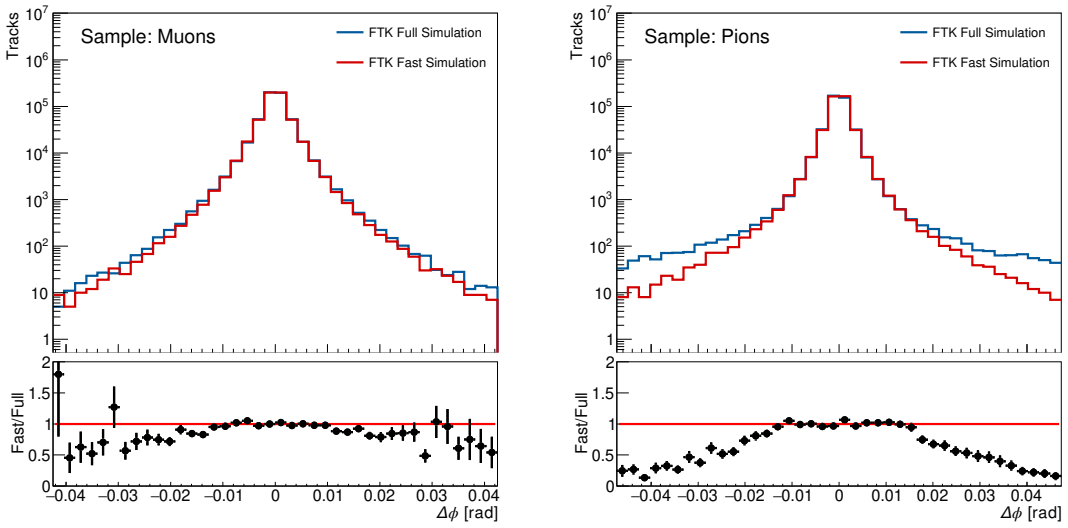

(a) Muon validation (b) Pion validation

Figure 6.13: ϕ FTKFullSim vs FTKFastSim comparison for (a) muons and (b) pions

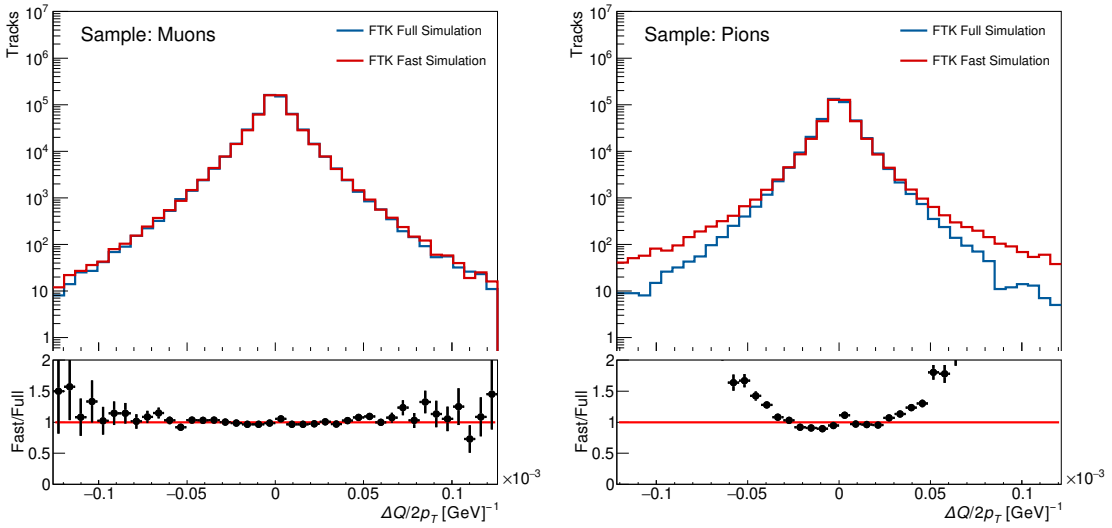

(a) Muon validation (b) Pion validation

Figure 6.14: $1/2p_T$ FTKFullSim vs FTKFastSim comparison for (a) muons and (b) pions

Chapter 7

ITk Strips Digitisation

In this chapter, we focus on the phase-II upgrade work for the Inner Tracker Strips detector (ITk strips). In the current ATLAS detector, we have a strips detector in the SCT, a core difference between the SCT and ITk is the inversion of the silicon doping and module geometry designs. The studies in this chapter summarise the SCT digitisation methods, and answer the question on whether the ITk can utilise the SCT digitisation software.

7.1 Phase-II Upgrade Overview

The ATLAS inner detector was designed for 10 years of operation. The operating conditions were forecasted for an instantaneous luminosity of $\mathcal{L} = 1.0 \times 10^{34}\,\mathrm{cm}^{-2}\mathrm{s}^{-1}$ with a centre-of-mass energy of $14\ \mathrm{TeV}$, $25\ \mathrm{ns}$ between bunch crossings and an average pileup of 23 proton–proton interactions per bunch crossing.

As early as 2016, the LHC exceeded some of these design parameters. The peak instantaneous luminosity in 2018 reached $2.1 \times 10^{34}\ \mathrm{cm}^{-2}\mathrm{s}^{-1}$; the centre-of-mass energy remained at $13\ \mathrm{TeV}$, the time between bunch crossings was $25\ \mathrm{ns}$, and the average pileup per bunch crossing peaked in 2017 at 37.8, before being reduced to 36.1 in 2018.

The HL-LHC is planned to operate at a centre-of-mass energy of $14\ \mathrm{TeV}$ with an average luminosity of $\mathcal{L} = 5\times10^{34}\,\mathrm{cm}^{-2}\mathrm{s}^{-1}$ and an ultimate extension to $\mathcal{L} = 7.5\times10^{34}\,\mathrm{cm}^{-2}\mathrm{s}^{-1}$. This corresponds to an average inelastic proton–proton collisions of $\langle\mu\rangle = 140$ per beam crossing, with an ultimate design goal of $\langle\mu\rangle = 200$. Over the course of 10 years, the HL-LHC is expected to provide the ATLAS experiment with a $3000\ \mathrm{fb}^{-1}$ proton–proton collision dataset.

The current ATLAS inner detector has several hurdles which will be prohibitive for its continued use through to the HL-LHC. The ATLAS inner detector silicon system can tolerate a radiation fluence equivalent to an integrated luminosity of $300\ \mathrm{fb}^{-1}$, which is consistent with an end-of-lifetime in 2023; beyond this level the intrinsic hit efficiencies drop below the limits required for efficient pattern recognition [136][137].

The pixel detector and SCT are able to accommodate an average number of proton–proton collisions per bunch crossing of 50, which comes in conjunction with a peak instantaneous luminosity of $2 \times 10^{34}\,\mathrm{cm}^{-2}\mathrm{s}^{-1}$. For an average pileup of 70 at an L1 rate of $100\ \mathrm{kHz}$ much of the innermost strips barrel can not be read out due to bandwidth saturation. In a HL-LHC scenario, the occupancy of the SCT and TRT would approach 100%, and this would diminish our track-finding efficiencies. These track finding inefficiencies will significantly affect the physics reach of the HL-LHC. The final point, which

is prohibitive for the continued use of the current inner detector for HL-LHC conditions is the track trigger. As it stands, the current inner detector does not provide any tracking information to the Level-1 trigger. In the HL-LHC conditions, we will require a dedicated hardware tracking solution. Given the designed specifications and the end-of-lifetime approaching, the Inner Tracker (ITk) is in the process of being designed and built.

The ITk detector has been designed to accommodate the HL-LHC operating conditions. To summarise, $\langle\mu\rangle = 200$, $\mathcal{L} = 7.5 \times 10^{34}$ cm^{-2}s^{-1} and a total proton–proton dataset $L = 3000$ fb^{-1} The layouts have evolved over time and have been modeled in Geant4 [138].

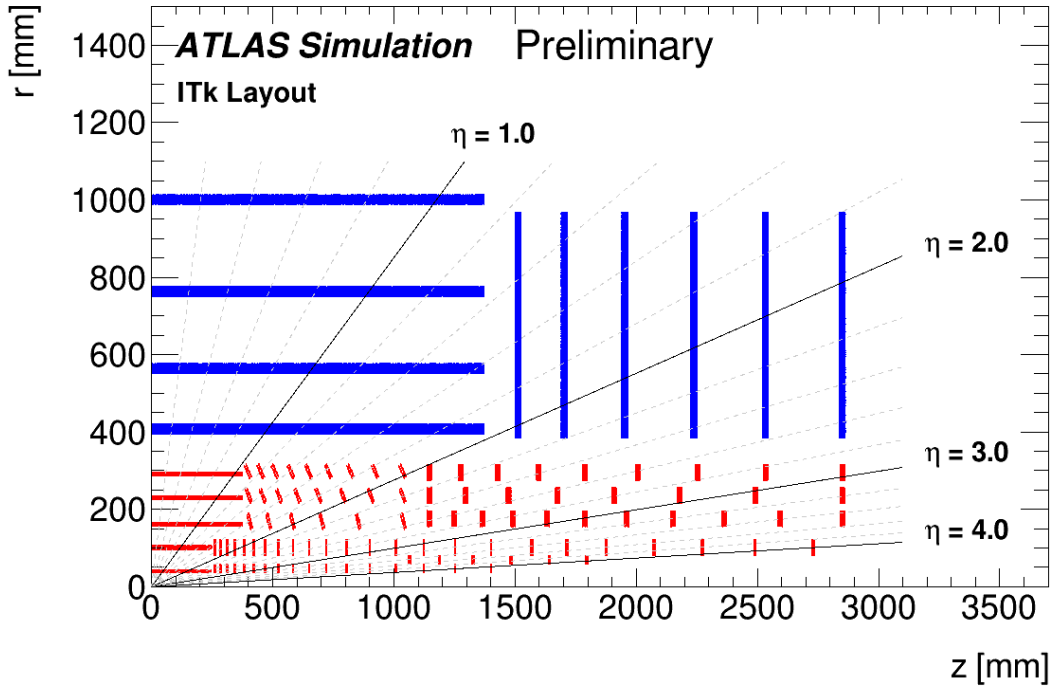

Figure 7.1: The ITk design layout [136].

We show the current layout of a single ITk quadrant in Figure 7.1. The horizontal axis is the longitudinal coordinate of the detector, ranging from 0 to 2800 mm. The vertical axis is the radius r of the layer, which ranges from 0 to 1000 mm. We show the detector distribution for the ITk pixels detector in red and the ITk strips detector in blue. Important η ranges of 1.0, 2.0, 3.0 and 4.0 are overlaid to show the number of layers a track with a given η will pass through. A key design principle is maximising the tracking capability up to $\eta = 4.0$. In the barrel region of both the pixel and strips sub detectors the various sensors are arranged cylindrically around the beampipe. There are five pixel layers and 4 strips layers. The endcap regions are aligned radially, with the strips detector having six disks and the pixel detector having a much larger number, of approximately 28 layers, depending on your choice of η. We show a visualisation of the ITk in Figure 7.2. The ITk strips detector is a system which covers 2.7 units of absolute pseudorapidity, with the barrel region extending to 1400 mm from the nominal interaction point. The endcap

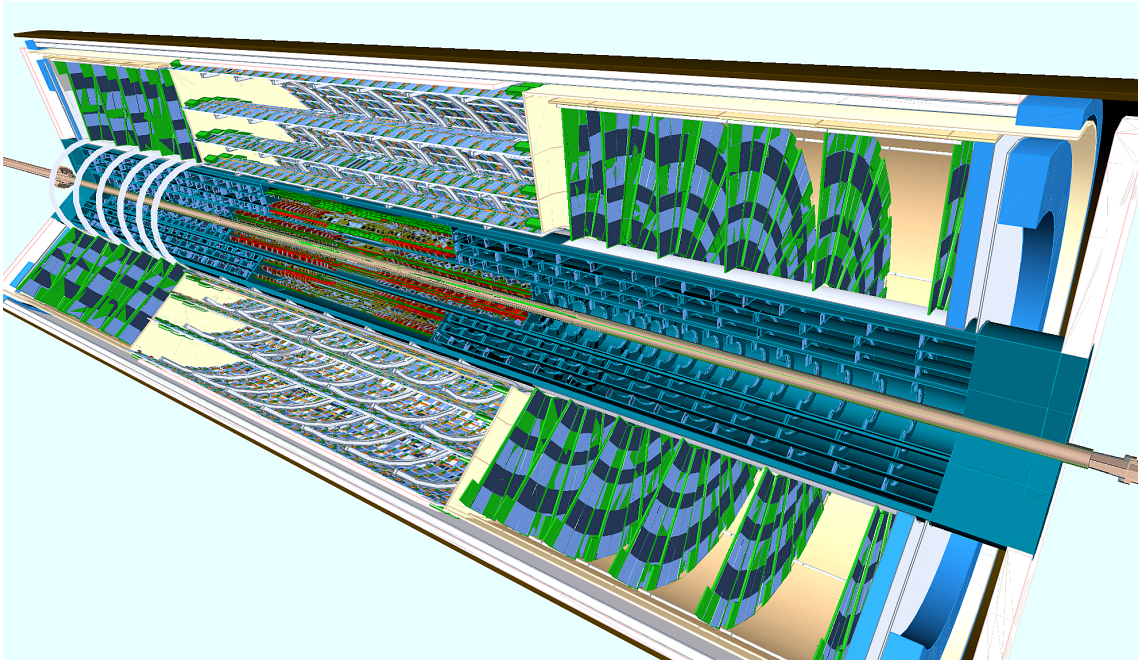

Figure 7.2: An ITk visualisation [136].

system further extends from 1512 mm to 3000 mm.The ITk strips barrel contains four layers, with each layer consisting of paired modules. The endcap consists of 6 identical layers. The base unit for the detector is the ITk strips module. In Figure 7.3 we show the short strips design. The strips sensor has dimensions 97 mm × 97 mm and is attached to the module at the base. Located above the sensor is the front-end hardware, which is responsible for sensor readout and support services. For our digitisation work, we only focus on the sensor. We show a schematic for a strips-based sensor technology in Figure

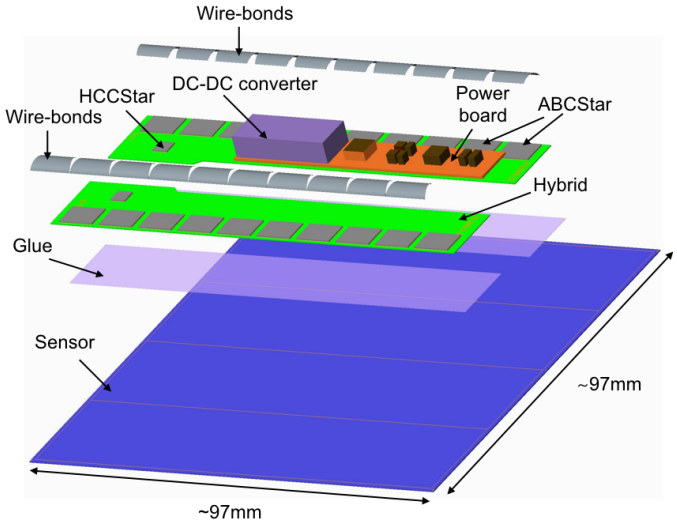

Figure 7.3: A schematic for the ITk barrel modules [136].

7.4. The ITk strips detector utilises a strips sensor configuration which relies on a p-type

float-zone silicon bulk region with thickness $300 - 320\ \mu\text{m}$. We dope the silicon bulk with n-type silicon strips, which are covered by a SiO_2 dielectric layer. The n-type strips are conductively coupled to the readout strips, which are located above the dielectric layer. We refer to the distance between the centre of two strips as the strip pitch. In the case of the ITk barrel modules, the strip pitch is $75.5\ \mu\text{m}$; for endcaps the situation is more complex, as there are different types of endcap modules, with non-parallel strip configurations. The backplane of the strips sensor is called the High Voltage plane (HV). During operation, there are two key voltages in play across the detector. The first is the depletion voltage. The second is the bias voltage which can be put in place to counteract radiation damage effects. We show diagrams of these two types of voltages in Figure 7.5

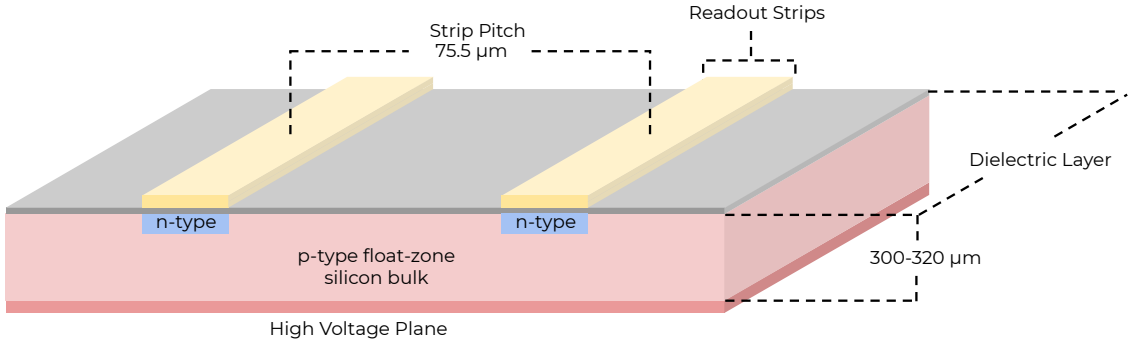

Figure 7.4: A schematic for the ITk sensor geometry [136].

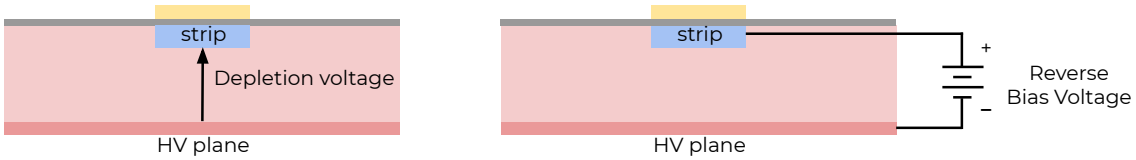

Figure 7.5: A schematic for the sensor depletion voltage and bias voltage.

The barrel module parameters are summarised in Table 7.1. The first column numbers each barrel layer. The second is the radius of the given barrel layer, these are $405\ \text{mm}$, $562\ \text{mm}$, $762\ \text{mm}$ and $1000\ \text{mm}$. The third column states how many channels are present in each module, with the first being 28×1280 and the last layer being 72×1280 channels. The strip pitch for the barrels is uniform. There are two strip lengths for the barrel systems: the short and the long. The first two layers of the ITk strips barrel utilise short strips with a typical strip length of $24.1\ \text{mm}$ and the second two layers use long strips with a typical length of $48.2\ \text{mm}$. The final column in this table is the tilt angle, measured in degrees, where the first layer is $11.5°$, the second is $11.0°$, and the final layers are $10.0°$.

The endcap module parameters are more complex than the barrel modules, with their details summarised in Table 7.2. The first column is Ring/Row, which specifies the endcap ring and also rows from the beampipe. The second column is the inner radius of the endcap layer; starting from $384.5\ \text{mm}$ and extending to $907.6\ \text{mm}$ for the final Ring and Row pair. The strip length is a more complicated situation than the barrel case,

which only had two types. For the endcap case strip length varies between 19.0 mm and extends to 60.2 mm. The strip pitch is also a more complex variable where, unlike the barrel, the strips do not run parallel. In the endcap case, we quote the average strip pitch for a given layer, ranging from 69.9 mm to 80.7 mm. We wish to simulate the

Table 7.1: ITk strips detector barrel layout parameters [136].

Layer	Radius [mm]	Channels in ϕ	Strip Pitch [μm]	Strip Length [mm]	Tilt Angle [°]
0	405	28×1280	75.5	24.1	11.5
1	562	40×1280	75.5	24.1	11.0
2	762	56×1280	75.5	48.2	10.0
3	1000	72×1280	75.5	48.2	10.0

Table 7.2: Layout parameters for the ITk strips detector endcaps [136].

Ring/Row	Inner Radius [mm]	Strip Length [mm]	Strip Pitch [μm]
Ring 0 Row 0	384.5	19	75.0
Ring 0 Row 1	403.5	24	79.2
Ring 0 Row 2	427.5	29	74.9
Ring 0 Row 3	456.4	32	80.2
Ring 1 Row 0	489.8	18.1	69.9
Ring 1 Row 1	507.9	27.1	72.9
Ring 1 Row 2	535	24.1	75.6
Ring 1 Row 3	559.1	15.1	78.6
Ring 2 Row 0	575.6	30.8	75.7
Ring 2 Row 1	606.4	30.8	79.8
Ring 3 Row 0	638.6	32.2	71.1
Ring 3 Row 1	670.8	26.2	74.3
Ring 3 Row 2	697.1	26.2	77.5
Ring 3 Row 3	723.3	32.2	80.7
Ring 2 Row 0	756.9	54.6	75.0
Ring 2 Row 1	811.5	54.6	80.3
Ring 2 Row 0	867.5	40.2	76.2
Ring 2 Row 1	907.6	60.2	80.5

effect of an incident charged particle on the modules of the ITk as laid out in this section. The digitization must be fast and accurate, given its role in trigger decisions. Given the SCT used a similar technology to the ITk strips system, our goal was to learn the SCT digitization techniques which were implemented in the early 2000s, and to determine if

these techniques could be transferred to the ITk sub-systems. The goal of this project is to advise follow up teams on their digitization approaches.

7.2 The Induced Charge Model

We now wish to take the geometry of the ITk strips detector and simulate the effect of ionising radiation. In doing this, we explain the digitisation process which sensors undergo in order to generate a hit in the detector. The first method we explore is the Induced Charge Model (ICM), and the second is a simplified digitisation model. In the way of contrast, the ICM can be refered to as the detailed model. The ordering of these sections is to explain the dynamics first and then simplify later. The actual implementation was inverse to this, as the ICM was developed after the simplified model.

The ICM provides a detailed simulation and digitisation model for the charge carriers in a given sensor design. The ICM incorporates the effects of both the majority and the minority charge carrier drift as well as carrier diffusion throughout the silicon bulk, and also allows for a varying electric field throughout the sensor.

The ICM is a ballistic model which calculates the drift velocity of a carrier every 0.1ns via,

$$\vec{v}_d = \mu_d \vec{E}(x, y), \tag{7.1}$$

where $\mu_d^{e/h}$ is the carrier drift mobility and the sensor electric field is given by $\vec{E}(x, y)$. The drift mobility in the simplified model is given as a single nominal value, but in the ICM we parameterise the mobility via:

$$\mu_d = \frac{v_s / E_c}{(1 + (E/E_c)^\beta)^{1/\beta}}, \tag{7.2}$$

where s is the drift velocity, E_C is a critical electric field of the material. β is a saturation factor. There are different μ_d for electrons and holes.

The effects of diffusion are incorporated by parameterising the diffusion with a Gaussian distribution with standard deviation,

$$\sigma = \sqrt{2D\delta t}, \tag{7.3}$$

where the diffusion constant D is given by:

$$D = k_B T \mu_d / e. \tag{7.4}$$

In the presence of a magnetic field $\vec{B}$, the trajectory of a carrier is rotated by the Lorentz angle θ_L which is a function of position within the sensor, the magnitude of the magnetic

field, temperature, and carrier mobilities. The Lorentz angle is given by:

$$\tan\theta_{\mathrm{L}} = \mu_H|\vec{B}| = r\mu_d|\vec{B}|, \tag{7.5}$$

where μ_H is the Hall mobility of a carrier and r is known as the Hall factor. The movement of charge through the bulk induces a current on the strips. The current is present until the charge carriers carriers recombine at the electrode they are propagating toward. Using Ramo's theorem [139, 140], we can calculate the induced charge over time, first by calculating the current:

$$i = qv\vec{E}_v, \tag{7.6}$$

where v is the instantaneous velocity of the charge carrier and E_v is the weighting (or Ramo) field. It is *not* the electric field. The Ramo potential is the potential associated with the electric field E_v.

In practice, the Ramo potential is calculated by setting the potential of the strip in question to 1 V and setting all other conductive surfaces to 0 V. The Ramo potential shows us where the current on a conductor is generated, from the presence of a charge carrier's motion. To calculate the drift field, we first set the HV plane to 500 V and the strips to zero. The drift field provides the drift directions of the charge carriers throughout the silicon bulk, minus the perturbations due to magnetic field presence.

In Figure 7.6, we show the Ramo potential for an SCT strips sensor. We calculate the potential with a bias voltage of 150 V, a depletion voltage of 50 V and an operating temperature of 276.85 K. The HV plane corresponds to a sensor depth of 0 μm; the nominal SCT sensor depth also called the strip plane is located at 285 μm. The distances between the strips are to scale, the strip pitch here is 75.5 μm. We denote the direction perpendicular to the strips as X, and the units are μm. We show five strips either side of the central strip. The first notable feature of Figure 7.6 is the substantial peak around the core strip. This strip is the one with the potential set to 1 V. We see the expected decrease of the Ramo potential as we move away from the strip plane and toward the HV plane. Where our intuition may break down is the complex behaviour around neighbour strips. A given charge carrier will contribute less to a neighbouring strip, as compared to a nearby strip. We fully incorporate this effect in the ICM model.

In Figure 7.7 we shown the x and y components of the SCT drift field $\vec{E}$. The left plot shows E_x as a function of sensor depth and relative position to a given strip's centre X. We can see that the electric field has a lobe feature, with high electric field strengths for positions close to the strip itself. The right plot shows E_y, which has is symmetric relative to the centre of the strip. We see the magnitude of the y component is typically much larger than the value of the x component.

Propagating a charge throughout the silicon bulk every 0.1 ns is computationally expensive, as is a continual reference to a 5 μm $\times$ 5 μm reference Ramo potential and reference electric fields; this requires constant knowledge of detector conditions, as well as the sil-

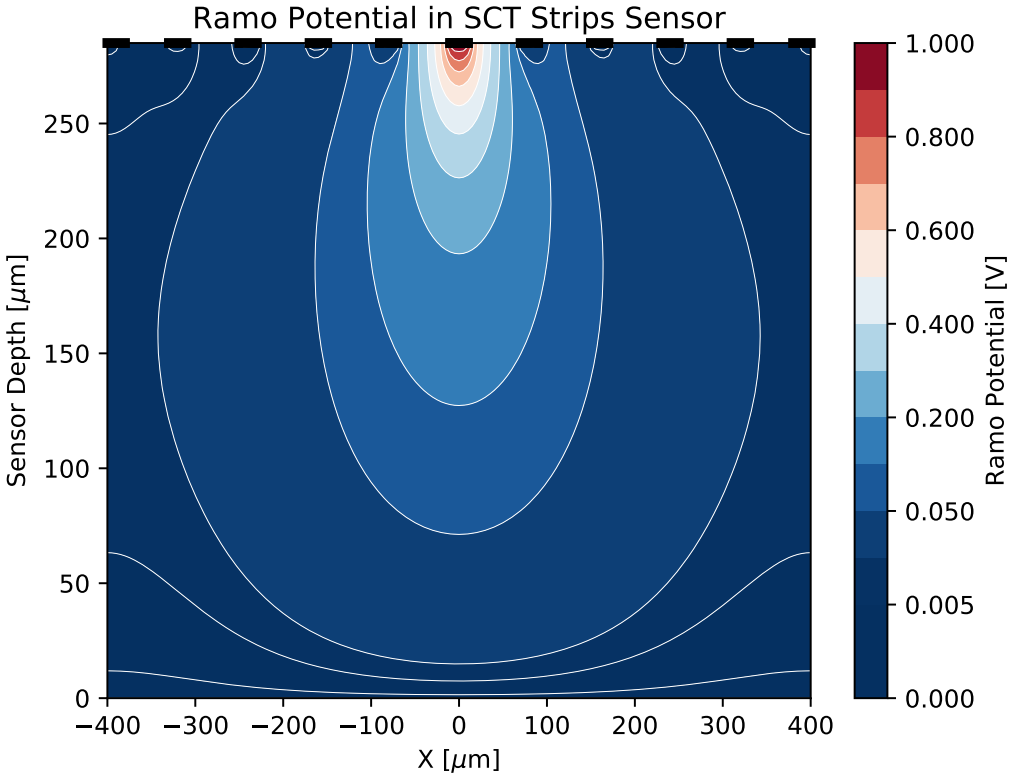

Figure 7.6: The SCT Ramo potential as a function of sensor depth [μm] and X μm away from a central strip; $X = 0$ μm. The top of the plot contains black bands, which correspond to the location of the strips. The Ramo potential is in units of Volts and is also a function of bias voltage, depletion voltage and temperature.

Table 7.3: Summary of SCT silicon bulk properties.

Parameter	Electrons	Holes
v_s [cm/s]	$1.53 \times 10^9 \cdot T^{-0.87}$	$1.62 \times 10^8 \cdot T^{-0.52}$
E_C [V/cm]	$1.01 \cdot T^{1.55}$	$1.24 \cdot T^{1.68}$
β	$2.57 \times 10^{-2} \cdot T^{0.66}$	$0.46 \cdot T^{0.17}$
r	$1.13 + 0.0008 \cdot (T - 273)$	$0.72 - 0.0005 \cdot (T - 273)$

icon bulk properties of electrons and holes, as shown in Table 7.3. In order to use the ICM model for the ITk strips system, we require the silicon bulk properties, Ramo potential and drift fields to be updated. At present these quantities are hardcoded in the SCT digitisation software package. The implementation of strip modules in the SCT digitisation code requires a constant lookup for each local X and local Y positions in each module. The ITk strips modules will need to be incorporated into the simulation. In the SCT digitisation software there is an inherent assumption of longitudinal symmetry along the strips themselves, and for this reason, we can not use the ICM model in the endcaps, as the assumption of longitudinal symmetry breaks down, i.e. the strip pitch

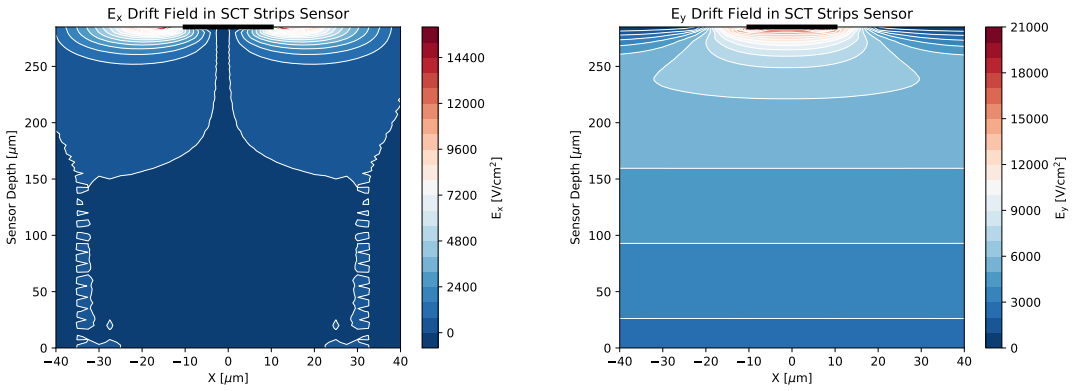

(a) E_x (b) E_y

Figure 7.7: We show SCT $\vec{E}^{\text{drift}}$ function of sensor depth in μ m and X μ m relative to the centre of the strip as shown at the top of each plot as a black band. The drift field is in units of V/cm^3. The x component is shown in (a) and the y drift field component is shown in (b).

is not constant. This endcap limitation was present in SCT system, and is therefore not a new limitation for digitisation, but rather a continued one. We find we can apply the ICM to the ITk system, we now introduce the simplified model and benchmark it against the ICM.

7.3 Simplified Digitization Model

We now provide a description of the simplified digitisation model. A schematic of the model is provided in Figure 7.8. The simplified model begins with a deposit of energy in the silicon bulk. The energy deposits are assumed to in the form of a cloud of hole majority carriers. The model divides the energy deposit based on 5 μm step sizes, called sub-hits distributes the energy deposit across each step and from there we propagate these divided energy deposits according to:

$$\delta y = \delta z \tan \theta_{\text{L}}, \tag{7.7}$$

where δy is the drift distance of the energy deposit parallel to the surface of the silicon bulk δz is the shift of the energy deposit toward the surface of the silicon bulk and θ_L is the Lorentz angle. The Lorentz angle is a function of temperature T, electric field $\vec{E}$ and carrier mobility μ_d. The drift time can then be calculated as a function of sensor properties, carrier mobility and the bias and depletion voltages. The total time it takes for the energy deposit to drift to the strip is calculated with:

$$t_{\text{drift}}(\delta z) = \frac{d^2}{2\mu_d V_{\text{D}}} \ln\left(\frac{V_{\text{B}} + V_{\text{D}}}{V_{\text{B}} + V_{\text{B}} - \frac{2V_{\text{D}}\delta z}{d}}\right). \tag{7.8}$$

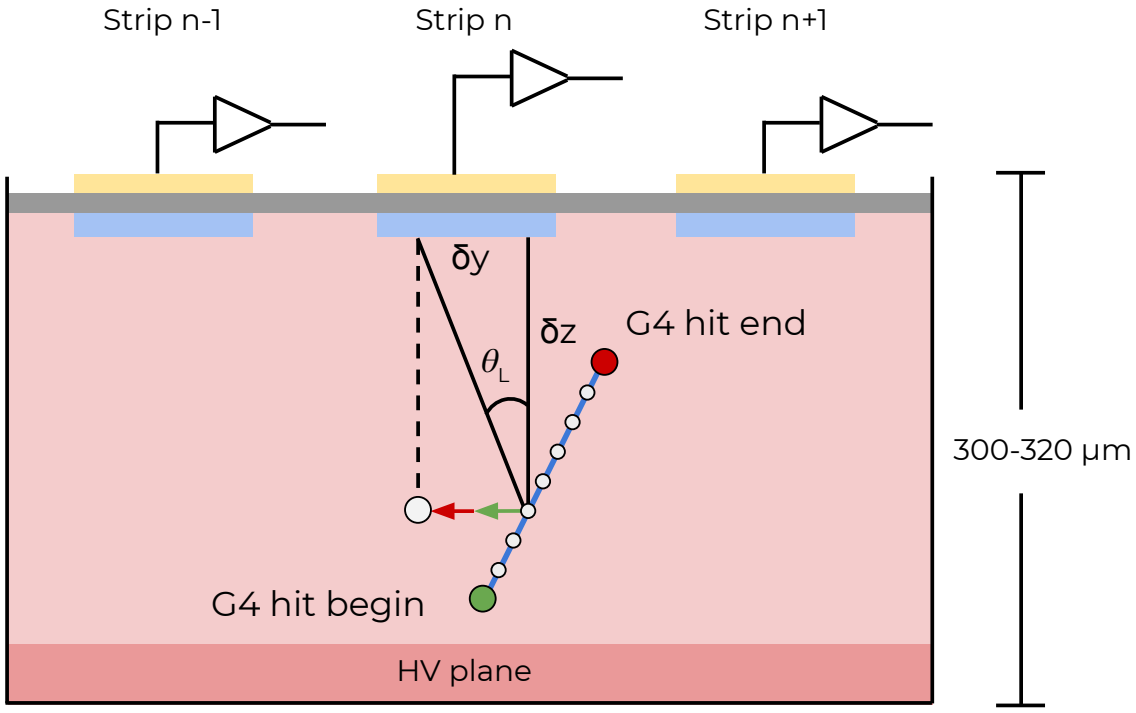

Figure 7.8: A schematic of the simplified model implementation for the ITk. The full description is provided in text.

The y motion of the carrier originating from diffusive motion and is given as:

$$\delta y_{\text{diff}} = \sqrt{2Dt_{\text{drift}}\delta z}, \tag{7.9}$$

and

$$D = \frac{k_{\text{B}}T\mu_d}{e}. \tag{7.10}$$

This gives us a total δy motion as given in:

$$\delta y = \delta z \tan\theta_{\text{L}} + \delta y_{\text{diff}}. \tag{7.11}$$

We can then get a total time to readout of t_{total}:

$$t_{\text{total}} = \underbrace{t_{\text{drift}} + t_{\text{surf}}}_{\text{drift term}} + t_{\text{TOF}}, \tag{7.12}$$

where t_{surf} is a correction for the simplified model. Once we have projected the G4 hit to the strip we calculate the number of electron–hole pairs by calculating the energy deposited per G4 sub-hit and then normalise to the energy required to form an electron–

hole pair. The total number of electron–hole pairs is given by:

$$n_{\text{pair}} = \frac{dE}{dX}\frac{1}{n_{\text{step}}}\frac{1}{3.62\text{eV}}, \tag{7.13}$$

where 3.62 eV is the energy required to form an electron–hole pair at room temperature. We can take the number of pairs and calculate the charge accumulated with:

$$Q = en_{\text{pair}}. \tag{7.14}$$

This charge relation is the key assumption of the simplified model, as we implicitly assume all the current, or charge produced on the strip is produced by incident charge carriers and not via an electromotive force. In practice, the charge on a given strip is

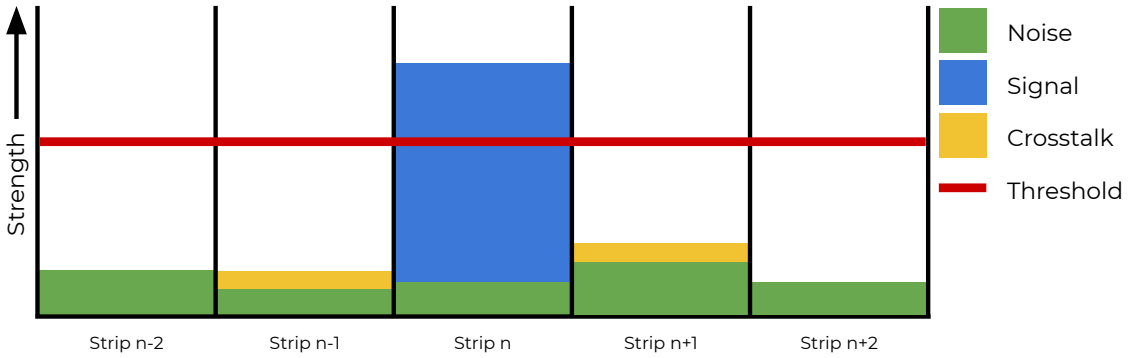

Figure 7.9: We show a schematic of the digitisation effects in the ITk strips modules. We show a given strip n and the adjacent strips, with a corresponding accumulated charge for a given 25 ns window. There is a charge threshold required to be met for a strip to register a hit, and we show the threshold in red. The electronic noise is shown in green. A given strip n can then have an accumulation of charge which is above the threshold, and we call this a signal. We denote the signal in blue. We show the effect of cross-talk in yellow.

reduced by strip–strip interactions as well as strip–HV–plane interactions. This results in reduction of charge on the target strip, and is incorporated with $f_{\text{crosstalk}}$, $f_{\text{crosstalk+1}}$ and f_{HV}. Typically $f_{\text{crosstalk}}$ corresponds to 90% with $f_{\text{crosstalk+1}}$ corresponding to 5%, and f_{HV} is approximately 93%. We show a breakdown of the various strip effects in Figure 7.9. The total charge on a given strip is given by:

$$q_{\text{strip}} = f_{\text{crosstalk}} f_{HV} Q, \tag{7.15}$$

$$q_{\text{strip+1}} = f_{\text{crosstalk+1}} f_{HV} Q. \tag{7.16}$$

Every 10 ns we check the charge accumulation on a given strip and if it breaches the threshold $q_{\text{threshold}}$ of 1 fC then we say that strip has a hit. Using this method, we can simulate the effect of incident charged particles on the ITk strips system. Once we have implemented the digitisation, we generate MC simulation of single muon and single pion

production using typical values of track parameters from proton–proton collisions. We implement the ITk geometry and validate the geometry.

7.4 Validation and Conclusions

In order to validate the implementation of the ITk geometry, we look at the (x, y) position of each hit in our simulation of the ITk inner detector. When we do this, we see that the (x, y) position traces out the geometry of the ITk. Given the agreement between Figure 7.10 and Table 7.1, we can be confident the geometry has been implemented correctly.

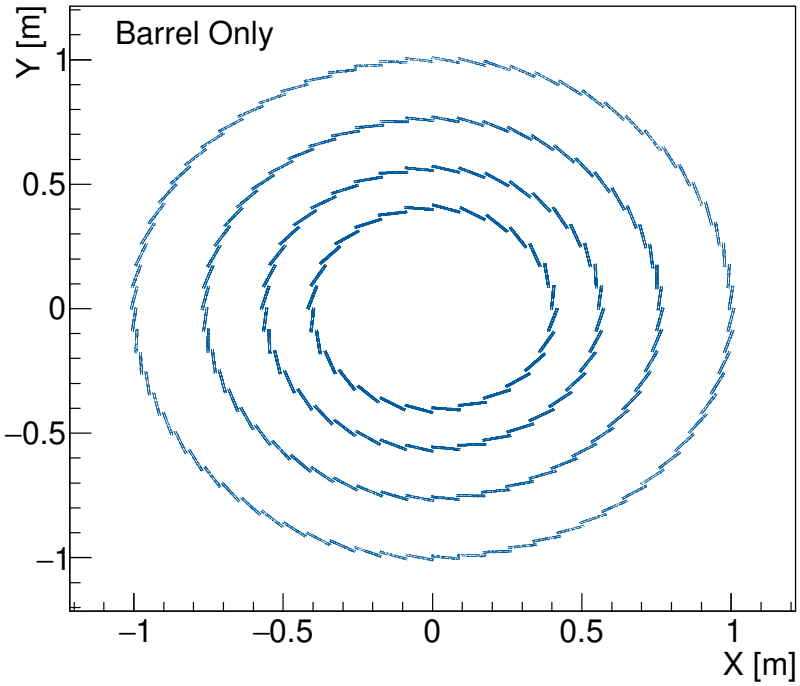

Figure 7.10: The geometry of the ITk strips detector as traced out by the (x,y) position of each track in our simulation. This is a good cross-check for our geometry implementation.

Next, we wish to compare the reconstructed track quantities between the simplified and ICM simulations of the ITk strips digitisation. We split the validation between the two models into different sectors, the first sector being the barrel of the detector and the second being the end caps. As discussed earlier, the ICM model makes an assumption of a longitudinal symmetry along the sensor module. As the endcap's strip pitch varies radially, the ICM can not be used here. Given the limitations of the ICM model, we only compare the two models in the barrel sectors.

The quantities we wish to compare are the widths of the cluster hits, called the cluster width. In Figure 7.11, we show the cluster widths for the simplified and the ICM mod-

els. We see that the simplified digitisation approach produces approximately 20% more single hit clusters, and the ICM model produces more two to four-hit wide clusters than the simplified. Ultimately the larger the cluster width, the better agreement between the simplified and ICM models. It is reassuring that the two methods produce similar behaviour for the most complex detector situations.

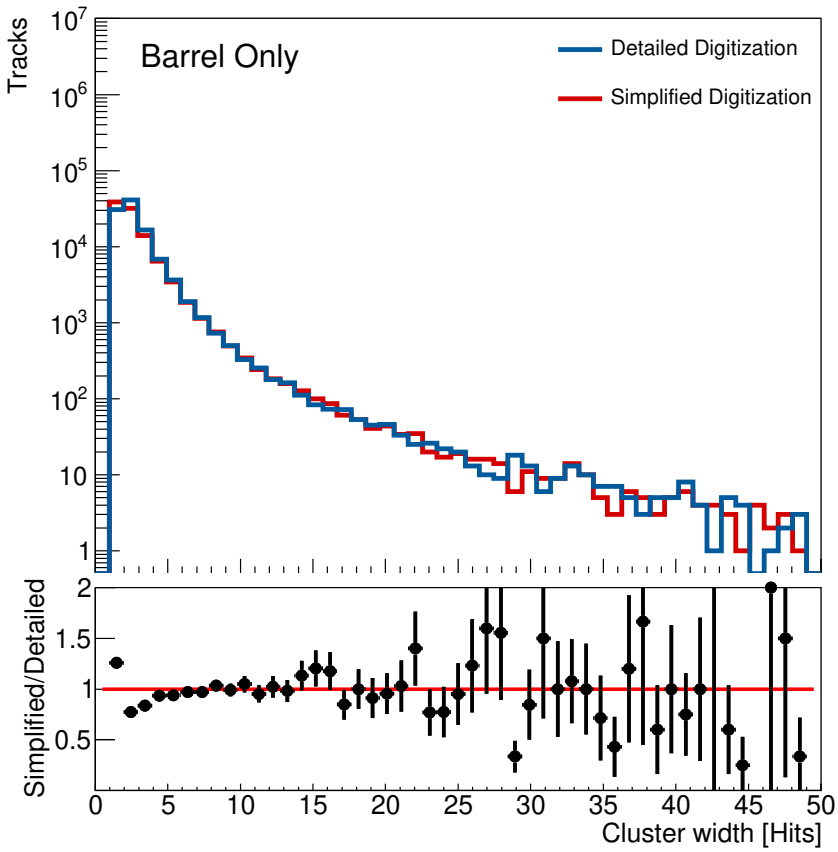

Figure 7.11: Cluster widths of tracks using simplified vs induced charge model.

In Figure 7.12, we have a number of track parameters for the incident particles on simulated ITk geometry. We see that for all track parameters, the simplified and ICM methodologies produce nearly identical results. We see that the reconstruction of a given track does not depend on the choice of digitisation procedure. We do see that the reconstructed track χ^2 has a distinctly different shape, with the simplified model producing tracks with smaller χ^2.

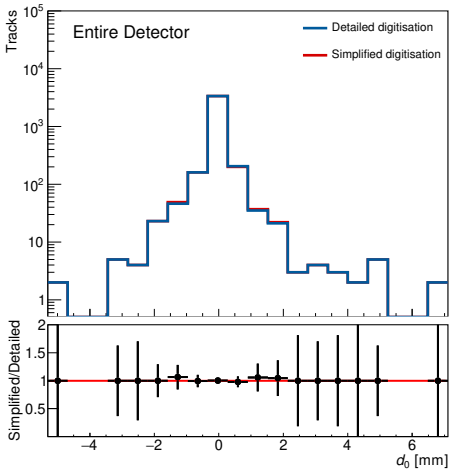

(a) d_0

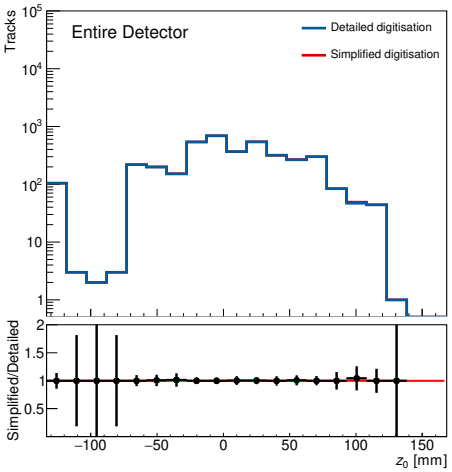

(b) z_0

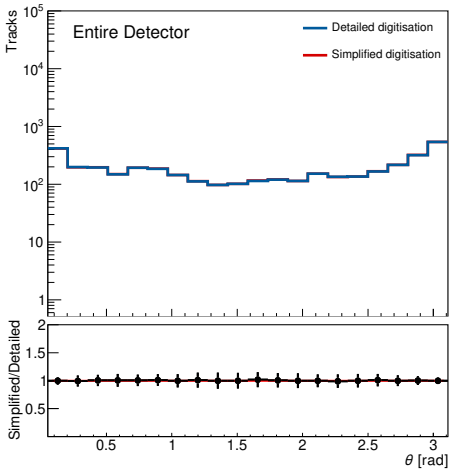

(c) θ

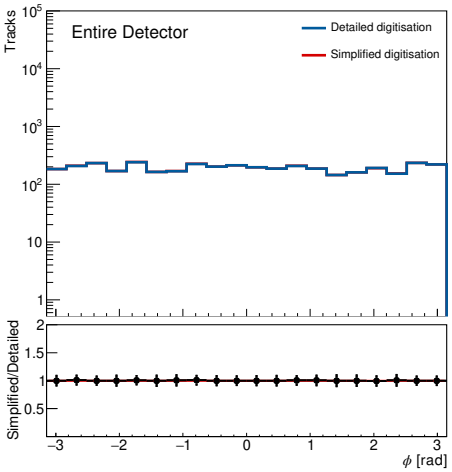

(d) ϕ

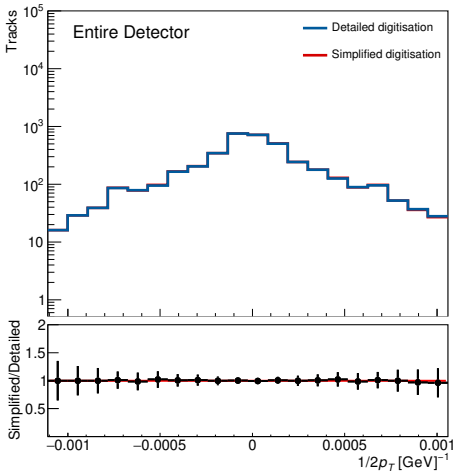

(e) $Q/2p_T$

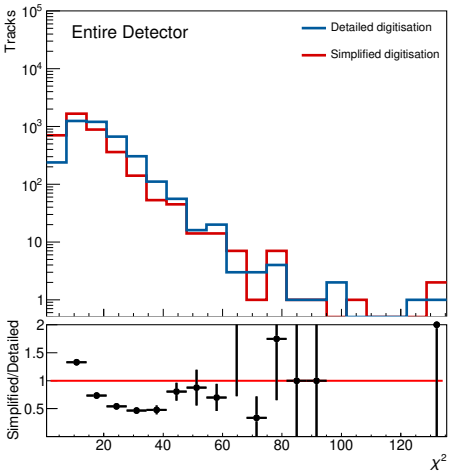

(f) χ^2

Figure 7.12: The comparison between the simplified and induced charge digitization models for d_0, z_0, θ, ϕ, $1/2p_T$ and χ^2. We find good agreement between the two models for the track parameters, with a difference of shape for χ^2

Chapter 8

Concluding Remarks

The work contained within this document represents a broad summary of my contributions to the ATLAS collaboration. The four core topics central to my thesis were: the search for supersymmetric electroweak production; a measurement of the Higgs boson production cross-section; the development of FTK fast simulation; and finally, characterising the ITk strips digitisation implementation.

In the search for supersymmetric electroweak production, I provided a full overview of the full run-II excess follow up for the recursive jigsaw electroweak search for chargino-neutralino production with two lepton and three lepton final states. I provided a detailed overview of the background estimation methods, including a data-driven background estimation technique known as the ABCD method. Using the ABCD method, we were able to provide a robust estimate of the Z+jets background contribution, which was dominant in our 2ℓ signal regions. Ultimately I determined that the observed number of events was in good agreement with the expected background estimates. I presented the results in terms of model-independent limits for each of the four signal regions defined in our analysis.

In the measurement of the gluon-gluon fusion Higgs boson production cross section via $H \rightarrow WW^* \rightarrow e\nu\mu\nu$, I highlighted the work undertaken to get a data-driven estimate of the b-tagging efficiency. The analysis was very dependent on the b-tag efficiency systematic and I was able to implement a method which significantly reduced this dependency. I then summarised the full run-II combined measurements, which represents the culmination of many years of hard work by the ATLAS collaboration.

In the FTK fast simulation project, I introduced the FTK and then provided an overview of the FTK hardware implementation. I described the CPU intensive full simulation and its full implementation. I finally introduced the fast simulation approach to parameterising the resolution of full simulation on individual tracks. I detailed the methodology and finally provided benchmarking of the fast simulation method against the full simulation method.

The final project explored the implementation of the SCT digitisation software for ITk purposes. In pursuing this goal, I provided a detailed overview of the geometry of the ITk strips detector and individual modules and strips. I then introduced the induced charge model and a time-of-flight based simplified model. I introduced vital concepts such as the Ramo potential and drift field, which was core to the software implementation. I found that the Induced Charge Model can not be applied to the endcaps of the ITk strips due to variable strip pitch. I found the simplified and induced charge models reconstructed track parameters had a strong agreement and determined that the bottle-

neck for applying the SCT digitisation code to the ITk strips detector is not the model, but rather the implementation of the ITk's different strip geometries.

These projects act as a summary of some critical directions forward for the ATLAS collaboration. For ATLAS to remain successful, we must continue to innovate to extract the maximum amount of information from the full Run-II, and future Run-III dataset. Concurrently, we must invest time into our core upgrade projects. These projects represent the future of the collaboration; they will take high energy particle physics into the 2030s and continue inspire to thousands of aspiring physicists.

Bibliography

[1] F. Englert and R. Brout. "Broken Symmetry and the Mass of Gauge Vector Mesons". In: *Phys. Rev. Lett.* 13 (9 Aug. 1964), pp. 321–323. DOI: 10.1103/PhysRevLett.13.321. URL: https://link.aps.org/doi/10.1103/PhysRevLett.13.321.

[2] P.W. Higgs. "Broken symmetries, massless particles and gauge fields". In: *Physics Letters* 12.2 (1964), pp. 132–133. ISSN: 0031-9163. DOI: https://doi.org/10.1016/0031-9163(64)91136-9. URL: http://www.sciencedirect.com/science/article/pii/0031916364911369.

[3] Peter W. Higgs. "Broken Symmetries and the Masses of Gauge Bosons". In: *Phys. Rev. Lett.* 13 (16 Oct. 1964), pp. 508–509. DOI: 10.1103/PhysRevLett.13.508. URL: https://link.aps.org/doi/10.1103/PhysRevLett.13.508.

[4] G. S. Guralnik, C. R. Hagen, and T. W. B. Kibble. "Global Conservation Laws and Massless Particles". In: *Phys. Rev. Lett.* 13 (20 Nov. 1964), pp. 585–587. DOI: 10.1103/PhysRevLett.13.585. URL: https://link.aps.org/doi/10.1103/PhysRevLett.13.585.

[5] Peter W. Higgs. "Spontaneous Symmetry Breakdown without Massless Bosons". In: *Phys. Rev.* 145 (4 May 1966), pp. 1156–1163. DOI: 10.1103/PhysRev.145.1156. URL: https://link.aps.org/doi/10.1103/PhysRev.145.1156.

[6] T. W. B. Kibble. "Symmetry Breaking in Non-Abelian Gauge Theories". In: *Phys. Rev.* 155 (5 Mar. 1967), pp. 1554–1561. DOI: 10.1103/PhysRev.155.1554. URL: https://link.aps.org/doi/10.1103/PhysRev.155.1554.

[7] Wikipedia contributors. *Standard Model — Wikipedia, The Free Encyclopedia*. [Online; accessed 17-August-2020]. 2020. URL: https://en.wikipedia.org/w/index.php?title=Standard_Model&oldid=970721485.

[8] M. Tanabashi et al. "Review of Particle Physics". In: *Phys. Rev. D* 98.3 (2018), p. 030001. DOI: 10.1103/PhysRevD.98.030001.

[9] Wikimedia Commons. *File:Elementary particle interactions.svg — Wikimedia Commons, the free media repository*. [Online; accessed 17-August-2020]. 2016. URL: https://commons.wikimedia.org/w/index.php?title=File:Elementary_particle_interactions.svg&oldid=201507070.

[10] Paul Langacker. *The Standard Model and Beyond*. CRC press, 2009.

[11] S Heinemeyer et al. *Handbook of LHC Higgs Cross Sections: 3. Higgs Properties: Report of the LHC Higgs Cross Section Working Group*. Ed. by S Heinemeyer. CERN Yellow Reports: Monographs. July 2013. DOI: 10.5170/CERN-2013-004. URL: https://cds.cern.ch/record/1559921.

[12] Silvia Necco and Rainer Sommer. "The N(f) = 0 heavy quark potential from short to intermediate distances". In: *Nucl. Phys.* B622 (2002), pp. 328–346. DOI: 10.1016/S0550-3213(01)00582-X. arXiv: hep-lat/0108008 [hep-lat].

[13] Sidney Coleman and Jeffrey Mandula. "All Possible Symmetries of the S Matrix". In: *Phys. Rev.* 159 (5 July 1967), pp. 1251–1256. DOI: 10.1103/PhysRev.159.1251. URL: http://link.aps.org/doi/10.1103/PhysRev.159.1251.

[14] Csaba Csaki. "The Minimal Supersymmetric Standard Model". In: *Modern Physics Letters A* 11.08 (1996), pp. 599–613.

[15] Stephen P Martin. "A Supersymmetry Primer (2011)". In: *arXiv preprint hep-ph/9709356* 161 (2011), p. 162.

[16] Glennys R. Farrar and Pierre Fayet. "Phenomenology of the Production, Decay, and Detection of New Hadronic States Associated with Supersymmetry". In: *Physics Letters B* 76.5 (1978), pp. 575–579.

[17] Abdelhak Djouadi. "The Anatomy of Electroweak Symmetry Breaking Tome II: The Higgs Bosons in the Minimal Supersymmetric Model". In: *Physics reports* 459.1 (2008), pp. 1–241.

[18] Masaaki Kuroda. "Complete Lagrangian of MSSM". In: *arXiv preprint hep-ph/9902340* 3 (2005).

[19] Katherine Garrett and Gintaras Duda. "Dark Matter: A Primer". In: *Advances in Astronomy* 2011 (2011), pp. 1–22. ISSN: 1687-7977. DOI: 10.1155/2011/968283. URL: http://dx.doi.org/10.1155/2011/968283.

[20] Lyndon R Evans and Philip Bryant. "LHC Machine". In: *JINST* 3 (2008). This report is an abridged version of the LHC Design Report (CERN-2004-003), S08001. 164 p. DOI: 10.1088/1748-0221/3/08/S08001. URL: https://cds.cern.ch/record/1129806.

[21] *LEP design report*. Copies shelved as reports in LEP, PS and SPS libraries. Geneva: CERN, 1984. URL: https://cds.cern.ch/record/102083.

[22] Esma Mobs. "The CERN accelerator complex. Complexe des accélérateurs du CERN". In: (July 2016). General Photo. URL: https://cds.cern.ch/record/2197559.

[23] L Arnaudon et al. *Linac4 Technical Design Report*. Tech. rep. CERN-AB-2006-084. CARE-Note-2006-022-HIPPI. revised version submitted on 2006-12-14 09:00:40. Geneva: CERN, Dec. 2006. URL: http://cds.cern.ch/record/1004186.

[24] ATLAS Collaboration. "Diagram of an LHC dipole magnet. Schéma d'un aimant dipôle du LHC". June 1999. URL: https://cds.cern.ch/record/40524.

[25] The ATLAS Collaboration. "The ATLAS Experiment at the CERN Large Hadron Collider". In: *Journal of Instrumentation* 3.08 (Aug. 2008), S08003–S08003. DOI: 10.1088/1748-0221/3/08/s08003. URL: https://doi.org/10.1088%2F1748-0221%2F3%2F08%2Fs08003.

[26] The CMS Collaboration. "The CMS experiment at the CERN LHC". In: *Journal of Instrumentation* 3.08 (Aug. 2008), S08004–S08004. DOI: 10.1088/1748-0221/3/08/s08004. URL: https://doi.org/10.1088%2F1748-0221%2F3%2F08%2Fs08004.

[27] The ALICE Collaboration. "The ALICE experiment at the CERN LHC". In: *Journal of Instrumentation* 3.08 (Aug. 2008), S08002–S08002. DOI: 10.1088/1748-0221/

3/08/s08002. URL: https://doi.org/10.1088%2F1748-0221%2F3%2F08%2Fs08002.

[28] The LHCb Collaboration. "The LHCb Detector at the LHC". In: *Journal of Instrumentation* 3.08 (Aug. 2008), S08005–S08005. DOI: 10.1088/1748-0221/3/08/s08005. URL: https://doi.org/10.1088%2F1748-0221%2F3%2F08%2Fs08005.

[29] M Capeans et al. *ATLAS Insertable B-Layer Technical Design Report*. Tech. rep. CERN-LHCC-2010-013. ATLAS-TDR-19. Sept. 2010. URL: https://cds.cern.ch/record/1291633.

[30] The ATLAS Collaboration. "ATLAS pixel detector electronics and sensors". In: *Journal of Instrumentation* 3.07 (July 2008), P07007–P07007. DOI: 10.1088/1748-0221/3/07/p07007. URL: https://doi.org/10.1088%2F1748-0221%2F3%2F07%2Fp07007.

[31] The ATLAS collaboration. "Operation and performance of the ATLAS semiconductor tracker". In: *Journal of Instrumentation* 9.08 (Aug. 2014), P08009–P08009. ISSN: 1748-0221. DOI: 10.1088/1748-0221/9/08/p08009. URL: http://dx.doi.org/10.1088/1748-0221/9/08/P08009.

[32] The ATLAS TRT collaboration et al. "The ATLAS Transition Radiation Tracker (TRT) proportional drift tube: design and performance". In: *Journal of Instrumentation* 3.02 (Feb. 2008), P02013–P02013. DOI: 10.1088/1748-0221/3/02/p02013. URL: https://doi.org/10.1088%2F1748-0221%2F3%2F02%2Fp02013.

[33] The ATLAS TRT collaboration et al. "The ATLAS TRT end-cap detectors". In: *Journal of Instrumentation* 3.10 (Oct. 2008), P10003–P10003. DOI: 10.1088/1748-0221/3/10/p10003. URL: https://doi.org/10.1088%2F1748-0221%2F3%2F10%2Fp10003.

[34] The ATLAS TRT collaboration et al. "The ATLAS TRT Barrel Detector". In: *Journal of Instrumentation* 3.02 (Feb. 2008), P02014–P02014. DOI: 10.1088/1748-0221/3/02/p02014. URL: https://doi.org/10.1088%2F1748-0221%2F3%2F02%2Fp02014.

[35] S Fratina and E Klinkby. *The Geometry of the ATLAS Transition Radiation Tracker*. Tech. rep. ATL-COM-INDET-2010-002. Geneva: CERN, Jan. 2010. URL: https://cds.cern.ch/record/1232064.

[36] *Particle Identification Performance of the ATLAS transition Radiation Tracker*. Tech. rep. ATLAS-CONF-2011-128. Geneva: CERN, Sept. 2011. URL: https://cds.cern.ch/record/1383793.

[37] The ATLAS Collaboration. "Performance of the ATLAS track reconstruction algorithms in dense environments in LHC Run 2". In: *The European Physical Journal C* 77.10 (2017), p. 673. DOI: 10.1140/epjc/s10052-017-5225-7. URL: https://doi.org/10.1140/epjc/s10052-017-5225-7.

[38] G. Aad et al. "Performance of the ATLAS muon trigger in pp collisions at s=8TeV". In: *The European Physical Journal C* 75.3 (2015), p. 120. DOI: 10.1140/epjc/

s10052-015-3325-9. URL: https://doi.org/10.1140/epjc/s10052-015-3325-9.

[39] Milene Calvetti and Nicolò Vladi Biesuz. "Integration and Commissioning of the ATLAS Fast TracKer system". In: *PoS* LHCP2018 (2018), p. 028. DOI: 10.22323/1.321.0028.

[40] "The ATLAS Data Acquisition and High Level Trigger system". In: *Journal of Instrumentation* 11.06 (June 2016), P06008–P06008. DOI: 10.1088/1748-0221/11/06/p06008. URL: https://doi.org/10.1088%2F1748-0221%2F11%2F06%2Fp06008.

[41] The ATLAS Collaboration. "Performance of the ATLAS trigger system in 2015". In: *The European Physical Journal C* 77.5 (May 2017). ISSN: 1434-6052. DOI: 10.1140/epjc/s10052-017-4852-3. URL: http://dx.doi.org/10.1140/epjc/s10052-017-4852-3.

[42] *Trigger Menu in 2017*. Tech. rep. ATL-DAQ-PUB-2018-002. Geneva: CERN, June 2018. URL: https://cds.cern.ch/record/2625986.

[43] Joao Pequenao and Paul Schaffner. "How ATLAS detects particles: diagram of particle paths in the detector". Jan. 2013. URL: https://cds.cern.ch/record/1505342.

[44] The ATLAS collaboration. "A neural network clustering algorithm for the ATLAS silicon pixel detector". In: *Journal of Instrumentation* 9.09 (Sept. 2014), P09009–P09009. ISSN: 1748-0221. DOI: 10.1088/1748-0221/9/09/p09009. URL: http://dx.doi.org/10.1088/1748-0221/9/09/P09009.

[45] T G Cornelissen et al. "The global $\chi 2$ track fitter in ATLAS". In: *Journal of Physics: Conference Series* 119.3 (July 2008), p. 032013. DOI: 10.1088/1742-6596/119/3/032013. URL: https://doi.org/10.1088%2F1742-6596%2F119%2F3%2F032013.

[46] R. Frühwirth. "Application of Kalman filtering to track and vertex fitting". In: *Nuclear Instruments and Methods in Physics Research Section A: Accelerators, Spectrometers, Detectors and Associated Equipment* 262.2 (1987), pp. 444–450. ISSN: 0168-9002. DOI: https://doi.org/10.1016/0168-9002(87)90887-4. URL: http://www.sciencedirect.com/science/article/pii/0168900287908874.

[47] The ATLAS Collaboration. "Electron reconstruction and identification in the ATLAS experiment using the 2015 and 2016 LHC proton–proton collision data at s=13 TeV". In: *The European Physical Journal C* 79.8 (Aug. 2019). ISSN: 1434-6052. DOI: 10.1140/epjc/s10052-019-7140-6. URL: http://dx.doi.org/10.1140/epjc/s10052-019-7140-6.

[48] W Lampl et al. *Calorimeter Clustering Algorithms: Description and Performance*. Tech. rep. ATL-LARG-PUB-2008-002. ATL-COM-LARG-2008-003. Geneva: CERN, Apr. 2008. URL: https://cds.cern.ch/record/1099735.

[49] The ATLAS Collaboration. "Topological cell clustering in the ATLAS calorimeters and its performance in LHC Run 1". In: *The European Physical Journal C* 77.7 (2017), p. 490. DOI: 10.1140/epjc/s10052-017-5004-5. URL: https://doi.org/10.1140/epjc/s10052-017-5004-5.

[50] The ATLAS Collaboration. "Measurement of the photon identification efficiencies with the ATLAS detector using LHC Run 2 data collected in 2015 and 2016". In: *The European Physical Journal C* 79.3 (Mar. 2019). ISSN: 1434-6052. DOI: 10.1140/epjc/s10052-019-6650-6. URL: http://dx.doi.org/10.1140/epjc/s10052-019-6650-6.

[51] The ATLAS Collaboration. "Electron and photon performance measurements with the ATLAS detector using the 2015–2017 LHC proton-proton collision data". In: *Journal of Instrumentation* 14.12 (Dec. 2019), P12006–P12006. ISSN: 1748-0221. DOI: 10.1088/1748-0221/14/12/p12006. URL: http://dx.doi.org/10.1088/1748-0221/14/12/P12006.

[52] The ATLAS Collaboration. "Muon reconstruction performance of the ATLAS detector in proton–proton collision data at sqrt(s) =13TeV". In: *The European Physical Journal C* 76.5 (May 2016). ISSN: 1434-6052. DOI: 10.1140/epjc/s10052-016-4120-y. URL: http://dx.doi.org/10.1140/epjc/s10052-016-4120-y.

[53] Matteo Cacciari, Gavin P Salam, and Gregory Soyez. "The anti-ktjet clustering algorithm". In: *Journal of High Energy Physics* 2008.04 (Apr. 2008), pp. 063–063. DOI: 10.1088/1126-6708/2008/04/063. URL: https://doi.org/10.1088%2F1126-6708%2F2008%2F04%2F063.

[54] Matteo Cacciari, Gavin P. Salam, and Gregory Soyez. "FastJet user manual". In: *The European Physical Journal C* 72.3 (2012), p. 1896. DOI: 10.1140/epjc/s10052-012-1896-2. URL: https://doi.org/10.1140/epjc/s10052-012-1896-2.

[55] The ATLAS Collaboration. "Measurements of b-jet tagging efficiency with the ATLAS detector using ttbar events at sqrt(s)=13TeV". In: *Journal of High Energy Physics* 2018.8 (2018), p. 89. DOI: 10.1007/JHEP08(2018)089. URL: https://doi.org/10.1007/JHEP08(2018)089.

[56] The ATLAS Collaboration. "Performance of missing transverse momentum reconstruction with the ATLAS detector using proton–proton collisions at sqrt(s) = 13TeV". In: *The European Physical Journal C* 78.11 (2018), p. 903. DOI: 10.1140/epjc/s10052-018-6288-9. URL: https://doi.org/10.1140/epjc/s10052-018-6288-9.

[57] "LuminosityPublicResultsRun2". URL: https://twiki.cern.ch/twiki/bin/view/AtlasPublic/LuminosityPublicResultsRun2.

[58] "LuminosityPublicResults". URL: https://twiki.cern.ch/twiki/bin/view/AtlasPublic/LuminosityPublicResults.

[59] A. D. Martin et al. "Parton distributions for the LHC". In: *The European Physical Journal C* 63.2 (July 2009), pp. 189–285. ISSN: 1434-6052. DOI: 10.1140/epjc/s10052-009-1072-5. URL: http://dx.doi.org/10.1140/epjc/s10052-009-1072-5.

[60] *Standard Model Summary Plots Spring 2020*. Tech. rep. ATL-PHYS-PUB-2020-010. Geneva: CERN, May 2020. URL: http://cds.cern.ch/record/2718937.

[61] "LHCHXSWGCrossSectionsFigures". URL: https://twiki.cern.ch/twiki/bin/view/LHCPhysics/LHCHXSWGCrossSectionsFigures.

[62] Christoph Borschensky et al. "Squark and gluino production cross sections in p p collisions at s = 13 , 14 , 33 and 100 TeV". In: *The European Physical Journal C* 74.12 (Dec. 2014). ISSN: 1434-6052. DOI: 10.1140/epjc/s10052-014-3174-y. URL: http://dx.doi.org/10.1140/epjc/s10052-014-3174-y.

[63] C. Gütschow and Z. Marshall. *Setting limits on supersymmetry using simplified models*. 2012. arXiv: 1202.2662 [hep-ex].

[64] Apollinari G. et al. *High-Luminosity Large Hadron Collider (HL-LHC): Technical Design Report V. 0.1*. CERN Yellow Reports: Monographs. Geneva: CERN, 2017. DOI: 10.23731/CYRM-2017-004. URL: https://cds.cern.ch/record/2284929.

[65] The ATLAS Collaboration. "Search for chargino-neutralino production using recursive jigsaw reconstruction in final states with two or three charged leptons in proton-proton collisions at s=13 TeV with the ATLAS detector". In: *Physical Review D* 98.9 (Nov. 2018). ISSN: 2470-0029. DOI: 10.1103/physrevd.98.092012. URL: http://dx.doi.org/10.1103/PhysRevD.98.092012.

[66] Paul Jackson and Christopher Rogan. "Recursive jigsaw reconstruction: HEP event analysis in the presence of kinematic and combinatoric ambiguities". In: *Physical Review D* 96.11 (Dec. 2017). ISSN: 2470-0029. DOI: 10.1103/physrevd.96.112007. URL: http://dx.doi.org/10.1103/PhysRevD.96.112007.

[67] The ATLAS Collaboration. "Monte Carlo Generators for the Production of a W or Z/γ^* Boson in Association with Jets at ATLAS in Run 2". In: *ATL-PHYS-PUB-2016-003* (Jan. 2016). URL: https://cds.cern.ch/record/2120133.

[68] T. Gleisberg et al. "Event generation with SHERPA 1.1". In: *JHEP* 02 (2009), p. 007. DOI: 10.1088/1126-6708/2009/02/007. arXiv: 0811.4622 [hep-ph].

[69] Richard D. Ball et al. "Parton distributions for the LHC Run II". In: *JHEP* 04 (2015), p. 040. DOI: 10.1007/JHEP04(2015)040. arXiv: 1410.8849 [hep-ph].

[70] T. Gleisberg and S. Höche. "Comix, a new matrix element generator". In: *JHEP* 12 (2008), p. 039. DOI: 10.1088/1126-6708/2008/12/039. arXiv: 0808.3674 [hep-ph].

[71] Cascioli, Fabio and Maierhöfer, Philipp and Pozzorini, Stefano. "Scattering Amplitudes with Open Loops". In: *Phys. Rev. Lett.* 108 (2012), p. 111601. DOI: 10.1103/PhysRevLett.108.111601. arXiv: 1111.5206 [hep-ph].

[72] Steffen Schumann and Frank Krauss. "A Parton shower algorithm based on Catani-Seymour dipole factorisation". In: *JHEP* 03 (2008), p. 038. DOI: 10.1088/1126-6708/2008/03/038. arXiv: 0709.1027 [hep-ph].

[73] S. Höche, F. Krauss, M. Schönherr and F. Siegert. "QCD matrix elements + parton showers: The NLO case". In: *JHEP* 04 (2013), p. 027. DOI: 10.1007/JHEP04(2013)027. arXiv: 1207.5030 [hep-ph].

[74] Hung-Liang Lai et al. "New parton distributions for collider physics". In: *Phys. Rev. D* 82 (2010), p. 074024. DOI: 10.1103/PhysRevD.82.074024. arXiv: 1007.2241 [hep-ph].

[75] Simone Alioli et al. "A general framework for implementing NLO calculations in shower Monte Carlo programs: the POWHEG BOX". In: *JHEP* 06 (2010), p. 043. DOI: 10.1007/JHEP06(2010)043. arXiv: 1002.2581 [hep-ph].

[76] The ATLAS Collaboration. "Simulation of top quark production for the ATLAS experiment at $\sqrt{s} = 13$ TeV". In: *ATL-PHYS-PUB-2016-004* (Jan. 2016). URL: https://cds.cern.ch/record/2120417.

[77] Stefano Frixione, Paolo Nason, and Carlo Oleari. "Matching NLO QCD computations with parton shower simulations: the POWHEG method". In: *JHEP* 11 (2007), p. 070. DOI: 10.1088/1126-6708/2007/11/070. arXiv: 0709.2092 [hep-ph].

[78] P. Artoisenet, R. Frederix, O. Mattelaer and R. Rietkerk. "Automatic spin-entangled decays of heavy resonances in Monte Carlo simulations". In: *JHEP* 03 (2013), p. 015. DOI: 10.1007/JHEP03(2013)015. arXiv: 1212.3460 [hep-ph].

[79] T. Sjöstrand, S. Mrenna and P. Skands. "PYTHIA 6.4 Physics and Manual". In: *JHEP* 05 (2006), p. 026. DOI: 10.1088/1126-6708/2006/05/026. arXiv: hep-ph/0603175.

[80] J. Pumplin et al. "New generation of parton distributions with uncertainties from global QCD analysis". In: *JHEP* 07 (2002), p. 012. DOI: 10.1088/1126-6708/2002/07/012. arXiv: hep-ph/0201195.

[81] Peter Zeiler Skands. "Tuning Monte Carlo Generators: The Perugia Tunes". In: *Phys. Rev. D* 82 (2010), p. 074018. DOI: 10.1103/PhysRevD.82.074018. arXiv: 1005.3457 [hep-ph].

[82] Michał Czakon, Paul Fiedler, and Alexander Mitov. "Total Top Quark Pair Production Cross Section at Hadron Colliders Through $O(\alpha_S^4)$". In: *Phys. Rev. Lett.* 110 (2013), p. 252004. DOI: 10.1103/PhysRevLett.110.252004. arXiv: 1303.6254 [hep-ph].

[83] M. Czakon and A. Mitov. "Top++: A Program for the Calculation of the Top-Pair Cross-Section at Hadron Colliders". In: *Comput. Phys. Commun.* 185 (2014), p. 2930. DOI: 10.1016/j.cpc.2014.06.021. arXiv: 1112.5675 [hep-ph].

[84] Nikolaos Kidonakis. "Two-loop soft anomalous dimensions for single top quark associated production with a W^- or H^-". In: *Phys. Rev. D* 82 (2010), p. 054018. DOI: 10.1103/PhysRevD.82.054018. arXiv: 1005.4451 [hep-ph].

[85] Nikolaos Kidonakis. "Next-to-next-to-leading-order collinear and soft gluon corrections for t-channel single top quark production". In: *Phys. Rev. D* 83 (2011), p. 091503. DOI: 10.1103/PhysRevD.83.091503. arXiv: 1103.2792 [hep-ph].

[86] M. Aliev et al. "HATHOR: HAdronic Top and Heavy quarks crOss section calculatoR". In: *Comput. Phys. Commun.* 182 (2011), pp. 1034–1046. DOI: 10.1016/j.cpc.2010.12.040. arXiv: 1007.1327 [hep-ph].

[87] P. Kant et al. "HatHor for single top-quark production: Updated predictions and uncertainty estimates for single top-quark production in hadronic collisions". In: *Comput. Phys. Commun.* 191 (2015), pp. 74–89. DOI: 10.1016/j.cpc.2015.02.001. arXiv: 1406.4403 [hep-ph].

[88] J. Alwall et al. "The automated computation of tree-level and next-to-leading order differential cross sections, and their matching to parton shower simulations".

In: *JHEP* 07 (2014), p. 079. DOI: 10.1007/JHEP07(2014)079. arXiv: 1405.0301 [hep-ph].

[89] T. Sjöstrand et al. "An Introduction to PYTHIA 8.2". In: *Comput. Phys. Commun.* 191 (2015), pp. 159–177. DOI: 10.1016/j.cpc.2015.01.024. arXiv: 1410.3012 [hep-ph].

[90] The ATLAS Collaboration. "Modelling of the $t\bar{t}H$ and $t\bar{t}V$ $(V = W, Z)$ processes for $\sqrt{s} = 13$ TeV ATLAS analyses". In: *ATL-PHYS-PUB-2016-005* (Jan. 2016). URL: https://cds.cern.ch/record/2120826.

[91] A. Lazopoulos, T. McElmurry, K. Melnikov and F. Petriello. "Next-to-leading order QCD corrections to $t\bar{t}Z$ production at the LHC". In: *Phys. Lett. B* 666 (2008), pp. 62–65. DOI: 10.1016/j.physletb.2008.06.073. arXiv: 0804.2220 [hep-ph].

[92] John M. Campbell and R. Keith Ellis. "$t\bar{t}W^{\pm}$ production and decay at NLO". In: *JHEP* 07 (2012), p. 052. DOI: 10.1007/JHEP07(2012)052. arXiv: 1204.5678 [hep-ph].

[93] The ATLAS Collaboration. "Multi-Boson Simulation for 13 TeV ATLAS Analyses". In: *ATL-PHYS-PUB-2016-002* (Jan. 2016). URL: https://cds.cern.ch/record/2119986.

[94] John M. Campbell and R. Keith Ellis. "An Update on vector boson pair production at hadron colliders". In: *Phys. Rev. D* 60 (1999), p. 113006. DOI: 10.1103/PhysRevD.60.113006. arXiv: hep-ph/9905386.

[95] John M. Campbell, R. Keith Ellis, and Ciaran Williams. "Vector boson pair production at the LHC". In: *JHEP* 07 (2011), p. 018. DOI: 10.1007/JHEP07(2011)018. arXiv: 1105.0020 [hep-ph].

[96] Steffen Schumann and Frank Krauss. "A Parton shower algorithm based on Catani-Seymour dipole factorisation". In: *JHEP* 03 (2008), p. 038. DOI: 10.1088/1126-6708/2008/03/038. arXiv: 0709.1027 [hep-ph].

[97] S. Höche, F. Krauss, S. Schumann and F. Siegert. "QCD matrix elements and truncated showers". In: *JHEP* 05 (2009), p. 053. DOI: 10.1088/1126-6708/2009/05/053. arXiv: 0903.1219 [hep-ph].

[98] The ATLAS Collaboration. *Multi-Boson Simulation for 13 TeV ATLAS Analyses*. Tech. rep. ATL-PHYS-PUB-2017-005. Geneva: CERN, May 2017. URL: http://cds.cern.ch/record/2261933.

[99] G. Corcella et al. "HERWIG 6.5: an event generator for Hadron Emission Reactions With Interfering Gluons (including supersymmetric processes)". In: *JHEP* 01 (2001), p. 010. DOI: 10.1088/1126-6708/2001/01/010. arXiv: hep-ph/0011363.

[100] S. Dittmaier et al. "Handbook of LHC Higgs Cross Sections: 2. Differential Distributions". In: *CERN-2012-002* (2012). DOI: 10.5170/CERN-2012-002. arXiv: 1201.3084 [hep-ph].

[101] F. Maltoni and T. Stelzer. "MadEvent: Automatic event generation with MadGraph". In: *JHEP* 02 (2003), p. 027. DOI: 10.1088/1126-6708/2003/02/027. arXiv: hep-ph/0208156.

[102] *ATLAS Pythia 8 tunes to 7 TeV datas*. Tech. rep. ATL-PHYS-PUB-2014-021. Geneva: CERN, Nov. 2014. URL: https://cds.cern.ch/record/1966419.

[103] L. Lönnblad and S. Prestel. "Matching Tree-Level Matrix Elements with Interleaved Showers". In: *JHEP* 03 (2012), p. 019. DOI: 10.1007/JHEP03(2012)019. arXiv: 1109.4829 [hep-ph].

[104] W. Beenakker, R. Höpker, M. Spira and P.M. Zerwas. "Squark and gluino production at hadron colliders". In: *Nucl. Phys. B* 492 (1997), pp. 51–103. DOI: 10.1016/S0550-3213(97)00084-9. arXiv: hep-ph/9610490.

[105] A. Kulesza and L. Motyka. "Threshold resummation for squark-antisquark and gluino-pair production at the LHC". In: *Phys. Rev. Lett.* 102 (2009), p. 111802. DOI: 10.1103/PhysRevLett.102.111802. arXiv: 0807.2405 [hep-ph].

[106] A. Kulesza and L. Motyka. "Soft gluon resummation for the production of gluino-gluino and squark-antisquark pairs at the LHC". In: *Phys. Rev. D* 80 (2009), p. 095004. DOI: 10.1103/PhysRevD.80.095004. arXiv: 0905.4749 [hep-ph].

[107] Wim Beenakker et al. "Soft-gluon resummation for squark and gluino hadroproduction". In: *JHEP* 12 (2009), p. 041. DOI: 10.1088/1126-6708/2009/12/041. arXiv: 0909.4418 [hep-ph].

[108] W. Beenakker et al. "Squark and gluino hadroproduction". In: *Int. J. Mod. Phys. A* 26 (2011), pp. 2637–2664. DOI: 10.1142/S0217751X11053560. arXiv: 1105.1110 [hep-ph].

[109] Christoph Borschensky et al. "Squark and gluino production cross sections in pp collisions at $\sqrt{s}$ = 13, 14, 33 and 100 TeV". In: *Eur. Phys. J. C* 74 (2014), p. 3174. DOI: 10.1140/epjc/s10052-014-3174-y. arXiv: 1407.5066 [hep-ph].

[110] The ATLAS Collaboration. "Muon reconstruction performance of the ATLAS detector in proton–proton collision data at $\sqrt{s}$ =13 TeV". In: *Eur. Phys. J. C* 76.5 (2016), p. 292. DOI: 10.1140/epjc/s10052-016-4120-y. arXiv: 1603.05598 [hep-ex].

[111] *Electron efficiency measurements with the ATLAS detector using the 2015 LHC proton-proton collision data*. Tech. rep. ATLAS-CONF-2016-024. Geneva: CERN, June 2016. URL: https://cds.cern.ch/record/2157687.

[112] Matteo Cacciari, Gavin P. Salam, and Gregory Soyez. "The anti-k_t jet clustering algorithm". In: *JHEP* 04 (2008), p. 063. DOI: 10.1088/1126-6708/2008/04/063. arXiv: 0802.1189 [hep-ph].

[113] Matteo Cacciari and Gavin P. Salam. "Dispelling the N^3 myth for the k_t jet-finder". In: *Phys. Lett. B* 641 (2006), pp. 57–61. DOI: 10.1016/j.physletb.2006.08.037. arXiv: hep-ph/0512210.

[114] Matteo Cacciari, Gavin P. Salam, and Gregory Soyez. "FastJet User Manual". In: *Eur. Phys. J. C* 72 (2012), p. 1896. DOI: 10.1140/epjc/s10052-012-1896-2. arXiv: 1111.6097 [hep-ph].

[115] The ATLAS Collaboration. "Topological cell clustering in the ATLAS calorimeters and its performance in LHC Run 1". In: *Eur. Phys. J. C* 77 (2017), p. 490. DOI: 10.1140/epjc/s10052-017-5004-5. arXiv: 1603.02934 [hep-ex].

[116] Matteo Cacciari and Gavin P. Salam. "Pileup subtraction using jet areas". In: *Phys. Lett. B* 659 (2008), pp. 119–126. DOI: 10.1016/j.physletb.2007.09.077. arXiv: 0707.1378 [hep-ph].

[117] The ATLAS Collaboration. "Performance of pile-up mitigation techniques for jets in pp collisions at $\sqrt{s} = 8$ TeV using the ATLAS detector". In: *Eur. Phys. J. C* 76 (2016), p. 581. DOI: 10.1140/epjc/s10052-016-4395-z. arXiv: 1510.03823 [hep-ex].

[118] The ATLAS Collaboration. "Jet energy scale measurements and their systematic uncertainties in proton-proton collisions at $\sqrt{s} = 13$ TeV with the ATLAS detector". In: *Phys. Rev. D* 96 (2017), p. 072002. DOI: 10.1103/PhysRevD.96.072002. arXiv: 1703.09665 [hep-ex].

[119] The ATLAS Collaboration. "Tagging and suppression of pileup jets with the ATLAS detector". In: *ATLAS-CONF-2014-018* (2014). URL: https://cds.cern.ch/record/1700870.

[120] The ATLAS Collaboration. "Performance of b-Jet Identification in the ATLAS Experiment". In: *JINST* 11.04 (2016), P04008. DOI: 10.1088/1748-0221/11/04/P04008. arXiv: 1512.01094 [hep-ex].

[121] *Optimisation of the ATLAS b-tagging performance for the 2016 LHC Run*. Tech. rep. ATL-PHYS-PUB-2016-012. Geneva: CERN, June 2016. URL: https://cds.cern.ch/record/2160731.

[122] ATLAS Collaboration. "Performance of missing transverse momentum reconstruction with the ATLAS detector using proton–proton collisions at s=13TeV". In: *The European Physical Journal C* 78.11 (Nov. 2018). ISSN: 1434-6052. DOI: 10.1140/epjc/s10052-018-6288-9. URL: http://dx.doi.org/10.1140/epjc/s10052-018-6288-9.

[123] M. Baak et al. "HistFitter software framework for statistical data analysis". In: *Eur. Phys. J. C* 75 (2015), p. 153. DOI: 10.1140/epjc/s10052-015-3327-7. arXiv: 1410.1280 [hep-ex].

[124] ATLAS Collaboration. "Observation and measurement of Higgs boson decays to WW^* with the ATLAS detector". In: (2014). DOI: 10.1103/PhysRevD.92.012006. eprint: arXiv:1412.2641.

[125] The ATLAS Collaboration. "Measurement of the photon identification efficiencies with the ATLAS detector using LHC Run-1 data". In: *Eur. Phys. J. C* 76.12 (2016), p. 666. DOI: 10.1140/epjc/s10052-016-4507-9. arXiv: 1606.01813 [hep-ex].

[126] CMS Collaboration. "Observation of a new boson with mass near 125 GeV in pp collisions at $\sqrt{s}$ =7 and 8 TeV". In: (2013). DOI: 10.1007/JHEP06(2013)081. eprint: arXiv:1303.4571.

[127] T. Abajyan et al. "Observation of a new particle in the search for the Standard Model Higgs boson with the ATLAS detector at the LHC". In: *Physics Letters B* 716 (Sept. 2012), pp. 1–29.

[128] ATLAS and CMS Collaborations. "Measurements of the Higgs boson production and decay rates and constraints on its couplings from a combined ATLAS and

CMS analysis of the LHC pp collision data at $\sqrt{s} = 7$ and 8 TeV". In: (2016). DOI: 10.1007/JHEP08(2016)045. eprint: arXiv:1606.02266.

[129] ATLAS Collaboration. "Performance of the ATLAS Trigger System in 2015". In: (2016). DOI: 10.1140/epjc/s10052-017-4852-3. eprint: arXiv:1611.09661.

[130] ATLAS Collaboration. "Performance of missing transverse momentum reconstruction with the ATLAS detector using proton-proton collisions at $\sqrt{s}$ = 13 TeV". In: (2018). DOI: 10.1140/epjc/s10052-018-6288-9. eprint: arXiv:1802.08168.

[131] The ATLAS Collaboration. "Measurements of gluon–gluon fusion and vector-boson fusion Higgs boson production cross-sections in the $H \to WW^* \to e\nu\mu\nu$ decay channel in pp collisions at s=13TeV with the ATLAS detector". In: *Physics Letters B* 789 (2019), pp. 508–529. ISSN: 0370-2693. DOI: https://doi.org/10.1016/j.physletb.2018.11.064. URL: http://www.sciencedirect.com/science/article/pii/S0370269318309936.

[132] T. Plehn, D. Rainwater, and D. Zeppenfeld. "A method for identifying $H \to \tau\tau \to e\mu\ p_T^{\text{miss}}$ at the CERN LHC". In: (1999). DOI: 10.1103/PhysRevD.61.093005. eprint: arXiv:hep-ph/9911385.

[133] D. de Florian et al. "Handbook of LHC Higgs Cross Sections: 4. Deciphering the Nature of the Higgs Sector". In: (2016). DOI: 10.23731/CYRM-2017-002. eprint: arXiv:1610.07922.

[134] G. Aad et al. "Combined measurements of Higgs boson production and decay using up to 80 fb^{-1} of proton-proton collision data at $\sqrt{s} = 13$ TeV collected with the ATLAS experiment". In: *Phys. Rev. D* 101 (1 Jan. 2020), p. 012002. DOI: 10.1103/PhysRevD.101.012002. URL: https://link.aps.org/doi/10.1103/PhysRevD.101.012002.

[135] N C Benekos et al. *ATLAS Inner Detector Performance*. Tech. rep. ATL-INDET-2004-002. revised version number 1 submitted on 2004-01-15 18:11:09. Geneva: CERN, Dec. 2003. URL: https://cds.cern.ch/record/688762.

[136] The ATLAS Collaboration. *Technical Design Report for the ATLAS Inner Tracker Strip Detector*. Tech. rep. CERN-LHCC-2017-005. ATLAS-TDR-025. Geneva: CERN, Apr. 2017. URL: https://cds.cern.ch/record/2257755.

[137] The ATLAS Collaboration. *Technical Design Report for the ATLAS Inner Tracker Pixel Detector*. Tech. rep. CERN-LHCC-2017-021. ATLAS-TDR-030. Geneva: CERN, Sept. 2017. URL: https://cds.cern.ch/record/2285585.

[138] S. Agostinelli et al. "GEANT4: A simulation toolkit". In: *Nucl. Instrum. Meth. A* 506 (2003), pp. 250–303. DOI: 10.1016/S0168-9002(03)01368-8.

[139] S. Ramo. "Currents Induced by Electron Motion". In: *Proceedings of the IRE* 27.9 (1939), pp. 584–585.

[140] W. Shockley. "Currents to Conductors Induced by a Moving Point Charge". In: *Journal of Applied Physics* 9.10 (Oct. 1938), pp. 635–636. DOI: 10.1063/1.1710367.